



Università degli Studi di Verona

Dipartimento di Neuroscienze Biomedicina e Movimento

Scuola di Dottorato in Scienze della Vita e della Salute

Dottorato di Ricerca in

Medicina Biomolecolare, *curriculum* Biochimica

32° ciclo

*Calcium sensor proteins in hearing and sight.  
Biochemical investigation of diseases-associated variants.*

S.S.D. BIO/10

Coordinatore: Prof.ssa Lucia De Franceschi

Tutor: Prof. Daniele Dell'Orco

Dottoranda: Dott.ssa Giuditta Dal Cortivo

Quest'opera è stata rilasciata con licenza Creative Commons Attribuzione – non commerciale  
Non opere derivate 3.0 Italia . Per leggere una copia della licenza visita il sito web:

<http://creativecommons.org/licenses/by-nc-nd/3.0/it/>



**Attribuzione** Devi riconoscere una menzione di paternità adeguata, fornire un link alla licenza e indicare se sono state effettuate delle modifiche. Puoi fare ciò in qualsiasi maniera ragionevole possibile, ma non con modalità tali da suggerire che il licenziante avalli te o il tuo utilizzo del materiale.



**Non Commerciale** Non puoi usare il materiale per scopi commerciali.



**Non opere derivate** —Se remixi, trasformi il materiale o ti basi su di esso, non puoi distribuire il materiale così modificato.

*Calcium sensor proteins in hearing and sight.  
Biochemical investigation of diseases-associated variants.*

Giuditta Dal Cortivo

Tesi di Dottorato

Verona, 30 Aprile 2020

*To my Grandparents*



A scientist in his laboratory is not a mere technician: he is also a child confronting natural phenomena that impress him as though they were fairy tales.

*Marie Curie*



University of Verona

# ***Abstract***

Ph.D. Course in Biomolecular Medicine, 32nd cycle

Doctor of Philosophy

***Calcium sensor proteins in hearing and sight.***

***Biochemical investigation of disease-associated variants.***

by Giuditta DAL CORTIVO

Calcium is a cation which plays a pivotal role as second messenger, thus its concentration in cells needs to be finely regulated. Many systems work for that purpose, including  $\text{Ca}^{2+}$  sensor proteins, which undergo conformational changes upon  $\text{Ca}^{2+}$  coordination via EF-hands.  $\text{Ca}^{2+}$  sensors can be ubiquitous or tissue specific. Examples in this sense are represented by Guanylate Cyclase Activating Protein 1 (GCAP1) and Calcium- and Integrin-Binding Protein 2 (CIB2), involved in sight and hearing respectively. Missense point mutations in GCAP1 and CIB2 were found to be associated with genetic diseases characterized by retinal dystrophies and/or deafness. During my PhD, I focused my attention on the characterization of two point mutations namely p.Glu111Val (E111V) in GCAP1, leading to Cone/Rod dystrophy in an Italian family, and p.Glu64Asp (E64D) in CIB2, linked to Usher syndrome type 1J (USH1J), a rare disease characterized by the copresence of blindness and deafness. In particular, I spent the first part of the PhD investigating the role of CIB2 which is still under debate, finding that it is *per se* incapable to work as a  $\text{Ca}^{2+}$  sensor under physiological conditions and that the conservative mutation linked to USH1J perturbs an allosteric communication between pseudo-EF1 and EF3, thus blocking the protein in an unfunctional conformation. Then, I characterized E111V GCAP1, finding that it is incapable of regulating its molecular target (Guanylate Cyclase), leading to a constitutive active enzyme and thus a progressively high concentrations of  $\text{Ca}^{2+}$  and cGMP in cells, which may explain the pathological phenotype. Looking for a potential therapeutic approach for Cone-Rod dystrophies, we found that the well-established  $\text{Ca}^{2+}$ -relay model, explaining the gradual activation of Guanylate Cyclase by multiple GCAP molecules following gradual changes in intracellular  $\text{Ca}^{2+}$  concentrations, seems to

be species-specific, since it apparently does not work in the same way in humans as in mouse and bovine photoreceptors. Finally, we identified a general method for the characterization of the interaction between a ubiquitous  $\text{Ca}^{2+}$  sensor protein (calmodulin) and inorganic  $\text{CaF}_2$  nanoparticles, suggesting their suitability as devices for nanomedicine applications.







# Summary

<b>Introduction</b>	<b>15</b>
EF-hand motif and Ca <sup>2+</sup> binding proteins.....	17
Molecular basis of hearing.....	18
The Mechano-electrical transduction process .....	19
CIB2: an untypical calcium sensor protein and its biological target .....	20
CIB2 related disease: Usher syndrome type 1J and Non syndromic deafness (DFNB48) .....	22
Molecular basis of sight.....	23
Phototransduction cascade .....	24
Role of GCAP1 and its biological target .....	26
Diseases associated with GCAP1 point mutations .....	28
CaF <sub>2</sub> nanoparticles as carrier of Ca <sup>2+</sup> -sensor protein.....	31
Aims of this thesis work .....	33
<b>Materials and Methods</b>	<b>35</b>
Materials .....	37
Chemicals.....	37
DNA and peptides .....	37
Instruments.....	37
Columns.....	38
Software .....	38
Methods .....	39
Expression and purification of the recombinant CIB2 and GCAP1 .....	39
NPs preparation .....	42
Chromatographic techniques.....	43
Guanylate Cyclase assay (GC assay).....	46
Gel-based techniques .....	49
Biophysical techniques .....	51
<b>Results</b>	<b>67</b>
Calcium and integrin binding protein 2.....	69
Expression and purification.....	69
Structural analysis: CIB2 response to cations .....	70
Hydrophobicity evaluation.....	73

Affinity for cations .....	75
Oligomeric state investigation: a controversial issue .....	79
Interaction with the target peptide.....	84
Conclusions.....	90
<b>Guanylate Cyclase Activating Protein 1 (GCAP1) .....</b>	<b>93</b>
A novel mutation p.(Glu111Val) in <i>GUCA1A</i> appears in an Italian family with Cone-Rod Dystrophy .....	93
Proteins expression and purification.....	94
GC assay .....	94
Oligomeric state investigation.....	96
Hydrophobicity evaluation.....	98
Structural properties .....	98
Calcium affinity evaluation.....	101
<b>New hypothesis: replacement of mutant protein by extra delivery of WT-GCAP1 .....</b>	<b>103</b>
GCAP2 doesn't regulate GC1 activity.....	103
Exploring the effect of WT GCAP1 extra delivery .....	105
Conclusions.....	108
<b>Work in progress: study of point mutations on residues directly involved in Ca<sup>2+</sup> coordination.....</b>	<b>109</b>
State of art.....	110
Evaluation of hydrophobicity and aggregation propensity .....	110
Oligomeric state investigation.....	113
Structural characterization .....	114
Calcium binding evaluation .....	118
Enzymatic activity.....	119
Conclusions (partial) .....	120
<b>Inorganic NPs as specific carriers for Ca<sup>2+</sup> sensor protein in nanomedicine....</b>	<b>123</b>
Introduction.....	123
CaM had the same structure when in the presence of sole Ca <sup>2+</sup> or CaF <sub>2</sub> NPs.....	124
Affinity and kinetic investigations highlighted physiological relevance .....	126
Conclusions.....	128
<b>Introduction to papers .....</b>	<b>131</b>
Paper 1 <sup>18</sup> : <i>Preferential binding of Mg<sup>2+</sup> over Ca<sup>2+</sup> to CIB2 triggers an allosteric switch impaired in Usher Syndrome Type 1J.</i> .....	131
Paper 2 <sup>22</sup> : <i>Oligomeric state, hydrodynamic properties and target recognition of human calcium and integrin binding protein 2 (CIB2)</i> .....	133

Paper 3 <sup>59</sup> : <i>A novel p.(Glu111Val) missense mutation in GUCA1A associated with cone-rod dystrophy leads to impaired calcium sensing and perturbed second messenger homeostasis in photoreceptors</i> .....	135
Paper 4 <sup>106</sup> : <i>Normal GCAPs partially compensate for altered cGMP signaling in retinal dystrophies associated with mutations in GUCA1A</i> .....	137
Paper 5 <sup>76</sup> : <i>Luminescent and paramagnetic properties of nanoparticles shed light on their interactions with proteins</i> .....	139
List of figures .....	141
List of tables .....	143
List of abbreviations .....	145
References .....	147
Acknowledgments .....	155



# *Introduction*





## EF-hand motif and $\text{Ca}^{2+}$ binding proteins

The EF-hand motif is a super secondary structure element composed by two 10-residues  $\alpha$ -helices separated by a 12-residues loop (**Figure 1**) able to coordinate divalent cations, especially  $\text{Ca}^{2+}$ . The negative charges required for  $\text{Ca}^{2+}$  coordination in a pentagonal bi-pyramidal geometry are given by the side chains of residues 1, 3, 5, and 9, the C=O of residue 7 and a water molecule. Furthermore, EF-hand motifs can also coordinate other divalent cations such as  $\text{Zn}^{2+}$ ,  $\text{Cu}^{2+}$ ,  $\text{Fe}^{2+}$  e  $\text{Mg}^{2+}$ ;<sup>2</sup>. This latter is particularly interesting in a physiological context; thanks to its involvement in a broad variety of processes (i.e. cofactor for many enzymes) its concentration is kept around 1 mM<sup>3</sup>. Nevertheless, EF-hands display a lower affinity for  $\text{Mg}^{2+}$ , preferring the  $\text{Ca}^{2+}$ , due to a very strict  $\text{Mg}^{2+}$ -coordination geometry consisting in six ligands arranged in an octahedron and a smaller ionic diameter of  $\text{Mg}^{2+}$ , which requires a higher dehydration energy.

EF-hand proteins can be divided in two classes:  $\text{Ca}^{2+}$ -buffers and  $\text{Ca}^{2+}$ -sensors. The main difference is that  $\text{Ca}^{2+}$ -sensors change their structure upon cation coordination, and this makes them capable to interact with specific targets, while  $\text{Ca}^{2+}$ -buffers do not show any conformational change.  $\text{Ca}^{2+}$ -sensors can be ubiquitous, such as calmodulin (CaM), or tissue-specific as recoverin (Rec) and guanylate cyclase activating proteins (GCAPs), which are expressed in the retina.

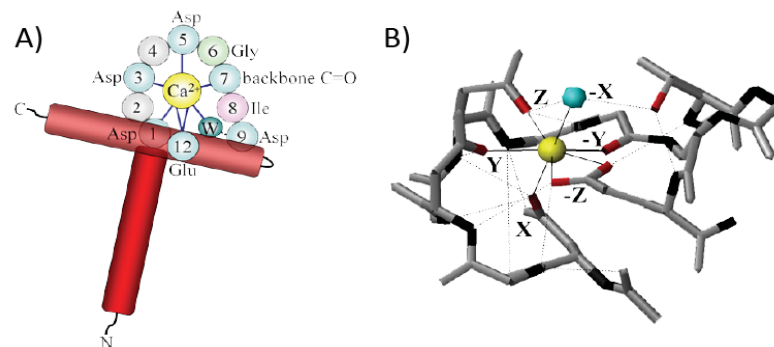


**Figure 1: Representation of EF-hand motif.** A) Schematic representation of  $\text{Ca}^{2+}$  bound EF-hand. Red tubes represent the entering and exiting helices, the numbered spheres represent the loop residues involved in  $\text{Ca}^{2+}$  coordination; W is the water molecule. B) Representation of the canonical EF-hand 1 from CaM with the pentagonal bi-pyramidal geometry highlighted (solid lines). This figure is an adaptation from Ref<sup>1</sup>.

## Molecular basis of hearing

Hearing is performed mainly in the auditory system, where a complex biomechanical machinery allows the conversion of sounds into electrical signals, the universal language used for neuronal communication. The processing of sounds is a thousand-fold faster respect to light processing<sup>4</sup> and, since human communication is mainly mediated by hearing, deafness is considered more debilitating than blindness.

The ear is a complex structure (**Figure 2A**) that can be functionally divided into: i) outer ear, which collects and carries the sound waves through the tympanic membrane; ii) middle ear, where three bones (malleus, incus and stapes) convert an air-diffusing wave to a liquid-diffusing vibration; iii) inner ear, where the cochlea is located, and frequency, amplitude and tone are coded in a mechanism known as mechano-electrical transduction. This process occurs in hair cells, so called for the presence of modified microvilli named stereocilia, located in the upper part of the cell (**Figure 2B**). Thirty to 100 hair cells are organized like a staircase, ranked for increasing height, forming a hair-cell bundle<sup>5</sup>. The stereocilia are connected to each other via tip-links, mainly formed by cadherin 23, protocadherin 15 and harmonin, and side-links, formed by cadherin 23 and protocadherin 15<sup>6</sup> (**Figure 2C**). This spatial organization allows the mechano-electrical transduction, mainly driven by Mechano-Electrical Transduction channels (MET, **Figure 2D**). The MET process is quite known, but molecular information is missing, probably due to the low number of functional MET channels for the analysis, estimated to be no more than 200 per cell in a cochlea, in a pool of 10'000 cells<sup>5</sup>.

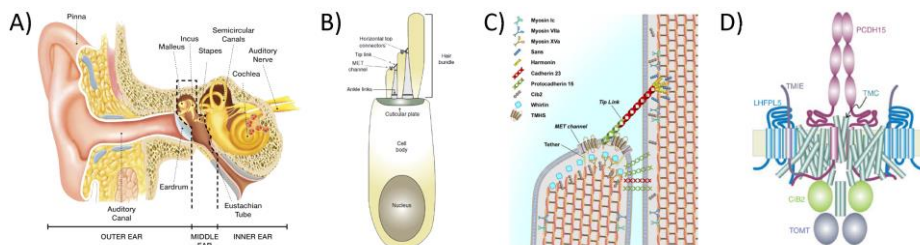


**Figure 2: Structural organization of the ear: from macro to micro.** A) Anatomical description of the ear. B) Schematic representation of a hair cell. C) Zoom in the tip link organization. D) Putative arrangement of the six proteins within the MET channel. Figures are from Refs <sup>6; 7; 8; 9</sup>.

## The Mechano-electrical transduction process

When the sound stimulus reaches the middle ear, the malleus, incus and stapes convert it into a moving wave that diffuses throughout the cochlea, leading to the displacement of the stereocilia (**Figure 3**). When the movement is directed towards the longest cilium, the tip-links stretching causes the opening of MET channels. These channels are selective for  $K^+$  and  $Ca^{2+}$ : higher  $K^+$  concentration induces cell depolarization, while the higher  $Ca^{2+}$  concentration modulates many processes, such as the fusion of neurotransmitter vesicles to the synaptic ribbon<sup>4</sup>. The  $Ca^{2+}$  concentration in the stereocilia is fundamental for many processes, including MET activation and adaptation, consisting in a decrease in MET channel sensitivity in the presence of high  $Ca^{2+}$  concentrations<sup>5</sup>. The MET channel is a complex structure, composed by at least six different proteins, among which the transmembrane channel-like protein 1 and 2 (TMC1 and TMC2) forming the channel pore, which interacts with CIB2<sup>10</sup> (**Figure 2D**), whose real function is yet to be clarified.

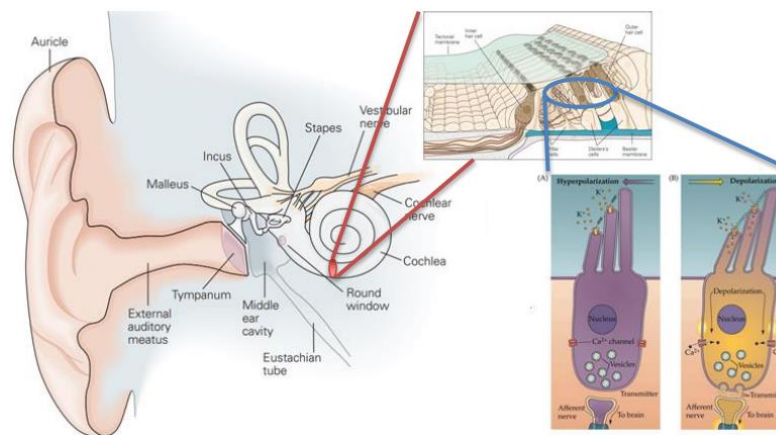


**Figure 3:** Schematic representation of the mechano-electrical transduction. Image in from Ref<sup>11</sup>.

## **CIB2: an untypical calcium sensor protein and its biological target**

CIB2 (*Calcium- and Integrin- Binding Protein 2*) is a 21.7 kDa protein that belongs to the CIB family together with other three members (CIB1, CIB3, CIB4)<sup>12</sup>. CIB2, homolog of CIB1, binds divalent cations like  $\text{Ca}^{2+}$  and  $\text{Mg}^{2+}$  via two canonical EF-hand motifs (**Figure 4**) and has the N-terminal consensus sequence for myristoylation, that may allow the association with membranes. Although CIB2 is expressed in a variety of tissues, its biological function is still unknown. Two recent papers<sup>13; 14</sup> demonstrated the contribution of CIB2 in the auditory cell maintenance, since knockout CIB2 mice show profound hearing loss. Other studies show that CIB2 exerts a role in: i) HIV entrance in cells<sup>15</sup>, ii) negative regulation of oncogenic signaling in ovarian cancer<sup>16</sup>, iii) a compensation system in platelets where its homologous CIB1 is knocked down<sup>17</sup>. Focusing on the CIB2 role in auditory cells, many hypotheses are still under investigation. First, as a possible component of MET channel, the  $\text{Ca}^{2+}$  coordination may be associated with a conformational change that propagates through the channel, resulting in its lower sensitivity during adaptation. Moreover, the lack of a specific compartment for  $\text{Ca}^{2+}$ -storage in the upper part of the hair cell, combined with the necessity to keep the  $\text{Ca}^{2+}$  concentration strictly controlled, may imply a role for CIB2 in  $\text{Ca}^{2+}$ -homeostasis, together with other  $\text{Ca}^{2+}$ -binding proteins such as parvalbumin  $\beta$ , calretinin and calbindin D28K<sup>6</sup>. Although some studies consider CIB2 as a  $\text{Ca}^{2+}$ -buffer<sup>6</sup>, our results show that both  $\text{Mg}^{2+}$  and  $\text{Ca}^{2+}$ -binding triggers a conformational change (**Paper 1**<sup>18</sup>), a typical feature of  $\text{Ca}^{2+}$ -sensor proteins. We furthermore measured the affinity for  $\text{Ca}^{2+}$  and  $\text{Mg}^{2+}$  and concluded that CIB2 is i) probably  $\text{Mg}^{2+}$ -bound under physiological conditions ( $K_d = 290 \mu\text{M}$ ) and ii) an untypical  $\text{Ca}^{2+}$ -sensor with an apparent  $K_d$  of 500  $\mu\text{M}$ , not compatible with the  $\text{Ca}^{2+}$  concentration in the endolymph (20  $\mu\text{M}$ ), the extracellular liquid in contact with the stereocilia<sup>5</sup>. CIB2 is also part of the Usher interactome<sup>19</sup> a group of proteins that, when mutated, lead to different types of Usher syndrome. In fact, CIB2 has been found localized in the upper part of the stereocilia where, together with myosin VIIa and whirlin, may mediate the tip-link assembly<sup>6</sup>. In fact, it was demonstrated that CIB2<sup>-/-</sup> mice show profound hearing loss mainly due to an abnormal assembly of the stereocilia<sup>14</sup> and abolished MET

currents<sup>13</sup>. Finally, CIB2 has been hypothesized to interact with the ATP-gated IP<sub>3</sub>-receptor, modulating purinergic response in outer hair cells<sup>19</sup>.

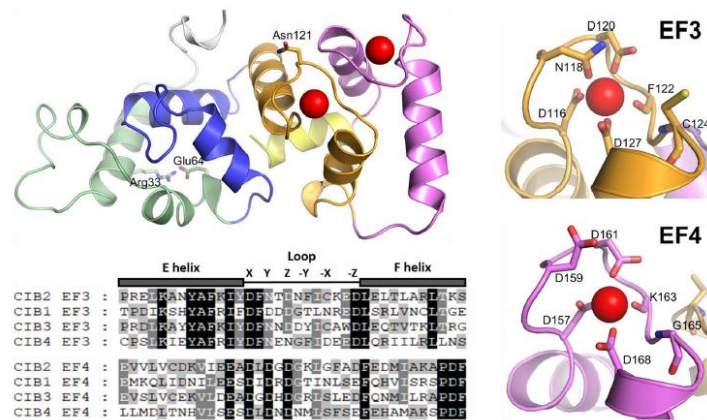


**Figure 4: Structural features of CIB2.** Cartoon representation of monomeric WT CIB2 in its Ca<sup>2+</sup>-bound form. The homology model is based on the X-RAY structure of Ca<sup>2+</sup>-bound CIB1. The N-terminal region is colored in gray, while the C-terminal region (helix 10) is colored in yellow. EF1, EF2, EF3, and EF4 are colored in green, blue, orange, and magenta, respectively. Asn 121 and Glu 64 are represented by sticks, as well as Arg 33, electrostatically interacting with Glu 64. The sequence alignment of CIB2 with CIB1, CIB3, and CIB4 is also shown, restricted to the metal-coordinating EF-hands, namely EF3 and EF4. Amino acids contributing to the coordination of Ca<sup>2+</sup> according to the canonical pentagonal bipyramid geometry are marked by their respective position and labeled in the zoomed-in protein cartoon on the right. Figure and legend are from **Paper 1**<sup>18</sup>.

Concerning the physiological targets, CIB2 can bind two integrins:  $\alpha$ IIB, a common interactor of all CIB family members<sup>17</sup>, and  $\alpha$ 7B, which seems to be a specific partner for CIB2. In this respect, the first interaction study was performed by Häger et al.<sup>20</sup> who found a specific binding with the cytosolic region of the integrin. Later, Huang et al.<sup>21</sup> firstly, and us later on (**Paper 2**<sup>22</sup>), demonstrated that CIB2 preferentially interacts with the fragment of  $\alpha$ 7B located close to the inner membrane, due to a conserved region consisting of eight residues, WK(V/L)GFFKR.

## **CIB2 related disease: Usher syndrome type 1J and Non syndromic deafness (DFNB48)**

Hearing loss is a debilitating disease increasingly widespread, caused by environmental, genetic factors or both. The hear impairment due to defects in the inner ear is named sensory neuronal hearing loss, and it can have different causes: i) noise-induced, a loud noise may cause the tympanic membrane impairment leading the stereocilia detachment; ii) drug-induced, triggered by ototoxic drugs as streptomycin, iii) age-related, resulting in different age of onset, severity or location of the lesion; iv) genetic defects<sup>5</sup>. Hereditary hearing loss has an incidence of 1:1500, it's mostly non-syndromic and monogenic<sup>23</sup> with an autosomal recessive (AR) mechanism of transmission. Up to date, 115 genes (<https://hereditaryhearingloss.org/>) have been found related to non-syndromic deafness, *Cib2* is one of these. Five missense mutations have been found in the CIB2-encoding gene resulting in the following substitutions: E64D, F91S, C99W, I123T<sup>19</sup> and R186W<sup>24</sup>. Four of them are associated with non-syndromic deafness (DFNB48) while E64D seems to be associated with Usher Syndrome type 1J (USH1J), a rare genetic disease characterized by profound hearing loss and blindness due to retinitis pigmentosa<sup>19</sup>. During my PhD I focused my attention on the characterization of E64D CIB2, and our study demonstrated how this conservative point mutation unexpectedly makes E64D CIB2 able to fold correctly only in the presence of extremely high and non-physiological Ca<sup>2+</sup> and Mg<sup>2+</sup> concentrations.

Differently from fishes<sup>25</sup>, which have the capability to replace damaged hair cells, in mammals the damage is permanent, making deafness hard to treat without using hearing aids or cochlear implants. Such external supports can improve the patient's quality life, but a deep understanding of the molecular bases of the disease could allow the development of a personalized therapy based on the mutations carried by each patient.

## Molecular basis of sight

Sight, together with hearing, touch, smell and taste, is one of the ways to acquire information from the environment, in particular, more than 80% of the total information comes from vision<sup>26</sup>. The retina, a multi-layer tissue that allows the conversion of the light stimuli into electrical signal is located at the bottom of the eyeball (**Figure 5A**). The retina is composed by many cell types, the photoreceptors are the ones responsible for light absorption (**Figure 5B**). In vertebrate, photoreceptor cells are classified as rods and cones, responsible for scotopic (dark) or photopic (light) vision, respectively. Photoreceptor cells are divided into three parts: the synaptic terminal, the inner and the outer segments (**Figure 5C**). The inner segment hosts the components required for the cell survival (nuclei, mitochondria, endoplasmic reticulum...), while the outer segment is constituted by a massive membrane system arranged in discs, where the visual process starts. The phototransduction initiates when a photon is absorbed by opsins, proteins belonging to the G-coupled receptor superfamily. At least three different opsins are present in cones, but only Rhodopsin (Rho) has been found in rods.

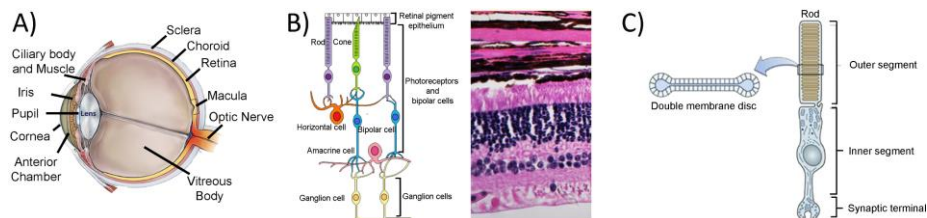


**Figure 5: Eye anatomy: from macro to micro.** A) Anatomical description of the eye structures<sup>27</sup>. B) Schematic<sup>28</sup> (left) and histochemical stain<sup>29</sup> (right) of the retina. C) Schematic representation of the rod structure<sup>30</sup>.

## Phototransduction cascade

In dark-adapted conditions, photoreceptors are partially depolarized, characterized by a membrane potential around -40 mV. This is the result of the equilibrium between the activity of two channels both located in the outer segment: i) cGMP-gated channels (CNG-channels), that allow the continuous influx of  $\text{Na}^+$  and  $\text{Ca}^{2+}$ , ii) a light-independent  $\text{Na}^+/\text{Ca}^{2+} + \text{K}^+$  exchanger (NCKX) that lead to the  $\text{Na}^+$  intake and  $\text{Ca}^{2+}$  and  $\text{K}^+$  efflux (following a stoichiometry of  $4\text{Na}^+ : 1\text{Ca}^{2+} : 1\text{K}^+$ )<sup>31</sup>. When a photon is absorbed by Rho, the isomerization of the photopigment leads to the activation of the G-protein transducin, responsible for the activation of the phosphodiesterase 6 (PDE6). The drop of cGMP concentration, due to the conversion of cGMP into 5'-GMP, leads to the closure of the cGMP-gated channels thus blocking  $\text{Ca}^{2+}$  and  $\text{Na}^+$  intake from the CNG-channels; at the same time NCKX activity is preserved, resulting in the  $\text{Ca}^{2+}$  concentration drop and thus an increase in the membrane potential, reaching values around -65 mV (depending on the stimulus intensity). In this context, a key role is played by  $\text{Ca}^{2+}$ : due to the CNG-channel closure its concentration drops from 600-500 nM to less than 100 nM<sup>32</sup> and this is sensed by Neuronal Calcium Sensor (NCS) proteins such as Rec and GCAPs, each involved in the cascade shut-off in different ways (**Figure 6B**). Low  $\text{Ca}^{2+}$  concentration triggers: i) rhodopsin phosphorylation via rhodopsin kinase (GRK) and ii) guanylate cyclase (GC) activation. These mechanisms are mediated by: recoverin (Rec) and GCAPs respectively. At high  $\text{Ca}^{2+}$  concentrations (dark) Rec is complexed to GRK, inhibiting the enzyme but, when  $\text{Ca}^{2+}$  concentration drops (light), the complex dissociates allowing GRK to phosphorylate rhodopsin, leading to the binding of arrestin<sup>33</sup>. How Rec is capable to change its conformation at these  $\text{Ca}^{2+}$  concentration is still under debate, especially because all the *in vitro* estimates of Rec affinity for  $\text{Ca}^{2+}$  pointed to an apparent  $K_d$  of 17  $\mu\text{M}$ <sup>34</sup>, a concentration way too high for physiological conditions in photoreceptor outer segments. The second mechanism involves GCAPs (GCAP1 and GCAP2), small proteins specifically capable in the activation of GC, the enzyme that converts the GTP into cGMP, restoring its dark-state concentration and ultimately the dark current via CNG-channel re-opening<sup>35, 36</sup> (**Figure 6A**). The specific role of GCAPs is described in the following paragraph.



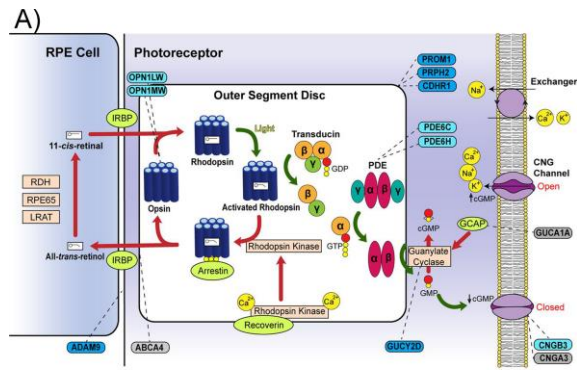
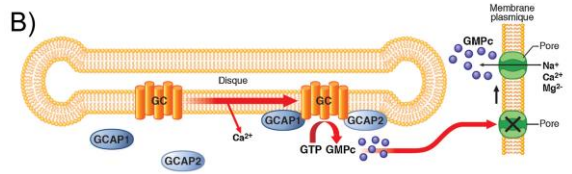


**Figure 6: Phototransduction cascade.**  
 A) Overview of the entire process<sup>37</sup>. B) Detail of the role of GCAP1 in the activation of GC<sup>38</sup>.



## Role of GCAP1 and its biological target

Three are the GCAPs isoforms in human genome: *GUCA1A* and *GUCA1B* genes, coding for GCAP1 and GCAP2 respectively, organized in a *tail-to-tail* array on 6p21.1 (probably from a duplication and inversion of the ancestral gene<sup>39</sup>); *GUCA1C*, coding for GCAP3, located on 3q13.1. Contrarily to GCAP3, expressed only in cones and apparently not involved in the phototransduction cascade<sup>40</sup>, GCAP1 and GCAP2 are expressed both in cone and rods and they are active players in the phototransduction process<sup>40; 41</sup>. In detail, GCAP1 has 4 EF-hand motifs (**Figure 7A**), of which only EF2, EF3 and EF4 are functional, therefore able to bind  $Mg^{2+}$  and  $Ca^{2+}$  ions<sup>42</sup>. Like many other NCSs, GCAP1 has a myristoyl group covalently bound to the N-terminal Gly, and even though it is not involved in the conformational change known as myristoyl-switch (like Rec and NCS1), such post-translational modification has been proved to exert a pivotal role in the modulation of cations affinity and target recognition/interaction<sup>36</sup>. GCAP1 physiological target is the membrane protein GC<sup>35; 43; 44</sup>. Many studies demonstrated how the  $Ca^{2+}/Mg^{2+}$  binding to the canonical EF2-4 led to a conformational change through the non-canonical EF1 which became the GC-binding region<sup>43; 44; 45</sup>. Two are the human retinal GC isoforms: isoform 1 (GC1 or RetGC-E) expressed by *GUCY2D* on 17p13.1, and isoform 2 (GC2 or RetGC-F) expressed by *GUCY2F* on Xp22<sup>46</sup>. Both are composed by: an extracellular domain, a transmembrane  $\alpha$ -helix, a juxtamembrane domain (JMD), a dimerization domain (DD) and a catalytic domain, active only in a dimeric form. Both the GC isoforms participate to the phototransduction giving different contributions<sup>47</sup>. I focused my attention on GC1 regulation and function mediated by GCAP1. Very interesting is that GC1 *per se* it is not sensible to  $Ca^{2+}$  but, in the late '80s Koch and Stryer postulated the existence of a  $Ca^{2+}$ -mediated negative feedback mechanism which makes the GC1 more active when the  $Ca^{2+}$  concentration is the photoreceptor is less than 100 nM<sup>48</sup>. The protein that mediates this process has been named GCAP. A peculiar feature about GCAP1 is its capability to exert on GC1 a role in activating and inhibiting it, based on the cation bound: at high  $Ca^{2+}$  concentrations (500-600 nM,) GCAP1 binds 3  $Ca^{2+}$  ions keeping the GC1 activity at a basal level; when a photon is absorbed and the signal transduction starts, GCAP1 releases  $Ca^{2+}$  ( $EF3 \rightarrow EF2 \rightarrow EF4$ )<sup>44</sup> and binds  $Mg^{2+}$

becoming a GC activator. Moreover, it has been proved the existence of a synergic activity between GCAP1 and GCAP2, at least in bovine, namely  $\text{Ca}^{2+}$ -relay (**Figure 7B**): when the light stimulus activate the cascade, the GCAP1 steps into action firstly, giving a first pulse of cGMP but, if the stimulus continues over time and the  $\text{Ca}^{2+}$  concentration further decreases, GCAP2 becomes an activator in turn. So, GCAP1 and GCAP2 are responsible for different light sensibilities<sup>36; 49</sup>.

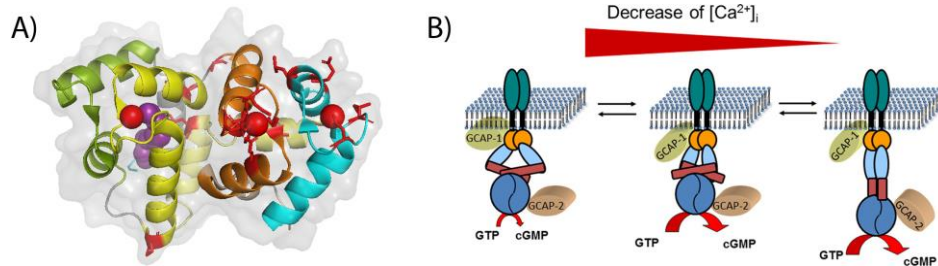


**Figure 7: GCAP1 tridimensional structure and  $\text{Ca}^{2+}$ -relay model.** A) Cartoon representation of human GCAP1 (PDB entry 2R2I). Myristoyl group is colored in deep purple; EF1, EF2, EF3, EF4 are colored in green, yellow, orange and cyan respectively;  $\text{Ca}^{2+}$  ions are represented as red spheres. Red sticks represent the known mutations. B)  $\text{Ca}^{2+}$  relay model from Ref<sup>49</sup>.

## Diseases associated with GCAP1 point mutations

Retinal dystrophies are a class of diseases that can be age-related or triggered by genetic mutations, characterized by autosomal dominant (AD) mechanism of transmission. They can be classified as Macular dystrophy (MD), Cone dystrophy (COD) or Cone-Rod dystrophy (CORD) based on the area of the retina and the cells involved. The clinical phenotype is highly heterogeneous, and the most common symptoms include nystagmus, photophobia, abnormal color perception, nyctalopia, hemeralopia, loss of the central and/or peripheral vision. To date, 22 missense mutations on the *GUCA1A* gene have been found in patients, namely P50L<sup>50</sup>, L84F<sup>51</sup>, G86R<sup>52</sup>, E89K<sup>53</sup>, Y99C<sup>54; 55</sup>, Y99S<sup>56</sup>, Y99N<sup>56</sup>, D100G/E<sup>57</sup>, E102H<sup>58</sup>, E111V<sup>59</sup>, N104K<sup>60</sup>, I107T<sup>51</sup>, T114I<sup>61</sup>, I143N/T<sup>61</sup>, D148E<sup>62</sup>, L151F<sup>46; 53</sup>, E155A/G<sup>63; 64</sup>, G159V<sup>53</sup>, L176F<sup>65</sup> (**Figure 7A**). Even if the first disease-related mutation (Y99C) was found in 1998, 12 of these were identified in the last five years (**Table 1**), probably thanks to the Next Generation Sequencing spread and a more careful investigation during the diagnostic process. All these mutations were deeply investigated and a common feature among them is the incapability in the regulation of GC under physiological conditions, leading to the accumulation of cGMP and Ca<sup>2+</sup> that freely diffuse to the inner segment triggering the cellular death by mechanisms still under investigation. Two are the main hypothesis: on one hand the excess of the cGMP may have cytotoxic effects<sup>66</sup>, on the other hand the high [Ca<sup>2+</sup>] in inner segment may destroy the mitochondria membrane potential, causing the release of Cytochrome C (CytC) and so the activation of the apoptosis process mediated by caspase<sup>63</sup>. However, it is still unclear the reason why some mutations cause COD and other CORD phenotypes.

**TABLE 1: LIST OF ALL GCAPI KNOWN MUTANTS ASSOCIATED WITH RETINAL DYSTROPHIES.**

<b>NUCLEOTIDE CHANGE</b>	<b>Protein change</b>	<b>Protein region</b>	<b>Clinical phenotype</b>	<b>Ref.</b>
<b>C.149C&gt;T</b>	P50L	EF1-EF2 link	COD, CORD	50
<b>C.250C&gt;T</b>	L84F	EF2 helix F	COD, CORD	51
<b>C.256G&gt;C</b>	G86R	EF2-EF3 link	CORD	52
<b>C.265G&gt;A</b>	E89K	EF2-EF3 link	COD, MD; CORD	67
<b>C.295T&gt;A</b>	Y99N	EF3 helix E	COD, CORD	56
<b>C.296A&gt;G</b>	Y99C	EF3 helix E	COD, CORD	54
<b>C.296A&gt;C</b>	Y99S	EF3 helix E	COD, CORD	56
<b>C.299A&gt;G</b>	D100G	EF3 loop, Ca <sup>2+</sup> binding	CORD, MD	57
<b>C.300T&gt;A</b>	D100E	EF3 loop, Ca <sup>2+</sup> binding	COD	67
<b>C.304G&gt;C</b>	D102H	EF3 loop, Ca <sup>2+</sup> binding	CORD	
<b>C.312C&gt;A</b>	N104K	EF3 loop, Ca <sup>2+</sup> binding	COD; CORD, CORD; MD	60
<b>C.320T&gt;C</b>	I107T	EF3 loop	MD	51; 68
<b>C.322A&gt;T</b>	E111V	EF3 helix F	CORD	59
<b>C.341C&gt;T</b>	T114I	EF3 helix F	Atypical RP	
<b>C.428DEL-TINS ACAC</b>	I143T/N	EF4 helix E	COD	61
<b>C.444T&gt;A</b>	D148E	EF4 loop	COD	
<b>C.451C&gt;T</b>	L151F	EF4 loop	COD	46; 56; 67
<b>C.464A&gt;G</b>	E155G	EF4 loop, Ca <sup>2+</sup> binding	COD	63
<b>C.464A&gt;C</b>	E155A	EF4 loop, Ca <sup>2+</sup> binding	CORD	
<b>C.476G&gt;T</b>	G159V	EF4 helix F	COD, CORD	67
<b>C.526C&gt;T</b>	L176F	C-ter	MD	43; 69

*Adaptation from Ref<sup>62</sup>.*



## CaF<sub>2</sub> nanoparticles as carrier of Ca<sup>2+</sup>-sensor protein

As already mentioned, genetic disorders are a class of diseases for which therapeutic treatments are not available yet, the sole treatment of symptoms is used in order to ameliorate the patient's quality of life. Nowadays, gene therapy is fully considered for the treatment of genetic diseases, even if we should keep in mind the high-risk drawbacks, such as the gene integration in unexpected positions. For these reasons, a promising and safer strategy is represented by the protein therapy, an approach based on the replacement of the disease-related protein with the recombinant wild-type (WT) in order to restore a WT-like condition<sup>70; 71</sup>. To do that, carriers are needed that allow the specific delivery in the right compartment (tissue, cell or organelles), with a kinetics compatible with the treatment, and minor or absent side effects. Thanks to the high surface-to-volume ratio, nanodevices (NDs) such as liposomes and inorganic nanoparticles (NPs) represent promising tools. Even if liposomes are almost perfect deliverers thanks to the biocompatibility of the components<sup>72</sup>, they cannot be traced in the organism, unless filled with signal emitting dyes. To overcome this problem, inorganic NPs may be considered as a valid choice. In the last years many studies were performed, also by us, in order to evaluate whether CaF<sub>2</sub> NPs may work as nanodevices suitable for NCSs delivery. It has pointed out that there is a huge variability based on the NPs properties and the protein system considered<sup>73; 74; 75</sup>. In fact, protein integrity is fundamental, from a structural and functional point of view. We used a combination of biophysical techniques in order to characterize the interaction between the prototypic Ca<sup>2+</sup>-sensor protein CaM and NPs composed by a CaF<sub>2</sub> core doped with a mixture of Er<sup>3+</sup> and Yb<sup>3+</sup>. These NPs are intriguing because when properly doped (i.e. mix of rare earth mentioned) they show an anti-Stokes phenomenon named upconversion, which consists in the photons emission at a wavelength that is lower than the wavelength used for the excitation (**Figure 8**). These NPs, if irradiated with IR laser (not penetrating or detrimental for tissue), show the emission at 550 nm. In the study published in 2018 (**Paper 5**<sup>76</sup>), we pointed out how this system may be suitable for CaM delivery since neither structure or function were compromised and that the

kinetics of protein dissociation from the NP was compatible with the usage in nanomedicine. Of course, a more detailed analysis is required in order to shed light about potential side effects or the organism responses.

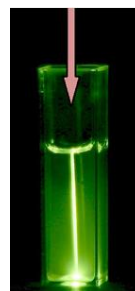


**Figure 8: Upconverting NPs.** The NPs in the figure converts the invisible NIR light into green light<sup>77</sup>.



## Aims of this thesis work

Sight and hearing are two senses by which the brain acquires most of the information about the environment so, genetic disorders causing blindness and deafness represent severe conditions, especially due to the absence of effective treatments. The aim of this PhD thesis is the characterization of the human WT and disease-related variants of CIB2 and GCAP1 in order to gain insights in the molecular basis of the diseases, focusing the attention in the perturbation of the second messenger's homeostasis. Going into details:

- about CIB2  $\Rightarrow$  since it has been proposed to be involved in the  $\text{Ca}^{2+}$  homeostasis in hair cells, I investigated its capability to work as a  $\text{Ca}^{2+}$  sensor and whether the conservative E64D-point mutation lead to the dysregulation of  $\text{Ca}^{2+}$  equilibrium and/or targets recognition capabilities;
- about GCAP1  $\Rightarrow$  after the characterization of the new COD-related point mutation (E111V), I extended the analysis to other known COD/COD-related mutants, where residues directly involved in  $\text{Ca}^{2+}$  coordination are affected (E155A/G and D100G), to better understand whether common features are present or not. Moreover, considering the AD nature of COD and COD diseases, I explored the effect of WT GCAP1 extra delivery with the final aim to slow down the disease progression.

Finally, since upconverting  $\text{CaF}_2$  NPs were demonstrated to be biocompatible and they can be tracked in cells, I investigated their potential employment in nanomedicine as specific nano-devices for NCSs.



# *Materials and Methods*



## Materials

### Chemicals

The chemicals were purchased by Sigma Aldrich, Invitrogen, Biorad, Roche, Life Technologies and Thermo Scientific and the purity level was the highest available.

### DNA and peptides

DNA plasmids:

- pET 24a – WT CIB2 (Genscript)
- pET 11a – WT GCAP1 (Genscript)
- pBB131 - yNMT

Primers:

- Mutagenesis on CIB2 to obtain E64D CIB2:  
FW: 5'-ATCATTCAAATGCCGGACCTGCGTGAGAACCCGTT-3'  
RV: 5'-AACGGGTTCTCACGCAGGTCCGGCATTGGAATGAT-3'
- Mutagenesis on GCAP1 to obtain E111V GCAP1:  
FW: 5'-GCATCGATCGCGACGTACTGCTGACCATTATC-3'  
RV: 5'-GATAATGGTCAGCAGTACGTCGCGATCGATGCA-3'

Peptides were purchased by Genscript:

- $\alpha$ 7B\_M, Ac-LLLWKMGGFFKRAKHPE-NH<sub>2</sub>, (HPLC purity = 96.7%)
- $\alpha$ 7B\_Scrb, Ac-KEFWGLHAKPRLKLMF-NH<sub>2</sub>, (HPLC purity = 96.3%)
- $\alpha$ 7B\_C, LAADHGPELGPDPGHPGTA (HPLC purity = 98.8%)

### Instruments

AKTA start FPLC

AKTA Purifier FPLC

Jasco J-710 spectropolarimeter equipped with a Peltier type cell holder

Jasco FP-750 spectrofluorometer

Zetasizer Nano-S Malvern

SensiQ Pioneer FortèBio

High-Mass Q-TOF II mass spectrometer, Water/MSVision

Ultraflex III MALDI TOF/TOF mass spectrometer, Bruker Daltonik, Bremen

Jasco BS-997-01 High Performance Liquid Chromatography (HPLC)

## **Columns**

HiPrep 26/60 Sephacryl S-200 HR (GE)

Superose 12 10/300 GL (GE)

HiPrep Q HP 16/10 (GE)

HisTrap FF-crude (GE)

LiChrosphere 100 RP-18 (Sigma-Millipore)

Chromolith Performance 100-2 RP-18 (Sigma-Millipore)

## **Software**

Spectra Analysis – Jasco corporation

Zetasizer software, version 7.13

SigmaPlot 12.5

PyMOL Molecular Graphics System, version 2.2.3

## Methods

**Guide:** the paragraphs can be introduced by two symbols:



: they contain theoretical information concerning the technique



: they report the experimental procedures.

### Expression and purification of the recombinant CIB2 and GCAP1



#### *WT CIB2 purification*

The cDNA of human CIB2 isoform 1 was cloned into a pET-24a vector (Genscript) containing a tail of 6 His residues followed by Tobacco Etch Virus protease (TEV) cleavage site. The plasmid was used to transform *E. coli* BL21 DE3 cells. Cells were grown in Luria Bertani (LB) broth at 37°C until the OD<sub>600</sub> reached a value around 0.4, then the flasks were cooled down and, after the induction with 0.5 mM IPTG at OD<sub>600</sub> = 0.6, bacteria were let grown at 15°C for 20h. After centrifugation (5500 rpm, 20 min, 4°C) pellets were suspended in lysis buffer (20 mM TRIS pH 7.5, 500 mM NaCl, 20 mM imidazole, 1 mM DTT, 5 U/mL DNase, 0.1 mg/mL lysozyme, 1 mM PMSF, 2.5 mM MgCl<sub>2</sub>) and incubated at 25°C for 30 min. In addition, 10-12 sonication cycles on ice, 10 sec each, were performed. Soluble and insoluble fractions were separated by centrifugation at 16000 g, 4°C for 30 min. WT CIB2 was found highly concentrated in soluble phase, thus it was filtered and directly loaded in a 5 mL His-trap FF crude column (GE) previously equilibrated with loading buffer (20 mM TRIS, 500 mM NaCl, 20 mM imidazole, 1 mM DTT). A one-step elution was chosen with 500 mM imidazole. To allow TEV-protease activity, His-CIB2 was dialyzed against 50 mM TRIS pH 8, 150 mM NaCl, 1 mM DTT and then incubated (ratio 1:30) with previously prepared His-tagged TEV-protease (**Paper 5<sup>76</sup>**) (or 1:100 ratio of commercial TEV by Promega) overnight at 8-16°C. Tagged free CIB2 was purified from His-TEV by reloading it into the His-trap column, collecting the flow-through. Protein concentration was measured by a CIB2-optimized Bradford assay where the standard line was prepared based on results of the amino acids analysis (Alphalyse). Finally, purified WT CIB2 was

washed in 20 mM TRIS pH 7.5, 150 mM KCl, 1 mM DTT using Amicon concentrator. Protein aliquots were shock-frozen and stored at -80°C.

### ***E64D CIB2: mutagenesis and purification***

E64D point mutation was obtained by site-directed mutagenesis on the complete cDNA of CIB2 using:

FW primer: 5'-ATCATTTCAAATGCCGGACCTGCGTGAGAACCCGTT-3'

RV primer: 5'-AACGGGTTCTCACGCAGGTCCGGCATTGGAATGAT-3'

and setting the thermocycler as follow:

I step: 30 sec at 95°C

<u>II step</u> : 30 sec at 95°C	16 cycles
1 min at 55°C	
7 min at 68°C	

DNA sequencing was provided by Eurofins. Differently from WT, E64D was found highly concentrated in the insoluble phase, thus a purification from inclusion bodies (IB) was required. IB were suspended in the unfolding buffer (20 mM TRIS pH 7.5, 500 mM NaCl, 6M guanidine hydrochloride, 1 mM DTT) and incubated overnight at 4°C. After the loading of unfolded His-CIB2 into the His-trap, a renaturation gradient from 0 to 100% with renaturation buffer (unfolding buffer guanidine-hydrochloride free) was set, with a flow rate of 1 mL/min, 100 mL as total volume. After elution with 500 mM imidazole E64D CIB2 was treated as the WT.



### ***WT and E11IV GCAP1 purification***

The cDNA of human GCAP1 (Uniprot: P43080) was cloned into a pET-11a vector. E6S point mutation was added to generate a suitable substrate for myristoylation by *S. Cerevisiae* N-myristoyl-transferase (yNMT). *E. coli* was co-transformed using both the plasmids and the selection was performed using the resistance for both ampicillin (from pET-11a plasmid) and kanamycin (from pBB131 plasmid).



E111V mutant was generated by polymerase chain reaction site-directed mutagenesis using:

FW primer: 5'- GCATCGATCGCGACGTACTGCTGACCATTATC-3'

RV primer: 5'-GATAATGGTCAGCAGTACGTCGCGATCGATGCA-3'

and setting the thermocycler as follow:

<u>I step</u> : 30 sec at 95°C	
<u>II step</u> : 30 sec at 95°C	16 cycles
1 min at 55°C	
7 min at 68°C	

DNA sequencing was provided by Eurofins. Heterologous expression of GCAP1 were obtained as previously<sup>59; 78</sup>. Briefly: E. coli BL21 DE3 cells were co-transformed using both pET11a and pBB131 plasmids, encoding for GCAP1 variants and yeast NMT respectively. Protein expression was performed at 37°C following the OD<sub>600</sub> values: at OD<sub>600</sub> 0.4 myristic acid (100 µg mg<sup>-1</sup>, in 50% EtOH, pH 7.5) was added, at OD<sub>600</sub> 0.6 protein expression was induced by 1 mM IPTG. Cells were let grow for 4h at 37°C. Proteins were purified from insoluble fraction. Protein denaturation was performed using 6M guanidinium-hydrochloride and incubating resuspended IB at 4°C ON. After 24h dialysis against 20 mM TRIS, 150 mM NaCl, 7.5 mM β-mercaptoethanol, size exclusion chromatography was performed. The purest fractions were then loaded in an anionic exchange column (for further details see below). Some milligrams of the protein obtained were washed against decalcified NH<sub>4</sub>HCO<sub>3</sub>, lyophilized and used for Br<sub>2</sub>-BAPTA chelator assay. The rest of the protein was aliquoted in 20 mM TRIS, 150 mM KCl, 1mM DTT, flash frozen and kept at -80°C.



## **NPs preparation**

$\text{Er}^{3+}$ ,  $\text{Yb}^{3+}$  co-doped  $\text{CaF}_2$  NPs were prepared using the hydrothermal technique described by Pedroni et al.<sup>79</sup>. Briefly,  $\text{Ca}^{2+}$ ,  $\text{Yb}^{3+}$  and  $\text{Er}^{3+}$  were combined at a stoichiometric ratio of 0.78:0.20:0.02 respectively. Sodium citrate was used as capping agent and ammonium fluoride was used as the fluorine precursor. The solution was heat-treated in a Teflon lined autoclave at 190°C for 6 hours and the obtained NPs were precipitated and collected by centrifugation.



## Chromatographic techniques

Chromatography is a widely used technique based on the separation of the single components present in a mixture, thanks to the flow of a mobile phase on a stationary phase. The chromatography techniques can be classified as i) preparative, when used for the purification of molecules, or ii) analytic, when used for the quantification of small amounts of molecules in a sample. During the PhD I had the chance to use many types of chromatography belonging to both categories and briefly described below<sup>80</sup>.

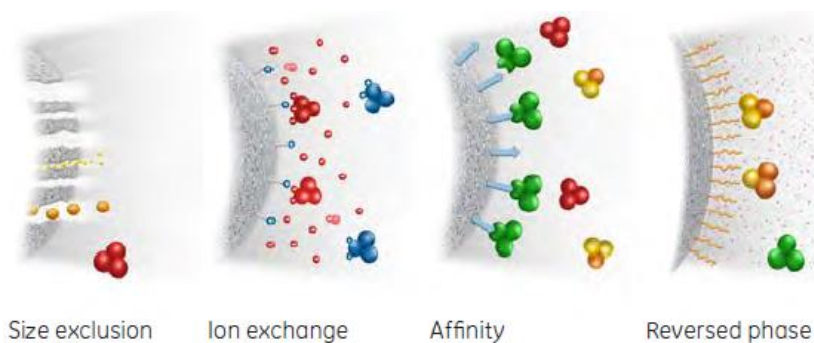


**Figure 9:** Schematic representation of the chromatographic techniques used. Picture is an adaptation from Ref<sup>80</sup>.

### ***Size exclusion chromatography (SEC)***

Size exclusion chromatography allows the separation of molecules based on the hydrodynamic diameter: the smaller the diameter, the higher the retention time (**Figure 9**). I performed preparative SEC as first purification step of GCAP1 and analytic SEC in order to measure the proteins molecular weight (MW).



### ***Preparative SEC***

A HiPrep 26/60 Sephacryl S-200 HR column was used. The column was equilibrated using 20 mM TRIS, 150 mM NaCl, 1 mM DTT. After the sample application (5-7 mL) the elution was followed monitoring the absorbance at 280 nm.



### ***Analytical gel filtration***

A Superose 12 10/300 GL column was used. Standard proteins were loaded in order to obtain a calibration line: *cytochrome C* (12.4 kDa), *carbonic anhydrase* (29 kDa),

*alcohol dehydrogenase* (150 kDa), *β-amylase* (200 kDa). The column was equilibrated using a buffer containing 20 mM TRIS, 150 mM NaCl, 1 mM DTT with either 3 mM EGTA, 2 mM EGTA + 3 mM MgCl<sub>2</sub>, 3 mM MgCl<sub>2</sub> + 2 mM CaCl<sub>2</sub> or 1 mM MgCl<sub>2</sub> + 2 mM CaCl<sub>2</sub>. Seventy to 113 μM proteins were loaded and the elution was followed monitoring absorbance at 280 nm. The elution volumes ( $V_e$ ) was used to measure the distribution coefficient ( $K_d$ ) according to the equation:

$$K_d = (V_e - V_0)/(V_i - V_0)$$

in which  $V_i$  is the total column volume (25 mL) and  $V_0$  is the void volume (8 mL). The MW were determined from a calibration line of log(MW) vs  $K_d$  (**Paper 1<sup>18</sup>**).



### **Anionic exchange chromatography (AEC)**

Ionic exchange chromatography allows the separation based on the net charge of the protein when put in contact with a mobile phase at a given pH (**Figure 9**). The AEC is normally used when the protein's net charge is above the pI, so it will bind positively charged matrixes, so-called anionic exchanger (AEC).



### **AEC purification**

A HiPrep Q HP 16/10 column was used. The column was equilibrated with 20 mM TRIS pH 8, 1 mM DTT and the separation was obtained performing a gradient using 20 mM TRIS pH 8, 1 M NaCl, 1 mM DTT. The protein elutes at an approximate NaCl concentration around 350 - 400 mM.



### **Affinity chromatography (IMAC)**

The affinity chromatography is commonly used when a specific tag is added to the N- or C-terminal of the protein of interest (**Figure 9**). Normally, it guaranties a high purity grade of the final preparation. I used the Immobilized Metal Affinity Chromatography (IMAC) since 6 His residues (His-tag) were added to CIB2 N-terminal. The specific interaction between Ni-NTA resin and the His-tag allows to get rid of the other proteins present in the total extract of *E. Coli*.



### ***His-trap purification***

The HisTrap FF-crude column (GE) was equilibrated using 20 mM TRIS pH 7.5, 500 mM NaCl, 20 mM imidazole, 1 mM DTT and, after the sample application, a one-step elution was chosen using 20 mM TRIS pH 7.5, 500 mM NaCl, 500 mM imidazole, 1 mM DTT. The IMAC column was also used after the His-tag cleavage by TEV-protease. In this case the flow through was kept.



### ***Reverse phase chromatography (RPC)***

The reverse phase chromatography is so called since the mobile phase is more polar than the stationary phase. The resin of these columns is normally composed by silica spheres where C8 or C18 carbon-chains are covalently bound; hydrophilic molecules elute first. In the last years another kind of stationary phase has been introduced, where the silica particles have been replaced by a monolithic matrix, characterized by the presence of mesopores and macropore.



### ***Measure the efficiency of myristoylation for GCAP1***

After the column (LiChrosphere 100 RP-18, Sigma Aldrich) equilibration using ddH<sub>2</sub>O + 0.1% TFA (0.22 nm filtered and degassed), 50 μM of non-myristoylated and myristoylated GCAP1 were loaded. A 55 min gradient was applied using acetonitrile + 0.1% TFA, from 0 to 100%. The comparison of the peak areas allows the measure of the myristoylation efficiency.



### ***Quantification of the cGMP produced during the GC assays***

The C18 (or monolithic) column was equilibrated using 5 mM KH<sub>2</sub>PO<sub>4</sub> and, after sample application (50 μL), a methanol (or acetonitrile) scalar gradient was applied.



## Guanylate Cyclase assay (GC assay)

In order to establish the effect of point mutations on GC1 regulation in the presence of mutant GCAP1, specific enzymatic assays were performed. In the past GC1 came from bovine retina conveniently treated for the extraction of functional rod outer segments (ROS)<sup>81</sup>. This meant that the raw materials were bovine eyes from slaughterhouses that required a specific treatment in order to avoid pigment photo-bleaching. Partially to overcome this issue in 2003 eukaryotic cells, namely HEK293 were engendered in order to obtain a semi-permanent cell line for the expression of human recombinant GC1<sup>40</sup>. Guanylate cyclase assays (GC assay) can be performed in three ways:

- **on-off mode:** it allows to check whether GC1 is regulated or not in the absence ( $< 19$  nM) or in the presence ( $\sim 30$   $\mu$ M) of  $\text{Ca}^{2+}$ .  $\text{K}_2\text{H}_2\text{EGTA}$  or  $\text{K}_2\text{CaEGTA}$  buffers are used (**Figure 10A**);
- **EC<sub>50</sub> estimation:** measuring the cGMP synthesis as function of [GCAP1] (**Figure 10B**) thus the concentration of protein at which GC1 activity is half maximal. Only  $\text{K}_2\text{H}_2\text{EGTA}$  is used in samples preparation. The obtained data are fitted using a ligand binding function with one site saturation:

$$y = \frac{B_{max} * x}{K_d + x}$$

where  $B_{max}$  is the maximum number of cGMP pmol,  $x$  is the [GCAP1] and  $K_d$  is the EC<sub>50</sub> value.

- **IC<sub>50</sub> estimation:** measuring the cGMP synthesis as function of [ $\text{Ca}^{2+}$ ] (**Figure 10C**) thus calculating the concentration of  $\text{Ca}^{2+}$  at which GC1 is half inhibited. Combinations of  $\text{K}_2\text{H}_2\text{EGTA}$  and  $\text{K}_2\text{CaEGTA}$  buffers are used to obtain a specific concentration of free calcium (measured using FURA2 dye). The obtained data are fitted using a Hill 4 parameter function.

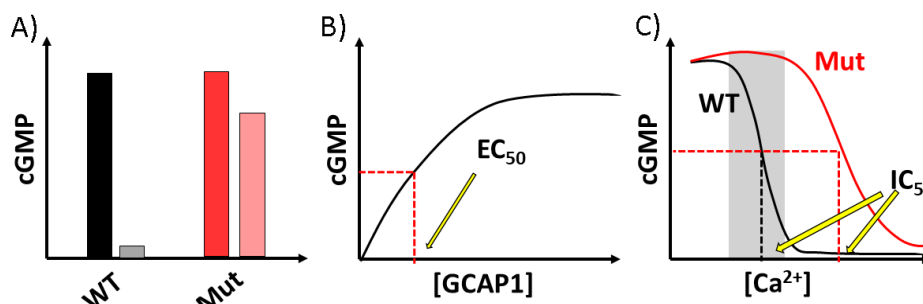


Figure 10: GC assay output. Possible output of GC assay experiments.



### *Semi-permanent cell line*

A semi-permanent cell line expressing human GC1 was obtained transfecting HEK293 cells with pIRES-EGFP plasmid mixed with polyethylenimine (PEI) reagent<sup>82</sup>, and selecting the transfected clones based on the resistance to geneticin (G418). Cells were cultured in DMEM media containing fetal bovine serum (10% v/v), streptomycin (100 µg/mL), penicillin (100 units/mL) and geneticin (500 µg/mL). At 90% confluence cells were harvested, washed with sterile PBS and stored at -80°C. GC1 expression was checked monitoring the GFP fluorescent signal and via western blot analysis, using a polyclonal antibody kindly provided by Prof. Karl Koch from the University of Olbenburg, where I spent three months to learn how to perform GC assay.



### *Guanylate Cyclase assay (GC assay)*

To perform the assay, membranes must be isolated so, firstly, cells pellets are suspended in lysis buffer (10 mM HEPES pH 7.4, 1 mM DTT, protease inhibitor cocktail 1X) and incubated on ice for 20 min. After 15 up-and-down cycles with a 1 mL syringe on ice, cells are centrifugated for 20 min at 10000 rpm. The obtained pellets were suspended in resuspension buffer (50 mM HEPES pH 7.4, 50 mM KCl, 20 mM NaCl, 1 mM DTT). GC assays were performed in three manners: i) on-off mode, 5-10 µM GCAPs was incubated with low (<19 nM) and high (30 µM) Ca<sup>2+</sup> concentrations, ii) titrating GCAPs (0-20 µM) to calculate the EC<sub>50</sub> value and iii) titrating 10 µM GCAPs with different Ca<sup>2+</sup> concentrations (<19 nM - 1 mM) to calculate the IC<sub>50</sub> value. Furthermore, to investigate the hypothesis for which an extra delivery of GCAP1 may compensate the presence of E111V GCAP1, special IC<sub>50</sub> GC assay were designed incubating: 5µM WT GCAP1 + 5µM E111V GCAP1 (simulation of the heterozygous conditions), 10 µM WT GCAP1 + 5µM E111V GCAP1 (2:1 ratio), 15 µM WT GCAP1 + 5µM E111V GCAP1 (3:1 ratio). The assay consists in the incubation for 5 minutes at RT of the diluted proteins with a fixed amount of extracted membranes, reaction buffer (30 mM MOPS pH 7.2, 20 mM KCl, 10 mM, 4 mM NaCl, 1 mM DTT, 3.5 mM MgCl<sub>2</sub>, 1 mM GTP, 300 µM ATP, 160 µM Zaprinast) is added and the samples are incubated for 5 minutes at 30°C. The reaction is stopped adding 50 mM EDTA and incubating the samples at

98°C for 5 minutes. After a centrifugation step at 13000 rpm, supernatant is loaded in C-18 reverse phase column (or monolith) and the amount of cGMP produced is evaluated calculating the area beneath the cGMP elution peak. Data are normalized based on the total amount of membrane-proteins measured via amido black assay.





## Gel-based techniques

Polyacrylamide Gel Electrophoresis (PAGE) is a simple and widely used technique that can be used in different ways. In denaturing conditions, thus in the presence of Sodium-Dodecyl-Sulphate (SDS-PAGE), not only the purity of a protein sample can be evaluated, but also it gives a rough idea about the capability of NCSs to bind  $\text{Ca}^{2+}$ . In fact, it is known that some NCSs migrate in an SDS-PAGE with a different MW whether in the presence or absence of  $\text{Ca}^{2+}$ , phenomenon named gel-shift<sup>83</sup>. Instead, in native conditions (Native-PAGE) it is possible to i) follow the complex formation between a protein and its biological target<sup>84</sup>, ii) roughly measure the MW, thus deducing the oligomeric state of a protein in certain conditions performing a Ferguson Plot<sup>85</sup>.



### *SDS-PAGE gel shift*

Thirty  $\mu\text{M}$  of any protein were incubated 5 minutes at  $25^\circ\text{C}$  with 5 mM EDTA or 5 mM EGTA + 1.1 mM  $\text{Mg}^{2+}$  or 1 mM  $\text{Mg}^{2+}$  + 5 mM  $\text{Ca}^{2+}$ , loaded in a 15% polyacrylamide gel, let run for 40-45 min at 200 V (constant) and Coomassie blue stained.



### *Ferguson plot*

Three native continuous gels were polymerized, using increasing acrylamide concentration (10%, 12% and 15%). Eight micrograms of CIB2 were incubated at room temperature in the presence of 4.5 mM EGTA, 3 mM EGTA + 4.5 mM  $\text{Mg}^{2+}$  and 4.5 mM  $\text{Mg}^{2+}$  + 3 mM  $\text{Ca}^{2+}$  (**Paper 1<sup>18</sup>**) and loaded on the gels. Three and 5  $\mu\text{g}$  of fresh BSA were used as a standard, since the BSA propensity to run in a native gel as monomer (66 kDa), dimer (134 kDa) and trimer (205 kDa). Gels run at constant voltage (200V) for 35 minutes and Coomassie blue stained overnight. BSA bands were used for creating a Ferguson plot, thus calibration curve that allow for the calculation of the molecular weight of CIB2 bands<sup>85</sup>.



### *Limited proteolysis*

**CIB2:** limited proteolysis experiments were performed incubating 25  $\mu\text{M}$  CIB2 in the presence of 1 mM EDTA or 500  $\mu\text{M}$  EGTA + 1 mM  $\text{Mg}^{2+}$  or 1 mM + 2 mM

Ca<sup>2+</sup> with Trypsin (Sigma) in ratio 1:100 (enzyme:CIB2). Working buffer was 20 mM TRIS pH 7.5, 150 mM KCl, 1 mM DTT. The reactions were blocked adding sample buffer (4X) and boiling the sample 5-10 min. Samples were loaded in polyacrylamide gel (15% or 18%), let for 45 min at 200 V and Coomassie blue stained.

**CaM:** 6 µg of CaM were incubated in the presence of 2 mM Ca<sup>2+</sup> or EGTA with 0.3 µM Trypsin (ratio 1:60 enzyme:CaM) at 25°C using 5 mM TRIS, 150 mM KCl, 1 mM DTT as working buffer. Proteolysis samples were collected at different times, from 30 min to 120 min. Since 30 min were found to be enough for a complete proteolysis, the experiment was repeated in order to assess the role of NPs. Thus, 3.8 mg/mL NPs (ratio 1:139, stoichiometric ratio calculated is in Ref<sup>73</sup>) were incubated with 21 µM CaM both in the presence and in the absence of 250 µM EGTA. A further sample was prepared, where 21 µM CaM was incubated with 250 µM EGTA or Ca<sup>2+</sup>. Reactions were blocked after 30 min and treated as previously described.

## Biophysical techniques



### *Br<sub>2</sub>-BAPTA chelator assay*

The chelator assay is an indirect technique that allows the measurement of macroscopic binding constants following the competition for  $\text{Ca}^{2+}$  binding between  $\text{Ca}^{2+}$ -binding proteins and chromophoric chelators such as  $\text{Br}_2\text{-BAPTA}$ <sup>86</sup>. The assay is relatively simple to perform and requires only a spectrophotometer and highly decalcified material (protein, buffer, cuvettes). The technique is based on the two different maxima exhibited by  $\text{Br}_2\text{-BAPTA}$  when in  $\text{Ca}^{2+}$ -free (263 nm) or  $\text{Ca}^{2+}$ -saturated (239.5 nm) condition (**Figure 11**). Thus, if the NCS and  $\text{Br}_2\text{-BAPTA}$  have roughly the same affinity for  $\text{Ca}^{2+}$ , is possible to perform a titration where the  $A_{263}$  progressively decreases: the higher the competition, the slower the absorbance decreases. The data are then analyzed using  $\text{CaLigator}$ <sup>87</sup> a specific software that, knowing total concentration of  $\text{Ca}^{2+}$ , chelator and protein can solve the macroscopic binding constant for each binding site. Both CIB2 and GCAP1 were tested in this sense, but only GCAP1 showed a real competition with  $\text{Br}_2\text{-BAPTA}$  (see Results). In order to measure the CIB2 affinity for  $\text{Ca}^{2+}$  I optimized an alternative method based on the variation in secondary structure (see below).



**Figure 11:  $\text{Br}_2\text{-BAPTA}$  features.** Structure and comparison of the  $\text{Ca}^{2+}$ -free (dashed line) and  $\text{Ca}^{2+}$ -saturated (solid line) spectra. The figure is and adaptation from Ref<sup>86</sup>.



### *Chelator assay*

Lyophilized proteins were dissolved in decalcified buffer (20 mM TRIS, 150 mM KCl, 1 mM  $\text{Mg}^{2+}$ , 1 mM DTT) in the presence of 24-25  $\mu\text{M}$   $\text{Br}_2\text{-BAPTA}$ ; protein concentration was measured by Bradford Assay optimized for human GCAP1 based on determination of precise protein content by amino acids analysis of initial stocks (Alphalyse). Absorbance at 263 nm was followed upon addition of small volumes (0.8  $\mu\text{L}$ ) of 3 mM  $\text{Ca}^{2+}$  stock. For both WT and E111V GCAP1 variants

the experiment was performed in triplicate. Data fitting was performed using Ca-Ligator<sup>87</sup> software, which allows to calculate the macroscopic binding constant (and then apparent affinity constants) fixing parameters like protein and chelator concentrations, the first and last points of the titrations, starting  $Ca^{2+}$  concentration. Since the fitting with 3 calcium binding sites gave extremely unreliable results, the model with two bind sites was considered. Presented data were normalized as follow:

$$y_{norm} = \frac{A_{263} - A_{min}}{A_{max} - A_{min}} \quad Ca^{2+}_{norm} = \frac{[Ca^{2+}]}{[Q] + 3 * [P]}$$

where [Q] and [P] are Br<sub>2</sub>-BAPTA and GCAP1 concentrations respectively.



## Circular dichroism

An electromagnetic radiation such as light consist of an electric and a magnetic field that oscillates perpendicularly to one another and to the direction of propagation, like a transverse wave. Light can be linearly polarized, by selecting one plane in which the electric field can oscillate in a fixed direction, or circularly polarized, by a combination of two linearly polarize perpendicular light planes, either clockwise (right-handed, R) or counterclockwise (left-handed, L). When circularly polarized light passes through an absorbing optically active medium (a solution containing chiral centers as amino acids), the L-component and the R-component are differently absorbed, with the resulting light being elliptically polarized (**Figure 12**).

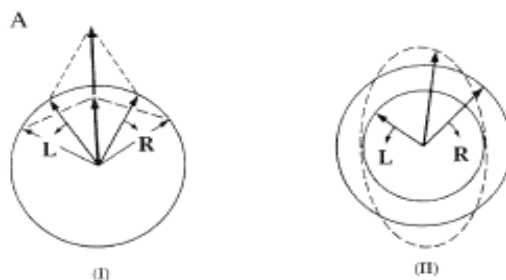


**Figure 12: Origin of the CD effect.** The left (L) and right (R) circularly polarized components of plane polarized radiation: (I) the two components have the same amplitude and when combined generate plane polarized radiation; (II) the components are of different magnitude and the resultant (dashed line) is elliptically polarized. Figure and legend are an adaptation from Refs<sup>8, 88</sup>

The instrument that allows the circularly polarized light analysis is called spectropolarimeter (or CD) that, based on his internal architecture, measures the different adsorption of L and R components<sup>88</sup>. CD output is a plot in which on abscissa there is wavelength, while on ordinate the ellipticity variation (measured in mdeg), mathematically express as:

$$\theta = \tan^{-1} \left( \frac{b}{a} \right)$$

where  $a$  and  $b$  are defined as the major and the minor ellipse components. Usually CD signal is particularly weak, with an ellipticity around 10 mdeg. CD allows to obtain different information, according to the setting of the instrument. Working in the far UV window (200-240 nm), one can gain information about the secondary structure since  $\alpha$ -helix,  $\beta$ -sheet or random coil have typical spectra (**Figure 13A**).

Moreover, in the presence of a protein formed by a combination of them, is possible to perform the spectra deconvolution using specific algorithms, in order to measure the contribution of each to the final structure. Working in the near UV window (260-320 nm) is possible to have information about the tertiary structure monitoring the aromatic amino acid environment (**Figure 13B**). In fact:

- phenylalanine (Phe) shows weaker but sharper bands with fine structure between 255- 270 nm;
- tyrosine (Tyr) shows a band between 275-282 nm;
- tryptophan (Trp) shows a band close to 290 nm with fine structure between 290-305.

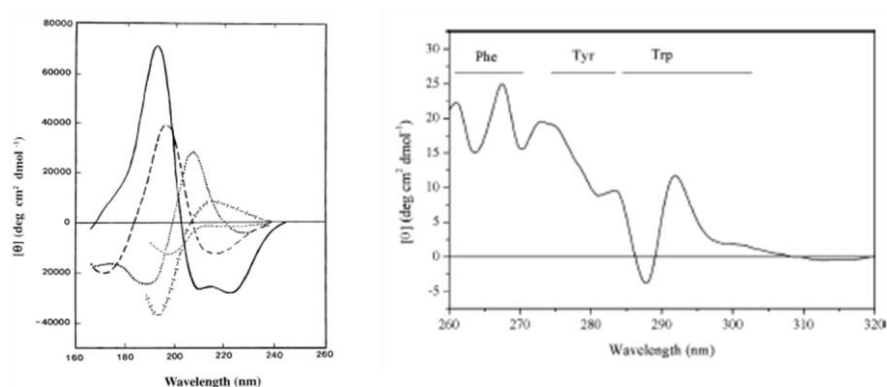


**Figure 13: Far UV and near UV spectra.** (A) Far UV CD spectra associated with various types of secondary structure. Solid line,  $\alpha$ -helix; long dashed line, anti-parallel  $\beta$ -sheet; dotted line, type I h-turn; cross dashed line, extended 31-helix or poly (Pro) II helix; short dashed line, irregular structure. (B) The near UV CD spectrum for type II hydroquinone from *Streptomyces coelicolor*. The wavelength ranges corresponding to signals from Phe, Tyr and Trp side chains are indicated, but it should be emphasized that there can be considerable overlap between the Tyr and Trp signals. Figure and legend are an adaptation from Ref<sup>88</sup>.



### Near-Far UV spectra and thermal denaturation profiles

Near UV spectra were recorded at 37°C using 20-30  $\mu$ M proteins after sequential additions of 0.5 mM EGTA, 1 mM MgCl<sub>2</sub> and 1 mM CaCl<sub>2</sub>. Far UV spectra were collected at 37°C using 10-12  $\mu$ M proteins after sequential additions of 300  $\mu$ M EGTA, 1 mM MgCl<sub>2</sub> and 600  $\mu$ M CaCl<sub>2</sub>. Spectra of the sole solvent (20 mM TRIS, 150 mM NaCl, 1 mM DTT) were collected and considered as blank. Quartz cuvette were used for both near UV (1 cm) and far UV (0.1 cm) recordings.

Thermal denaturation profiles were collected in the same conditions used for far UV measurements, monitoring the ellipticity at 222 nm in a temperature range between 20°C to 96°C (scan rate 90°C/h). Data were fitted using the Hill 3 parameter function.



### *Affinity estimation for Ca<sup>2+</sup> and Mg<sup>2+</sup> binding on CIB2*

Since CIB2 showed a low affinity for Ca<sup>2+</sup> (see Results), I optimized a titration method based on the huge variation in the secondary structure upon ions binding. Each titration point represents an independent sample where 0.5 µL of Ca<sup>2+</sup>/Mg<sup>2+</sup> stock solutions were added to the fixed volume (200 µL) of 12 µM WT or E64D CIB2 aliquots in the presence of 1 mM EGTA. After 3 min incubation at 25°C, three replicas were collected. The free ions concentrations in the stock solutions were determined using MaxChelator software (<http://maxchelator.stanford.edu/>), fixing ionic strength, pH and temperature. The titrations were performed either in the absence and in the presence of α7B\_M peptide.



## **Fluorescence spectroscopy**

Fluorescence is a physical phenomenon based on the capability of some molecules to emit light at a higher wavelength (low energy) after the excitation of their external electronic states. In fact, after the excitation, the promoted electrons must come back to the ground state. If collisions with other molecules take place, the promoted electrons lose part of the vibrational energy and return to the ground state emitting a photon<sup>89; 90</sup>. Proteins can act as fluorophores thanks to the presence of aromatic amino acids such as Phe, Tyr, Trp, and fluorescence spectroscopy can be used for many different investigations. Trp is the most commonly used natural probe thanks to the presence of the indole group that has a maximum of absorption at 280 nm and a peak of emission between 310-350 nm. Trp fluorescence gives information about the protein folding state: denaturation or increased solvent exposure of Trp lead a red-shift (bathochromic shift) of the maximum of emission, vice versa a more compact structure or interaction with other molecules leads to a blue-shift (hypsochromic shift)<sup>90; 91</sup>. In the absence of Trp residues, as for CIB2, to gain this information, I used a fluorescent probe named 8-anilino-1-naphthalensulfonic acid (ANS), an organic compound that has different fluorescence properties when bound to the hydrophobic patches of a protein. I used fluorescence spectroscopy to i) investigate structural variations on CIB2-ANS upon metal binding, ii) estimate a  $K_d^{app}$  and the stoichiometric ratio in the formation of the CIB2 –  $\alpha 7B\_M/scrB$  complex, monitoring the peptide intrinsic fluorescence.



## **ANS fluorescence**

Two micromolar CIB2 was incubated in the presence of 30  $\mu$ M ANS in 20 mM HEPES pH 7.5, 150 mM KCl, 1 mM DTT. Fluorescence spectra were measured at 37°C after sequential additions of 500  $\mu$ M EDTA, 1 mM  $MgCl_2$  and 1 mM  $CaCl_2$  using  $\lambda^{exc} = 380$  nm and recording in a range between 400-650 nm, 5 nm bandwidths. Three spectra for each condition were collected and averaged.





### Peptide titrations

Four micromolar of  $\alpha 7B\_M$  peptide was titrated at 37°C adding increasing concentrations of WT or E64D CIB2 in 20 mM HEPES, 150 mM KCl, 1 mM DTT, 1 mM MgCl<sub>2</sub> and 1 mM CaCl<sub>2</sub>. The Trp residue on the peptide was specifically excited at 295 nm and the spectra were recorded between 300-400 nm. Concerning the  $\alpha 7B\_scrb$ , only three WT CIB2 concentrations were tested (2, 4, 8  $\mu$ M). The apparent equilibrium dissociation constant ( $K_d$ ) was calculated using the equation:

$$y = y_0 + ax / (K_d + x)$$

where  $y_0$  is the wavelength of the maximum emission peak of  $\alpha 7B\_M$  without proteins,  $x$  is the protein concentration, and  $a$  is the difference between the maximum and normalized value  $(1/\lambda) \cdot 10^5$  of the peptide emission peak as function of  $x$  (**Pa-per 1<sup>18</sup>**).

## Dynamic light scattering

Dynamic Light Scattering (DLS) is a *in solution* technique that allow the estimation of size, volume and number of the particles that makes a sample. The technique is based on the fact that shining a coherent and monochromatic light beam (laser) onto a solution, the particles that are moving following Brownian motions, scatter the light behaving as a second light source. Performing measurements at increasing time intervals, the instrument follows the variations in intensity, correlating them with the diffusion coefficient which is inversely related to the particle size: the smaller the particle, the higher the diffusion coefficient (**Figure 14**). Since DLS measurements assume that the particles are spherical, using the Stokes-Einstein equation is possible to calculate the hydrodynamic radius (R):

$$D = \frac{kT}{6\pi\eta R}$$

In order to have a reliable estimation of the particle size, a monomodal Gaussian distribution is recommended.

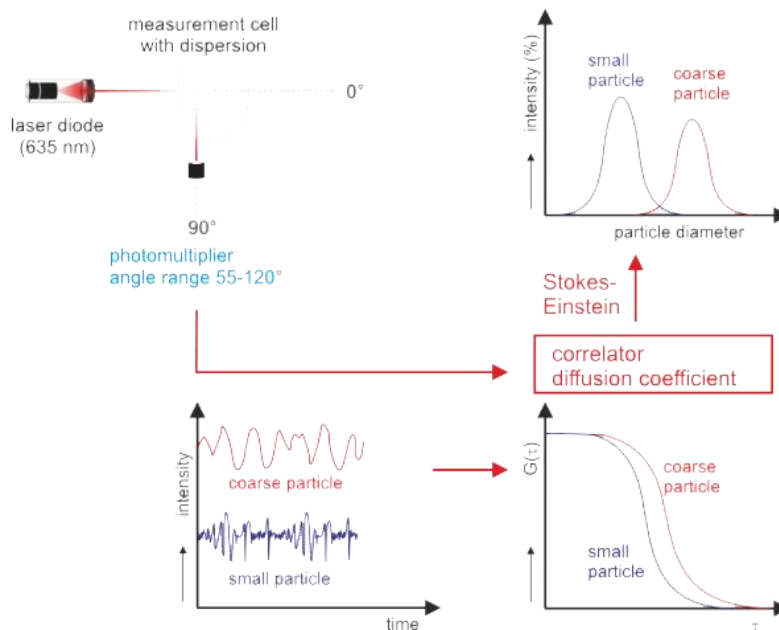


Figure 14: How DLS works<sup>92</sup>.



### ***DLS measurements***

DLS was used to investigate size variations upon ions binding. In order to estimate the hydrodynamic diameter of the proteins after analytical SEC separation, samples were tested both at 25°C and 37°C after 2 min equilibration. The estimation was based on 15-30 measurements, each consisting in 12 repetitions. Viscosity and refractive index were set to 0.6864 cP and 1.33 respectively (default values for water), measurement angle was 173° backscatter and the analysis model was multiple narrow modes. Performing measurements for longer time is possible to follow the protein propensity to form large aggregates monitoring the variation of the parameter named *mean count rate* (MCR), defined as the average scattering intensity. Variations in MCR are related to changes in colloidal properties of the solution, thus the identification of aggregation or precipitation processes.



## Surface plasmon resonance

Surface Plasmon Resonance (SPR) is a technique used for studying of binding phenomena between molecules, ranging from ions to viruses. The very low amount of material required, and the high sensitivity make SPR a powerful tool for the investigation of binding kinetics and specificity. The technique is based on the measurements of the variation in the refractive index of a light beam that collide with the chip surface, composed by a glass slide covered by a thin gold surface. The gold surface is covered by a dextran matrix where the *target* is immobilized and provide the hydrophilic environment for the interaction with the *analyte* (**Figure 15A**). Surface plasmon resonance phenomenon causes shift of the dip corresponding to the angle at which total internal reflection occurs. When a binding event takes place, the reflective index in proximity of the glass side changes. The results in monitoring the refractive index variation is named *sensorgram* (**Figure 15B**), a plot that show the binding response in y axis over time, x axis<sup>93</sup>.

SPR was used to investigate i) CIB2 oligomerization process, ii) kinetics of the interaction of CIB2 with three peptides ( $\alpha 7B\_M$ ,  $\alpha 7B\_Scrb$  and  $\alpha 7B\_C$ ); two immobilization protocols were used.

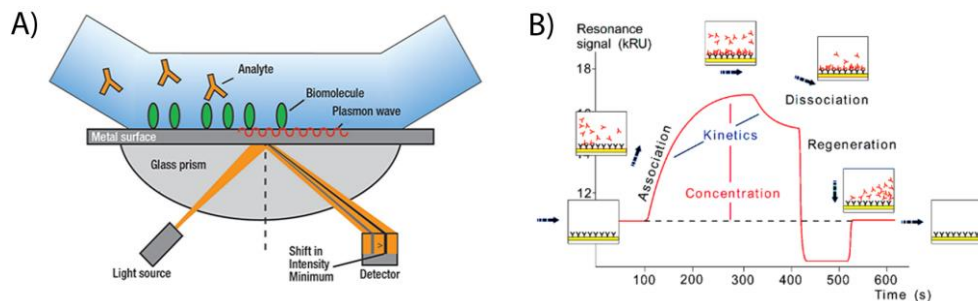


**Figure 15: How SPR works.** A) Schematic representation of the SPR principle<sup>94</sup>. B) Example of sensorgram<sup>95</sup>.



## SPR measurements

### Approach 1: heterogenous immobilization on COOH5 sensor chip

CIB2 was immobilized on the surface of a COOH5 sensor chip (FortèBio) using HBS (20 mM HEPES, 150 mM KCl, 1 mM DTT, 1mM MgCl<sub>2</sub>, 50  $\mu$ M EDTA, 0.005% Tween 20) as immobilization- and running-buffer. Carboxyl groups were mobilized performing sequential injections of 60  $\mu$ L of 10 mM H<sub>2</sub>PO<sub>4</sub> (or HCl), HBS, 10 mM NaOH and HBS, twice (flow rate 5  $\mu$ L min<sup>-1</sup>). Then, the sensor chip

surface was activated performing 7 min injection of a mixture of 10 mM H-hydroxysuccinimide (NHS) and N-ethyl-N'-(dimethylaminopropyl)carbodiimide (EDC) at a flow rate of 5  $\mu\text{L min}^{-1}$ . Fifty nanomolar of CIB2 in Na-acetate buffer (pH 3.1, 1.52 pKa units below the pI) was injected at 10  $\mu\text{L min}^{-1}$ ; 130 RU were immobilized in the flow cell (FC) 1, 226 in the FC3 (1 RU = 1  $\text{pg mm}^{-2}$ ). The reactive group in excess were blocked injecting 70  $\mu\text{L}$  of 1M ethanolamine hydrochloride-NaOH, pH 8.5. FC2 was activated and deactivated and considered as reference.

In order to test the oligomerization process, several CIB2 concentrations (ranging from 92 nM to 46  $\mu\text{M}$ ) were injected on the immobilized protein at a FR of 20  $\mu\text{L min}^{-1}$ . The same sensor chip was used to investigate the interaction with three peptides:  $\alpha 7\text{B\_M}$ ,  $\alpha 7\text{B\_Scrb}$  and  $\alpha 7\text{B\_C}$  were diluted in a range between 0.9 – 30  $\mu\text{M}$  and injected four times for 2 minutes with a FR of 20  $\mu\text{L min}^{-1}$  (**Paper 2<sup>22</sup>**).

#### *Approach 2: homogenous immobilization on HisCap sensor chip*

His-CIB2 was uniformly immobilized by the specific interaction between the His-tag and the functional group of Nitrilotriacetic resin (NTA) that specifically bind Nickel ions. Since previous experiments performed with the same sensor chip type showed a drift in the protein content over time, after the CIB2 orientation via His-tag, the activation of carboxy group as above allows a more stable protein immobilization. On the approximately 2250 RU immobilized, several peptide concentrations were injected ranging from 230 nM – 30  $\mu\text{M}$ . Each injection was repeated four times. Running buffer (HBS) was composed by 20 mM HEPES, 150 mM KCl, 1 mM DTT, 1 mM  $\text{MgCl}_2$ , 0.005% Tween 20. Two millimolar  $\text{CaCl}_2$  was further added to check whether the process was influenced by  $\text{Ca}^{2+}$ .



## Chemical cross-linking and mass spectrometry

To date, three are the mainly used techniques for the protein structure resolution: X-ray crystallography, Nuclear Magnetic Resonance (NMR) and cryo-electron microscopy (Cryo-EM). Unfortunately, all have limits that sometimes make them not reliable for studying protein's structure or protein-protein interactions. In fact, the huge amounts of purified protein required, combined with the high concentration, may lead the formation of artifact structures/complexes. Moreover, different proteins need different crystallographic conditions, and it's not sure that a protein can form diffracting crystals. To overcome these limits, in the last two decades a new technique has been getting popularity, named chemical cross-linking coupled with mass spectrometry<sup>96</sup>. It consists in blocking a protein, or a complex, in a certain structure using cross-linker molecules, which works as molecular ruler: only residues with a specific group can react with the cross-linker forming a covalent bond that keeps them together (**Figure 16**). I had the chance to use 3 different cross-linkers namely disuccinimidyls-dibutirric-urea (DSBU), 1,1'-carbonyldiimidazole (CDI) and photomethionine (PhotoMet) characterized by different lengths and reactivity, summarized in **Table 2**. Normally, after the cross-linking reaction the samples are digested and analyzed by mass spectrometer (Orbitrap Fusion Tribrid, Life Technologies); the output is processed using a specific software named MeroX<sup>97</sup> that allows the assignment of the interacting peptides with a library of proteins sequences. This kind of analysis is normally used for proteomic investigations and the protocol is fully described in Ref<sup>98</sup>. For my analysis, I used cross-linking in order to investigate i) the CIB2 oligomeric state and ii) to obtain stable complexes of CIB2 in the presence of three different peptides; the cross-linked samples I had were analyzed by using Matrix Assisted Laser Desorption Ionization (MALDI-TOF). To learn this technique, I spent around three months in Prof. Andrea Sinz lab in Halle (Leipzig).

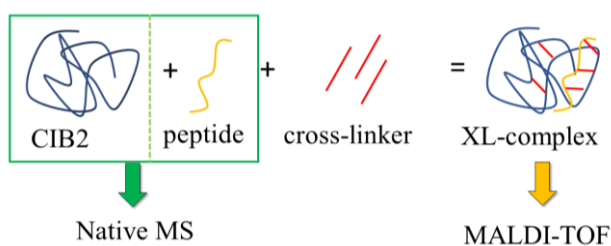


*Figure 16: Workflow followed for XL-MS experiments.*



### *Chemical cross-linking reaction*

Cross-linking reactions were performed as described in Ref <sup>98</sup> and published by us in **Paper 2<sup>22</sup>**. Briefly, 10  $\mu$ M CIB2 (in 20 mM HEPES pH 7.5, 150 mM KCl, 1 mM DTT, 1 mM MgCl<sub>2</sub>, 2 mM CaCl<sub>2</sub>) was incubated at RT for 10 min with increasing concentrations of peptides  $\alpha$ 7B\_M,  $\alpha$ 7B\_Scrb and  $\alpha$ 7B\_C, ranging from 1:0.5 to 1:2 protein:peptide ratios. Then, freshly prepared DSBU solution (dissolved in neat DMSO) was added at a 50-fold molar excess compared to CIB2 concentration. As the final volume of the reaction mixture was 50  $\mu$ L, 1  $\mu$ L of 25 mM DSBU was added to each sample. After 20 min, the cross-linking reactions were quenched by adding excess of primary amines (ammonium bicarbonate or TRIS) to a final concentration of 20 mM and then incubated for other 10 min. Cross-linking products were first analyzed loading the samples on an SDS-PAGE and then prepared for the MALDI-TOF measurements. In addition, ESI-MS (Native MS)<sup>99</sup> was used in order to investigate the protein oligomeric state under “physiological” conditions, namely in the absence of chemical modifications.



### *MALDI-TOF measurements*

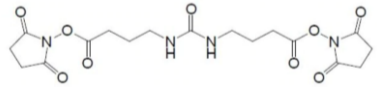
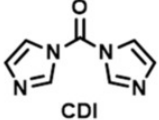
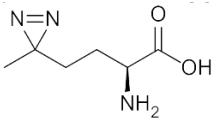
Samples for MALDI-TOF-MS were desalted by ZipTip C4 (Millipore). Protein was eluted with 70% (v/v) acetonitrile / 1% (v/v) formic acid. Each sample was mixed with a saturated solution of sinapinic acid (in 50% (v/v) methanol / 0.1% (v/v) TFA) at 1:1 ratio and spotted onto the MALDI target. Each MALDI-TOF spectrum represents the accumulation of 1000-3000 laser shots. Baseline subtraction and spectra smoothing were performed.



### *ESI-MS measurements*

For native ESI-MS analyses (High-Mass Q-TOF II mass spectrometer, Waters/MS Vision), CIB2 and the peptides were prepared in 200 mM ammonium acetate, pH 6.8. collision energy was set at 60 V (**Paper2<sup>22</sup>**).

**TABLE 2:** CHEMICAL FEATURES OF CROSS-LINKING MOLECULES.

Name	Molecule Structure	React.	Length (Å)	#re s <sup>1</sup>
<b>DSBU (BuUrBu)</b>	Disuccinimidyl dibutyric urea 	Lys, N-term	12.5 (spacer arm) <sup>98</sup>	1 3
<b>CDI</b>	1,1'-carbonyldiimidazole 	Lys, N-term hydroxy groups	2.6 <sup>100</sup>	7 1
<b>Photo-Met</b>	Photo-methionine 	No speci- ficity <sup>101</sup>		

<sup>1</sup> Number of residues in CIB2 sequence.



## Alexa Fluor 532 conjugation and luminescence titrations



### Dye conjugation

Alexa Fluor 532 (Thermofisher) is the dye used to covalently label CaM. The presence of maleimide-functional group allows the specific binding to thiol groups and, since WT CaM lacks Cys, site directed mutagenesis (performed by Doc. Helge Meyer, University of Oldenburg) was performed in order to replace the Thr26 to Cys. The dye was suspended in pure DMSO and a 10-fold excess was added drop-wise (at room temperature, in the dark to prevent light quenching) to the protein previously diluted in 50 mM TRIS pH 7.2, 150 mM KCl buffer. To get rid of unconjugated dye the sample was loaded on a PD10 desalting column. Considering that the conjugated dye exhibits  $\lambda^{\max}_{\text{exc}} = 532$  nm and  $\lambda^{\max}_{\text{emi}} = 554$  nm, the conjugation efficiency was calculated as follow:

$$\text{Efficiency (\%)} = \frac{A_{532}}{\varepsilon_{\text{Alexa}}} * \frac{MW_{\text{CaM}}}{[\text{CaM}]} * 100$$

where  $\varepsilon_{\text{Alexa}}$  is the dye extinction molar coefficient ( $78000 \text{ M}^{-1}\text{cm}^{-1}$ ), the  $MW_{\text{CaM}}$  is 16800 g/mol and  $[\text{CaM}]$  is expressed in mg/mL.



### Titration experiments

To study the interaction between CaM and CaF<sub>2</sub> NPs, titration experiments were performed moving from a protein free to a protein saturated solution. Each titration point consisted in 8.05  $\mu\text{L}$  addition of a CaM stock (31  $\mu\text{M}$ ) to a 500  $\mu\text{L}$  sample where 0.5 mg/mL NPs were present. After 12 sequential additions the measured volume was  $\sim 600$   $\mu\text{L}$  and the final CaM concentration was 5.5  $\mu\text{M}$  (concentration calculated considering the dilution factor). Thanks to the upconversion phenomenon, for each protein addition fluorescence emission spectra were collected (410-750 nm) upon excitation at 980 nm, following the Resonance Energy Transfer (RET). In this system, the fluorescence emission of upconverting NPs works as donor while conjugated Alexa Fluor 532 works as acceptor. Since the maximum efficiency in the energy transfer is inversely proportional to the sixth power of the

distance between donor and acceptor, RET intensity gives information about the NPs-CaM complex formation allowing the estimation of the affinity.



#### *Instrumentation for luminescence measurements*

The upconversion spectra were acquired using a 980-nm diode laser as excitation source. The emission was analyzed using a monochromator equipped with 1200 g/mm grating and CCD detector with a spectra resolution of 0.15 nm.

# *Results*



## Calcium and integrin binding protein 2

### Expression and purification

The optimized protocol for the expression and purification of CIB2 allowed us to obtain at least 10-15 mg of pure WT and E64D CIB2 per liter of LB. During SDS-PAGE CIB2 migrates with a profile compatible with a 21.7 kDa protein, even if its apparent MW is slightly higher (as already seen by Blazejczyk et al 2009<sup>102</sup>, Huang et al 2012<sup>103</sup>, **Figure 17A**). Moreover, a faint band is visible at lower MWs but since it has been recognized by the anti-CIB2 antibody (Abnova, **Figure 17B**), we excluded the presence of contaminants. Circular dichroism analysis was performed in order to check whether the presence of His-tag compromises the protein structure or its capability to coordinate cations, since His-CIB2 was immobilized on the surface of the His-Cap chip during SPR measurements (see below). We pointed out that the small differences seen comparing His-CIB2 (**Figure 17C**) and CIB2 (**Figure 17D**) were related to the presence of the TEV binding site that didn't compromise the capability of CIB2 to bind ions.

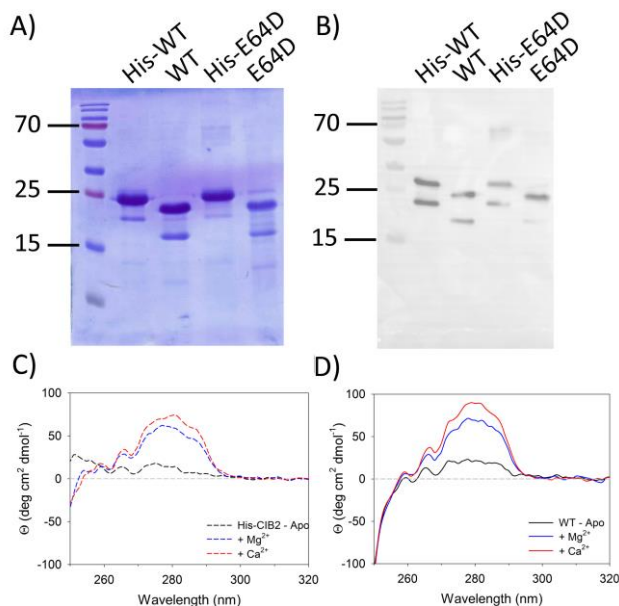


**Figure 17: CIB2 purity check.** A) SDS-PAGE of 15  $\mu$ M WT and E64D CIB2 before and after TEV incubation, in the presence of 1 mM DTT, 1 mM Mg<sup>2+</sup> and 2 mM Ca<sup>2+</sup>. B) Western blot of 100 ng of WT and E64D CIB2 in the same ionic concentrations as in (A), exposition time 30 sec. C-D) Near UV CD spectra (250-320 nm) of 20-30  $\mu$ M His-CIB2 (C) and CIB2 (D) were collected at 37°C starting from the apo protein (500  $\mu$ M EGTA, black lines) and after sequential additions of 1 mM Mg<sup>2+</sup> (blue lines) and 2 mM Ca<sup>2+</sup> (red lines). Data were normalized on proteins concentrations and each spectrum represents the average of 5 accumulations. Figure and legend have been adapted from Paper 2<sup>22</sup>.

## Structural analysis: CIB2 response to cations

*Circular dichroism analysis highlights the molten globule state of WT CIB2 and the incapability of E64D mutant to reach the functional folding.*

CIB2 structural properties were investigated using high- and low-resolution techniques, namely CD spectroscopy, NMR and SDS-PAGE. CD spectra were collected in the far UV and near UV regions in order to gain information about secondary and tertiary structures respectively. Since CIB2 lacks tryptophan, the near UV spectra were the result of the contribution of 16 phenylalanine and 5 tyrosine residues. In the absence of ions (0.5 mM EGTA), the combination of an almost flat near UV spectrum (**Figure 18A**, black dotted line) and the detection of the helical content in the far UV region (**Figure 18B**), indicates that apo-CIB2 is in a molten globule state. The addition of 1 mM  $Mg^{2+}$  leads to an increase in dichroic signal both in near UV (Phe and Tyr bands) (**Figure 18A**, dashed blue line) and far UV regions, suggesting a more compact and well-defined structure. Furthermore, the physiological  $Mg^{2+}$  allows CIB2 to reach the typical spectrum of an  $\alpha$ -helices protein, characterized by the two minima at 208 nm (localized at 206 nm in the apo protein) and 222 nm. The incubation with saturating  $Ca^{2+}$  (1 mM) completes the structural transition that consists in a further increase in ellipticity in the Tyr band (**Figure 18A**, solid red line), together with a slight increase in the far UV spectrum intensity (**Figure 18B**). E64D CIB2 showed a totally different ions response (**Figure 18C-D**). In fact, upon additions of  $Mg^{2+}$  and  $Ca^{2+}$  only slight changes in the near UV region were detected, while the far UV spectra were substantially overlapped in all the tested conditions, with the first minima stable at 206 nm. These evidences allowed us to conclude that replacing Glu with Asp in position 64 blocks the mutant in a molten globule conformation.

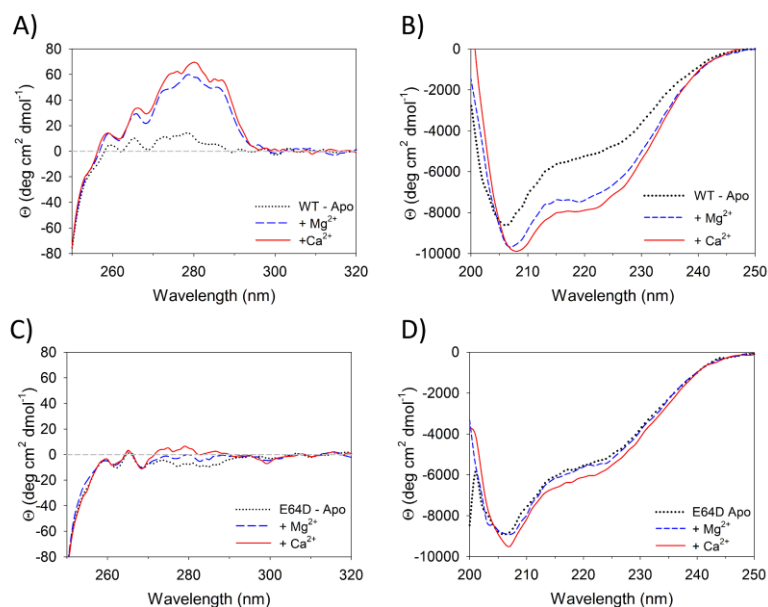


**Figure 18: Conformational changes in WT and E64D upon coordination of  $\text{Ca}^{2+}$  and  $\text{Mg}^{2+}$ .** A-C) Near UV spectra of 28  $\mu\text{M}$  WT (A) and 30  $\mu\text{M}$  E64D (C) CIB2 in the presence of 500  $\mu\text{M}$  EGTA (black dotted lines) and after sequential additions of 1 mM  $\text{Mg}^{2+}$  (dashed blue lines) and 1 mM  $\text{Ca}^{2+}$  (solid red lines). B-D) Far UV spectra of 12  $\mu\text{M}$  WT (B) and E64D (D) CIB2 in the presence of 300  $\mu\text{M}$  EGTA (black dotted lines) and after sequential additions of 1 mM  $\text{Mg}^{2+}$  and 600  $\mu\text{M}$   $\text{Ca}^{2+}$ . Figure and legend are adapted from **Paper1<sup>18</sup>**.

#### *Limited proteolysis experiment identifies $\text{Mg}^{2+}$ and $\text{Ca}^{2+}$ as CIB2 stabilizers*

Even if CD and NMR (see below) measurements suggested that the presence of the sole  $\text{Mg}^{2+}$  or both  $\text{Mg}^{2+}$  and  $\text{Ca}^{2+}$  generate very similar tertiary structures, it is also known that the binding of ligands may lead to the exposure of different regions thus changing the accessibility to proteases. Limited proteolysis is an easy and informative technique that allows us to obtain information about protein structure properties, like flexibility<sup>104</sup>. WT CIB2 was incubated with trypsin in the absence of ions (1 mM EDTA), in the presence of sole  $\text{Mg}^{2+}$  (0.5 mM EGTA + 1 mM  $\text{Mg}^{2+}$ ) and in co-presence of  $\text{Mg}^{2+}$  and  $\text{Ca}^{2+}$  (1 mM  $\text{Mg}^{2+}$  + 2 mM  $\text{Ca}^{2+}$ ). After a time-scan in search of the best conditions (**Figure S2, Paper 2<sup>22</sup>**), 5 min and 30 min (**Figure 19B**) were chosen as representative of the fact that ions work as stabilizers: after 30 min the apo-CIB2 was totally lost, while a mixture of undigested CIB2 and proteolytic bands were still present when ions were included. Molecular simulation performed by Dr. Valerio Marino (University of Verona) allowed us to hypothesize that the proteolytic bands may have derived from exposing the pseudo-EF1 motif, the link between EF3-EF4, the exiting helix of EF4, and the C-terminal (**Paper 2<sup>22</sup>**). We also noticed that CIB2 *per se* is prone to auto-degradation, as represented not

only by the appearance of a faint band in the absence of trypsin (**Figure 19A**) but also by the presence of 16-17 kDa fragments detected after MALDI measurements of CIB2 samples left at room temperature (data not shown).

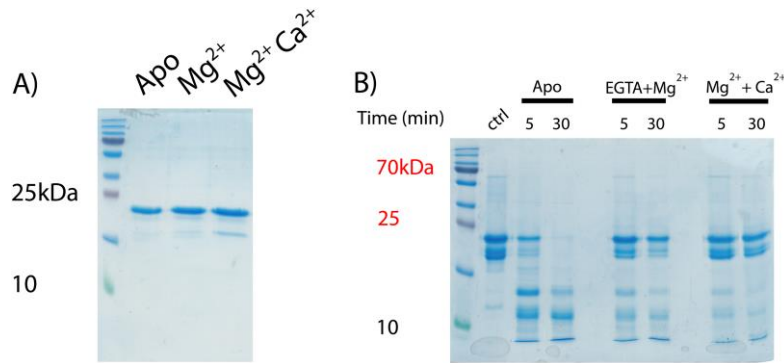


**Figure 19: Stabilization effect of ions.** A) Ten micromolar CIB2 was incubated at 25°C for 10 min in the presence of 1 mM EDTA (Apo), 500 μM EGTA + 1 mM Mg<sup>2+</sup> (Mg<sup>2+</sup>) and 1 mM Mg<sup>2+</sup> + 2 mM Ca<sup>2+</sup> (Mg<sup>2+</sup> Ca<sup>2+</sup>). Samples were boiled and loaded on a 18% polyacrylamide gel. B) Limited proteolysis experiments of 25 μM CIB2 were performed in the same ionic concentrations used for (A). Samples were incubated with trypsin (1:100 enzyme:protein ratio), loaded on 18% polyacrylamide gel and Coomassie blue stained. Figure and legend are adapted from **Paper 2<sup>22</sup>**.



## Hydrophobicity evaluation

The molten globule apo-form of both WT and E64D CIB2 suggests that many hydrophobic patches may be solvent exposed. In order to evaluate this feature, fluorescence spectra were collected in the presence of ANS, a molecule with different fluorescence properties based on its binding to hydrophobic surfaces (**Figure 20**). Both WT (**Figure 20A**) and E64D (**Figure 20B**) appear more hydrophobic than the sole ANS (green line) when in the absence of ions (dotted lines), as demonstrated by the intense blue shift (27 nm for the WT and 31 nm for the mutant). The sequential addition of 1 mM  $Mg^{2+}$  and 1 mM  $Ca^{2+}$  led to a slight reduction in fluorescence emission combined with a 1-2 nm red shift. However, even if both variants appear highly hydrophobic, the presence of ions exerted a more prominent effect on the WT compared to E64D (**Table 3**). To further investigate the protein structure stability, thermal denaturation profiles were collected monitoring the ellipticity variation at 222 nm at increased temperatures, ranging from 4-70°C (**Figure 20C-D**). In this respect, the experiments were performed in the absence of ions (grey circles) and the presence of sole  $Ca^{2+}$  (red squares),  $Mg^{2+}$  (blue diamonds) and in the co-presence of both (green triangles). All the distributions obtained were fitted with Hill 4 parameters function, data are reported in **Table 3**. As expected, apo-WT CIB2 was quite unstable showing a  $T_m = 35.1^\circ C$ . The addition of 1 mM  $Mg^{2+}$  led to an 11°C stabilization as did the addition of 1 mM  $Ca^{2+}$ , even if its effect was less pronounced (8°C). The co-presence of cations did not result in a higher effect compared to the sole  $Mg^{2+}$  as proved by the  $T_m = 45.9^\circ C$ . The lower  $h_c$  value of apo-WT CIB2 ( $h_c = 7.5$ ) compared to the cations-bound forms ( $h_c = 11-12.5$ ) showed a faster transition when  $Mg^{2+}$  and/or  $Ca^{2+}$  were present, even if the persistence of ellipticity at high temperature suggests that CIB2 can retain some secondary structure. Concerning the mutant, no transition was detected in the apo conditions, in line with the partially unfolded structure, and the further additions of  $Mg^{2+}$  and/or  $Ca^{2+}$  showed  $T_m$  values that resembles the apo-WT ones (34.2-36.7°C).

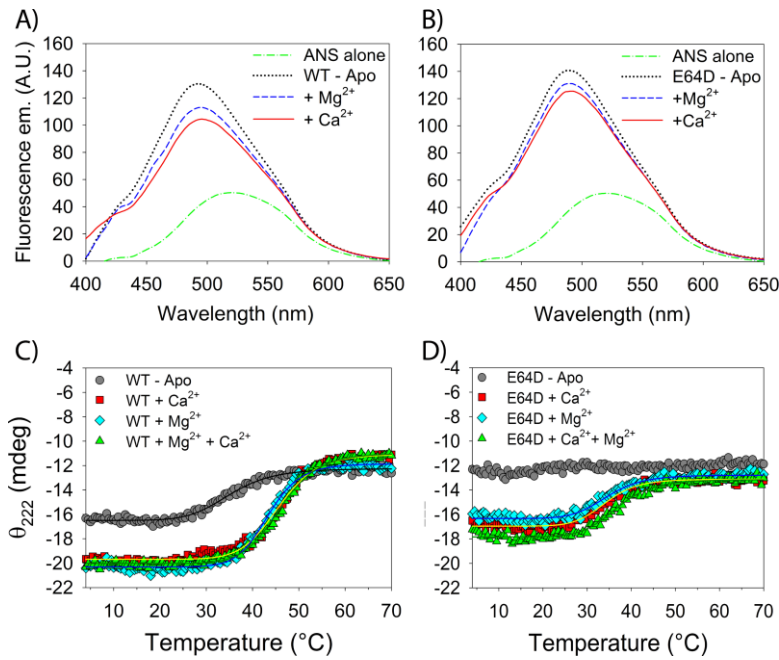


**Figure 20: CIB2 hydrophobicity and thermal stability investigation.** A-B) ANS fluorescence spectra of WT (A) and E64D (B) CIB2 in the presence of 0.5 mM EDTA (dotted black lines), 1 mM Mg<sup>2+</sup> (dashed blue lines), 1 mM Ca<sup>2+</sup> (solid red lines). ANS alone is also shown (dash dotted lines). C-D) Thermal denaturation profiles of 12 μM WT (C) and E64D (D) CIB2 were recorded between 4-70°C in the presence of 0.5 mM EDTA (grey dots), 2 mM Ca<sup>2+</sup> (red squares), 2 mM Mg<sup>2+</sup> (light blue diamonds) and 1 mM Mg<sup>2+</sup> + 1 mM Ca<sup>2+</sup> (green triangles). Solid lines represent the result of data fitting using Hill 4 parameters function. Figure and legend have been adapted from **Paper 1**<sup>18</sup>.

**TABLE 3: ANALYSIS OF ANS FLUORESCENCE AND CD THERMAL DENATURATION DATA FOR WT AND E64D CIB2.**

	Blue shift (nm) <sup>1</sup>	F <sup>max</sup> /F <sup>ref</sup> <sup>2</sup>	T <sub>m</sub> (°C) <sup>3</sup>	h <sub>c</sub> <sup>3</sup>
<b>WT – Apo</b>	27	2.6	35.1	7.5
<b>+ Mg<sup>2+</sup></b>	25	2.2	45.7	11
<b>+ Ca<sup>2+</sup></b>	25	2.1	43.4	12.5
<b>+ Mg<sup>2+</sup>/Ca<sup>2+</sup></b>	-	-	45.9	11.2
<b>E64D – Apo</b>	31	2.8	-	-
<b>+ Mg<sup>2+</sup></b>	30	2.6	34.2	9.5
<b>+ Ca<sup>2+</sup></b>	29	2.5	34.5	8.6
<b>+ Mg<sup>2+</sup>/Ca<sup>2+</sup></b>	-	-	36.7	8.9

<sup>1</sup> blue shift refers to the observed shift of the wavelength of maximum emission of the protein + ANS mixture upon excitation of 380 nm as referred to that of ANS alone.

<sup>2</sup> refers to the ratio between maximal fluorescence emission of the protein + ANS mixture and that of ANS alone.

<sup>3</sup> T<sub>m</sub> and h<sub>c</sub> represents the melting temperature and hill coefficient obtained by data fitting in thermal denaturation profiles.

Table is from **Paper 1**<sup>18</sup>

## Affinity for cations

*Nuclear Magnetic Resonance measurements reveal a preferential binding of  $Mg^{2+}$  over  $Ca^{2+}$  and the presence of an allosteric long-range communication.*

A well-established technique for the evaluation of  $Ca^{2+}$  affinity, is the spectroscopic method based on the measurements of the competition for  $Ca^{2+}$  between the protein of interest and a chromophoric chelator, namely 5,5'-Br<sub>2</sub> BAPTA. This was the first method applied for the characterization of WT CIB2's capability to work as a  $Ca^{2+}$  binding protein, but no competition was detected, excluding a  $K_d$  below 6  $\mu$ M (data not shown).

One of the main features of  $Ca^{2+}$  sensor proteins is their capability to undergo conformational changes upon coordination of cations. This aspect was fully investigated thanks to the collaboration with Prof. Mariapina D'Onofrio (Dept. of Biotechnology), who collected two-dimensional HSQC NMR spectra of WT and E64D CIB2 (**Figure 21**). <sup>1</sup>H-<sup>15</sup>N HSQC spectrum of apo-WT CIB2 is characterized by poorly dispersed peaks, a pattern compatible with a protein in a molten globule state (**Figure 21A-B**, black distribution). The addition of saturating  $Ca^{2+}$  and  $Mg^{2+}$  induce a more dispersed NMR signal (**Figure 21A-B**, blue and green distributions) and the appearance of downfield peaks are compatible with cations coordination. To better investigate the  $Ca^{2+}$  binding mechanism,  $Ca^{2+}$  was titrated on <sup>15</sup>N-WT CIB2 collecting several HSQC spectra. Three were the peaks that showed interesting chemical shifts: E64, N121 and G162 which can be considered as indicators for non-functional EF1, and the EF3 and EF4 loops respectively. Following the chemical shifts of these residues through the titration (**Figure 21D to F**), we saw that E64 (mutated in Asp in USH1J) and N121 follow the same hyperbolic shape, indicating that they belong to the same allosteric network. The data were fitted using a single one-site binding model that gives the  $K_d$  for both residues:  $0.55 \pm 0.13$  mM for E64 and  $0.48 \pm 0.15$  mM for N121. G162 on the other hand, showed a sigmoidal shape with positive cooperativity, data fitted gave  $K_d^{app} = 2.22 \pm 0.25$  mM and  $h_c = 2.27 \pm 0.38$ . It was noted that when E64 and N121 peaks appear, the protein is already well structured and further additions of  $Ca^{2+}$  lead only to small rearrangements.

Using NMR, we also investigated whether a preferential binding for  $Mg^{2+}$  or  $Ca^{2+}$  was present. To do that, the downfield peaks were considered as indicators of EF hands occupancy when solutions with different ratios of  $Mg^{2+}$  and  $Ca^{2+}$  were used. When  $Mg^{2+}$  is in excess, N121 appears in the  $Mg^{2+}$ -bound chemical shift while G162 (reporter for  $Ca^{2+}$  binding) is present but with low intensity. When  $Ca^{2+}$  is in excess, the N121 peak is still present in the  $Mg^{2+}$ -bound chemical shift, suggesting it retained its capability to bind with  $Mg^{2+}$ , while EF4 became occupied by  $Ca^{2+}$  (see **Figure S5 in Paper 1**<sup>18</sup>).

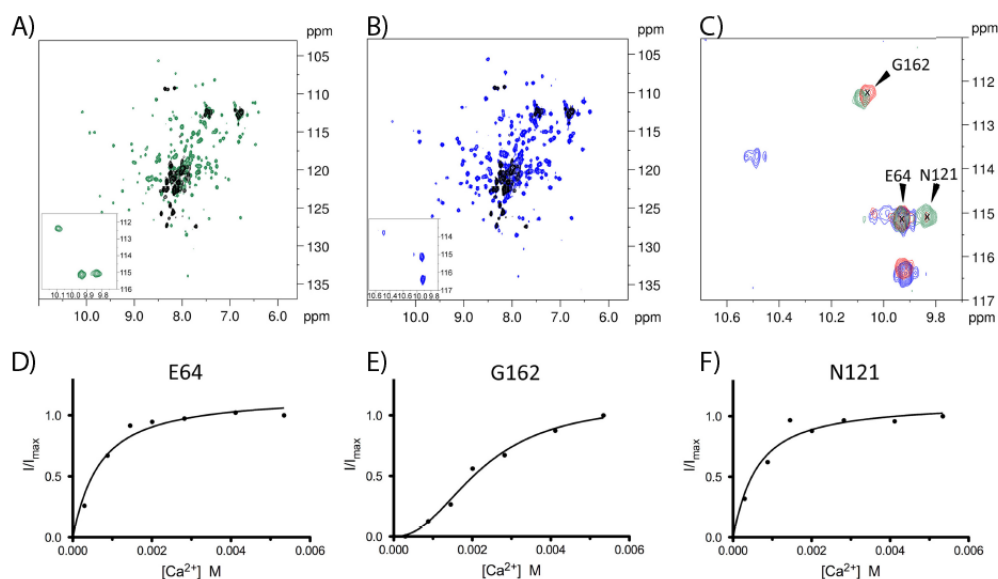


**Figure 21:**  $^1H$ - $^{15}N$  HSQC spectra of WT CIB2 in its apo form and in the presence of  $Mg^{2+}$  and  $Ca^{2+}$  highlight an allosteric communication between E64 and N121. A) Superimposition of the two-dimensional  $^1H$ - $^{15}N$  HSQC spectra of the apo- (black) and  $Ca^{2+}$ -bound (green)  $^{15}N$ -WT CIB2. B) Superimposition of the HSQC spectra of the apo- (black) and  $Mg^{2+}$ -bound (blue)  $^{15}N$ -WT CIB2 in the insets, zoom of the HSQC spectra of the downfield peaks of the metal-bound forms of  $^{15}N$ -WT CIB2. Metal ions were presented at a protein:metal ratio of 1:15. C) Superimposition of downfield region of the  $^1H$ - $^{15}N$  HSQC NMR spectra recorded on  $^{15}N$ -WT CIB2 containing 15 equivalents of  $Mg^{2+}$  (blue), 15 eq.  $Mg^{2+}$  + 15 eq.  $Ca^{2+}$  (ref). and 15 eq.  $Ca^{2+}$  (green). (D-F) Variation of  $^1H$ - $^{15}N$  HSQC peak intensities of WT CIB2 as a function of  $Ca^{2+}$  concentration. The peak intensities were normalized with respect to maximum value. The continuous line represents the data fitted against equations as indicated in Material and Methods in **Paper 1**. The plots refer to the amide peaks of residues E64 (D), G162 (E) and N121 (F). All the spectra were recorded at 600 MHz and 25°C. All samples were at protein concentration of 320  $\mu M$  in 20 mM HEPES, 100 mM KCl, 1 mM DTT, pH 7.5. Figure and legend are from **Paper 1**<sup>18</sup>.

*$K_d^{app}$  for  $Mg^{2+}$  and  $Ca^{2+}$  estimation following variations in CIB2 secondary structure.*

At this point we sought to quantify the affinity of CIB2 for  $Mg^{2+}$  and  $Ca^{2+}$  for both WT and E64D, in order to explore the role of CIB2 under physiological and disease-related conditions. Thus, titration experiments were designed monitoring the variation in CIB2 secondary structure upon addition of cations on the apo-CIB2 (1 mM free EGTA) looking for the concentration of  $Ca^{2+}/Mg^{2+}$  at which the structural change is half maximal ( $K_d^{app}$ ). All the data (**Figure 22**) were fitted with a Hill 4 parameters function (**Table 4**), suggesting the presence of cooperativity in structural conformation triggered by ions coordination. Going into details, we found for WT CIB2 (**Figure 22A and B**, gray dots) lowered  $K_d^{app}$  and higher cooperativity for  $Mg^{2+}$  binding (290  $\mu$ M,  $h_c = 2.3$ ) compared to  $Ca^{2+}$  (500  $\mu$ M,  $h_c = 1.1$ ), excluding its role as  $Ca^{2+}$  sensor under physiological conditions and confirming its preferential binding for  $Mg^{2+}$ . Concerning the USH1J-mutant (**Figure 22A and B**, red triangles), it preserved a higher affinity for  $Mg^{2+}$  ( $K_d^{app} = 1.5$  mM) compared to  $Ca^{2+}$  ( $K_d^{app} = 2$  mM), even if totally out of the physiological window.

Since we could detect the E64D's capability to respond to non-physiological ions concentrations in the far UV, we wondered if these may trigger the gain of a WT-like tertiary structure. Thus, further near UV spectra of E64D were collected increasing the cations concentrations (2 mM to 10 mM) and it was shown that E64D starts the conformational change when  $Ca^{2+}$  concentration was at least 5 mM, reaching a WT-like structure only in the presence of 10 mM  $Ca^{2+}$  (**Figure 22C**). The same was not detected for  $Mg^{2+}$ , for which even at 10 mM the spectrum was still far from the WT, both in shape and intensity (**Figure 22D**).

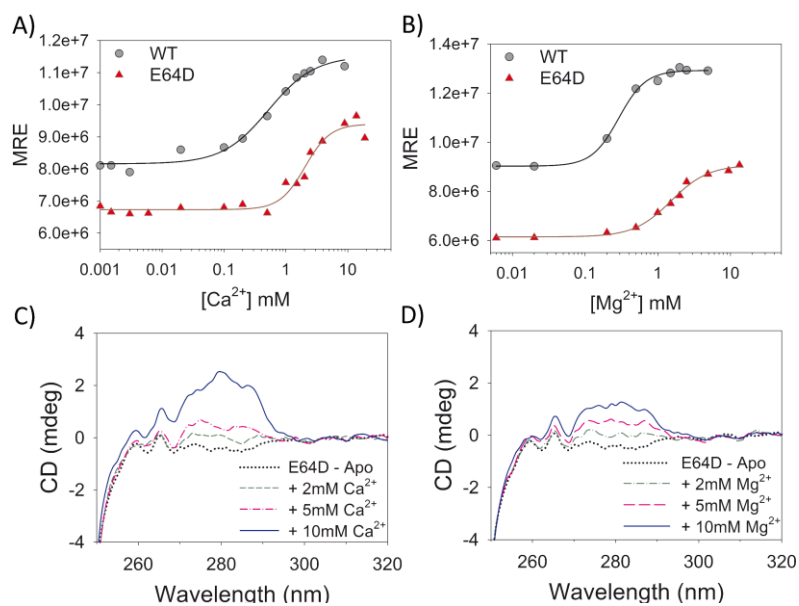


**Figure 22:  $\text{Ca}^{2+}$  and  $\text{Mg}^{2+}$  affinity assayed by monitoring secondary structure variations.** (A-B) WT (grey circles) and E64D (red triangles) were titrated with  $\text{Ca}^{2+}$  (A) and  $\text{Mg}^{2+}$  (B) starting from apo- protein (1 mM EGTA). (C-D) Near UV spectra of E64D CIB2 after sequential additions of  $\text{Ca}^{2+}$  (C) and  $\text{Mg}^{2+}$  (D) ranging from 2 mM to 10 mM. Figure and legend are an adaptation from Paper 1<sup>18</sup>.

**TABLE 4: APPARENT AFFINITY FOR  $\text{Ca}^{2+}$  AND  $\text{Mg}^{2+}$  OF WT AND E64D CIB2 ASSESSED BY CD TITRATIONS.**

	$\text{Mg}^{2+}$		$\text{Ca}^{2+}$	
	$K_d^{\text{app}}$ (mM)	$h_c$	$K_d^{\text{app}}$ (mM)	$h_c$
<b>WT CIB2</b>	$0.29 \pm 0.02$	$2.3 \pm 0.3$	$0.5 \pm 0.1$	$1.1 \pm 0.3$
<b>E64D CIB2</b>	$1.5 \pm 0.1$	$1.7 \pm 0.2$	$2.0 \pm 0.2$	$2.2 \pm 0.6$

Table is an adaptation from Paper 1<sup>18</sup>

## Oligomeric state investigation: a controversial issue

The CIB2 oligomeric state analysis was the tricky part of the investigation, since some results suggested a dimeric organization while others a monomeric one. To shed light on this feature many techniques were employed, from the old-fashion Ferguson plot to the advanced chemical cross-linking coupled with mass spectrometry.

### *Lines of evidence of dimeric state (Paper 1<sup>18</sup>)*

In the very first part of the project, the investigation of CIB2's oligomeric state was performed using three different techniques: native PAGE, analytical SEC, and DLS. While in the presence of SDS (**Figure 19A**) CIB2 had an electrophoretic mobility compatible with a 21.7 kDa protein, in native PAGE (see **Figure S1 in Paper 1**) multi bands appeared when reducing agent was absent, thus indicating the tendency to form high MW oligomers via oxidation of thiol groups of the 4 Cys residues. The multi band pattern disappeared when 1 mM DTT was included in sample preparation. To further investigate the single bands nature seen in native PAGE, analytical size exclusion chromatography measurements were performed. CIB2 was loaded into the previously equilibrated column and the elution volumes were used to extrapolate the MW via a calibration line obtained by loading standard proteins (see methods); this was done for both WT and E64D CIB2. Data are summarized in **Table 5**. Both WT and E64D in the presence of Mg<sup>2+</sup> and/or Ca<sup>2+</sup> eluted from the column as only one peak with an apparent MW of 37-39 kDa (**Figure 23**), suggesting that all CIB2 molecules is structured in dimers. Even if less precisely, the Ferguson plot analysis confirmed the high MWs for both WT and E64D CIB2 (**Table 5**) in all the tested conditions (52-53 kDa). The eluted proteins were immediately analyzed by DLS to check the variations in hydration shell upon cations coordination (**Figure 24**). While apo-WT CIB2 showed an intensity profile characterized by multiple unresolved peaks (**Figure 24A**), the further addition of Mg<sup>2+</sup> or Ca<sup>2+</sup> (**Figure 24B** and **C**) improved the colloidal properties allowing us to determine the hydrodynamic diameters, estimated to be:  $d^{\text{Mg}} = 8.43 \text{ nm}$  and  $d^{\text{Ca}} = 8.18 \text{ nm}$ . On the other hand, E64D never showed any amelioration in colloidal properties (**Figure 24E-G**), resulting in a high polydispersion index and thus preventing a

reliable hydrodynamic diameter determination. The combination of all these factors led us to conclude that CIB2 forms dimers under the tested conditions.

With the aim to identify the precise dimerization interface, we found some lines of evidence of the monomeric nature of CIB2.

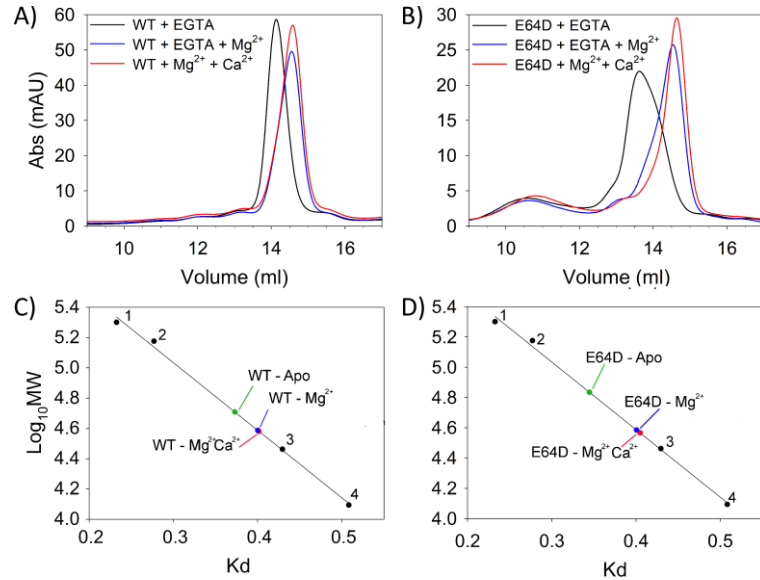


**Figure 23: SEC analysis.** Gel filtration elution profiles under reducing conditions of WT CIB2 (A) and E64D CIB (B) in the presence of 3 mM EGTA (black line), 2 mM EGTA + 3 mM Mg<sup>2+</sup> (blue line) and 3 mM Mg<sup>2+</sup> + 2 mM Ca<sup>2+</sup> (red line). C-D) Determination of MW for apo-, Mg<sup>2+</sup> and Ca<sup>2+</sup>-bound WT and E64D CIB2. Calibration curve were prepared by plotting the Log<sub>10</sub> MW value for each standard protein versus its corresponding K<sub>d</sub> value. Standard globular proteins were used for the preparation of the calibration line (1. B-amylase, 2. Alcohol Dehydrogenase, 3. Carbonic anhydrase, 4. Cytochrome C). Figure and legend are an adaptation from **Paper 1**.

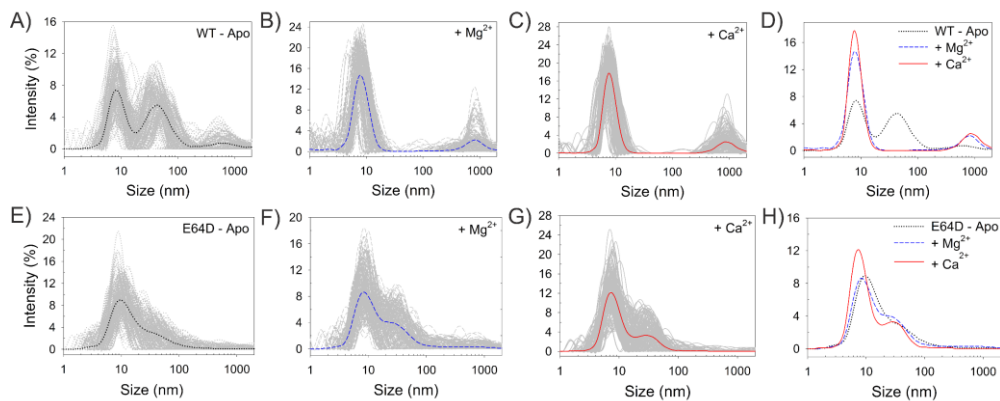


**Figure 24: Dynamic light scattering spectroscopy.** Comparison between diameters measured at 37°C for WT (A-D) and E64D (E-H) CIB2 in the presence of 3 mM EGTA (A, E), 2 mM EGTA + 3 mM Mg<sup>2+</sup> (B, F), 3 mM Mg<sup>2+</sup> + 2 mM Ca<sup>2+</sup> (C, G). Superimposition of the average curves obtained by (A-C) for the WT and (E-G) for the E64D CIB2. Figure and legend are an adaptation from **Paper 1**.



**TABLE 5: MOLECULAR WEIGHT OF WT AND E64D CIB2 ESTIMATED BY ANALYTICAL SEC AND FERGUSON PLOTS (FP).**

	MW <sup>SEC</sup> (kDa)	MW <sup>FP</sup> (kDa)
WT-apo	51.1	51
+ Mg <sup>2+</sup>	38.6	52
+ Ca <sup>2+</sup>	38.1	53
E64D-apo	68.4	53
+ Mg <sup>2+</sup>	38.5	53
+ Ca <sup>2+</sup>	36.9	53

*Table is an adaptation from Paper 1.*

### *Lines of evidence of monomeric state (Paper 2<sup>22</sup>)*

With the purpose to identify and characterize the dimerization interface, and thus the residues directly involved in dimer formation, chemical cross linking coupled with mass spectrometry (XL-MS) experiments were performed<sup>97</sup>. Surprisingly, none of them showed CIB2 dimers, not even after using shorter molecules as CDI or photo-methionine. Native-MS spectra were also collected (**Figure 25A**) and CIB2 appeared in charge states from +8 to +10 with signals at  $m/z$  2178, 2420 and 2722 respectively. The spectrum deconvolution gave a mass equal to 21787 Da, fully compatible with monomeric CIB2. Dimers or higher oligomers were never detected. Since these last pieces of evidence appeared in contradiction with the previous analytical SEC findings, both SEC and DLS measurements were repeated in the same conditions used for XL-MS (**Figure 25C**), and the product loaded on SEC column. **Figure 25B** shows how native CIB2 (black line, peak #1) and cross-linked CIB2 (green line, peak #2) elute at the same retention volume, which gives MW values of 35.9 kDa and 36.7 kDa respectively, very similar to those previously published (**Paper 1**). The second peak (green curve, peak #3) represents DSBU reaction products (confirmed by NMR measurements, data not shown), visible also in the sole presence of reacted DSBU (black line, peak #4). To shed light on this weird behavior that shows CIB2 as a monomer but with a Stokes radius more similar to a dimer, the analysis was extended to other two Ca<sup>2+</sup> sensors namely Rec and CaM (**Figure 25C**). As we did with CIB2, the eluted peaks of CaM and Rec were immediately assessed by DLS (**Figure 25D**), and their tridimensional structure was used to calculate the theoretical hydrodynamic radius using HydroPro (measurements performed by Dr. Valerio Marino). Results are summarized in **Table 6**. The elution

peaks of Ca<sup>2+</sup>-bound CIB2, Rec and CaM gave MWs equal to 37.8 kDa, 33.5 kDa and 20 kDa respectively, slightly higher with respect to the theoretical values. Moreover, zooming on the CIB2 elution profile (**Figure 25C**, inset) it was possible to identify a shoulder (band A<sub>1</sub>) whose estimated MW is 81.3 kDa. In previous measurements, bands A<sub>1</sub> and A<sub>2</sub> were collected together, resulting in a hydrodynamic diameter of 8.18 nm. In this experiment the two bands were collected separately, and the prominent one (band A<sub>2</sub>) resulted in a lower hydrodynamic diameter (5.4 nm), similar to Rec (5.0 nm) and CaM (5.8 nm). A common feature of CIB2 and Rec is the significantly higher MW with respect to the theoretical values; HydroPro measurements pointed out that both share a high hydrophobic solvent-accessible surface (SAS) that may interfere with the column resin, leading to elution at lower volumes, and therefore higher MWs. Moreover, the size measured by DLS and the radius of gyration seemed to correlate for CIB2 and Rec, while CaM showed a higher radius of gyration, probably due to the elongated forms assumed upon Ca<sup>2+</sup> binding.

Finally, to further confirm the monomeric nature of CIB2, a low amount of WT proteins was immobilized on the surface of a SPR sensor chip, and several CIB2 (0.4 μM – 140 μM) concentrations were poured on the immobilized protein in the presence of 1 mM Mg<sup>2+</sup> and 1 mM Mg<sup>2+</sup> + 2 mM Ca<sup>2+</sup>. All the obtained sensorgrams were flat (data not shown) thus excluding the formation of dimers.

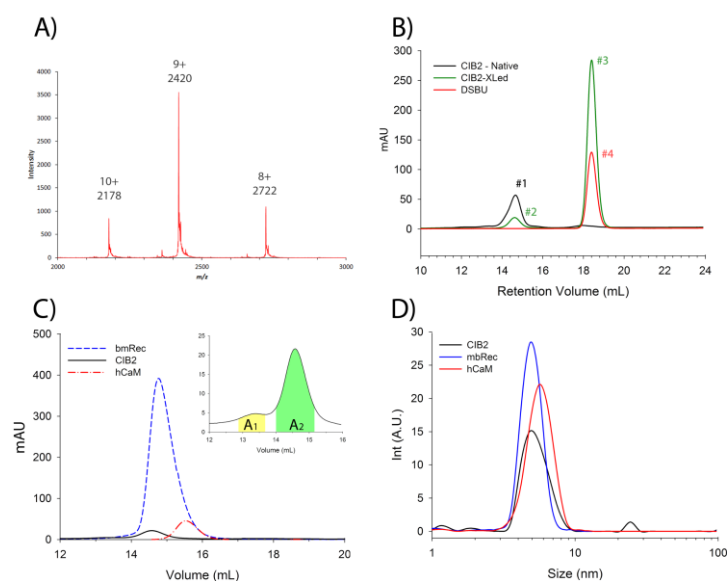


**Figure 25: Lines of evidences of monomeric CIB2.** A) Native ESI mass spectra collected in the presence of 14  $\mu\text{M}$  WT CIB2 in 200 mM ammonium acetate, pH 6.8. Collision energy was set to 60V. B) MW investigation of CIB2 before (black) and after (green line) modification with DSBU. One reaction was performed in the presence of sole DSBU (red line). C) CIB2 ( $\sim 70 \mu\text{M}$ ), Rec ( $\sim 80 \mu\text{M}$ ) and CaM ( $\sim 110 \mu\text{M}$ ) were loaded into an analytical SEC column previously equilibrated with 20 mM HEPES pH 7.5, 150 mM KCl, 1 mM DTT, 1 mM  $\text{Mg}^{2+}$ , 2 mM  $\text{Ca}^{2+}$ . The inset shows the zoom of CIB2 elution profile that was collected in two different fractions, represented by the colored areas. D) The hydrodynamic diameters of the eluted peaks were assessed by DLS: 15 to 30 measurements were collected for each sample at 37°C, consisting in at least 13-15 repetitions. The presented curves represent the average distribution. The protein concentrations in the eluted fractions was found to be: 11  $\mu\text{M}$  (Rec), 7.4  $\mu\text{M}$  (CaM), 1.8  $\mu\text{M}$  (CIB2). Figure and legend are an adaptation from Paper2.

**TABLE 6: COMPARISON OF THE HYDRODYNAMIC PROPERTIES OF CIB2, CaM AND Rec.**

	Hydro-Pro $\Phi$ (nm)	Gyration radius (nm)	DLS $\Phi$ [n] (nm) <sup>a</sup>	Hydrophobic SAS (nm <sup>2</sup> )	Hydrophilic SAS (nm <sup>2</sup> )	MW (kDa)	MW <sup>SEC</sup> (kDa)
<b>CIB2 (13-184)<sup>b</sup></b>	4.736	1.88	5.4 $\pm$ 0.2 [15]	59.64	55.34	21.3	37.8 (A <sub>2</sub> band)
<b>Rec (1-201)<sup>b</sup></b>	5.112	1.94	5.0 <sup>a</sup> $\pm$ 0.1 [18]	62.54	64.68	23.3	33.5
<b>CaM (1-149)<sup>b</sup></b>	5.076	2.22	5.8 $\pm$ 0.1 [30]	50.28	54.97	16.8	20.5

<sup>a</sup>Data are reported as mean  $\pm$  SEM; n represents the number of measurements used for the calculation.

<sup>b</sup>Sequence coverage of the structural models used for hydrodynamic diameter calculation.

## Interaction with the target peptide

As described in the introduction, several targets have been identified for CIB2, based on the cells, tissue or mechanism considered. One of these is the integrin  $\alpha 7B$ , even if the exact portion involved in the interaction was still under investigation. Two were the main hypothesis: Hager et al.<sup>20</sup> identified the entire cytosolic portion, especially the one close to the C-terminal stretch, while later Huang et al.<sup>21</sup> demonstrated this region as restricted to a short sequence close to the membrane. To shed light on this open question, we purchased (Genscript) two peptides covering the portions named  $\alpha 7B\_C$  (for the cytosolic) and  $\alpha 7B\_M$  (for the proximal-membrane portion) of the human  $\alpha 7B$  integrin, plus a negative control peptide with the same amino acid content of  $\alpha 7B\_M$ , but whose sequence was scrambled ( $\alpha 7B\_Scrb$ ). The investigation of the interaction between WT CIB2 and these peptides was assayed using a combination of indirect (fluorescence spectroscopy) and direct (MALDI-TOF and SPR) techniques.

### *Fluorescence spectroscopy suggests a specific interaction between WT/E64D CIB2 and the $\alpha 7B\_M$ peptide*

Fluorescence spectroscopy allowed us to investigate the interaction between WT/E64D CIB2 with  $\alpha 7B\_M$  and  $\alpha 7B\_Scrb$  peptides;  $\alpha 7B\_C$  was excluded due to the lack of Trp residue which was instead present in the mouse sequence (used for the first interaction study<sup>2, 5</sup>). Since CIB2 is also Trp-free, the fluorescence on the only Trp residue present in the peptides was monitored. In **Figure 26A** is reported the comparison between the fluorescence emission of the sole  $\alpha 7B\_M$  peptide (solid line), and after the incubation with saturating concentration of CIB2 (dashed line). The 17 nm blue shift and the 1.7-fold increase in fluorescence signal support the presence of a specific interaction, never seen in the presence of  $\alpha 7B\_Scrb$  peptide (**Figure 26B**). Based on this evidence, titration experiments were performed incubating increasing protein concentrations on a fixed amount of  $\alpha 7B\_M$  peptide (**Figure 26C**). This led us to have an estimation of the stoichiometry and the  $K_d^{app}$  for both WT and E64D. Surprisingly, despite its molten globule conformation, E64D is capable to interact with the peptide, with an affinity similar to the WT ( $K_d^{app} = 4.99 \pm 1.01 \mu M$  for WT CIB2 and  $K_d^{app} = 3.1 \pm 0.2 \mu M$  for E64D) and a

stoichiometric ratio of 2:1 protein : peptide. This appears to agree with the formation of a complex formed by 2 CIB2 and one peptide molecule, as described below (see SPR results).

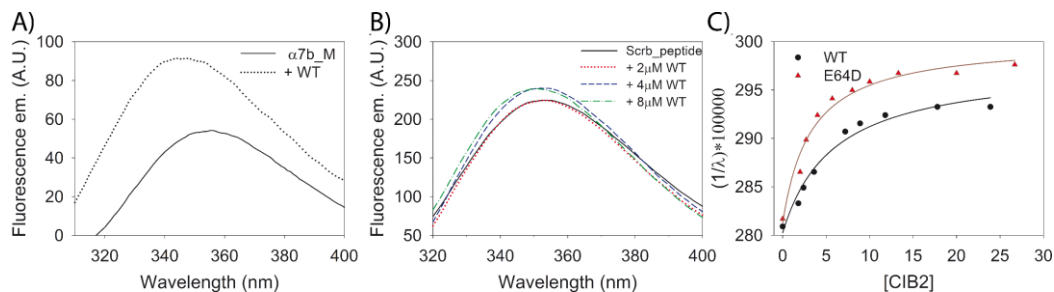


**Figure 26: Interaction between CIB2 variants and  $\alpha 7B\_M$  peptide monitored by fluorescence spectroscopy.** A) Trp fluorescence emission spectra of  $4\ \mu\text{M}$   $\alpha 7B\_M$  peptide alone (solid line) and incubated with  $8\ \mu\text{M}$  CIB2 (dotted line) in the presence of  $1\ \text{mM}$   $\text{Mg}^{2+}$  and  $2\ \text{mM}$   $\text{Ca}^{2+}$ . B) Trp fluorescence emission spectra in  $1\ \text{mM}$   $\text{Mg}^{2+}$  +  $1\ \text{mM}$   $\text{Ca}^{2+}$  of  $4\ \mu\text{M}$  Scrb peptide alone (solid black line) and in the presence of increasing CIB2 concentrations:  $2\ \mu\text{M}$  (red dotted line),  $4\ \mu\text{M}$  (short-dashed blue line) and  $8\ \mu\text{M}$  (green dashed-dotted line). C) Fluorescence titration of  $4\ \mu\text{M}$   $\alpha 7B\_M$  peptide with WT (black circles) and E64D (red triangles) CIB2 in the presence of  $1\ \text{mM}$   $\text{Mg}^{2+}$  and  $1\ \text{mM}$   $\text{Ca}^{2+}$ . Figure and legend are from **Paper 1**<sup>18</sup>.

#### *MALDI measurements show the formation of 1:1 complex between WT CIB2: $\alpha 7B\_M$*

In order to assess the complex formation, chemical cross-linking reactions of CIB2 in the presence of increasing concentrations of  $\alpha 7B\_M$ / $\alpha 7B\_Scrb$  peptides were performed, and the samples were examined by MALDI-TOF MS (**Figure 27**). CIB2 should be able to specifically interact with  $\alpha 7B\_M$ , therefore no interactions were expected for  $\alpha 7B\_Scrb$ . CIB2 without chemical modifications appeared in MALDI-TOF MS as an only one peak at  $m/z$  21770 (fully compatible with the theoretical MW). **Figure 27A** shows how increased concentrations of the  $\alpha 7B\_M$  peptide led to the formation of 1:1 complex with  $m/z$  between 24000-26000 (the calculated mass of the complex formed by one CIB2 molecule, one peptide and at least one DSBU reacted molecule is 23964 Da). Also 1:2 complexes appear at  $m/z$  between 26500-28000, but the explanation for this can be found in the highly crowded environment. Contrary to our expectations, the peak of non-complexed CIB2 never disappeared, not even in the presence of a huge amount of  $\alpha 7B\_M$  peptide; this may be due to the low affinity of the complex formation. Cross linking reactions were performed also in the presence of  $\alpha 7B\_Scrb$  peptide (**Figure 27B**), where the mainly found peak is the one represented by non-complexed CIB2 decorated by

one to five DSBU molecules, even though a weak signal of 1:1 complex appeared. Of course, this interaction has not biological meaning, and can find an explanation in the highly hydrophobic surface that characterizes CIB2. Also in this case,  $\alpha 7B\_C$  was excluded due to the absence of lysine residues that specifically react with DSBU.

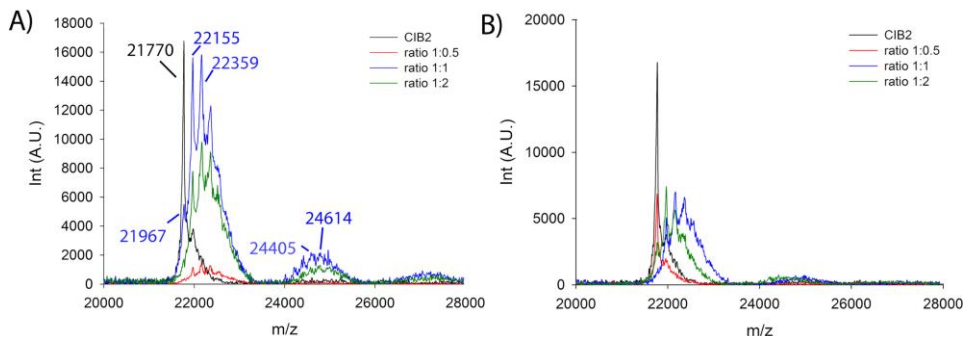


**Figure 27: Evidences of 1:1 complex formation between WT CIB2 and  $\alpha 7B\_M$  peptide.** MALDI-TOF MS measurements of cross-linked CIB2 samples with peptides  $\alpha 7B\_M$  (A) and  $\alpha 7B\_Scrb$  (B). Ten micromolar CIB2 was cross-linked with 50-fold molar excess of DSBU with increasing peptide concentrations: 5  $\mu M$  (red line), 10  $\mu M$  (blue line) and 20  $\mu M$  (green line). Between 1000-3000 laser shots were accumulated to one MALDI-TOF mass spectrum. CIB2 without DSBU cross-linker was included as initial control (black line). Figure and legend have been adapted from **Paper 2<sup>22</sup>**.

### *Surface plasmon resonance analysis reveals a low-affinity interaction with $\alpha 7B$ integrin*

To directly measure the kinetics and affinity describing the interaction between CIB2 and all the peptides (overcoming the absence of Trp and Lys residues on  $\alpha 7B\_C$ ) SPR measurements were performed. To do that, we immobilized CIB2 via i) non-specific amine coupling and ii) specific coupling of His-CIB2 on the His-cap sensor chip (after having checked that the presence of His-tag does not modify CIB2's structural properties, **Figure 17C-D**). We also tried the immobilization of sole peptides, but the signals obtained were low and non-reproducible, therefore this approach was not investigated any further. Sensorgrams from the two different immobilization approaches (**Figure 28A-B**) gave reproducible results, though with different shapes, which suggested a more specific interaction with  $\alpha 7B\_M$  peptide compared to  $\alpha 7B\_Scrb$ , and the absence of interaction with  $\alpha 7B\_C$  peptide. The sensorgram's shape is incompatible with the 1:1 Langmuir model and characterized by a different association but similar dissociation kinetics, far from a mono exponential process.

To better investigate the affinity that led to the CIB2 –  $\alpha$ 7B\_M complex formation, several peptide concentrations (230 nM – 30  $\mu$ M, **Figure 28C**) were injected into the homogeneously immobilized His-CIB2, in the presence of sole 1 mM  $Mg^{2+}$  and in the co-presence of 1 mM  $Mg^{2+}$  + 2 mM  $Ca^{2+}$ . The obtained sensorgrams were fitted using the bivalent analyte model (see Methods in paper 2), which considers the possibility of one  $\alpha$ 7B\_M peptide to bind with two CIB2 molecules in a process driven by the avidity effect (**Figure 28D**). In fact, data suggested that the first CIB2 -  $\alpha$ 7B\_M binding event may trigger the binding with another CIB2 molecule, resulting in a sort of dimerization process, as already seen in fluorescence spectroscopy (**Figure 26**). This phenomenon resulted in two sets of constants (**Table 7**) and may explain the high RU signal obtained during the experiment, even if its biological meaning remains to be clarified. Moreover, ions seemed to influence the kinetic: the two binding events took place faster when only  $Mg^{2+}$  was present, while the presence of  $Ca^{2+}$  sped up the second dissociation event. Thus, considering only the first binding event, the presence of the sole  $Mg^{2+}$  resulted in a higher affinity (11.6  $\mu$ M) with respect to the time when both cations were present (25  $\mu$ M). On the other hand, keeping the avidity contribution in mind and considering that  $Ca^{2+}$  accelerates the second dissociation event, the affinity of  $\alpha$ 7B\_M was higher in the co-presence of  $Ca^{2+}$  and  $Mg^{2+}$  (154  $\mu$ M) than in the presence of only  $Mg^{2+}$  (210  $\mu$ M).

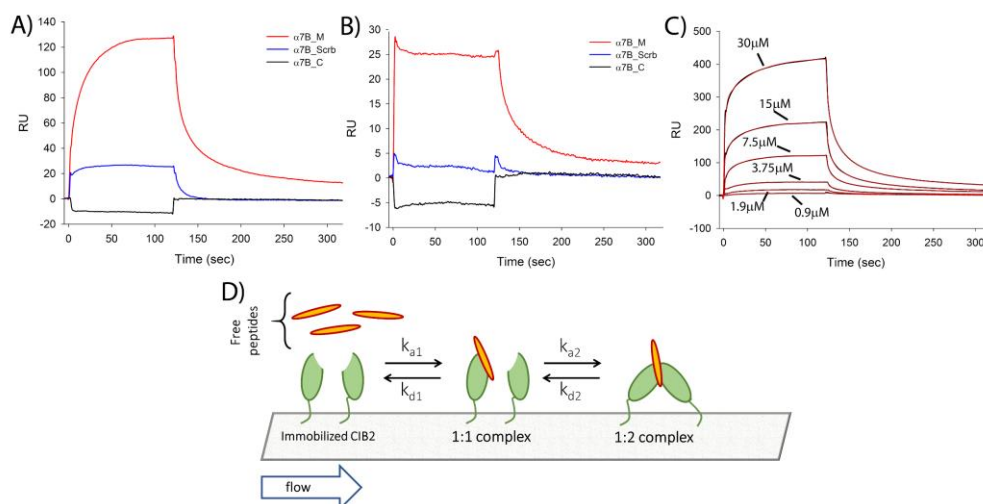


**Figure 28: SPR measurements of CIB2-peptide interaction.** A) Either  $\alpha 7B\_M$ ,  $\alpha 7B\_Scrb$  or  $\alpha 7B\_C$  peptides ( $7.5 \mu M$ ) were injected over His-CIB2 homogeneously immobilized by His-tag on the chip surface. B) Thirty micromolar of the same peptides were injected over untagged CIB2 previously immobilized on the surface of a COOH5 chip via amine coupling. C) Increasing concentrations of  $\alpha 7B\_M$  peptide were injected on His-CIB2 immobilized as in A). Experimental data (black curves) were fitted to a bivalent analyte kinetic model (red curves). All the experiments were performed using  $20 \text{ mM}$  HEPES pH 7.5,  $150 \text{ mM}$  KCl,  $1 \text{ mM}$  DTT,  $1 \text{ mM}$   $Mg^{2+}$ ,  $2 \text{ mM}$   $Ca^{2+}$ ,  $50 \mu M$  EDTA,  $0.005\%$  Tween as buffer. Two minutes injections were performed using a flow rate of  $20 \mu L \text{ min}^{-1}$ , dissociations were followed for 200 seconds. D) A possible interaction scheme of CIB2- $\alpha 7B\_M$  interaction compatible with the kinetic model. The interaction of a CIB2 monomer immobilized on the chip (green) with a peptide (orange) can lead to the binding of another CIB2 molecule; all steps are fully reversible. Figure and legend are from **Paper 2**<sup>22</sup>.

**TABLE 7: RESULTS FROM SURFACE PLASMON RESONANCE ANALYSIS OF CIB2 – A7B\_M INTERACTION.**

	$k_{a1} (M^{-1}s^{-1})$	$k_{a2} (RU^{-1}s^{-1})$	$k_{d1} (s^{-1})$	$k_{d2} (s^{-1})$	$K_D^{app1} (\mu M)^b$	$K_D^{appTOT} (\mu M)^c$ (N=28)
<b>1 mM <math>Mg^{2+}</math></b> (N = 16)	$(3.1 \pm 0.1) \times 10^4$	$(1.9 \pm 0.4) \times 10^{-3}$	$(3.6 \pm 0.5) \times 10^{-1}$	$(2.0 \pm 1.7) \times 10^{-2}$	$11.6 \pm 1.8$	$220 \pm 20$
<b>1 mM <math>Mg^{2+}</math></b> <b>2 mM <math>Ca^{2+}</math></b> (N = 15)	$(1.6 \pm 0.2) \times 10^4$	$(4.2 \pm 0.5) \times 10^{-4}$	$(4.0 \pm 0.3) \times 10^{-1}$	$(5.3 \pm 0.5) \times 10^{-2}$	$25 \pm 5$	$154 \pm 8$

<sup>a</sup> Kinetic constants were determined according to a bivalent analyte model as explained in Methods of **Paper 2**. N refers to the number of independently analyzed sensorgrams. Results refer to average  $\pm$  SEM.

<sup>b</sup> Apparent affinity for the first binding event, determined by the ratio  $k_{d1}/k_{a1}$ .

<sup>c</sup> Apparent affinity constants accounting for avidity, determined by steady state analysis, measured by taking the maximum response  $RU^{max}$  for a series of 4 repetitions of 7 injections of  $\alpha 7B\_M$  at increasing concentrations. Table and legend are from **Paper 2**<sup>22</sup>.



*The interaction with  $\alpha 7B\_M$  peptide does not increase significantly the affinity for cations*

Frequently, the presence of the biological target induces in the  $\text{Ca}^{2+}$  sensor protein an increase in the affinity for  $\text{Ca}^{2+}$ <sup>84</sup>. Based on this, new titrations were performed in order to assess whether the presence of the  $\alpha 7B\_M$  peptide (**Figure 29**). WT CIB2 showed an increase in  $\text{Ca}^{2+}$  (from 0.5 mM to 0.2 mM) and a decrease in  $\text{Mg}^{2+}$  affinity (from 0.29 mM to 0.49 mM) as E64D, whose  $\text{Ca}^{2+}$  affinity increased from 2 mM to 1.5 mM while the  $\text{Mg}^{2+}$  affinity decreased from 1.5 mM to 1.8 mM (**Table 8**). Even so, E64D is still incapable to bind cations under physiological conditions and WT CIB2 is still far from being functional under relevant  $\text{Ca}^{2+}$  concentrations.

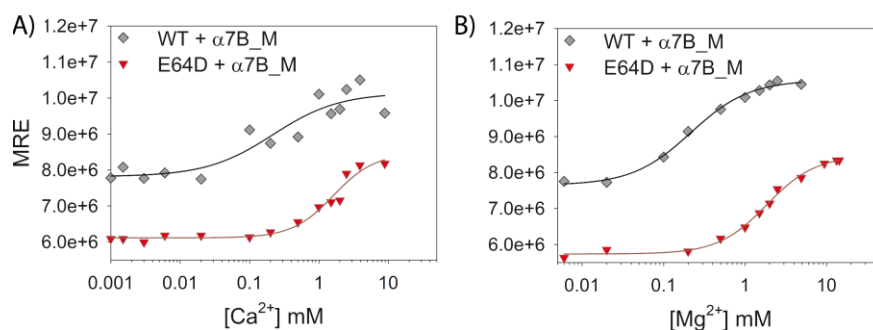


**Figure 29:**  $\text{Ca}^{2+}$  and  $\text{Mg}^{2+}$  affinity assayed by monitoring secondary structure variations in the presence of  $\alpha 7B\_M$  peptide. Twelve micromolar of WT (grey diamonds) and E64D (downwards triangles) CIB2 were titrated with  $\text{Ca}^{2+}$  (A) and  $\text{Mg}^{2+}$  (B) starting from apo-protein (1 mM EGTA). The titrations were performed at 37°C, ions concentrations ranged between 1  $\mu\text{M}$  and 10 mM, each point represents 3 accumulations and data were normalized for protein concentrations and fitted using the Hill 4 parameters function. Figure and legend are an adaptation from **Paper 1**<sup>18</sup>.

**TABLE 8:** APPARENT AFFINITY FOR  $\text{Ca}^{2+}$  AND  $\text{Mg}^{2+}$  OF WT AND E64D CIB2 ASSESSED BY CD TITRATIONS.

	$\text{Mg}^{2+}$		$\text{Ca}^{2+}$	
	$K_d^{\text{app}}$ (mM)	$h_c$	$K_d^{\text{app}}$ (mM)	$h_c$
<b>WT CIB2 + <math>\alpha 7B\_M</math></b>	$0.49 \pm 0.03$	$1.4 \pm 0.1$	$0.2 \pm 0.2$	$0.9 \pm 0.6$
<b>E64D CIB2 + <math>\alpha 7B\_M</math></b>	$1.8 \pm 0.2$	$1.4 \pm 0.2$	$1.5 \pm 0.3$	$1.4 \pm 0.3$

Table is an adaptation from **Paper 1**.

## Conclusions

All the evidences described here show that the features and properties of CIB2 make this “Ca<sup>2+</sup>-sensor protein” worth to be further investigated, first its low affinity for Ca<sup>2+</sup>. In fact, contrary to its homologous CIB1, which has Asn and Glu residues in positions -X and -Z (N169 and E172) in EF4 (Ca<sup>2+</sup> binding motif), optimal for the pentagonal bipyramidal geometry, CIB2 has Gly and Asp (G165 and D168) thus losing the side chain contribution and the possibility to work as bidentate residue respectively. The combination of three different techniques, namely CD, NRM, and chelator assay, showed a Ca<sup>2+</sup> affinity for CIB2 in the high mM range (0.5 mM) and, even though the presence of the target peptide doubled the affinity (0.2 mM), it is still insufficient to make CIB2 a Ca<sup>2+</sup> sensor under physiological conditions. The affinity for Mg<sup>2+</sup> (290 μM) was higher, fully compatible with the fluctuations in cells, which also make the interaction with the target peptide (confirmed to be the membrane-proximal region of the α7B integrin) easier. Our hypothesis consists in the formation of a 1:1 protein:peptide complex that may lead to the attachment of another CIB2 molecule, forming some sort of CIB2 dimer bridged by one peptide molecule. This may explain the sensorgram’s shapes incompatible with the Langmuir model, as suggested by the reaching of saturation in all the tested conditions. This hypothesis found support in the fluorescence emission upon titration, where the signal appeared when the double concentration of CIB2 was incubated with a fixed peptide amount.

The highly hydrophobic surface made the oligomeric state investigation tricky, driving to an erroneous interpretation of the first dataset collected (**Paper 1**<sup>18</sup>). Now, the combination of mass spectrometry, chemical cross-linking, SEC and DLS (**Paper 2**<sup>22</sup>) allowed us to identify CIB2 as a monomeric protein, just like its homologous CIB1. Finally, NMR measurements identified an allosteric communication between E64 (located in the N-terminal, far away from the metal binding loop) and N121 (in EF3), which stabilized the EF1 structure via electrostatic interaction mediated by R33 (hypothesis based on the homology model). Results from the NMR titrations showed EF3 as the putative EF hand for Mg<sup>2+</sup> coordination and EF4 for Ca<sup>2+</sup> coordination under physiological conditions. The replacement of Glu64

with Asp, an extremely conservative mutation, blocked the allosteric communication thus making the mutant incapable to reach its functional folding. Our hypothesis is that the extremely low  $\text{Ca}^{2+}$  affinity coupled with the loss in  $\text{Mg}^{2+}$  binding capability may mediate the lack of correct folding. Despite this, E64D CIB2 is still capable to interact with the biological target showing a WT-like affinity, thus leading us to conclude that the disease-related phenotype doesn't reside in a compromised interaction with the integrin.



## Guanylate Cyclase Activating Protein 1 (GCAP1)

### A novel mutation p.(Glu111Val) in *GUCA1A* appears in an Italian family with Cone-Rod Dystrophy

In 2018 a new GCAP1 mutation was found in an Italian 53-years old patient who reported symptoms like congenital nystagmus, photophobia and low vision acuity since childhood. After the first physical examination he reported to have three daughters, two of them (16 and 22 years old) afflicted by the same but milder father's symptoms, due to the age of the disease. **Figure 30A-C** reports the fundus of the proband (A) and the two daughters (B-C), where is clearly visible the macular degeneration over time. The segregation study (**Figure 30D**) and the genetic analysis validation highlighted a novel mutation in *GUCA1A* gene (p.Glu111Val). This mutation was never detected before but hypothesized as detrimental and deleterious by *in silico* pathogenicity prediction software. Indeed, located in the EF3 (the GCAP1's EF hand motif with the highest affinity for Ca<sup>2+</sup>) E111 is the bidentate residue that supports the Ca<sup>2+</sup> coordination with two oxygen atoms. Thus, the replacement with the hydrophobic Val leads to the loss of two out of seven oxygens required for a stable and functional Ca<sup>2+</sup> coordination.

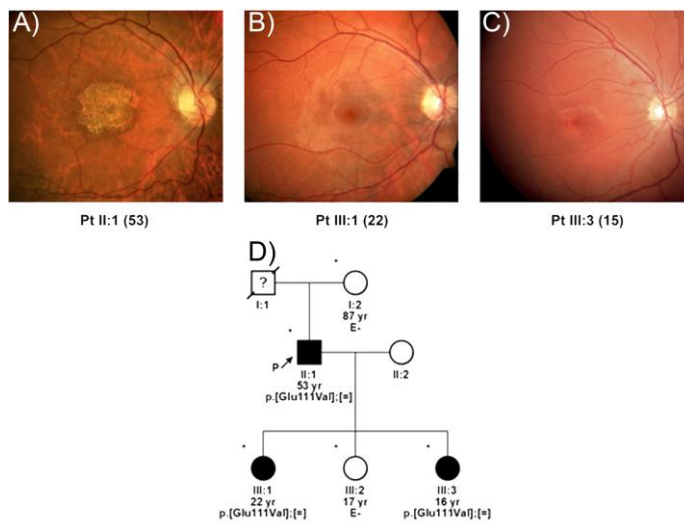


**Figure 30: Clinical and genetic data.** A-C) Color fundus image of the right eye of patient II:1 (A, age 53), III:1 (B, age 22) and III:3 (C, age 16). D) Family tree showing the matching genotype-phenotype segregation of the mutant allele of *GUCA1A* harboring the c.332A>T transition causing the substitution E11V. Legend: square, male subject; circles, female subjects; black symbols, affected subjects; white symbols, healthy subjects. Figure and legend are an adaptation from **Paper 3**<sup>59</sup>.

## Proteins expression and purification

### *WT and E111V GCAP1 purification*

In order to raise the knowledge about the molecular mechanism behind the pathological phenotype, recombinant WT and E111V GCAP1 were expressed in heterologous system (*E. Coli*). Despite the accumulation of GCAP1 in the inclusion bodies, the protocol based on 6M guanidium hydrochloride denaturation followed by in dialysis renaturation allowed a total yield of ~15 mg of pure protein per liter of LB. The myristoylation efficiency was tested and calculated to be >98% (data not shown).

### *Semi-permanent cell line*

In order to reconstruct the system *in vitro*, human GC1 was permanently expressed in Human Embryonic Kidney flip cells (HEK293), upon transfection via PEI reagent and selection with G418 antibiotic. The GC1 expression was monitored by following the fluorescence emission (due to the GFP expression) and via western blot.

## GC assay

In order to assess the capability of WT and E111V GCAP1 to exert the role of GC1 regulator, the system was reconstituted *in vitro* combining purified GCAPs and HEK's membranes conveniently prepared. WT and E111V GCAP1 show an approximately equal capability to stimulate the GC1 in the absence of free  $\text{Ca}^{2+}$  (< 19 nM) but, raising the  $\text{Ca}^{2+}$  concentration at value at which WT GCAP1 totally inhibits the enzyme, E111V shows a residual activation profile (~60%) (**Figure 31A**). Evaluating the cGMP synthesis as function of  $\text{Ca}^{2+}$  ( $\text{IC}_{50}$ ), WT GCAP1 showed an activating-to-inhibiting switch at physiological  $\text{Ca}^{2+}$  concentration ( $\text{IC}_{50} = 0.26 \mu\text{M}$ ), differently E111V showed an  $\text{IC}_{50} = 10 \mu\text{M}$ , leading to the generation of a constitutively active enzyme (**Figure 31C**). To exclude the dysregulation as consequence of decreased affinity of E111V GCAP1 for GC1,  $\text{EC}_{50}$  measurements were performed ([GCAP1] at which the GC1 activity is half maximal). The quite similar values obtained ( $\text{EC}_{50}^{\text{WT}} = 3.2 \mu\text{M}$  vs.  $\text{EC}_{50}^{\text{E111V}} = 3.5 \mu\text{M}$ ) suggest no compromised complex formation (**Figure 31B**).

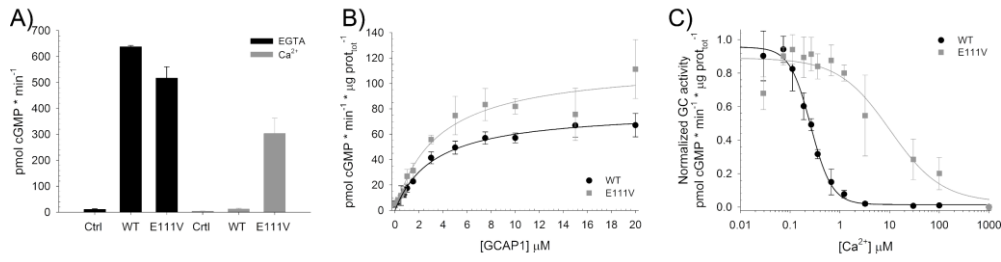


**Figure 31. Guanylate cyclase 1 (GC1) regulation by WT and E111V GCAP1.** **A)** Membranes containing GC were reconstituted with 5  $\mu\text{M}$  WT or E111V GCAP1 and  $<19\text{ nM}$   $\text{Ca}^{2+}$  (black) or  $\sim 30\text{ }\mu\text{M}$  free  $\text{Ca}^{2+}$  (grey); membranes with no GCAP1 were used as control. **B)** GC activity as a function of WT (black) or E111V (grey) GCAP1 concentration (0–20  $\mu\text{M}$ ) in the presence of  $<19\text{ nM}$  free  $\text{Ca}^{2+}$ . **C)** GC activity as a function of  $\text{Ca}^{2+}$  concentration ( $<19\text{ nM}$  – 1  $\text{mM}$ ) of 5  $\mu\text{M}$  WT (black) or E111V (grey) GCAP1. The physiological window of variation in  $\text{Ca}^{2+}$  concentration during the phototransduction cascade is shaded in grey. Figure and legend are an adaptation from **Paper 3**<sup>59</sup>.

**TABLE 9: RESULTS OF GC REGULATION AND  $\text{Ca}^{2+}$  BINDING EXPERIMENTS.**

	$\text{IC}_{50}$ ( $\mu\text{M}$ ) <sup>a</sup>	$h_c$ <sup>b</sup>	$\text{EC}_{50}$ ( $\mu\text{M}$ ) <sup>c</sup>	X-fold <sup>d</sup>	$\log k_1$ <sup>e</sup>	$\log k_2$ <sup>e</sup>	$K_d^{\text{app}}$ <sup>f</sup>
<b>WT</b>	$0.26 \pm 0.01$	$2.05 \pm 0.21$	$3.2 \pm 0.3$	16	$7.07 \pm 0.13$	$5.55 \pm 0.19$	0.49
<b>E111V</b>	$10 \pm 5$	$0.83 \pm 0.27$	$3.5 \pm 0.9$	15.7	$4.3 \pm 1.1$	$0.46 \pm 1.6$	$\sim 40$

<sup>a</sup>  $\text{IC}_{50}$  is the half-maximal activating  $\text{Ca}^{2+}$  concentration.

<sup>b</sup>  $h_c$  is the Hill Coefficient.

<sup>c</sup>  $\text{EC}_{50}$  is the half-maximal activating GCAP1 concentration.

<sup>d</sup> X-fold activation is  $(\text{GC}_{\text{max}} - \text{GC}_{\text{min}})/\text{GC}_{\text{min}}$ .

<sup>e</sup> Decimal logarithm of the macroscopic  $\text{Ca}^{2+}$ -binding constants after fitting data to a two independent binding sites model with CaLigato<sup>r</sup><sup>87</sup>.

<sup>f</sup> Apparent affinity is the average of the significant  $\log K_i$  (see Materials and Methods for details). Table and legend are an adaptation from **Paper 3**<sup>59</sup>

## Oligomeric state investigation

In a recent publication it was demonstrated that bovine GCAP1 forms active dimers<sup>105</sup> and to assess whether the E111V mutation leads to a different oligomeric state, SEC and DLS measurements were performed (**Figure 32**). WT and E111V GCAP1 elution profiles were collected both in the presence of sole  $Mg^{2+}$  (500  $\mu$ M EGTA + 1 mM  $Mg^{2+}$ ) and in the co-presence of  $Mg^{2+}$  and  $Ca^{2+}$  (1 mM  $Mg^{2+}$  + 1 mM  $Ca^{2+}$ ) to check the effect of the two cations. **Figure 32A-B** shows no differences in both GCAP1 variants, with an estimated MW of 43.7 kDa (WT) and 47.8 kDa (E111V), fully compatible with dimeric organization, considering that 22.9 kDa is the MW of monomeric GCAP1. The eluted peaks were analyzed by DLS (25°C), resulting in monodisperse peaks with hydrodynamic diameters of  $6.33 \pm 0.03$  nm for WT GCAP1 and  $5.98 \pm 0.05$  nm for E111V, in the presence of sole  $Mg^{2+}$ . The addition of  $Ca^{2+}$  didn't change neither the size nor the mean count rate (MCR, indicator of the aggregation propensity). Increasing the measurement time at physiological temperature to assess the stability, something different was seen (**Figure 33**). In the sole presence of  $Mg^{2+}$ , WT GCAP1 shows a moderate tendency to form large aggregates, as highlighted by the MCR variations over time. MCR values for WT remain approximately stable for the first 4 hours, starting to increase with a constant slope describing a slow aggregation process, culminating in a 4-fold increase in MRC at the end of the data collection. Conversely, E111V GCAP1 shows a more prominent aggregation tendency in the  $Mg^{2+}$ -bound GC1-activating condition, that starts immediately with a steep linear slope, ending after 16 hours with a 10-fold MCR value increased, compatible with a severe and constant protein aggregation.



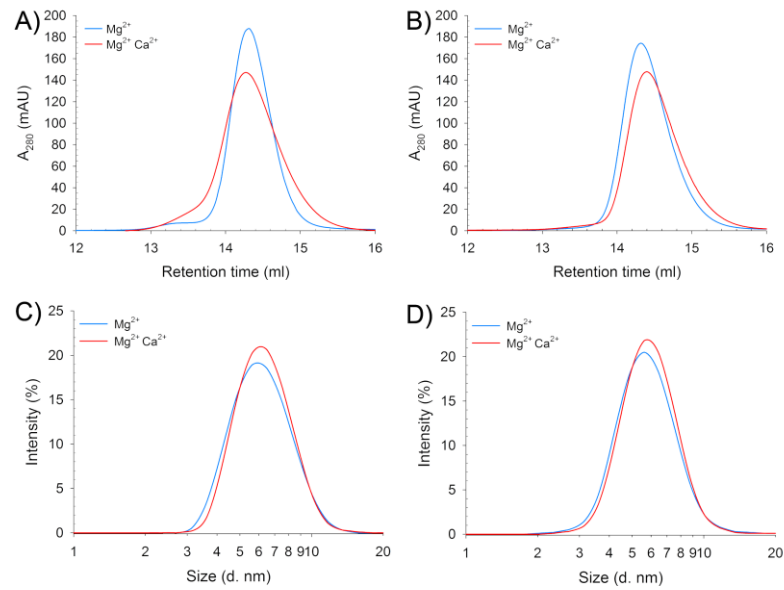


**Figure 32: Results from Size Exclusion Chromatography and Dynamic Light Scattering experiments.** Chromatograms of Size Exclusion Chromatography of  $\sim 40 \mu M$  WT (A) and E111V (B) GCAP1 in the presence of  $500 \mu M$  EGTA and  $1 mM Mg^{2+}$  (blue), or  $1 mM Mg^{2+}$  and  $500 \mu M Ca^{2+}$  (red). Hydrodynamic diameter estimation of  $\sim 20 \mu M$  WT (C) and E111V (D) GCAP1 in the presence of  $500 \mu M$  EGTA and  $1 mM Mg^{2+}$  (blue), or  $1 mM Mg^{2+}$  and  $500 \mu M Ca^{2+}$  (red). DLS measurements were collected approximately every minute, each measurement was an accumulation of 6 runs. Figure and legend are from Paper 3<sup>59</sup>

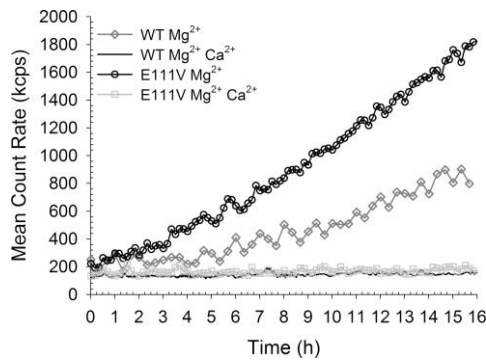


**Figure 33: Aggregation propensity at physiological temperature.** Mean Count Rate evolution over 16 h of  $\sim 20 \mu M$  WT GCAP1 in  $20 mM$  Tris-HCl pH 7.5,  $150 mM$  KCl,  $1 mM$  DTT, in the presence of  $500 \mu M$  EGTA and  $1 mM Mg^{2+}$  (grey diamonds), or  $1 mM Mg^{2+}$  and  $500 \mu M Ca^{2+}$  (black line), and  $\sim 20 \mu M$  E111V in the presence of  $500 \mu M$  EGTA and  $1 mM Mg^{2+}$  (black circles), or  $1 mM Mg^{2+}$  and  $500 \mu M Ca^{2+}$  (light grey squares). Measurements were collected at  $37^\circ C$  approximately every minute; each measurement was an accumulation of 6 runs. Figure and table are from Paper 3<sup>59</sup>.

## Hydrophobicity evaluation

Considering the replacement of the hydrophilic Glu with the hydrophobic Val, and the propensity to form large aggregates of both variants in the presence of  $Mg^{2+}$ , ANS fluorescence was used to detect changes in the protein surface properties. The comparison between fluorescence emission of sole ANS and apo-WT GCAP1 shows an intense blue shift (31 nm) and an increased intensity, thus suggesting a highly hydrophobic surface. The addition of 1 mM  $Mg^{2+}$  causes a 7 nm red shift and a reduction of fluorescence emission, then slightly increased by the addition of saturating  $Ca^{2+}$  concentration. This trend is partially shared by E111V GCAP1 which showed an intense blue shift (29 nm) and an increased fluorescent emission in the absence of ions but only 3 nm red shift upon addition of  $Mg^{2+}$  and  $Ca^{2+}$  (**Table 10**). Taken together, these evidences suggest that different aggregation propensity were not related to changes in protein's surface.

	$\lambda_{max}$	$I/I_{max}$	$\Delta\lambda$
<b>ANS alone</b>	517		
<b>WT GCAP1</b>			
<b>EDTA</b>	468	1	31
<b>+ <math>Mg^{2+}</math></b>	493	0.73	24
<b>+ <math>Ca^{2+}</math></b>	493	0.76	24
<b>E111V GCAP1</b>			
<b>EDTA</b>	488	1	29
<b>+ <math>Mg^{2+}</math></b>	494	0.62	23
<b>+ <math>Ca^{2+}</math></b>	494	0.70	23

*$\Delta\lambda$  is the variation of the maximal wavelength w.r.t ANS alone.*

## Structural properties

As mentioned in the introduction, GCAP1 is a small protein formed by 4 EF-hand motifs, a helix-loop-helix structural organization that, when irradiated by circularly polarized light in the far UV range (200-250 nm), is described by a typical spectrum characterized by the presence of two minima (208 nm 222 nm). The ratio between the ellipticity signals at 222 nm and 208 nm ( $\theta_{222}/\theta_{208}$ ) is used for describing the total structural variation as consequence of cation-coordination events. To obtain the fingerprint of human WT and E111V GCAP1, near UV CD spectra were col-

lected in different conditions (**Figure 34**). In the absence of ions both GCAP1 variants were correctly folded and, while the addition of 1 mM  $Mg^{2+}$  had no effect in WT GCAP1 folding, small but significant changes were instead detected for E111V (**Table 11**). When saturating  $Ca^{2+}$  was added on  $Mg^{2+}$ , a ~6% and ~4% variation was detected for WT and E111V respectively.

Sliding the wavelength window in the near UV region (250-320 nm), information describing the tertiary structure can be obtained, more specifically due to changes in the aromatic amino acid environment. Apo-WT and -E111V GCAP1 showed very similar spectra in shape, but not in intensity, and the mutant spectrum was shifted to more positive values. The addition of 1 mM  $Mg^{2+}$  induced in E111V a more intense structural variation toward negative values, not seen for WT GCAP1. Finally, in the presence of saturating  $Ca^{2+}$ , a further shift to more negative values was detected for both WT and E111V resulting in similar final shape. In general, the structural variations detected were more pronounced for E111V than WT GCAP1.

Many evidences suggest a crucial role of  $Mg^{2+}$  in E111V structural properties. To better investigate the role of  $Ca^{2+}$  and  $Mg^{2+}$  in structure stabilization, thermal denaturation (20-96°C) profiles were collected in the same conditions used for far UV spectra. As expected, the presence of saturating  $Ca^{2+}$  prevents the clear transition from a folded to an unfolded state, as already seen for other  $Ca^{2+}$  sensors. Instead, the presence of 1 mM  $Mg^{2+}$  led in E111V a 5.5°C stabilization with the respect to WT GCAP1 ( $T_m^{E111V} = 54.5^\circ C$  vs  $T_m^{WT} = 49^\circ C$ ), further emphasizing the crucial role of magnesium.

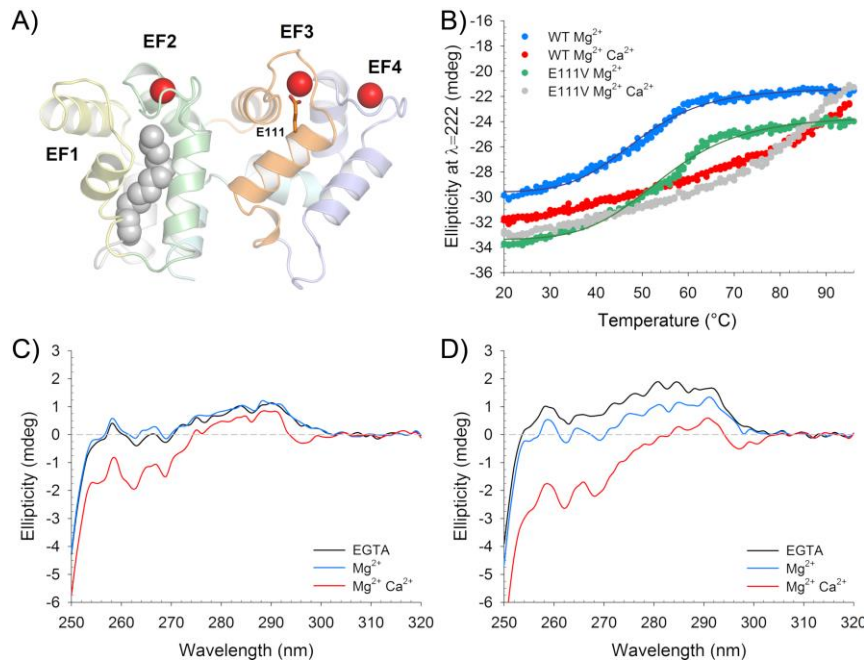


**Figure 34: Structural features and stability changes in WT and E111V GCAP1 upon ion binding monitored by circular dichroism.** A) Cartoon representation of the three-dimensional homology model of  $\text{Ca}^{2+}$ -loaded human GCAP1; EF1 is colored in yellow, EF2 in green, EF3 in orange and EF4 in light blue. N- and C-terminal are represented in light grey and light cyan, respectively; the myristoyl group is represented in grey spheres,  $\text{Ca}^{2+}$  ions are shown as red spheres and residue E111 is shown as sticks. B) Thermal denaturation profiles of  $\sim 10 \mu\text{M}$  WT GCAP1 in the presence of  $300 \mu\text{M}$  EGTA and  $1 \text{mM}$   $\text{Mg}^{2+}$  (blue), or  $1 \text{mM}$   $\text{Mg}^{2+}$  and  $300 \mu\text{M}$   $\text{Ca}^{2+}$  (red), and  $\sim 10 \mu\text{M}$  E111V in the presence of  $300 \mu\text{M}$  EGTA and  $1 \text{mM}$   $\text{Mg}^{2+}$  (green), or  $1 \text{mM}$   $\text{Mg}^{2+}$  and  $300 \mu\text{M}$   $\text{Ca}^{2+}$  (grey). Thermal denaturation was performed in  $20 \text{mM}$  TRIS-HCl pH 7.5,  $150 \text{mM}$  KCl by following the decrease in ellipticity at  $222 \text{nm}$  over the  $20\text{--}96^\circ\text{C}$  temperature range. When possible, data were fitted to a four-parameter Hill sigmoid (**Table II**). Near UV CD spectra of  $\sim 35 \mu\text{M}$  WT (C) and E111V (D) GCAP1 in the presence of  $500 \mu\text{M}$  EGTA (black) and after sequential additions of  $1 \text{mM}$   $\text{Mg}^{2+}$  (blue) and  $500 \mu\text{M}$  free  $\text{Ca}^{2+}$  (red). CD spectra were recorded at  $37^\circ\text{C}$  in  $20 \text{mM}$  TRIS-HCl pH 7.5,  $150 \text{mM}$  KCl,  $1 \text{mM}$  DTT. Figure and legend are from **Paper 3**<sup>59</sup>.

**TABLE II: RESULTS FROM CD FAR UV SPECTROSCOPY AND THERMAL DENATURATION PROFILES.**

	$\theta_{222}/\theta_{208}$	$\Delta\theta/\theta$ (%)	$T_m$ ( $^\circ\text{C}$ )
<b>WT GCAP1</b>			
EGTA	0.94		
+ $\text{Mg}^{2+}$	0.94	2	49.0
+ $\text{Ca}^{2+}$	0.96	6	> 96
<b>E111V GCAP1</b>			
EGTA	0.92		
+ $\text{Mg}^{2+}$	0.93	-1	54.5
+ $\text{Ca}^{2+}$	0.93	4	> 96

$\theta_{222}/\theta_{208}$  is the intensity ratio at  $\lambda = 222$  and  $\lambda = 208 \text{nm}$ ,  $\Delta\theta/\theta$  is calculated as  $((\theta_{\text{ion}} - \theta_{\text{EGTA}})/\theta_{\text{EGTA}}) * 100$  at  $\lambda = 222 \text{nm}$ ,  $T_m$  is the transition after fitting the signal at  $222 \text{nm}$  to a 4-parameter Hill sigmoid. Table is an adaptation from **Paper 3**.

## Calcium affinity evaluation

Functional assays showed  $IC_{50}$  value for E111V GCPA1 shifted to non-physiological  $[Ca^{2+}]$ , implying a constitutive activity of the enzyme. To shed light on this,  $Ca^{2+}$  binding properties of GCAP1 variants were assayed by two methods: gel shift (low-resolution) and chelator assay (high-resolution).

The gel-shift is an easy and informative low-resolution technique that allows to assess whether the  $Ca^{2+}$ -binding properties are affected or not by the mutations. It is based on the fact that some  $Ca^{2+}$  binding proteins retain a partial folding when  $Ca^{2+}$ -bound, leading to the resistance to both thermal and detergent-induced denaturation. In fact, apo- and  $Mg^{2+}$ -bound WT GCAP1 have the same electrophoretic mobility, compatible with a 23 kDa proteins, but the presence of  $Ca^{2+}$  make WT GCAP1 faster, with an apparent MW of ~17 kDa (**Figure 35A**). Something different was seen for E111V, which also showed the gel-shift, even if less pronounced, suggesting compromised  $Ca^{2+}$ -binding properties. To quantitatively determine the affinity, a spectroscopic-based method was used, namely chelator assay, consisting in the measurement of the competition for  $Ca^{2+}$  binding in the presence of 5-5'-Br<sub>2</sub> BAPTA (**Figure 35B**). The sigmoidal shape of WT GCAP1 data distribution highlights the presence of competition that resulted in a high-affinity (low nM) and a moderate-affinity (low  $\mu$ M)  $Ca^{2+}$  binding sites (**Table 9**), with a physiologically relevant apparent affinity ( $K_d^{app} = 490$  nM). The same didn't happen with E111V, whose profile was more similar to the sole chelator, implying the absence of competition. In fact, two low-affinity binding sites were recognized upon data fitting, resulting in a  $K_d^{app} = 40$   $\mu$ M, extremely incompatible with physiological  $Ca^{2+}$ -sensing.

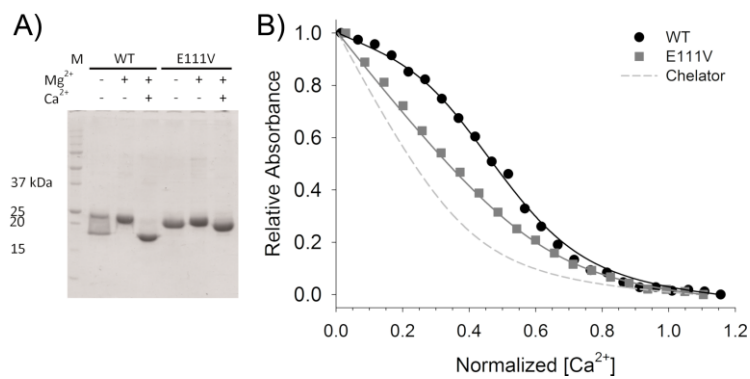


**Figure 35:  $\text{Ca}^{2+}$  sensitivity of WT and E111V monitored by gel mobility shift SDS-PAGE and absorption spectroscopy.** **A)** 15% SDS-PAGE of  $\sim 30 \mu\text{M}$  WT or E111V GCAP1 in the absence of ions (5 mM EDTA), in the presence of  $\text{Mg}^{2+}$  (5 mM EGTA and 1 mM free  $\text{Mg}^{2+}$ ) and in the presence of  $\text{Mg}^{2+}$  and  $\text{Ca}^{2+}$  (1 mM  $\text{Mg}^{2+}$  and 5 mM  $\text{Ca}^{2+}$ ). **B)** Normalized  $\text{Ca}^{2+}$  titration curves obtained by a competition assay with the chromophoric 5,5'-Br<sub>2</sub>-BAPTA of WT (black circles) and E111V GCAP1 (grey squares) in the presence of 1 mM  $\text{Mg}^{2+}$ .  $\text{Ca}^{2+}$  concentrations include dilution effects upon titration; normalization details are reported in the Methods section. Experimental data are shown together with the optimal curve obtained by computer fitting (black and grey solid lines, respectively) and the theoretical (Chelator) curve simulating the titration of the chelator (grey dashed line); estimation of  $\log k_i$  is reported in **Table 9**. Figure and legend are an adaptation from **Paper 359**.

## **New hypothesis: replacement of mutant protein by extra delivery of WT-GCAP1**

### **GCAP2 doesn't regulate GC1 activity**

Collectively, all these evidences highlight the higher sensitivity of E111V GCAP1 for  $Mg^{2+}$  (GC-activating form) with respect to  $Ca^{2+}$  (GC-inhibiting form), as confirmed by chelator assays and  $IC_{50}$  measurements. However, the  $IC_{50}$  was evaluated in the sole presence of E111V GCAP1, condition that never occurs because of the autosomal dominant mechanism of inheritance; in fact, COD/CORD patients carry half WT and half mutated GCAP1. Moreover, GCAP1 is not the only regulator of phototransduction shut-off; other GCAPs isoforms are present in human, as GCAP2 and GCAP3. Particularly, GCAP2 is directly involved in the calcium-relay, mechanism for which while GCAP1 is responsible for the first boost of cGMP upon illumination, GCAP2 is activated by prolonged light stimulation (at least in mouse and bovine). In this respect, our initial hypothesis was to investigate whether the presence of GCAP2 may lead to a compensation effect, thus shifting the total  $IC_{50}$  to WT-like values with the final aim to slow down the progression of the disease. After having checked the GCAPs variants via gel-shift (**Figure 36A**) and the presence of GC1 in HEK cells (**Figure 36B**), GC assays were performed in the on-off mode to confirm GCAP2 capability in GC regulation (**Figure 36C**). Surprisingly, the cGMP synthesis in GCAP2-GC1 reconstructed system was very similar to the basal activity (in the absence of regulators). The measurements were also performed incubating equal amounts of GCAP1 and GCAP2 (5  $\mu$ M GCAP1 + 5  $\mu$ M GCAP2) looking for synergic activity but even if cGMP was detected, the lower amount (compared to the yield of cGMP in the presence of sole GCAP1) and the highly scattered data, suggested no significant contribution by GCAP2. To exclude that this unexpected result was due to a decreased affinity of GCAP2 for  $Mg^{2+}$ , the measurements were also performed at higher non-physiological  $Mg^{2+}$  concentrations (12 mM, **Figure 36C**, right), resulting in the same trend.

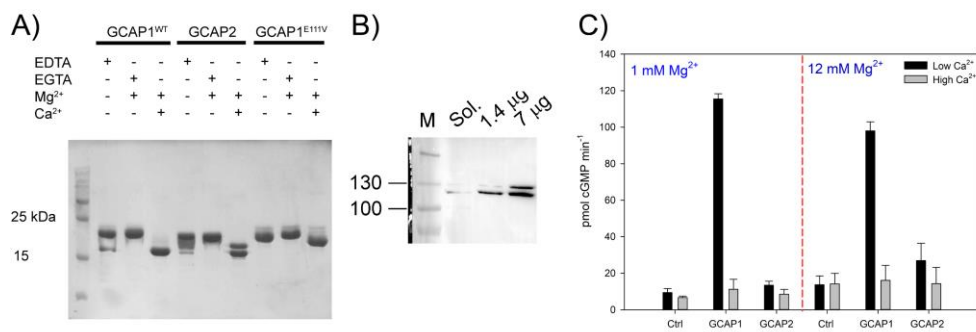


**Figure 36: Ca<sup>2+</sup>-induced gel shift, GC1 western blot and enzymatic assay.** A) SDS-PAGE of WT/E111V GCAP1 and GCAP2 in the presence of 5 mM EDTA, 4 mM EGTA + 1.4 mM Mg<sup>2+</sup>, 1 mM Mg<sup>2+</sup> + 4 mM Ca<sup>2+</sup>. Twenty micromolar WT GCAP1, E111V GCAP1 and WT GCAP2 were incubated for 10 min at 30°C in the presence or absence of ions and loaded in a 15% SDS-PAGE. Gel was Coomassie blue stained. B) Western blot of GC1 extracted from the membranes used for the assay. After have quantified the total amount of proteins by amido black assay, samples were boiled for 5 min and loaded in a 10% polyarylamide gel. Ab#3 against GC1 (1:1000) was diluted in 3% milk + 0.01% tween and icubated overnight at 4°C. Secondary antibody was incubated (1:10000) at room temperature for 1 h and chemoluminescence was revealed by ECL reagent. C) GC enzymatic assay of 10 μM GCAP1 or GCAP2 were performed in the presence of low (< 19 nM) and high (~30 μM) Ca<sup>2+</sup> concentration and in the presence of 1 mM Mg<sup>2+</sup> (left) and 12 mM Mg<sup>2+</sup> (right). Each measurement represent the avarage of 3 replicas ± standard deviation. Figure and legend are an adation from **Paper 4**<sup>106</sup>.



## Exploring the effect of WT GCAP1 extra delivery

Since GCAP2 seems not to participate in GC1 regulation, the compensatory effect was studied by monitoring the  $\text{Ca}^{2+}$ -dependent cGMP synthesis at increased WT GCAP1 concentration thus mimicking sort of extra delivery (**Figure 37**). Firstly, keeping in mind the AD nature of the disease,  $\text{IC}_{50}$  measurements were performed simulating the heterozygous patient who carries 50% WT and 50% E111V GCAP1 (**Figure 37, green line**). Comparing the trend obtained with the one in the sole presence of E111V (**Figure 37, red line**) the amelioration of the  $\text{IC}_{50}$  was clearly visible, from  $10 \pm 5 \mu\text{M}$  (sole E111V) to  $694 \pm 75 \text{ nM}$ . This means that the functionally active WT GCAP1 partially buffers the presence of the mutant, explaining the time-related progression of the disease. To investigate the effect of the extra delivery, 3-fold WT GCAP1 concentration was used on a heterozygous background (**Figure 37, yellow line**). Interestingly, a statistically significant positive effect was detected both in  $\text{Ca}^{2+}$ -sensitivity ( $\text{IC}_{50} = 497 \pm 49 \text{ nM}$ , one-tailed  $p = 0.029$ ) and in cooperativity ( $h_c = 1.49 \pm 0.35$  vs  $0.87 \pm 0.18$ ), even if the E111V residual activity is still quite high (~45%) (**Table 12**).

In order to better investigate the role of each of the GCAPs variant (WT and E111V GCAP1, GCAP2) in shaping the photoresponse, system biology simulations were performed by Prof. Daniele Dell'Orco by using a comprehensive biochemical model of phototransduction in mouse rod (**Paper 4<sup>106</sup>**). Two conditions were initially simulated namely heterozygosis (WT/E111V), found in CORD-patient, and homozygosis (E111V/E111V) (**Figure 37B**). **Figure 37B right** shows how the presence of the sole mutant led to a prolonged photoresponse with increased time to peak. This behavior seems to be related to the E111V relative abundance since a similar but milder trend was detected in the heterozygosis case (**Figure 37B left**). In fact, in the co-presence of WT and E111V GCAP1 the detected increase in dark levels of  $\text{Ca}^{2+}$  (3.1-fold) and cGMP (1.4-fold) were significantly lower with respect to homozygosis case (X-fold  $[\text{Ca}^{2+}] = 12.5$ , X-fold  $[\text{cGMP}] = 2.0$ ) (**Table 13**). The  $\text{IC}_{50}$  values from *in vitro* measurements were also used to simulate the effect of the 3-fold extra delivery of WT GCAP1 on the heterozygous background, both including (in line with the  $\text{Ca}^{2+}$ -relay mechanism) and excluding (in line with last findings) the contribution of GCAP2. The results obtained showed that the presence of

GCAP2 is fundamental in shaping a WT-like photoresponse (**Figure 37C left**), as confirmed by the fact that its absence led to a trend more similar to the heterozygosis (**Figure 37C right**).

Taken together, these results allow to conclude that the calcium-relay mechanism involving GCAP1 and GCAP2 might be species-dependent and the identification of alternative molecular partners, capable to exert in human the same effect exerted by GCAP1 and GCAP2 in mouse or bovine, remain to be clarified.

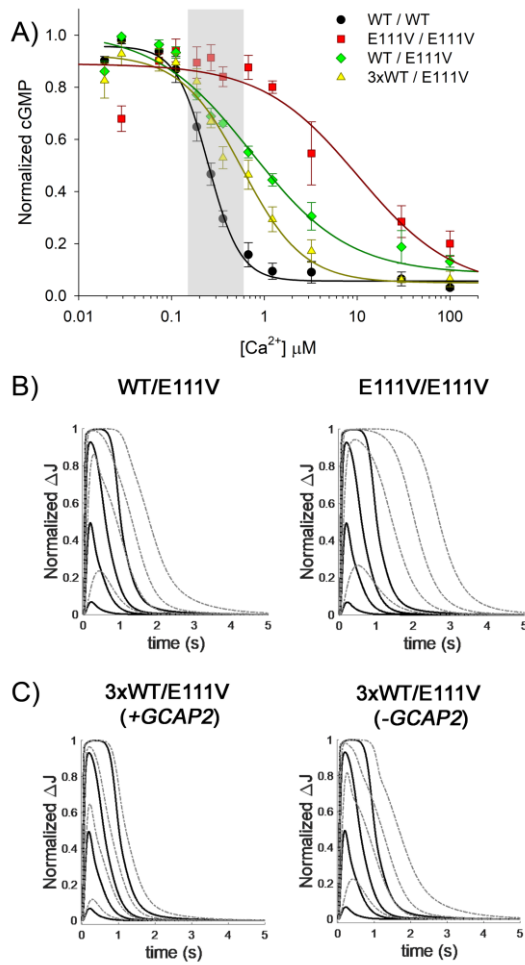


**Figure 37: in vitro and in silico results.** A) The GCI activity as function of  $[Ca^{2+}]$  was measured in the presence of 10 μM WT GCAP1 (black circles), 5 μM WT GCAP1 + 5 μM E111V GCAP1 (green diamonds) and 15 μM GCAP1 + 5 μM E111V GCAP1 (yellow triangles). E111V GCAP1 activity is referred to the curve reported in **Paper 3**<sup>59</sup>. Each data set is relative to 4-6 replicas and data are normalized according to both total content in membranes and maximum and minimum GCI activity recorded in each replica. Error bars represent s.e.m. Solid lines represent the results of data fitting while the gray box the physiological  $Ca^{2+}$  fluctuations in rod photoreceptors. B-C) Simulations of flash responses from dim to bright light conditions. After equilibration of the rod outer segment in the dark, 24 ms flashes were delivered, leading to 1.54, 18, 87 and 500 photoisomerizations of rhodopsin. Black traces: WT GCAPs-containing rods. Dash-dotted gray lines: photoresponses in a WT/E111V heterozygous case (B, left), E111V/E111V homozygous case (B, right) and in the presence (C, left) and in the absence (C, right) of endogenous GCAP2. Photocurrents represent the suppression of the dark current at each light intensity and have been normalized. Figure and legend are an adaptation from **Paper 4**<sup>106</sup>.

**TABLE 12: RESULTS FROM ENZYMATIC ASSAY: HUMAN GCI ACTIVITY AS A FUNCTION OF FREE  $[Ca^{2+}]$ .**

	GCAP1 <sup>WT</sup> (n = 6)	GCAP1 <sup>E111V</sup> <sup>b</sup> (n = 4)	GCAP1 <sup>WT/E111V</sup> (n = 6)	3xGCAP1 <sup>WT</sup> / GCAP1 <sup>E111V</sup> (n = 6)
IC <sub>50</sub> (nM)	251 ± 19 <sup>a</sup>	(10 ± 5) × 10 <sup>3</sup>	694 ± 75	497 ± 49
h <sub>c</sub>	2.60 ± 0.42	0.83 ± 0.27	0.87 ± 0.18	1.49 ± 0.35

<sup>a</sup> mean ± s.e.m.; <sup>b</sup> data from **Paper 4**<sup>106</sup>

**TABLE 13: INCREASE IN DARK LEVEL OF  $Ca^{2+}$  AND cGMP ACCORDING TO NUMERICAL SIMULATION OF A MOUSE ROD OUTER SEGMENT COMPARED TO A WT CASE.**

	GCAP1 <sup>WT/E111V</sup>	GCAP1 <sup>E111V/E111V</sup>	3xGCAP1 <sup>WT</sup> / GCAP1 <sup>E111V</sup> <b>+GCAP2</b>	3xGCAP1 <sup>WT</sup> / GCAP1 <sup>E111V</sup> <b>-GCAP2</b>
<b>X-fold</b> <b>[Ca<sup>2+</sup>]<sub>free</sub></b>	3.1	12.5	1.4	3.0
<b>X-fold</b> <b>[cGMP]</b>	1.4	2.0	1.1	1.4

*Table and legend are an adaptation from Paper 4<sup>106</sup>, for further elucidation see Methods of Paper 4<sup>106</sup>.*

## Conclusions

E111V GCAP1 point mutation has been found in an Italian family where three members (father and two daughters) are affected by COD. The biochemical and biophysical analysis suggested that the mutation doesn't affect the protein structure or the oligomeric state, even if E111V GCAP1 shows a higher sensitivity to  $Mg^{2+}$ . This leads to an increased thermal stability and a serious propensity to form large aggregates at physiological temperature not mediated by changes on surface hydrophobicity. As other GCAP1 mutants, E111V is characterized by a decreased affinity for  $Ca^{2+}$  that find explanation in the replacement of the bidentate residue in EF3 with a hydrophobic Val residue, thus losing two out of seven oxygen residues required for  $Ca^{2+}$  coordination. Molecular simulations performed by Dr. Valerio Marino pointed out a more rigid structure of  $Mg^{2+}$ -E111V that explains the higher thermostability but also highlights a structural distortion of EF3 loop. The crucial difference between WT and E111V is the total loss of GC regulation, leading to a constitutive active enzyme. This triggers the increase of the free  $Ca^{2+}$  and cGMP concentrations in the outer segment. These can diffuse through the inner segment mediating cellular death mechanisms causing the disease phenotype. Since COD are autosomal dominant diseases, *in vitro* and *in silico* experiments were performed in order to investigate the effect of GCAPs extra delivery. Surprisingly, GCAP2 seems to be incapable in GC1 regulation in human (evidence obtained also in others independent laboratories), even if it actively participates to  $Ca^{2+}$ -relay in mouse and bovine. Thus, the extra delivery of 3-fold WT GCAP1 was investigated resulting in an amelioration of the  $IC_{50}$  values. Unfortunately, it is not enough to totally buffer the presence of E111V. Our hypothesis is that, even if GCAP1 has been demonstrated to be a dimer, GC1 is regulated by monomeric GCAP1 so, probably, the combination of high amounts of protein during the assay and different equilibria between WT and E111V GCAP1, decrease the concentration of monomeric GCAP1 available for GC1 regulation. Moreover, system biology simulation underlines the pivotal role played by GCAP2 in shaping WT-like photoresponses in a heterozygous context. Thus, the  $Ca^{2+}$  relay mechanism seems to be species-dependent, implying the presence of alternative compensatory effects in human capable to exert the same role played by GCAP2 in mouse and bovine.

### *Work in progress: study of point mutations on residues directly involved in Ca<sup>2+</sup> coordination*

As mentioned in the introduction, 22 point mutations have been found in *GUCA1A* gene, some of them affecting residues that actively participate in Ca<sup>2+</sup> coordination (i.e. E111V), others located in the surrounding areas. Sometimes, more than one substitution on the same amino acid is possible, for instance Ile143 was found mutated in Thr and Asn (I143T/N)<sup>61</sup>. The aim of this manuscript still under preparation, is to focus the attention on residues directly involved in Ca<sup>2+</sup> coordination namely D100G, E155A and E155G, in order to identify distinctive features that may improve the knowledge on the molecular basis of the disease and, combined with bioinformatic tools, predict the effects of different mutations on the same residue. For these reasons an extensive analysis is ongoing, involving Asp100Gly (D100G), located in EF3, and the double mutation on Glu155, bidentate residue of EF4, into Ala or Gly (E155A/G) (**Figure 38**). These mutants have been already partially described with specific focus on genic validation, clinical evidences and some experimental data (mostly fluorescence spectroscopy experiments). A comprehensive biochemical and biophysical characterization is still missing.

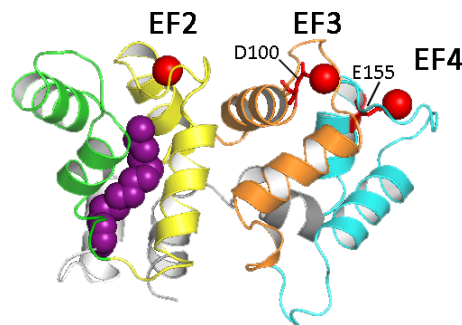


**Figure 38:** *GCAP1 Ca<sup>2+</sup> bound tridimensional model.* Myristoyl-moiety was colored in deep purple, EF1, EF2, EF3 and EF4 are colored in green, yellow, orange and cyan respectively. Red sticks represent residues D100 and E155.

## State of art

D100G GCAP1 was found in three family members afflicted by symptoms like nystagmus, intraretinal pigment migration, loss of RPE and macular atrophy with a childhood onset (first decade) that led to CORD diagnosis<sup>57</sup>. E155G point mutation was found during an extensive genetic study where 67 individuals were involved, 33 of those were found affected by CORD<sup>63</sup>. The phenotype consisted in decreased visual acuity with early onset (8-24 years old with a mean of 16 years) and central macular lesion with pigmentary changes. Some biochemical analyses were performed including fluorescence titration and enzymatic assay for the determination of the EC<sub>50</sub> and IC<sub>50</sub> values. The authors concluded that the structural properties of the mutant were preserved, and, even if EC<sub>50</sub> value was similar to WT GCAP1, the IC<sub>50</sub> was shifted to higher values (~ 1 μM)<sup>63</sup>. Finally, E155A was found in one of 130 unrelated Chinese probands, and its analysis was extended to four generations. Nine people were found afflicted by CORD, having symptoms like poor vision, photophobia, myopia, defective color perception and showing signs as temporal disc pallor, attenuated retinal arterioles, macular atrophy, or pigmentary anomaly in the central macula<sup>64</sup>.

## Evaluation of hydrophobicity and aggregation propensity

To test whether the replacement of the negatively charged side chain of Asp and Glu residues with a small (Gly) or hydrophobic (Ala) side chain led changes in the hydrophobicity, ANS fluorescence was used (**Figure 39**). As already seen for E111V, all the mutants were more hydrophobic when in the absence of ions, showing a 34-35 nm blue shift (**Table 14**). The addition of 1 mM Mg<sup>2+</sup> (blue solid lines) caused in D100G effects similar to those in WT GCAP1, considering both red-shift (7 nm upon Mg<sup>2+</sup> addition and 1-2 nm upon Ca<sup>2+</sup> addition) and variation in fluorescence emission. Interestingly, Mg<sup>2+</sup> exerts different effects on E155A and E155G (**Figure 39C-D**). In fact, while E155G shows a more pronounced Δint with respect to WT GCAP1 upon Mg<sup>2+</sup> addition (0.54 vs. 0.73 respectively), Mg<sup>2+</sup>-bound E155A shows a spectrum located in between apo- and Ca<sup>2+</sup>-bound suggesting its higher hydrophobic surface, despite the 4-nm red shift. The addition of Ca<sup>2+</sup> exerts

small changes in E155G hydrophobic properties, while it allows E155A to complete structural transition.

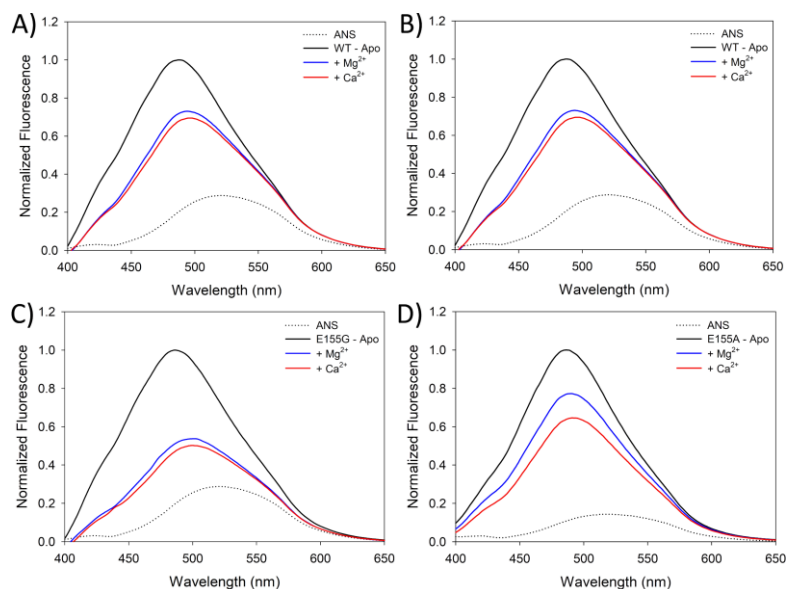


**Figure 39: ANS fluorescence results.** ANS fluorescence spectra of WT (A), D100G (B), E155G (C) and E155A (D) collected at 37°C incubating 2  $\mu\text{M}$  GCAPs and 30  $\mu\text{M}$  ANS in the presence of 250  $\mu\text{M}$  EDTA (black lines) and after sequential additions of 1 mM  $\text{Mg}^{2+}$  (blue lines) and 50  $\mu\text{M}$   $\text{Ca}^{2+}$  (red lines). Spectra of sole ANS in represented by dotted lines. Fluorescence intensity is reported as normalized with respect to the maximum value.

**TABLE 14: ANS FLUORESCENCE.**

	$\lambda_{max}$	$\Delta\lambda^*$	$I/I_{Max}$
WT - Apo	487	34	1
+ $\text{Mg}^{2+}$	494	27	0.73
+ $\text{Ca}^{2+}$	496	25	0.69
D100G - Apo	487	34	1
+ $\text{Mg}^{2+}$	494	27	0.68
+ $\text{Ca}^{2+}$	493	28	0.66
E155G - Apo	486	35	1
+ $\text{Mg}^{2+}$	502	19	0.54
+ $\text{Ca}^{2+}$	500	21	0.50
E155A - Apo	486	34	1
+ $\text{Mg}^{2+}$	490	30	0.77
+ $\text{Ca}^{2+}$	491	29	0.65

\*With respect to ANS alone.

Looking for correlations between the hydrophobicity properties and the protein stability, DLS measurements were performed following the MCR variation over time at physiological temperature. Samples were incubated in the presence or absence of ions, Anotop filtered (0.02  $\mu\text{m}$ ) before each measurement and MCR was monitored for  $\sim 3.5$  h (**Figure 40**). All the mutants showed fluctuations of MCR when in the presence of 500  $\mu\text{M}$  EGTA and a tendency to form large aggregates following

a slow process, more pronounced for E155G (**Figure 40B**). The addition of 1 mM  $Mg^{2+}$  stabilized all mutants in the time frame analyzed, exerting its maximum effect for E155G (**Figure 40B**), contrarily to D100G that, even if stable, showed continuous fluctuations. The same happened adding saturating  $Ca^{2+}$ , except for E155G that immediately showed higher MCR values. It has to be clarified whether the addition of  $Ca^{2+}$  trigger an immediate aggregation or if something wrong happened with the sample.

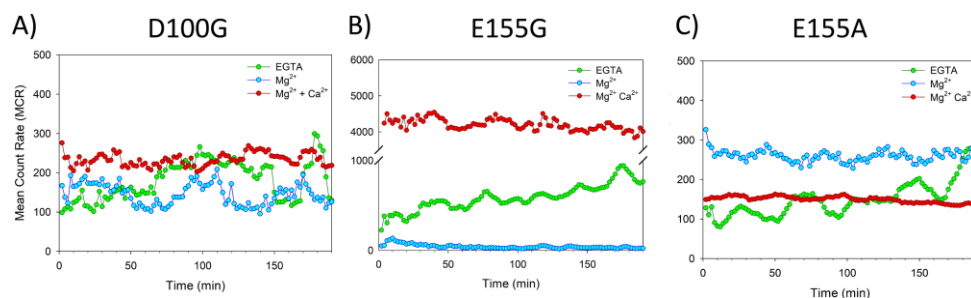


**Figure 40: DLS measurement for the analysis of aggregation propensity.** DLS data were collected incubating  $\sim 30 \mu M$  GCAPs in the presence of  $500 \mu M$  EGTA (green),  $500 \mu M$  EGTA +  $1 mM$   $Mg^{2+}$  (cyan) and  $1 mM$   $Mg^{2+}$  +  $1 mM$   $Ca^{2+}$  (red) using  $20 mM$  TRIS pH 7.5,  $150 mM$  KCl,  $1 mM$  DTT as working buffer. Each data set represent independent sample freshly prepared, Anotop filtered and equilibrated at  $37^{\circ}C$  for 2 min before data collection. Plots represents the variation of mean count rate (MCR) over time ( $\sim 3.5$  h).



## Oligomeric state investigation

The oligomeric state investigation, performed as previously described, suggested no compromised capability in dimer formation. All the GCAP1 variants analyzed elute from the column at 14.23-14.35 mL, giving MWs between 45-47 kDa, all compatible with dimeric organization (**Figure 41**). The colloidal properties of the eluted peaks were also assessed at 25°C by DLS (**Table 15**) where small differences were detected comparing the presence or not of Ca<sup>2+</sup>. In general, all the mutants were slightly bigger in the presence of Ca<sup>2+</sup> respect to Mg<sup>2+</sup>. The only exception is represented by D100G (**Figure 41A, Table 15**), which didn't show any changes in both the conditions tested.

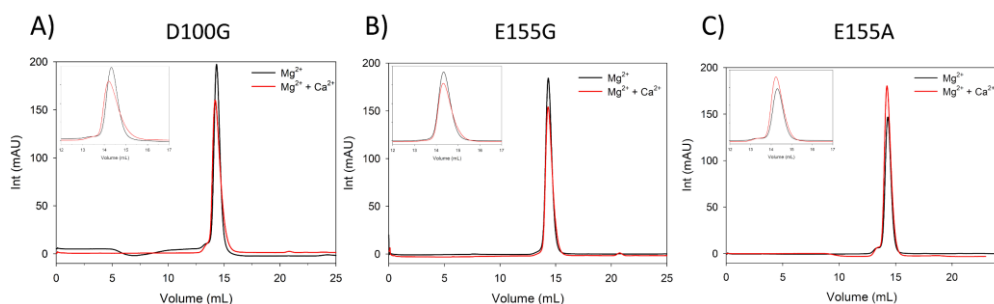


**Figure 41: Analytical gel filtration.** Oligomeric state investigation of D100G (A), E155G (B) and E155A (C) in the presence of 500  $\mu$ M EGTA + 1 mM Mg<sup>2+</sup> (black lines) and in the copresence of 1 mM Mg<sup>2+</sup> + 500  $\mu$ M Ca<sup>2+</sup>. Measurements were performed at room temperature. Insets represent the peaks zoom between 12-17 mL.

**TABLE 15: OLIGOMERIC STATE INVESTIGATION.**

		V <sub>E</sub> <sup>a</sup> (mL)	MW <sup>SEC</sup> (kDa)	d (nm) ± std dev <sup>b</sup> [#meas.] <sup>c</sup>	PdI <sup>d</sup>
WT	Mg <sup>2+</sup>	14.32	45.9	6.3±0.4 [27]	0.342±0.1
	Mg <sup>2+</sup> Ca <sup>2+</sup>	13.26	47.8	6.9±0.6 [19]	0.306±0.1
D100G	Mg <sup>2+</sup>	14.32	45.9	6.9±0.7 [29]	0.434±0.1
	Mg <sup>2+</sup> Ca <sup>2+</sup>	14.33	45.6	7.1±0.7 [9]	0.272±0.1
E155G	Mg <sup>2+</sup>	14.35	45	6.4±0.5 [52]	0.381±0.1
	Mg <sup>2+</sup> Ca <sup>2+</sup>	14.33	45.6	7.2±0.8 [23]	0.217±0.1
E155A	Mg <sup>2+</sup>	14.35	45.9	6.2±0.5 [71]	0.384±0.1
	Mg <sup>2+</sup> Ca <sup>2+</sup>	14.23	47.7	ND <sup>e</sup>	ND <sup>e</sup>

<sup>a</sup>V<sub>E</sub>: elution volume; <sup>b</sup>diameter ± standard deviation, <sup>c</sup> number of measurements, <sup>d</sup>polydispersity index, <sup>e</sup> non determined yet

## Structural characterization

The structural characterization of GCAP1 variants was performed by monitoring variations in secondary and tertiary structure upon addition of ions. Spectra collected in the near UV region (**Figure 42A-D**) highlight a major response to  $Mg^{2+}$  by mutants where the bidentate residue was involved. In fact, comparing the spectra of apo-E155A and E155G (**Figure 42C-D**, black lines) with  $Mg^{2+}$ -E155A and E155G (**Figure 42C-D**, blue lines) a significative transition to more positive values was observed (similar to E111V, **Figure 34**), not seen for WT and D100G GCAP1. Moreover, D100G had a tertiary structure very similar to E111V, characterized by a totally positive spectrum when in the absence of ions or in the presence of sole  $Mg^{2+}$  (**Figure 42B**). The more intense structure variation took place when saturating  $Ca^{2+}$  was added (red lines): while a slight loss of structure was detected for D100G and E155G in the Phe and Tyr bands (less refined respect to the WT), a totally negative Tyr band was seen for E155A (**Figure 42C**). This evidence, together with small differences in Phe band, suggest that this mutation may lead a structural rearrangement of all the other hydrophobic residues. Moreover, E155A appeared more dichroic respect the other GCAP1 variants, even if the working conditions were the same. These changes in the near UV region didn't appear such intense in the far UV. Far UV spectra (**Figure 42E-H**) confirmed that none mutation led to protein unfolding, since all mutants displayed the typical spectrum characterized by the two minima (208-222 nm), however small variations are noteworthy. In general, none of the mutants showed an intensity variation trend as WT GCAP1, whose progressively increased ellipticity upon cations coordination was explained by a more compact structure. E155A and D100G showed far UV spectra overlapped in all the tested conditions, suggesting no changes in protein compactness; the only exception was E155G, whose ellipticity decreased upon  $Mg^{2+}$  coordination, indicating a more opened conformation, even if the  $\theta_{222}/\theta_{208}$  remained constant (apo = 0.88,  $Mg^{2+}$  = 0.89) (**Table 16**). Considering the total structural rearrangement in the transition from apo to  $Ca^{2+}$  bound ( $\Delta\theta/\theta$ ), all the mutants appeared less compact with respect to the WT, as demonstrated by low  $\Delta\theta/\theta$  values, (0.2% for E155G and D100G and 1% for E155A, against 7.7% of WT GCAP1).

Thermal denaturation profiles showed that all the mutants were generally less stable in the  $\text{Ca}^{2+}$  bound form (**Figure 42I-L**). In fact, while WT GCAP1 didn't show transition from the folded to unfolded structure (making the data fitting impossible, **Figure 42I**), all the mutants were characterized by an almost complete transition, even if the final structure was never associated with the total folding loss (residual signal was present at the high temperature). Interesting is the effects exerted by magnesium:  $\text{Mg}^{2+}$ -D100G GCAP1 was the only mutant characterized by a higher thermal stability compared to WT GCAP1 ( $\sim 3^\circ\text{C}$  more stable) while, concerning E155A and E155G, it is clear how the replacement with Gly or Ala exerts different effects. In fact, E155G appeared  $\sim 5^\circ\text{C}$  less stable with respect to E155A GCAP1, which showed a  $T_m$  very similar to WT GCAP1 (**Table 16**). Apparently, the substitution of bidentate residues (E111, E155) with hydrophobic amino acids (i.e. Val, Ala) in EF hands that do not directly coordinate  $\text{Mg}^{2+}$  (bound in EF2), may generate a more packed structure of those EF hand, making the protein more stable at high temperature. The fact that this effect was seen only in the presence of  $\text{Mg}^{2+}$  might suggest this ion as an allosteric stabilizer.

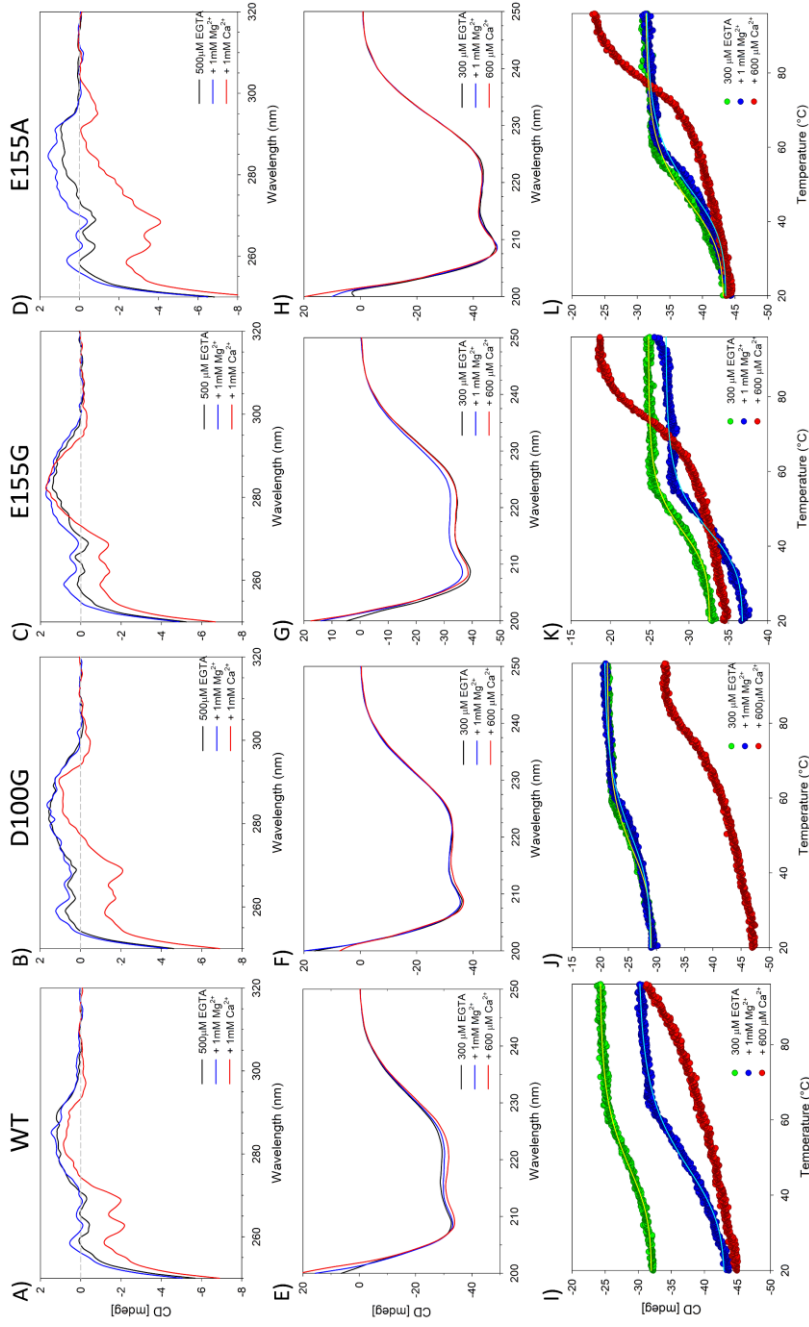


**Figure 42: Structural characterization by circular dichroism.** A-D) Near UV spectra of 30  $\mu\text{M}$  WT (A), D100G (B), E155G (C) and E155A (D) GCAP1 were collected in the presence of 500  $\mu\text{M}$  EGTA and after sequential additions of 1 mM  $\text{Mg}^{2+}$  and 1 mM  $\text{Ca}^{2+}$ . E-H) Far UV spectra of 12  $\mu\text{M}$  WT (E), D100G (F), E155G (G) and E155A (H) GCAP1 were collected in the presence of 300  $\mu\text{M}$  EGTA and after further additions of 1 mM  $\text{Mg}^{2+}$  and 600  $\mu\text{M}$   $\text{Ca}^{2+}$ . Twenty-millimolar TRIS, 150 mM KCl, 1 mM DTT was used as working buffer and its spectrum was considered as blank. Temperature was set at 37°C, 1 nm data pitch, 4 sec response, each spectrum represents the average of 5 accumulations. I-L) Thermal denaturation profiles of WT (I), D100G (J), E155G (K), E155A (L) GCAP1 were collected in the same conditions used for far UV, scanning the range between 20–96°C, scan rate 90°C/h. Solid lines represent the result of data fitting using Hill 4 parameters function.

**TABLE 16: SHAPE OVERVIEW.**

<b>GCAPI</b>	$\theta_{222}/\theta_{208}$	$\Delta\theta/\theta$ (%)*	$T_m$ (°C)
WT – Apo	0.90		49.8
+ Mg <sup>2+</sup>	0.90	7.7	50.4
+ Ca <sup>2+</sup>	0.95		-
D100G – Apo	0.91		48.4
+ Mg <sup>2+</sup>	0.92	0.2	53.1
+ Ca <sup>2+</sup>	0.90		
E155G – Apo	0.88		45.4
+ Mg <sup>2+</sup>	0.89	0.2	45.7
+ Ca <sup>2+</sup>	0.90		74.9
E155A – Apo	0.92		47.1
+ Mg <sup>2+</sup>	0.89	1	50.4
+ Ca <sup>2+</sup>	0.90		

\*calculates as  $(\theta_{222}^{Ca^{2+}} - \theta_{222}^{EGTA}) / \theta_{222}^{EGTA}$

## Calcium binding evaluation

The affinity for  $\text{Ca}^{2+}$  was studied by using the two techniques previously mentioned. Gel shift experiments gave the first evidence of decreased  $\text{Ca}^{2+}$  affinity, since all the mutants showed lower electrophoretic mobility in the presence of  $\text{Ca}^{2+}$ , compared to the WT (**Figure 44A**). This was confirmed and quantified by chelator assay (**Figure 44B**). A feature shared by all the mutants was the loss of one binding site, since the log  $k$  values measured by CaLigator were too far from the one of Br<sub>2</sub>-BAPTA to be considered reliable (see methods). Thus, the comparison between GCAP1 variants could be done only considering the high affinity site (nM). As expected, all the mutants showed lower affinity for  $\text{Ca}^{2+}$ , especially D100G that had a 10-fold reduction in  $K_d^{\text{app}}$  (0.9  $\mu\text{M}$ ) respect to WT GCAP1 (84 nM); this is not surprising considering that EF3 is the highest affinity EF hand motif. Also the replacement of E155 had a deleterious effect in calcium sensing, less pronounced for E155G ( $K_d^{\text{app}} = 117$  nM, 1.4-fold) than for E155A (453 nM, 5.4-fold) suggesting that the presence of hydrophobic Ala may compromise the loop conformation, destabilizing the geometry required for  $\text{Ca}^{2+}$  coordination (**Figure 43**).

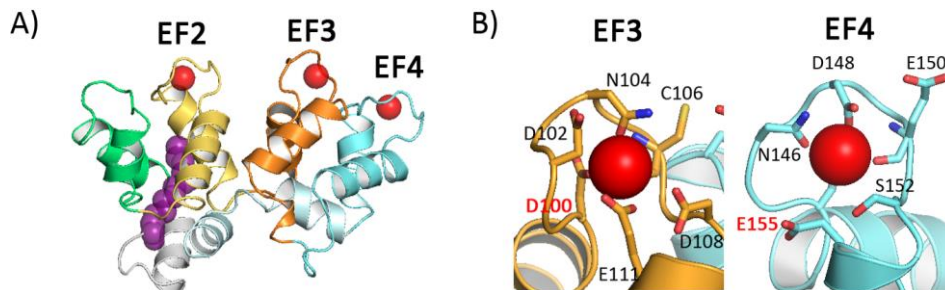


**Figure 43:** *Cartoon representations of WT monomeric GCAP1. A) N-terminal and C-terminal are colored in grey; myristoyl group is colored in deep purple; EF1, EF2, EF3 and EF4 are colored in green, yellow, orange and cyan, respectively;  $\text{Ca}^{2+}$  ions are represented as red spheres. B) Zoom in the EF3 and EF4. Amino acids contributing to  $\text{Ca}^{2+}$  coordination are represented as sticks and colored by element. D100 and E155 residues are marked in red.*

## Enzymatic activity

Finally, the capability of GCAP1 variants to regulate the cyclase activity was assayed in on-off GC assay experiments (**Figure 44C**). In activating conditions, the mutants showed profile very similar to WT GCAP1, except for E155G that seems 50% more active with the respect of WT. However, the real deleterious feature is the compromised capability in GC1 shut-off. Even if these are still preliminary results ( $EC_{50}$  and  $IC_{50}$  measurements are in progress), apparently none of these mutants showed a WT-like profile, especially D100G which is characterized by the presence of the same amount of synthesized cGMP in both the conditions tested. In fact, contrarily to E111V that showed a partial regulation, D100G is apparently incapable to regulate GC1 in the tested range.

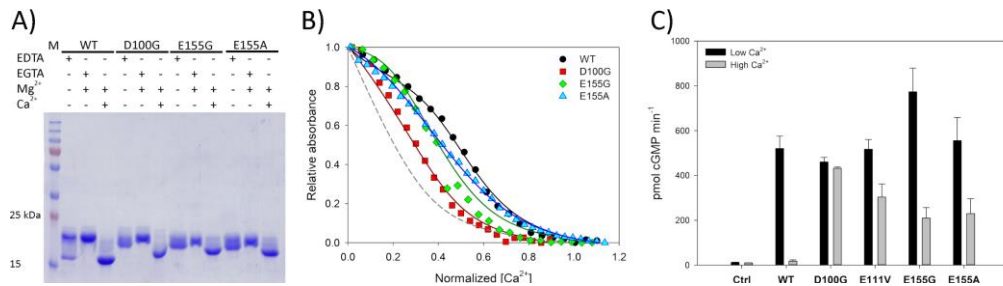


**Figure 44: mutations effects on  $Ca^{2+}$  binding capability and enzymatic regulation.** A) Gel shift of 20  $\mu$ M GCAP1 variants incubated in the presence of 2 mM EDTA, 1 mM EGTA + 1.1 mM  $Mg^{2+}$  or 1 mM  $Mg^{2+}$  + 1 mM  $Ca^{2+}$ . After 5 min incubation at room temperature, samples were boiled, loaded on 15% polyacrylamide gel. After 40-45 min at 200V gel was Coomassie blue stained. B) Representative chelator assay results. Data were normalized as follow:  $y_{norm} = (A_{263} - A_{min}) / (A_{max} - A_{min})$  and  $x_{norm} = [Ca^{2+}] / ([Q] + 3 * [GCAP1])$ , where  $Q$  is the  $Br_2$ -BAPTA concentration. C) The GC1 activity was assayed in the presence of different GCAP1 mutants at low ( $< 19$  nM) and high ( $\sim 30$   $\mu$ M)  $Ca^{2+}$  concentrations.

## Conclusions (partial)

Many are the pathogenic mutations known in *GUCAIA* gene and most of them were fully characterized by a clinical and biochemical point of view. The aim of this still-running project is to identify specific features among mutants that affect specifically  $\text{Ca}^{2+}$  binding residues; for this reason, D100G, E155A and E155G were taken in consideration. The results collected so far suggest that none of this point mutations led to alteration of the oligomeric state, since all were dimeric under the tested conditions. Moreover, even if small changes in the hydrophobic surface were detected, all of them followed a WT-like trend and no one showed aggregation propensity as E111V, except for E155A that seems to aggregate upon the addition of saturating  $\text{Ca}^{2+}$  (to confirm). As expected, a reduced capability in  $\text{Ca}^{2+}$  sensing was detected for all mutants, most severe for D100G. This found demonstrations in the compromised capability in GC1 shut-off, at least till 30  $\mu\text{M}$  (the calcium concentration in the  $\text{K}_2\text{CaEGTA}$  buffer). Further enzymatic experiments are required, as the evaluation of  $\text{IC}_{50}$ ,  $\text{EC}_{50}$  and catalytic efficiency, as previously done by Huang J. et al<sup>40</sup>. The more interesting finding is about the variations in tertiary structure upon  $\text{Ca}^{2+}$  addition showed by E155A. Looking the structure of the homology model of human WT GCAP1 (**Figure 45**) three residues were identified as possibly disturbed by the mutation: I143, L151, V145 (all found mutated in COD/CORD). Performing a mutagenesis *in silico* and measuring the variation of the distances between the  $\text{C}_\beta$ -Ala and the side chains of these residues, the  $\text{C}_{\gamma 1}$ -I143,  $\text{C}_{\gamma 2}$ -V145 and  $\text{C}_\delta$ -L151 were found closer to each other ( $\sim 5\text{\AA}$ , **Figure 45A**), thus leading the F140 and L151 approaching (**Figure 45B**), that on one hand may distort the EF4 loop conformation, on the other hand may explained the enhanced thermal stability (compared to E155G). Since it has already demonstrated the presence of an allosteric communication between the myristoyl group (fundamental for the GC regulation) and EF4<sup>43; 45</sup>, mutations in EF4 might have crucial effects in the transmission of the information through the protein structure. This hypothesis needs to be further confirmed by MD simulations.



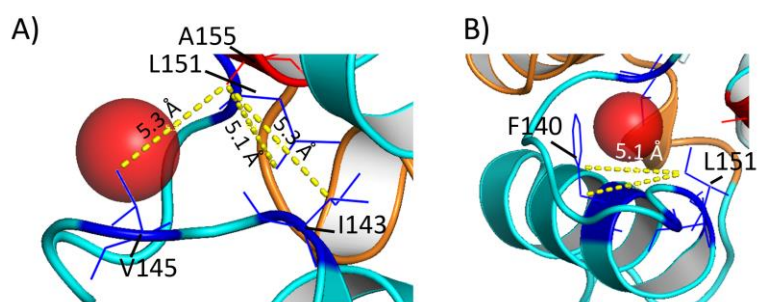


**Figure 45: Effect of E155A mutation in amino acids distances.** After the *in silico* mutagenesis the measurements of the distances between I143, V145 and L151 (A) and between F140 and L151 (B) were performed using PyMOL.



## *Inorganic NPs as specific carriers for Ca<sup>2+</sup> sensor protein in nanomedicine*

### **Introduction**

NPs are defined as small particles characterized by a size lower than 100 nm and a high surface-to-volume ratio. They can be easily produced through a hydrothermal technique which consists in putting together the different elements at defined stoichiometric ratio (see methods) and put the solution in an autoclave at high temperature (190°C): the longer the incubation the bigger the resulting NPs. For this study CaF<sub>2</sub> NPs were used since their specific binding with Ca<sup>2+</sup> sensor proteins as Rec<sup>73</sup>, GCAP1<sup>75</sup> and CaM<sup>74</sup> has been previously demonstrated. The special feature of these NPs is the strong upconversion triggered by the presence of a coating composed by a mix of rare earth as erbium (Er<sup>3+</sup>) and ytterbium (Yb<sup>3+</sup>) meaning that, when irradiated with infrared laser (980 nm), they emit in the visible range wavelength, which makes them traceable using non-detrimental light source.

CaM is a ubiquitous prototypical Ca<sup>2+</sup> sensor protein, highly conserved in eukaryotic cells, formed by four functional EF-hands (EF1-4) organized in two domains namely N-terminal and C-terminal lobe, linked by a central flexible  $\alpha$ -helix. In the apo state the protein is mostly globular but upon Ca<sup>2+</sup> coordination a conformational change takes place resulting in a more opened structure (**Figure 46**). CaM is involved in many processes including cells proliferation, apoptosis, ions transport, cell motility, cytoskeleton remodeling, metabolic homeostasis and protein folding<sup>107;108</sup>. Moreover, in the last years many point mutations on CaM encoding genes (*CALM1*, *CALM2* and *CALM3*) have been associated with arrhythmogenic diseases, such as long QT syndrome (LQTS) and catecholaminergic polymorphic ventricular tachycardia (CPVT)<sup>109</sup>. In this study (**Paper 5<sup>76</sup>**) we optimized a protocol for the characterization of the interactions that occur between CaF<sub>2</sub> NPs and human CaM using a combination of biochemical and biophysical techniques.



**Figure 46:** Structure of human CaM in the Ca<sup>2+</sup> bound form. EF1, EF2, EF3 and EF4 are colored in orange, yellow, cyan and blue respectively; the central linker is colored in green and Ca<sup>2+</sup> ions are represented as red spheres. PDB entry 1CLL.

## CaM had the same structure when in the presence of sole Ca<sup>2+</sup> or CaF<sub>2</sub> NPs.

Circular dichroism analyses were performed monitoring CaM secondary and tertiary structures upon Ca<sup>2+</sup> addition or in the presence of sole NPs. **Figure 47** shows that in all the tested conditions CaM was correctly folded, showing the typical spectra of all- $\alpha$ -helix proteins. In the presence of saturating Ca<sup>2+</sup> (**Figure 47**, red line) or sole NPs (**Figure 47**, blue line) CaM shows the same secondary structure, characterized by equal values of  $\theta_{222}/\theta_{208}$  ratio (**Table 17**), even if holo CaM is slightly more compact as suggested by the more negative ellipticity. Interestingly, the addition of saturating EGTA resulted in two spectra totally overlapped (**Figure 47A**, black and green lines), suggesting that the detachment of CaM from the NP's surface is perfectly reversible and that its structural properties were not compromised (**Table 17**). Thermal denaturation profiles further confirmed this finding, since holo-CaM and CaM+NPs showed almost identical profiles where the transition from folded to unfolded was never reached, contrary to what happened to apo-CaM. The behavior showed by CaM in the far UV was confirmed in the near UV range, even if the only 8 Phe and 2 Tyr residues resulted in less intense structural variations (**Figure 47B**). Despite this, holo CaM and CaM+NP had very similar spectra, but significantly different from apo-CaM.

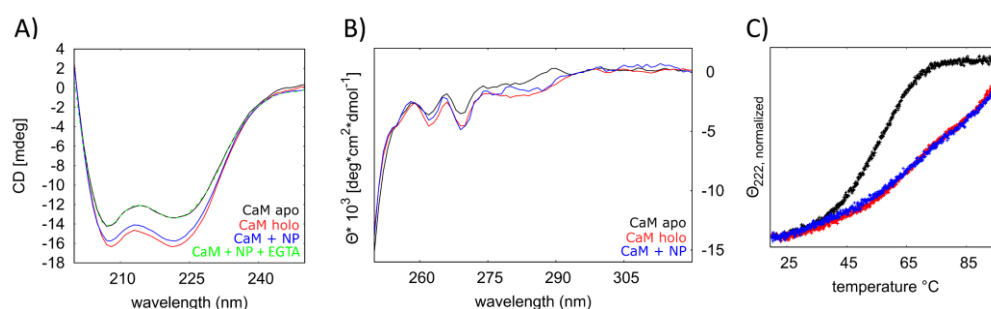


**Figure 47: Circular dichroism characterization of CaF<sub>2</sub> NPs and CaM.** A-B) Far- and near UV spectra (of ~12  $\mu$ M CaM or 30  $\mu$ M, respectively) in the presence of equal amounts (400  $\mu$ M) of saturating EGTA (black) or Ca<sup>2+</sup> (red), and CaM previously incubated with 5.7 mg/mL NPs (blue). c) Thermal denaturation profiles of ~12  $\mu$ M CaM previously incubated with 1.7 mg/mL NPs (blue) and in the presence of saturating (120  $\mu$ M) EGTA (black) and Ca<sup>2+</sup> (red).  $\theta_{222}$  has been normalized to account for different starting values ( $\theta_{222, \text{normalized}} = \theta_{222} / \theta_{222} \text{ at } 20^\circ\text{C}$ ). Figure and legend are an adaptation from *Paper 576*.

To further investigate these structural differences, limited proteolysis experiments were performed. **Figure 48A** shows how  $\text{Ca}^{2+}$  is a structure stabilizer, as demonstrated by the persistence of undigested protein after 90 min incubation with trypsin. Differently, in the presence of EGTA the protein is almost totally digested after 30 min. In order to assess the effect of the NPs on the proteolysis pattern, the experiment was repeated incubating CaM with saturating NPs (1:139 NPs:protein ratio) for 30 minutes. **Figure 48B** shows that holo-CaM and CaM+NPs share the same proteolysis pattern (**Figure 48B**, downwards arrows) and that the addition of EGTA results in the same trypsin susceptibility, regardless whether NPs were present or not (**Figure 48B**, upwards arrows).

**TABLE 17: FARUV CD DATA: SPECTRAL SHAPES OF CaM IN THE PRESENCE AND ABSENCE OF NPs.**

	$\theta_{222}/\theta_{208}$	$\Delta\theta/\theta$ (%)
CaM $\text{Ca}^{2+}$	1.00	21.7
CaM EGTA	0.95	
CaM + NPs	1.00	17.6%
CaM + NPs+ EGTA	0.95	

*Adapted from Paper 576.*

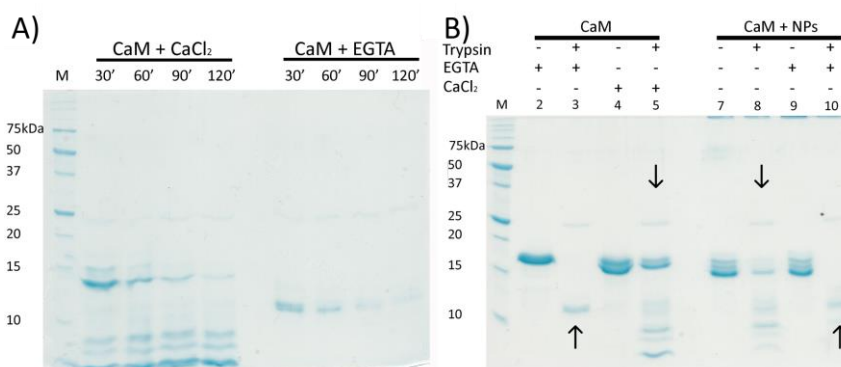


**Figure 48: Limited proteolysis pattern of CaM in the presence and in the absence of NPs.** A) Proteolysis reactions were performed at 25°C by 30-120 min incubation with saturating (2 mM) EGTA or  $\text{Ca}^{2+}$ , using a CaM:TPCK-trypsin ratio equal to 1:60. Lane M refers to the protein marker. B) Proteolysis experiments in the presence of NPs were performed by 30 min incubation with saturating (240  $\mu\text{M}$ ) EGTA or  $\text{Ca}^{2+}$ , using a CaM:TPCK-trypsin ratio equal to 1:60. Lanes 3 and 5 refer to the digested apo (lane 3) and  $\text{Ca}^{2+}$ -bound (lane 5) CaM. Lanes 8 and 10 refer to the digested CaM previously incubated with NPs (lane 8) and after the addition of EGTA (lane 10). Undigested CaM was loaded in the same conditions in lanes 2, 4, 7 and 9. The similar effect exerted by either free  $\text{Ca}^{2+}$  or NPs and excess EGTA on the proteolytic patterns is highlighted by downwards and upwards arrows, respectively. Figure and legend are from Paper 576.

## Affinity and kinetic investigations highlighted physiological relevance

To directly study the binding of CaM to CaF<sub>2</sub> NPs, Resonance Energy Transfer (RET) was used. Upconverting NPs emit light at a wavelength that can be absorbed by CaM previously labeled with Alexa Fluor 532 fluorophore (see methods). Titration experiments (**Figure 49**) showed a RET phenomenon characterized by concentration dependency, with decreased emission at 540 nm and 544 nm but conserved spectral properties in 650-670 range (**Figure 49A**). Fitting the fluorescence variation ( $\Delta F$ ) as function of [CaM] a  $K_D = 2.5 \mu\text{M}$  was calculated (**Figure 49C-D**), in line with previous findings obtained by CaM from *A. Thaliana*<sup>74</sup>.

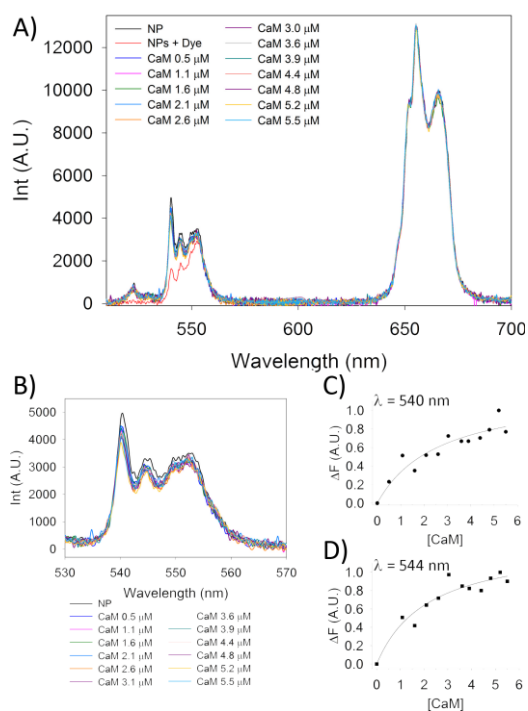


**Figure 49: RET analysis of CaM-NP interaction** A) Upconversion spectra of CaF<sub>2</sub> NPs in CaM titration experiments. The resonance energy transfer (RET) phenomenon is evident by a strong decrease of the Er<sup>3+</sup> emission in the 520-560 nm optical range. Band assignment: (i)  $^2H_{1/2} \rightarrow ^4I_{15/2}$ ; (ii)  $^4S_{3/2} \rightarrow ^4I_{15/2}$ ; (iii)  $^4F_{9/2} \rightarrow ^4I_{15/2}$ . B-D) Example of titration experiments of Alexa Fluor 532-conjugated CaM with a 0.5 mg/mL NPs dispersion. B) Zoom of the spectral area showing the RET phenomenon. Notice the change in NPs emission at 540 (C) and 544nm (D). Figure and legend are from Paper 5<sup>76</sup>.

To better investigate the kinetics of this mechanism, SPR was used. First, NPs were incubated with CaM to form a protein-corona (0.1 mg/mL NPs + 1.6  $\mu\text{M}$  CaM) and the so-complexed NPs were directly injected on the chip resulting in their incapability to interact with the immobilized protein (**Figure 50A**, grey line), as previously seen with GCAP<sup>75</sup>. Then, several concentrations of bare NPs, ranging from 0.1 to 0.5 mg/mL, were injected; **Figure 50A** (black line) shows an example. The

sensorgram obtained can be divided in three parts, which give us different information: i) the binding process does not follow a Langmuir absorption model, as no dependency on NPs concentration was detected (data not shown); ii) at least 400 seconds are needed before the real dissociation starts, explained by a combination of phenomena like protein structural rearrangements and NPs diffusion on the dextran matrix. Finally, iii) when the dissociation starts, it can be described by a single exponential function resulting in  $k^{\text{off}} = (3.5 \pm 0.4) \times 10^{-3} \text{ s}^{-1}$ , a fairly fast dissociation that is completed in 2000 sec (**Figure 50B**).

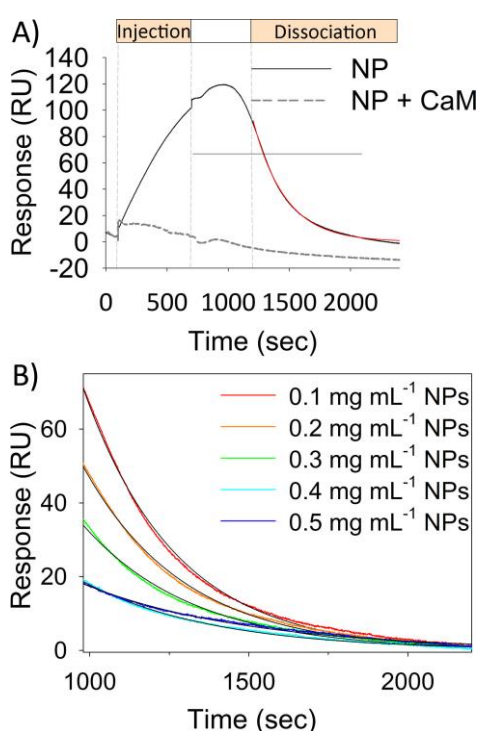


**Figure 50** SPR analysis of CaM-NP interaction. A) Example of sensorgram obtained by flowing NPs (0.1mg/mL) on a flow cell where 2400 RU of CaM were previously immobilized via amine coupling. Injections were performed for 600 s (flow rate 10  $\mu\text{L}/\text{min}$ ) and dissociation was followed for 1800 s. The red curve refers to data fitting using a single exponential function. The dashed grey line refers to injection of the same amount of NPs previously incubated with 1.6  $\mu\text{M}$  CaM. B) Example of dissociation curves obtained by SPR overlapped to the fitting curves according to a single exponential in the 0.1-0.5 mg/mL NP range. Figure and legend are from **Paper 5**<sup>76</sup>.

## Conclusions

The data reported here further emphasize the suitability of CaF<sub>2</sub> NPs as nanodevices for the delivery of Ca<sup>2+</sup> sensor proteins such as CaM. The investigation performed by CD and limited proteolysis suggests that the presence of CaF<sub>2</sub> NPs or Ca<sup>2+</sup> as free ion exert on the CaM structure the same effect, as shown by almost identical far UV and near UV spectra together with proteolysis patterns. Our results also show the reversibility of this process, fundamental for nanodevices, since the addition of saturating EGTA in samples where Ca<sup>2+</sup> or NPs were present results in CD spectra and digestion patterns very similar to those of the apo-CaM. Moreover, PRE experiments performed by Dr. Helge Meyer (University of Oldenburg, **Paper 5<sup>76</sup>**), shed light on the detailed mechanism through which CaM recognizes the NP's surface. This occurs via two steps: after the first recognition of the NP's surface by the CaM N-terminal, CaM can i) dissociate from the NP or ii) be converted to a more stable conformation that involves the two EF-hands in the N-terminal lobe (**Figure 51**). Our hypothesis is that the presence of saturating EGTA may hide the Ca<sup>2+</sup> ions on the NP surface, thus preventing these interactions and leaving CaM molecules free in solution. Finally, RET and SPR were used in order to better investigate the affinity and the kinetics that trigger the CaM – NPs interaction. The results obtained allowed us to conclude that the affinity for the CaM – NPs complex formation ( $K_D = 2.5 \mu\text{M}$ ) together with the fast dissociation (complete in 2000 seconds), may suggest that CaF<sub>2</sub> NPs are nanodevices suitable for nanomedicine applications, such as protein delivery for the treatment of complex diseases.



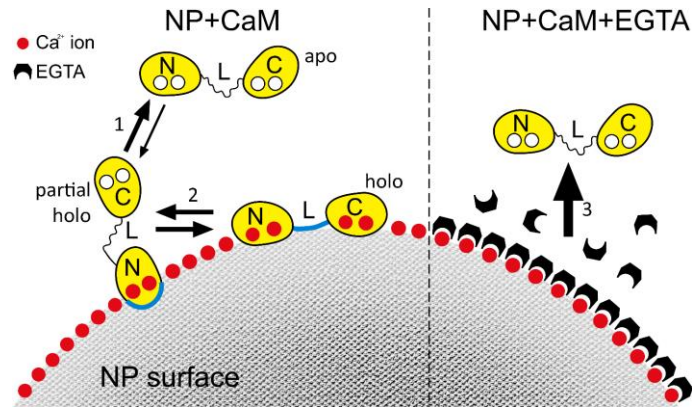


**Figure 51: Schematic representation of NP-CaM interactions.** Left side: when apo CaM is incubated with NPs, two different equilibria establish. CSP experiments suggest that the first contact between CaM and NP is mediated by the N-terminal domain. At this point, CaM can either return to the apo state (1) through a rapid dissociation by the NP surface or be converted into a more stable NP-bound conformation (holo), in a linker-mediated process (2), as suggested by PRE experiments (**Paper 5**). Right side: when an excess of EGTA (black blocks) is added, the chelator binds  $\text{Ca}^{2+}$  ions on the NP surface, thus restoring the apo-CaM conformation (3), as suggested by near- and far UV spectra. Blue thick lines represent the areas mostly involved in CaM/NPs interaction. Figure and legend are an adaptation from **Paper 5**<sup>76</sup>.



## *Introduction to papers*

### **Paper 1 : Preferential binding of $Mg^{2+}$ over $Ca^{2+}$ to CIB2 triggers an allosteric switch impaired in Usher Syndrome Type 1J.**

Rosario Vallone, Giuditta Dal Cortivo\*, Mariapina D'Onofrio and Daniele Dell'Orco

*Front. Mol. Neurosci.* (2018), 11:274, doi: 10.3389/fnmol.2018.00274.

\*co-first author

Calcium- and integrin binding protein 2 is a small protein whose properties and function are still under investigation. In the last years, many studies described CIB2 as involved in  $Ca^{2+}$  homeostasis in hair cells in the inner ear since four point mutations have been linked to deafness. Particularly, in 2012 E64D point mutation has been related to Usher syndrome type 1J, a rare autosomal recessive disorder characterized by the co-presence of deafness and blindness (due to retinitis pigmentosa). Since the lack of information about CIB2, we focused our attention in its characterization combining low- and high-resolution techniques, namely circular dichroism, size exclusion chromatography and nuclear magnetic resonance in order to elucidate its role in physiological and pathological conditions. Our findings suggested a dimeric organization of WT CIB2, and lower affinity for  $Ca^{2+}$  ( $K_d^{app} = 0.5$  mM) respect to  $Mg^{2+}$  ( $K_d^{app} = 290$   $\mu$ M) making CIB2 preferentially bound to  $Mg^{2+}$  and incapable to work as a  $Ca^{2+}$  sensor under physiological conditions. Moreover, by NMR, a long-range allosteric communication between E64 (pseudo-EF1) and N121 (EF3) was identified as crucial for the correct folding upon addition of cations, since its conservative mutation into Asp lead the impaired capability of CIB2 to switch to its  $Mg^{2+}$ -bound form. The interaction with its  $\alpha$ 7B integrin target, hypothesized to occur with the portion close to the membrane, was investigated by fluorescence spectroscopy resulting in a stoichiometric ratio of 2:1 CIB2: $\alpha$ 7B\_M characterized by a low affinity. Since both WT and E64D CIB2 were found able to interact with  $\alpha$ 7B\_M showing approximately the same affinity, we concluded that the pathological phenotype is not associated with a compromised target recognition.



**Paper 2 : *Oligomeric state, hydrodynamic properties and target recognition of human calcium and integrin binding protein 2 (CIB2)***

Giuditta Dal Cortivo, Valerio Marino, Claudio Iacobucci, Rosario Vallone, Christian Arlt, Anne Rehkamp, Andrea Sinz and Daniele Dell'Orco

*Scientific Reports* (2019), 9:15058, doi: 10.1038/s41598-019-51573-3

In paper 2 a deeper characterization of WT CIB2 was performed since, looking for the dimerization interface, lines of evidences of monomeric organization were found. In fact, combining chemical cross-linking and analytic gel filtration we found that cross-linked CIB2 (monomeric) elutes with an apparent molecular mass of a dimer. Performing *in silico* analysis using HydroPro software it has been pointed out that CIB2 has a large hydrophobic surface exposed to the solvent that lead interactions with the column's resin resulting in a misleading interpretation. Further investigations were performed to better characterize the interaction with the integrin peptide, in order to shed light on binding specificity and kinetics. By SPR analysis we found that the specific binding with the integrin portion proximal to the membrane occurs with a low affinity and consists in the formation of a 1:1 complex that may trigger the binding to another CIB2 molecule. The kinetics of recognition is influenced by cations since the presence of physiological  $Mg^{2+}$  favor the binding process.



**Paper 3** : *A novel p.(Glu111Val) missense mutation in GUCA1A associated with cone-rod dystrophy leads to impaired calcium sensing and perturbed second messenger homeostasis in photoreceptors.*

Valerio Marino, Giuditta Dal Cortivo\*, Elisa Oppici, Paolo Enrico Maltesi, Fabiana D'Esposito, Elena Manara, Lucia Ziccardi, Benedetto Falsini, Adriano Magli, Matteo Bertelli and Daniele Dell'Orco

*Human Molecular Genetics* (2018), Vol. 27, No. 24, doi: 10.1093/hmg/ddy311

\*co-first author

Guanylate cyclase activating protein 1 (GCAP1) is the molecular regulator of retinal guanylate cyclase (GC1), an enzyme responsible for restoring the dark state in photoreceptors upon photons absorption. A novel point mutation was found in *CORD*-patients consisting in the replacement of Glu111 into Val (E111V), the bidentate residue of the high-affinity EF3. The thorough biochemical characterization presented in this paper highlighted that the impaired  $\text{Ca}^{2+}$  affinity (~80-fold higher  $K_d^{\text{app}}$  with respect to the WT) triggers the GC1 dysregulation. In fact, E111V loses the capability to switch from the activating ( $\text{Mg}^{2+}$ -bound) to inhibiting ( $\text{Ca}^{2+}$ -bound) form over a physiological range of  $[\text{Ca}^{2+}]$ , thus leading to constitutively active enzyme ( $\text{IC}_{50} = 10 \mu\text{M}$ ) even if the affinity for the enzyme is unchanged. Both WT and E111V GCAP1 form dimers independently on the presence of cations, even if a time-dependent aggregation was observed in E111V  $\text{Mg}^{2+}$ -bound form. Molecular dynamics simulations suggested a more flexible EF3 loop with a distorted geometry and a more rigid backbone that explains the higher thermal stability.





**Paper 4** : *Normal GCAPs partially compensate for altered cGMP signaling in retinal dystrophies associated with mutations in GUCA1A.*

Daniele Dell'Orco and Giuditta Dal Cortivo

*Sci Re* **9**, 20105 (2019), doi: 10.1038/s41598-019-56606-5

Missense point mutations in *GUCA1A* gene are associated with cone- and cone-rod dystrophies (COD, CORD), autosomal dominant diseases characterized by photophobia, congenital nystagmus and progressive vision loss. From Paper 3 we found that WT and E111V GCAP1 have similar  $EC_{50}$  values for the target GC1. Considering that the autosomal dominant inheritance pattern implies the co-presence of 50% WT and mutant GCAP1 and that GCAP2 is involved in phototransduction regulation by  $Ca^{2+}$  relay mechanism, we further investigate whether GCAP1 and GCAP2 can similarly regulate GC1 in the presence of E111V GCAP1 combining *in vitro* and *in silico* approaches. Surprisingly, GC assay experiments highlighted that human GCAP2 contribution in GC1 regulation is negligible, while the presence of WT GCAP1 only partially attenuates the presence of E111V GCAP1. Nevertheless, *in silico* simulations performed using a well-established model of phototransduction in murine system resulted in a crucial role of GCAP2 in the attenuation of the phenotype due to the presence of E111V GCAP1. For these reasons we propose a species-dependent compensatory mechanism that may mitigate the mutant presence in human as GCAP2 does in mouse.



**Paper 5 : *Luminescent and paramagnetic properties of nanoparticles shed light on their interactions with proteins.***

Giuditta Dal Cortivo, Gabriel E. Wagner, Paolo Cortelletti, Krishna Mohan Padmanabha Das, Klaus Zangger, Adolfo Speghini, Daniele Dell'Orco and N. Helge Meyer

*Scientific Reports* (2018), 8:3420, doi: 10.1038/c41598-018-21571-y

Nanoparticles are considered a promising tool for the delivery of proteins for therapeutic treatments. However, the dynamic of nanoparticles-protein interaction is protein-dependent and not totally understood. In paper 5 we propose a methodology for the characterization of the interaction between CaF<sub>2</sub> nanoparticles and calmodulin, a prototypical Ca<sup>2+</sup> sensor protein highly conserved but found mutated in rare cardiac diseases such as catecholaminergic polymorphic ventricular tachycardia (CPVT) and long QT syndrome (LQTS). A combination of circular dichroism, limited proteolysis, nuclear magnetic resonance and resonance energy transfer were used. CD and limited proteolysis suggest that the CaM structural features are preserved, since its structure in the presence of Ca<sup>2+</sup> is the same also in the presence of NPs. Thanks to nuclear magnetic resonance it has been pointed out that the nanoparticles-CaM interaction occurs in two phases consisting firstly in the formation of a transient complex (mediated by N-terminal lobe), that became more stable when the central linker is involved. Finally, the combination of resonance energy transfer and surface plasmon resonance experiments resulted in a fully reversible NP-CaM interaction characterized by an affinity compatible with nanomedicine applications.



## List of figures

Figure 1: Representation of EF-hand motif.....	17
Figure 2: Structural organization of the ear: from macro to micro. ....	18
Figure 3: Schematic representation of the mechano-electrical transduction. ....	19
Figure 4: Structural features of CIB2.....	21
Figure 5: Eye anatomy: from macro to micro. ....	23
Figure 6: Phototransduction cascade. ....	25
Figure 7: GCAP1 tridimensional structure and Ca <sup>2+</sup> -relay model. ....	27
Figure 8: Upconverting NPs.....	32
Figure 9: Schematic representation of the chromatographic techniques used. ....	43
Figure 10: GC assay output.....	46
Figure 11: Br <sub>2</sub> -BAPTA features. ....	51
Figure 12: Origin of CD effect. ....	53
Figure 13: FarUV and nearUV spectra. ....	54
Figure 14: How DLS works. ....	58
Figure 15: How SPR works.....	60
Figure 16: Workflow followed for XL-MS experiments. ....	62
Figure 17: CIB2 purity check.....	69
Figure 18: Conformational changes in WT and E64D upon addition of Ca <sup>2+</sup> and Mg <sup>2+</sup> .....	71
Figure 19: Stabilization effect of ions.....	72
Figure 20: CIB2 hydrophobicity and thermal stability investigation.....	74
Figure 21: <sup>1</sup> H- <sup>15</sup> N HSQC spectra of WT CIB2 in its apo form and in the presence of Mg <sup>2+</sup> and Ca <sup>2+</sup> . .....	76
Figure 22: Ca <sup>2+</sup> and Mg <sup>2+</sup> affinity by monitoring secondary structure variations.....	78
Figure 23: SEC analysis.....	80
Figure 24: Dynamic light scattering spectroscopy.....	80
Figure 25: Lines of evidences of monomeric CIB2.....	83
Figure 26: Interaction between CIB2 variants and a7B_M peptide monitored by fluorescence spectroscopy. ....	85
Figure 27: Evidences of 1:1 complex formation between WT CIB2 and a7B_M peptide. ....	86
Figure 28: SPR measurements of CIB2-peptide interaction.....	88
Figure 29: Ca <sup>2+</sup> and Mg <sup>2+</sup> affinity assayed by monitoring secondary structure variations in the presence of a7B_M peptide. ....	89
Figure 30: Clinical and genetic data. ....	93
Figure 31: Guanylate cyclase (GC1) regulation made by WT and E111V GCAP1. ....	95
Figure 32: Results from Size Exclusion Chromatography and Dynamic Light Scattering experiments. ....	97
Figure 33: Aggregation propensity at physiological temperature.....	97
Figure 34: Structural and stability changes in WT and E111V GCAP1 upon ion binding monitored by circular dichroism.....	100
Figure 35: Ca <sup>2+</sup> sensitivity of WT and E111V monitored by gel mobility shift SDS-PAGE and absorption spectroscopy. ....	102
Figure 36: Ca <sup>2+</sup> -induced gel shift, GC1 western blot and enzymatic assay.....	104
Figure 37: <i>In vitro</i> and <i>in silico</i> results. ....	106
Figure 38: GCAP1 Ca <sup>2+</sup> -bound tridimensional model. ....	109
Figure 39: ANS fluorescence results. ....	111
Figure 40: DLS measurements for the analysis of the aggregation propensity.....	112
Figure 41: Analytical gel filtration. ....	113
Figure 42: Structural characterization by circular dichroism. ....	116
Figure 43: Cartoon representations of WT monomeric GCAP1.....	118
Figure 44: Mutations effect on Ca <sup>2+</sup> binding capability and enzymatic regulation.....	119
Figure 45: Effect of E155A mutation in amino acids distances. ....	121
Figure 46: Structure of human CaM in the Ca <sup>2+</sup> -bound form.....	123

Figure 47: Circular dichroism characterization of CaF <sub>2</sub> NPs and CaM. ....	124
Figure 48: Limited proteolysis pattern of CaM in the presence and in the absence of NPs. ....	125
Figure 49: RET-analysis of CaM-NP interaction. ....	126
Figure 50: SPR analysis of CaM-NP interaction. ....	127
Figure 51: Schematic representation of NP-CaM interaction. ....	129

## List of tables

Table 1: List of all GCAP1 known mutants associated with retinal dystrophies. ....	29
Table 2: Chemical features of cross-linking molecules. ....	64
Table 3: Analysis of ANS fluorescence and CD thermal denaturation data for WT and E64D CIB2. ....	74
Table 4: Apparent affinity for $\text{Ca}^{2+}$ and $\text{Mg}^{2+}$ of WT and E64D CIB2 assessed by CD titrations. .	78
Table 5: Molecular weight of WT and E64D CIB2 estimated by analytical SEC and Ferguson plots (FP). ....	81
Table 6: Comparison of the hydrodynamic properties of CIB2, CaM and Rec. ....	83
Table 7: Results from Surface Plasmon Resonance analysis of CIB2 – $\alpha 7\text{B}_\text{M}$ interaction. ....	88
Table 8: Apparent affinity for $\text{Ca}^{2+}$ and $\text{Mg}^{2+}$ of WT and E64D CIB2 assessed by CD titrations. .	89
Table 9: Results of GC regulation and $\text{Ca}^{2+}$ binding experiments. ....	95
Table 10: Results from ANS measurements. ....	98
Table 11: Results from CD far UV spectroscopy and thermal denaturation profiles. ....	100
Table 12: Results from enzymatic assay: human GC1 activity as a function of free $[\text{Ca}^{2+}]$ . ....	106
Table 13: Increase in dark level of $\text{Ca}^{2+}$ and cGMP according to numerical simulation of a mouse rod outer segment compared to a WT case. ....	107
Table 14: ANS fluorescence. ....	111
Table 15: Oligomeric state investigation. ....	113
Table 16: Shape overview. ....	117
Table 17: FarUV CD data: spectral shapes of CaM in the presence and absence of NPs. ....	125





## List of abbreviations

AD: autosomal dominant  
ANS: 8-Anilino-naphthalene-1-sulfonic acid  
AR: autosomal recessive  
AEC: anionic exchange chromatography  
CaF<sub>2</sub> NPs: calcium fluoride nanoparticles  
CaM: calmodulin  
CD: circular dichroism  
CDI: 1,1'-carbonyldiimidazole  
cGMP: cyclic GMP  
CIB2: Calcium- and Integrin-binding protein 2  
COD: cone dystrophy  
CORD: cone-rod dystrophy  
CPVT: catecholaminergic polymorphic ventricular tachycardia  
Cryo-EM: cryo-electron microscopy  
DFNB48: non-syndromic deafness  
DLS: dynamic light scattering  
DTT: 1,4-dithiothreitol  
DSBU: disuccinimidyl dibutyric urea  
EC<sub>50</sub>: [GCAP1] at which GC1 is half activated  
EDC: N-ethyl-N'-(dimethylaminopropyl)carbodiimide  
ESI-MS: electrospray ionization mass spectrometry  
FC: flow cell  
G418: geneticin  
GC: guanylate cyclase 1  
GCAP: guanylate cyclase activating protein 1  
GFP / EGFP: green fluorescent protein / enhanced green fluorescent protein  
GRK: rhodopsin kinase  
h<sub>c</sub>: Hill coefficient  
HEK293: human embryonic kidney 293  
HIV: human immunodeficiency virus  
IB: inclusion bodies  
IC<sub>50</sub>: [Ca<sup>2+</sup>] at which GC1 is half inhibited  
IMAC: immobilized metal affinity chromatography  
IPTG: Isopropyl β- d-1-thiogalactopyranoside  
LB: Luria Bertani  
LQTS: Long QT Syndrome  
MALDI-TOF: matrix-assisted laser desorption ionization time of flight  
MD: macular dystrophy  
MET: mechano-electrical transduction  
MW: molecular weight

NCKX: Na<sup>+</sup>/Ca<sup>2+</sup> + K<sup>+</sup> exchanger  
NCS: neuronal calcium sensor  
NDs: nanodevices  
NMR: nuclear magnetic resonance  
Ni-NTA: Nickel-Nitrilotriacetic acid  
NHS: N-hydroxysuccinimide  
NPs: nanoparticles  
OD: optical density  
PCR: polymerase chain reaction  
PDB: protein data bank  
PDE6: phosphodiesterase  
PEI: polyethylenimine  
Rec: recoverin  
PRE: paramagnetic relaxation enhancement  
RPC: reverse phase chromatography  
RET: resonance energy transfer  
ROS: rod outer segment  
SDS-PAGE: sodium-dodecyl-sulphate poly acrylamide gel electrophoresis  
s.e.m.: standard error of the mean  
SEC: size exclusion chromatography  
SPR: surface plasmon resonance  
TEV: tobacco etch virus protease  
TFA: trifluoroacetic acid  
T<sub>m</sub>: melting temperature  
TMC1/2: transmembrane channel-like  
USH1J: Usher syndrome type 1J  
WT: wild type  
XL-MS: cross-linking mass spectrometry  
YNMT: yeast N-myristoyl transferase

## References

1. Gifford, J. L., Walsh, M. P. & Vogel, H. J. (2007). Structures and metal-ion-binding properties of the Ca<sup>2+</sup>-binding helix-loop-helix EF-hand motifs. *Biochem J* **405**, 199-221.
2. Ikura, M. (1996). Calcium binding and conformational response in EF-hand proteins. *Trends Biochem Sci* **21**, 14-7.
3. Chen, C., Nakatani, K. & Koutalos, Y. (2003). Free magnesium concentration in salamander photoreceptor outer segments. *J Physiol* **553**, 125-35.
4. D. Purves, G. J. A., D. Fitzpatrick, W.C. Hall, A.-S. LaMantia, J.O. McNamara, L.E. White. (2009). *Neuroscienze*.
5. Fettiplace, R. & Hackney, C. M. (2006). The sensory and motor roles of auditory hair cells. *Nat Rev Neurosci* **7**, 19-29.
6. Ahmed, Z. M., Frolenkov, G. I. & Riazuddin, S. (2013). Usher proteins in inner ear structure and function. *Physiol Genomics* **45**, 987-9.
7. Life, A. H. S.-H. How we hear.
8. Cunningham, C. L. & Muller, U. (2019). Molecular Structure of the Hair Cell Mechanoelectrical Transduction Complex. *Cold Spring Harb Perspect Med* **9**.
9. Corey, D. P., Akyuz, N. & Holt, J. R. (2019). Function and Dysfunction of TMC Channels in Inner Ear Hair Cells. *Cold Spring Harb Perspect Med* **9**.
10. Giese, A. P. J., Tang, Y. Q., Sinha, G. P., Bowl, M. R., Goldring, A. C., Parker, A., Freeman, M. J., Brown, S. D. M., Riazuddin, S., Fettiplace, R., Schafer, W. R., Frolenkov, G. I. & Ahmed, Z. M. (2017). CIB2 interacts with TMC1 and TMC2 and is essential for mechanotransduction in auditory hair cells. *Nat Commun* **8**, 43.
11. Anthony G. Au, Y. W., Sibai Xie. (2013). Modeling of Mechanoelectrical Transduction of Hair Cells to Action Potentials in the Auditory Nerve.
12. Yamniuk, A. P., Nguyen, L. T., Hoang, T. T. & Vogel, H. J. (2004). Metal ion binding properties and conformational states of calcium- and integrin-binding protein. *Biochemistry* **43**, 2558-68.
13. Wang, Y., Li, J., Yao, X., Li, W., Du, H., Tang, M., Xiong, W., Chai, R. & Xu, Z. (2017). Loss of CIB2 Causes Profound Hearing Loss and Abolishes Mechanoelectrical Transduction in Mice. *Front Mol Neurosci* **10**, 401.
14. Michel, V., Booth, K. T., Patni, P., Cortese, M., Azaiez, H., Bahloul, A., Kahrizi, K., Labbe, M., Emptoz, A., Lelli, A., Degardin, J., Dupont, T., Aghaie, A., Oficjalska-Pham, D., Picaud, S., Najmabadi, H., Smith, R. J., Bowl, M. R., Brown, S. D., Avan, P., Petit, C. & El-Amraoui, A. (2017). CIB2, defective in isolated deafness, is key for auditory hair cell mechanotransduction and survival. *EMBO Mol Med* **9**, 1711-1731.
15. Godinho-Santos, A., Hance, A. J., Goncalves, J. & Mammano, F. (2016). CIB1 and CIB2 are HIV-1 helper factors involved in viral entry. *Sci Rep* **6**, 30927.
16. Zhu, W., Jarman, K. E., Lokman, N. A., Neubauer, H. A., Davies, L. T., Gliddon, B. L., Taing, H., Moretti, P. A. B., Oehler, M. K., Pitman, M. R. & Pitson, S. M. (2017). CIB2 Negatively Regulates Oncogenic Signaling in Ovarian Cancer via Sphingosine Kinase 1. *Cancer Res* **77**, 4823-4834.
17. Denofrio, J. C., Yuan, W., Temple, B. R., Gentry, H. R. & Parise, L. V. (2008). Characterization of calcium- and integrin-binding protein 1 (CIB1) knockout platelets: potential compensation by CIB family members. *Thromb Haemost* **100**, 847-56.

18. Vallone, R., Dal Cortivo, G., D'Onofrio, M. & Dell'Orco, D. (2018). Preferential Binding of Mg(2+) Over Ca(2+) to CIB2 Triggers an Allosteric Switch Impaired in Usher Syndrome Type 1J. *Front Mol Neurosci* **11**, 274.
19. Riazuddin, S., Belyantseva, I. A., Giese, A. P., Lee, K., Indzhukulian, A. A., Nandamuri, S. P., Yousaf, R., Sinha, G. P., Lee, S., Terrell, D., Hegde, R. S., Ali, R. A., Anwar, S., Andrade-Elizondo, P. B., Sirmaci, A., Parise, L. V., Basit, S., Wali, A., Ayub, M., Ansar, M., Ahmad, W., Khan, S. N., Akram, J., Tekin, M., Cook, T., Buschbeck, E. K., Frolenkov, G. I., Leal, S. M., Friedman, T. B. & Ahmed, Z. M. (2012). Alterations of the CIB2 calcium- and integrin-binding protein cause Usher syndrome type 1J and nonsyndromic deafness DFNB48. *Nat Genet* **44**, 1265-71.
20. Hager, M., Bigotti, M. G., Meszaros, R., Carmignac, V., Holmberg, J., Allamand, V., Akerlund, M., Kalamajski, S., Brancaccio, A., Mayer, U. & Durbeej, M. (2008). Cib2 binds integrin alpha7Bbeta1D and is reduced in laminin alpha2 chain-deficient muscular dystrophy. *J Biol Chem* **283**, 24760-9.
21. Huang, H., Ishida, H., Yamniuk, A. P. & Vogel, H. J. (2011). Solution structures of Ca2+-CIB1 and Mg2+-CIB1 and their interactions with the platelet integrin alphallb cytoplasmic domain. *J Biol Chem* **286**, 17181-92.
22. Dal Cortivo, G., Marino, V., Iacobucci, C., Vallone, R., Arlt, C., Rehkamp, A., Sinz, A. & Dell'Orco, D. (2019). Oligomeric state, hydrodynamic properties and target recognition of human Calcium and Integrin Binding protein 2 (CIB2). *Sci Rep* **9**, 15058.
23. Friedman, T. B. & Griffith, A. J. (2003). Human nonsyndromic sensorineural deafness. *Annu Rev Genomics Hum Genet* **4**, 341-402.
24. Patel, K., Giese, A. P., Grossheim, J. M., Hegde, R. S., Delio, M., Samanich, J., Riazuddin, S., Frolenkov, G. I., Cai, J., Ahmed, Z. M. & Morrow, B. E. (2015). A Novel C-Terminal CIB2 (Calcium and Integrin Binding Protein 2) Mutation Associated with Non-Syndromic Hearing Loss in a Hispanic Family. *PLoS One* **10**, e0133082.
25. Monroe, J. D., Rajadinakaran, G. & Smith, M. E. (2015). Sensory hair cell death and regeneration in fishes. *Front Cell Neurosci* **9**, 131.
26. Rosenblum, L. D. (2010). *See what I'm Saying: The Extraordinary Powers of Our Five Senses*, W. W. Norton.
27. Morreale, B. Anatomical description of the human eye.
28. Schwitzer, T., Schwan, R., Angioi-Duprez, K., Giersch, A. & Laprevote, V. (2016). The Endocannabinoid System in the Retina: From Physiology to Practical and Therapeutic Applications. *Neural Plast* **2016**, 2916732.
29. Savalli, U. Histochemical stains of the retina.
30. Schematic representation of a Rod photoreceptor.
31. Cervetto, L., Lagnado, L., Perry, R. J., Robinson, D. W. & McNaughton, P. A. (1989). Extrusion of calcium from rod outer segments is driven by both sodium and potassium gradients. *Nature* **337**, 740-3.
32. DeGrip, W. J., Pugh, E. N. & Stavenga, D. G. (2000). *Molecular mechanisms in visual transduction*. 1st edit. Handbook of biological physics,, Elsevier, Amsterdam ; New York.
33. Senin, II, Koch, K. W., Akhtar, M. & Philippov, P. P. (2002). Ca2+-dependent control of rhodopsin phosphorylation: recoverin and rhodopsin kinase. *Adv Exp Med Biol* **514**, 69-99.
34. Ames, J. B., Porumb, T., Tanaka, T., Ikura, M. & Stryer, L. (1995). Amino-terminal myristoylation induces cooperative calcium binding to recoverin. *J Biol Chem* **270**, 4526-33.

35. Koch, K. W., Duda, T. & Sharma, R. K. (2010). Ca<sup>2+</sup>-modulated vision-linked ROS-GC guanylate cyclase transduction machinery. *Mol Cell Biochem* **334**, 105-15.
36. Dizhoor, A. M., Olshevskaya, E. V. & Peshenko, I. V. (2010). Mg<sup>2+</sup>/Ca<sup>2+</sup> cation binding cycle of guanylyl cyclase activating proteins (GCAPs): role in regulation of photoreceptor guanylyl cyclase. *Mol Cell Biochem* **334**, 117-24.
37. Gill, J. S., Georgiou, M., Kalitzeos, A., Moore, A. T. & Michaelides, M. (2019). Progressive cone and cone-rod dystrophies: clinical features, molecular genetics and prospects for therapy. *British Journal of Ophthalmology* **103**, 711-720.
38. Salesse, C. (2017). [Physiology of the visual retinal signal: From phototransduction to the visual cycle]. *J Fr Ophthalmol* **40**, 239-250.
39. Semple-Rowland, S. L., Larkin, P., Bronson, J. D., Nykamp, K., Streit, W. J. & Baehr, W. (1999). Characterization of the chicken GCAP gene array and analyses of GCAP1, GCAP2, and GC1 gene expression in normal and rd chicken pineal. *Mol Vis* **5**, 14.
40. Hwang, J. Y., Lange, C., Helten, A., Hoppner-Heitmann, D., Duda, T., Sharma, R. K. & Koch, K. W. (2003). Regulatory modes of rod outer segment membrane guanylate cyclase differ in catalytic efficiency and Ca<sup>2+</sup>-sensitivity. *Eur J Biochem* **270**, 3814-21.
41. Mendez, A., Burns, M. E., Sokal, I., Dizhoor, A. M., Baehr, W., Palczewski, K., Baylor, D. A. & Chen, J. (2001). Role of guanylate cyclase-activating proteins (GCAPs) in setting the flash sensitivity of rod photoreceptors. *Proc Natl Acad Sci U S A* **98**, 9948-53.
42. Peshenko, I. V. & Dizhoor, A. M. (2004). Guanylyl cyclase-activating proteins (GCAPs) are Ca<sup>2+</sup>/Mg<sup>2+</sup> sensors: implications for photoreceptor guanylyl cyclase (RetGC) regulation in mammalian photoreceptors. *J Biol Chem* **279**, 16903-6.
43. Peshenko, I. V., Olshevskaya, E. V., Lim, S., Ames, J. B. & Dizhoor, A. M. (2012). Calcium-myristoyl Tug is a new mechanism for intramolecular tuning of calcium sensitivity and target enzyme interaction for guanylyl cyclase-activating protein 1: dynamic connection between N-fatty acyl group and EF-hand controls calcium sensitivity. *J Biol Chem* **287**, 13972-84.
44. Lim, S., Peshenko, I., Dizhoor, A. & Ames, J. B. (2009). Effects of Ca<sup>2+</sup>, Mg<sup>2+</sup>, and myristoylation on guanylyl cyclase activating protein 1 structure and stability. *Biochemistry* **48**, 850-62.
45. Marino, V. & Dell'Orco, D. (2016). Allosteric communication pathways routed by Ca<sup>2+</sup>/Mg<sup>2+</sup> exchange in GCAP1 selectively switch target regulation modes. *Sci Rep* **6**, 34277.
46. Sokal, I., Dupps, W. J., Grassi, M. A., Brown, J., Jr., Affatigato, L. M., Roychowdhury, N., Yang, L., Filipek, S., Palczewski, K., Stone, E. M. & Baehr, W. (2005). A novel GCAP1 missense mutation (L151F) in a large family with autosomal dominant cone-rod dystrophy (adCORD). *Invest Ophthalmol Vis Sci* **46**, 1124-32.
47. Vinberg, F., Peshenko, I. V., Chen, J., Dizhoor, A. M. & Kefalov, V. J. (2018). Guanylate cyclase-activating protein 2 contributes to phototransduction and light adaptation in mouse cone photoreceptors. *J Biol Chem* **293**, 7457-7465.
48. Koch, K. W. & Stryer, L. (1988). Highly cooperative feedback control of retinal rod guanylate cyclase by calcium ions. *Nature* **334**, 64-6.
49. Koch, K. W. & Dell'orco, D. (2013). A calcium-relay mechanism in vertebrate phototransduction. *ACS Chem Neurosci* **4**, 909-17.
50. Downes, S. M., Holder, G. E., Fitzke, F. W., Payne, A. M., Warren, M. J., Bhattacharya, S. S. & Bird, A. C. (2001). Autosomal dominant cone and cone-rod

- dystrophy with mutations in the guanylate cyclase activator 1A gene-encoding guanylate cyclase activating protein-1. *Arch Ophthalmol* **119**, 96-105.
51. Kamenarova, K., Corton, M., Garcia-Sandoval, B., Fernandez-San Jose, P., Panchev, V., Avila-Fernandez, A., Lopez-Molina, M. I., Chakarova, C., Ayuso, C. & Bhattacharya, S. S. (2013). Novel GUCA1A mutations suggesting possible mechanisms of pathogenesis in cone, cone-rod, and macular dystrophy patients. *Biomed Res Int* **2013**, 517570.
  52. Peshenko, I. V., Cideciyan, A. V., Sumaroka, A., Olshevskaya, E. V., Scholten, A., Abbas, S., Koch, K. W., Jacobson, S. G. & Dizhoor, A. M. (2019). A G86R mutation in the calcium-sensor protein GCAP1 alters regulation of retinal guanylyl cyclase and causes dominant cone-rod degeneration. *J Biol Chem* **294**, 3476-3488.
  53. Kitiratschky, V. B., Behnen, P., Kellner, U., Heckenlively, J. R., Zrenner, E., Jagle, H., Kohl, S., Wissinger, B. & Koch, K. W. (2009). Mutations in the GUCA1A gene involved in hereditary cone dystrophies impair calcium-mediated regulation of guanylate cyclase. *Hum Mutat* **30**, E782-96.
  54. Payne, A. M., Downes, S. M., Bessant, D. A., Taylor, R., Holder, G. E., Warren, M. J., Bird, A. C. & Bhattacharya, S. S. (1998). A mutation in guanylate cyclase activator 1A (GUCA1A) in an autosomal dominant cone dystrophy pedigree mapping to a new locus on chromosome 6p21.1. *Hum Mol Genet* **7**, 273-7.
  55. Michaelides, M., Wilkie, S. E., Jenkins, S., Holder, G. E., Hunt, D. M., Moore, A. T. & Webster, A. R. (2005). Mutation in the gene GUCA1A, encoding guanylate cyclase-activating protein 1, causes cone, cone-rod, and macular dystrophy. *Ophthalmology* **112**, 1442-7.
  56. Mizobuchi, K., Hayashi, T., Katagiri, S., Yoshitake, K., Fujinami, K., Yang, L., Kuniyoshi, K., Shinoda, K., Machida, S., Kondo, M., Ueno, S., Terasaki, H., Matsuura, T., Tsunoda, K., Iwata, T. & Nakano, T. (2019). Characterization of GUCA1A-associated dominant cone/cone-rod dystrophy: low prevalence among Japanese patients with inherited retinal dystrophies. *Sci Rep* **9**, 16851.
  57. Nong, E., Lee, W., Merriam, J. E., Allikmets, R. & Tsang, S. H. (2014). Disease progression in autosomal dominant cone-rod dystrophy caused by a novel mutation (D100G) in the GUCA1A gene. *Doc Ophthalmol* **128**, 59-67.
  58. Huang, L., Xiao, X., Li, S., Jia, X., Wang, P., Sun, W., Xu, Y., Xin, W., Guo, X. & Zhang, Q. (2016). Molecular genetics of cone-rod dystrophy in Chinese patients: New data from 61 probands and mutation overview of 163 probands. *Exp Eye Res* **146**, 252-8.
  59. Marino, V., Dal Cortivo, G., Oppici, E., Maltese, P. E., D'Esposito, F., Manara, E., Ziccardi, L., Falsini, B., Magli, A., Bertelli, M. & Dell'Orco, D. (2018). A novel p.(Glu111Val) missense mutation in GUCA1A associated with cone-rod dystrophy leads to impaired calcium sensing and perturbed second messenger homeostasis in photoreceptors. *Hum Mol Genet* **27**, 4204-4217.
  60. Jiang, L., Wheaton, D., Bereta, G., Zhang, K., Palczewski, K., Birch, D. G. & Baehr, W. (2008). A novel GCAP1(N104K) mutation in EF-hand 3 (EF3) linked to autosomal dominant cone dystrophy. *Vision Res* **48**, 2425-32.
  61. Nishiguchi, K. M., Sokal, I., Yang, L., Roychowdhury, N., Palczewski, K., Berson, E. L., Dryja, T. P. & Baehr, W. (2004). A novel mutation (I143NT) in guanylate cyclase-activating protein 1 (GCAP1) associated with autosomal dominant cone degeneration. *Invest Ophthalmol Vis Sci* **45**, 3863-70.
  62. Manes, G., Mamouni, S., Herald, E., Richard, A. C., Senechal, A., Aouad, K., Bocquet, B., Meunier, I. & Hamel, C. P. (2017). Cone dystrophy or macular

- dystrophy associated with novel autosomal dominant GUCA1A mutations. *Mol Vis* **23**, 198-209.
63. Wilkie, S. E., Li, Y., Deery, E. C., Newbold, R. J., Garibaldi, D., Bateman, J. B., Zhang, H., Lin, W., Zack, D. J., Bhattacharya, S. S., Warren, M. J., Hunt, D. M. & Zhang, K. (2001). Identification and functional consequences of a new mutation (E155G) in the gene for GCAP1 that causes autosomal dominant cone dystrophy. *Am J Hum Genet* **69**, 471-80.
  64. Huang, L., Li, S., Xiao, X., Jia, X., Sun, W., Gao, Y., Li, L., Wang, P., Guo, X. & Zhang, Q. (2013). Novel GUCA1A mutation identified in a Chinese family with cone-rod dystrophy. *Neurosci Lett* **541**, 179-83.
  65. Weisschuh, N., Mayer, A. K., Strom, T. M., Kohl, S., Glockle, N., Schubach, M., Andreasson, S., Bernd, A., Birch, D. G., Hamel, C. P., Heckenlively, J. R., Jacobson, S. G., Kamme, C., Kellner, U., Kunstmann, E., Maffei, P., Reiff, C. M., Rohrschneider, K., Rosenberg, T., Rudolph, G., Vamos, R., Varsanyi, B., Weleber, R. G. & Wissinger, B. (2016). Mutation Detection in Patients with Retinal Dystrophies Using Targeted Next Generation Sequencing. *PLoS One* **11**, e0145951.
  66. Power, M., Das, S., Schutze, K., Marigo, V., Ekstrom, P. & Paquet-Durand, F. (2019). Cellular mechanisms of hereditary photoreceptor degeneration - Focus on cGMP. *Prog Retin Eye Res*, 100772.
  67. Dell'Orco, D., Sulmann, S., Zagel, P., Marino, V. & Koch, K. W. (2014). Impact of cone dystrophy-related mutations in GCAP1 on a kinetic model of phototransduction. *Cell Mol Life Sci* **71**, 3829-40.
  68. Marino, V., Scholten, A., Koch, K. W. & Dell'Orco, D. (2015). Two retinal dystrophy-associated missense mutations in GUCA1A with distinct molecular properties result in a similar aberrant regulation of the retinal guanylate cyclase. *Hum Mol Genet* **24**, 6653-66.
  69. Vocke, F., Weisschuh, N., Marino, V., Malfatti, S., Jacobson, S. G., Reiff, C. M., Dell'Orco, D. & Koch, K. W. (2017). Dysfunction of cGMP signalling in photoreceptors by a macular dystrophy-related mutation in the calcium sensor GCAP1. *Hum Mol Genet* **26**, 133-144.
  70. Gorzelany, J. A. & de Souza, M. P. (2013). Protein replacement therapies for rare diseases: a breeze for regulatory approval? *Sci Transl Med* **5**, 178fs10.
  71. Crunkhorn, S. (2013). Regulatory watch: enhanced chance of success for protein replacement therapies. *Nat Rev Drug Discov* **12**, 414.
  72. Guidotti, M. Liposomes pharmaceutical preparations.
  73. Marino, V., Astegno, A., Pedroni, M., Piccinelli, F. & Dell'Orco, D. (2014). Nanodevice-induced conformational and functional changes in a prototypical calcium sensor protein. *Nanoscale* **6**, 412-23.
  74. Astegno, A., Maresi, E., Marino, V., Dominici, P., Pedroni, M., Piccinelli, F. & Dell'Orco, D. (2014). Structural plasticity of calmodulin on the surface of CaF<sub>2</sub> nanoparticles preserves its biological function. *Nanoscale* **6**, 15037-47.
  75. Marino, V., Borsatto, A., Vocke, F., Koch, K. W. & Dell'Orco, D. (2017). CaF<sub>2</sub> nanoparticles as surface carriers of GCAP1, a calcium sensor protein involved in retinal dystrophies. *Nanoscale* **9**, 11773-11784.
  76. Dal Cortivo, G., Wagner, G. E., Cortelletti, P., Padmanabha Das, K. M., Zangger, K., Speghini, A., Dell'Orco, D. & Meyer, N. H. (2018). Luminescent and paramagnetic properties of nanoparticles shed light on their interactions with proteins. *Sci Rep* **8**, 3420.
  77. Universität Regensburg, I. f. A. C.

78. Dell'Orco, D., Behnen, P., Linse, S. & Koch, K. W. (2010). Calcium binding, structural stability and guanylate cyclase activation in GCAP1 variants associated with human cone dystrophy. *Cell Mol Life Sci* **67**, 973-84.
79. M. Pedroni, F. P., T. Passuello, S. Polizzi, J. Ueda, P. Haro-González, L. Martinez Maestro, D. Jaque, J. García-Solé, M. Bettinelli, A. Speghini. (2013). Water (H<sub>2</sub>O and D<sub>2</sub>O) Dispersible NIR-to-NIR Upconverting Yb<sup>3+</sup>/Tm<sup>3+</sup> Doped MF<sub>2</sub> (M = Ca, Sr) Colloids: Influence of the Host Crystal. *ACS* **13**, 4906-4913.
80. Healthcare, G. Ion Exchange chromatography - Principle and methods.
81. Kisselev, S. J. F. O. G. (2008). Signal Transduction in the retina.
82. Longo, P. A., Kavran, J. M., Kim, M. S. & Leahy, D. J. (2013). Transient mammalian cell transfection with polyethylenimine (PEI). *Methods Enzymol* **529**, 227-40.
83. Viviano, J., Krishnan, A., Wu, H. & Venkataraman, V. (2016). Electrophoretic mobility shift in native gels indicates calcium-dependent structural changes of neuronal calcium sensor proteins. *Anal Biochem* **494**, 93-100.
84. Astegno, A., La Verde, V., Marino, V., Dell'Orco, D. & Dominici, P. (2016). Biochemical and biophysical characterization of a plant calmodulin: Role of the N- and C-lobes in calcium binding, conformational change, and target interaction. *Biochim Biophys Acta* **1864**, 297-307.
85. B., H. D., Biology, S. o. B. a. M. & University of Leeds, L. L. J., UK. (1998). Gel Electrophoresis of proteins: a practical approach.
86. Linse, S. (2002). Calcium binding to proteins studied via competition with chromophoric chelators. *Methods Mol Biol* **173**, 15-24.
87. Andre, I. & Linse, S. (2002). Measurement of Ca<sup>2+</sup>-binding constants of proteins and presentation of the CaLigator software. *Anal Biochem* **305**, 195-205.
88. Kelly, S. M., Jess, T. J. & Price, N. C. (2005). How to study proteins by circular dichroism. *Biochim Biophys Acta* **1751**, 119-39.
89. A., J. (1935). Über den mechanismen des photolumineszenz von Farbstoffphosphore. *Zeitschrift für Physik*.
90. Vivian, J. T. & Callis, P. R. (2001). Mechanisms of tryptophan fluorescence shifts in proteins. *Biophys J* **80**, 2093-109.
91. Loving, G. S., Sainlos, M. & Imperiali, B. (2010). Monitoring protein interactions and dynamics with solvatochromic fluorophores. *Trends Biotechnol* **28**, 73-83.
92. INSTRUMENTS, P.
93. Healthcare, G. How Surface Plasmon Resonance works.
94. Katie, T. (2019). The Role of Surface Plasmon Resonance in Clinical Laboratories. *Clinical Laboratory News*.
95. BioMart, C. (2019). Principle and Protocol of Surface Plasmon Resonance (SPR).
96. Piotrowski, C. & Sinz, A. (2018). Structural Investigation of Proteins and Protein Complexes by Chemical Cross-Linking/Mass Spectrometry. *Adv Exp Med Biol* **1105**, 101-121.
97. Gotze, M., Iacobucci, C., Ihling, C. H. & Sinz, A. (2019). A Simple Cross-Linking/Mass Spectrometry Workflow for Studying System-wide Protein Interactions. *Anal Chem* **91**, 10236-10244.
98. Iacobucci, C., Gotze, M., Ihling, C. H., Piotrowski, C., Arlt, C., Schafer, M., Hage, C., Schmidt, R. & Sinz, A. (2018). A cross-linking/mass spectrometry workflow based on MS-cleavable cross-linkers and the MeroX software for studying protein structures and protein-protein interactions. *Nat Protoc* **13**, 2864-2889.
99. Leney, A. C. & Heck, A. J. (2017). Native Mass Spectrometry: What is in the Name? *J Am Soc Mass Spectrom* **28**, 5-13.



100. Hage, C., Iacobucci, C., Rehkamp, A., Arlt, C. & Sinz, A. (2017). The First Zero-Length Mass Spectrometry-Cleavable Cross-Linker for Protein Structure Analysis. *Angew Chem Int Ed Engl* **56**, 14551-14555.
101. Piotrowski, C., Ihling, C. H. & Sinz, A. (2015). Extending the cross-linking/mass spectrometry strategy: Facile incorporation of photo-activatable amino acids into the model protein calmodulin in *Escherichia coli* cells. *Methods* **89**, 121-7.
102. Blazejczyk, M., Sobczak, A., Debowska, K., Wisniewska, M. B., Kirilenko, A., Pikula, S., Jaworski, J., Kuznicki, J. & Wojda, U. (2009). Biochemical characterization and expression analysis of a novel EF-hand Ca<sup>2+</sup> binding protein calmyrin2 (Cib2) in brain indicates its function in NMDA receptor mediated Ca<sup>2+</sup> signaling. *Arch Biochem Biophys* **487**, 66-78.
103. Huang, H., Bogstie, J. N. & Vogel, H. J. (2012). Biophysical and structural studies of the human calcium- and integrin-binding protein family: understanding their functional similarities and differences. *Biochem Cell Biol* **90**, 646-56.
104. Fontana, A., de Laureto, P. P., Spolaore, B., Frare, E., Picotti, P. & Zamboni, M. (2004). Probing protein structure by limited proteolysis. *Acta Biochim Pol* **51**, 299-321.
105. Lim, S., Roseman, G., Peshenko, I., Manchala, G., Cudia, D., Dizhoor, A. M., Millhauser, G. & Ames, J. B. (2018). Retinal guanylyl cyclase activating protein 1 forms a functional dimer. *PLoS One* **13**, e0193947.
106. Dell'Orco, D. & Dal Cortivo, G. (2019). Normal GCAPs partly compensate for altered cGMP signaling in retinal dystrophies associated with mutations in GUCA1A. *Sci Rep* **9**, 20105.
107. Carafoli, E. (2002). Calcium signaling: a tale for all seasons. *Proc Natl Acad Sci U S A* **99**, 1115-22.
108. Chin, D. & Means, A. R. (2000). Calmodulin: a prototypical calcium sensor. *Trends Cell Biol* **10**, 322-8.
109. Jensen, H. H., Brohus, M., Nyegaard, M. & Overgaard, M. T. (2018). Human Calmodulin Mutations. *Front Mol Neurosci* **11**, 396.



## Acknowledgments

Moltissime sono le persone che mi hanno tenuto per mano, accompagnandomi al raggiungimento di questo importante traguardo.

Il primo ringraziamento va al *Prof. Dell'Orco* per avermi accolto nel suo laboratorio quando ho iniziato a muovere i primi passi nella Scienza ed avermi portato qui oggi, tre tesi dopo. Lo ringrazio per il tempo e le energie investite nella mia formazione professionale e non solo. Mi ha insegnato cosa sia il rigore, l'attenzione al dettaglio, il mettersi in discussione. La sua passione e la voglia di fare la differenza sono state, e sono tutt'ora, di grandissima ispirazione.

Vorrei ringraziare *Valerio*, mio mentore e guida ormai da anni, e *Ros*. Con la loro calma e tranquillità mi hanno insegnato che a tutto c'è soluzione.

Nonostante con noi solo da due anni anche *Anna* merita uno speciale ringraziamento. La sua dolcezza è stata fondamentale nell'affrontare i momenti più tristi degli ultimi due anni.

Il dottorato mi ha offerto l'occasione di approfondire un'amicizia nata per caso. Tra un western e l'altro abbiamo condiviso le gioie di un buon risultato e i dolori delle lastre bianche. Grazie *Diana* per esserci sempre stata e ricorda: “*dipende dall'anti-corpo*”.

Dal nostro primo incontro è passato solo un anno, ma sembra una vita. Vorrei ringraziare *Carmen* per la sua gioia di vivere, per l'entusiasmo, e le lunghe serate in laboratorio per “*l'ultimo risultato da inserire nella tesi*”. Spero che sia solo l'inizio di una lunga storia.

Un ringraziamento va anche ad *Elena (Buttu)*, *Giada*, *Rik* e *Gio* per aver contribuito alla mia formazione e condiviso lunghe serate in laboratorio.

Vorrei ringraziare *Michela Lanza*, professoressa di Lettere (e non solo) del Liceo G. Cotta. Come Virgilio ha guidato Dante nell'Inferno, lei ha guidato me in quegli anni in cui l'incertezza è l'unica certezza. Grazie a lei ho capito quale fosse la mia strada. Prof, questa volta l'inchiostro delle stampe è asciutto.

Charles Dickens ha scritto che gli amici sono regali che la vita sceglie di farti. Posso dire che la mia vita è stata molto generosa perché mi ha dato *Elisa*, *Alex* e *Luca*, un sostegno sempre presente, nonostante la vita stessa abbia scelto per noi strade diverse.

Un grazie speciale mio *Fratello*. Nonostante le strade intraprese siano diametralmente opposte, in lui ho sempre trovato una parola di conforto. Gli auguro di trovare la sua strada come io ho trovato la mia, e di ricordarsi che per lui ci sarò sempre.

Un grazie a *Flavia, Marco, Alessio, Stefano (Gogo), Sara, Carlotta* e piccoli *Giulia* e *Filippo*, la mia seconda famiglia.

Un pensiero speciale va alla persona che è stata per me un muro portante fin da quando ero una studentessa, *Christian*. In questi nove anni insieme ha creduto in me con forza e convinzione, non vacillando mai. Questo traguardo è tanto mio quanto suo.

Come nell'*authorship* di un paper, se il "primo nome" è colui che esegue la gran parte del lavoro sperimentale, l'"ultimo nome" è il coordinatore, colui che concepisce l'idea, che la sviluppa, che ci crede. Il mio "ultimo nome" sono *Mamma* e *Papà*. Nonostante tutto sono sempre stati lì, con una parola di conforto quando ero prossima a cedere, o una battuta per stemperare la tensione. Loro, che hanno sempre messo i figli al primo posto trasmettendogli i valori e la forza necessari per sopravvivere in questo mondo che non guarda in faccia e nessuno, e se può schiacciarti lo fa. Grazie di avermi permesso questo, grazie di crederci sempre.



# Preferential Binding of $Mg^{2+}$ Over $Ca^{2+}$ to CIB2 Triggers an Allosteric Switch Impaired in Usher Syndrome Type 1J

Rosario Vallone<sup>1†</sup>, Giuditta Dal Cortivo<sup>1†</sup>, Mariapina D'Onofrio<sup>2</sup> and Daniele Dell'Orco<sup>1\*</sup>

<sup>1</sup> Section of Biological Chemistry, Department of Neurosciences, Biomedicine and Movement Sciences, University of Verona, Verona, Italy; <sup>2</sup> Department of Biotechnology, University of Verona, Verona, Italy

## OPEN ACCESS

### Edited by:

Teresa Duda,  
Salus University, United States

### Reviewed by:

Marina Mikhaylova,  
Universitätsklinikum  
Hamburg-Eppendorf, Germany  
Andrea Sinz,  
Martin Luther University of  
Halle-Wittenberg, Germany

### \*Correspondence:

Daniele Dell'Orco  
daniele.dellorco@univr.it

<sup>†</sup>These authors have contributed  
equally to this work

**Received:** 26 April 2018

**Accepted:** 20 July 2018

**Published:** 17 August 2018

### Citation:

Vallone R, Dal Cortivo G, D'Onofrio M  
and Dell'Orco D (2018) Preferential  
Binding of  $Mg^{2+}$  Over  $Ca^{2+}$  to CIB2  
Triggers an Allosteric Switch Impaired  
in Usher Syndrome Type 1J.  
*Front. Mol. Neurosci.* 11:274.  
doi: 10.3389/fnmol.2018.00274

Calcium and integrin binding protein 2 (CIB2) shares with the other members of the CIB family the ability to bind  $Ca^{2+}$  and  $Mg^{2+}$  via two functional EF-hand motifs, namely EF3 and EF4. As a cation sensor, CIB2 is able to switch to a conformation likely associated with specific biological functions yet to be clarified. Recent findings demonstrate the involvement of CIB2 in hearing physiology and a single, conservative point mutation (p.E64D) has been related to Usher Syndrome type 1J (USH1J) and non-syndromic hearing loss. We present an exhaustive biochemical and biophysical characterization of human wild type (WT) and E64D CIB2. We found that CIB2 does not possibly work as a calcium sensor under physiological conditions, its affinity for  $Ca^{2+}$  ( $K_d^{app} = 0.5$  mM) being too low for detecting normal intracellular levels. Instead, CIB2 displays a significantly high affinity for  $Mg^{2+}$  ( $K_d^{app} = 290$   $\mu$ M), and it is probably  $Mg^{2+}$ -bound under physiological conditions. At odds with the homologous protein CIB1, CIB2 forms a non-covalent dimer under conditions that mimic the physiological ones, and as such it interacts with its physiological target  $\alpha$ 7B integrin. NMR spectroscopy revealed a long-range allosteric communication between the residue E64, located at the N-terminal domain, and the metal cation binding site EF3, located at the C-terminal domain. The conservative E64D mutation breaks up such inter-domain communication resulting in the impaired ability of CIB2 to switch to its  $Mg^{2+}$ -bound form. The ability to bind the target integrin peptide was substantially conserved for E64D CIB2, thus suggesting that the molecular defect associated with USH1J resides in its inability to sense  $Mg^{2+}$  and adopt the required conformation.

**Keywords:** calcium sensor, Usher syndrome 1J, DFNB48, nuclear magnetic resonance, hearing loss, calcium and integrin binding protein, allostery, magnesium

## INTRODUCTION

Calcium and integrin binding protein 2 (CIB2) is a 21.6 kDa protein sharing with the other members of the CIB family the ability to bind  $Ca^{2+}$  and  $Mg^{2+}$  via two functional EF-hand motifs, namely EF3 and EF4, therefore switching to a specific conformation likely associated with specific biological functions (Huang et al., 2012). Since its discovery as a ubiquitously expressed DNA-dependent protein kinase interacting protein (Seki et al., 1999), CIB2 has been found to be

expressed in a variety of tissues but its physiological role remains largely unknown. It has been established that CIB2 binds specifically to the integrin  $\alpha 7\text{B}$  cytoplasmic domain (Häger et al., 2008; Huang et al., 2012), however the protein interacts also with the  $\alpha \text{IIb}$  integrin (Huang et al., 2012), thus broadening its potential involvement in a variety of signal transduction processes.

Recent lines of evidence demonstrate the direct involvement of CIB2 in hearing physiology, as CIB2 knockout mice showed abolished mechanoelectrical transduction in auditory cells leading to profound hearing loss (Wang et al., 2017). Interestingly, four missense mutations in the gene encoding for CIB2 [p.F91S, p.C99W, p.I123T (Riazuddin et al., 2012) and more recently p. R186W (Patel et al., 2015)] have been found to be associated with non-syndromic deafness (DFNB48) while a single, conservative point mutation (p.E64D) (Riazuddin et al., 2012) has been related to Usher Syndrome type 1J (USH1J, OMIM entry: 614869), a genetic disorder characterized by hearing loss and progressive vision loss due to retinitis pigmentosa. Altogether, these recent findings suggest that CIB2 is an essential component for the normal development of both hair cells and photoreceptor cells.

Among the members of the CIB family, CIB1 is the protein that has been characterized in deeper biochemical and structural detail (Yamniuk et al., 2004, 2006, 2007; Gentry et al., 2005; Yamniuk and Vogel, 2005; Huang et al., 2011). CIB1 and CIB2 are homologous proteins, but both the sequence identity (37.4%) and the overall similarity (60%) are not extremely high. Differences are found throughout the primary structure and importantly, key residues are substituted in the metal-ion binding sites EF3 and EF4 (**Figure 1**). These differences may be reflected in an overall distinct structure/function behavior of CIB2 as compared to CIB1. To date, only few studies have focused on the biochemical and biophysical characterization of CIB2 (Häger et al., 2008; Blazejczyk et al., 2009; Huang et al., 2012) and a comprehensive picture that allows a molecular-level understanding of its biological properties under physiological conditions as well as their alteration in USH1J is currently missing.

In this work, we present an exhaustive characterization of human wild type (WT) and E64D CIB2 by using an integrated biochemical and biophysical approach to highlight the molecular defects of the variant associated with USH1J. Interestingly, we found that CIB2 does not possibly work as a calcium sensor under physiological conditions, because its affinity for  $\text{Ca}^{2+}$  is too low for normal intracellular levels. Instead, CIB2 has a fairly high affinity for  $\text{Mg}^{2+}$  and it is probably  $\text{Mg}^{2+}$ -bound under physiological conditions. At odds with CIB1, which is monomeric both when isolated and when interacting with its target (Gentry et al., 2005), we found that CIB2 is a non-covalent dimer under conditions that mimic the physiological ones, and as such it interacts with its physiological target  $\alpha 7\text{B}$  integrin. NMR spectroscopy revealed a long range allosteric communication between the residue E64, located at the N-terminal domain, and the metal cation binding site EF3, located at the C-terminal domain (**Figure 1**). The E64D mutation associated with USH1J, although conservative, apparently breaks up such inter-domain

communication resulting in the impaired ability of CIB2 to switch to its  $\text{Mg}^{2+}$  (and  $\text{Ca}^{2+}$ )-bound form, thus suggesting that the molecular defect associated with CIB2 and causing USH1J resides in its inability to sense  $\text{Mg}^{2+}$  and adopt the required conformation.

## MATERIALS AND METHODS

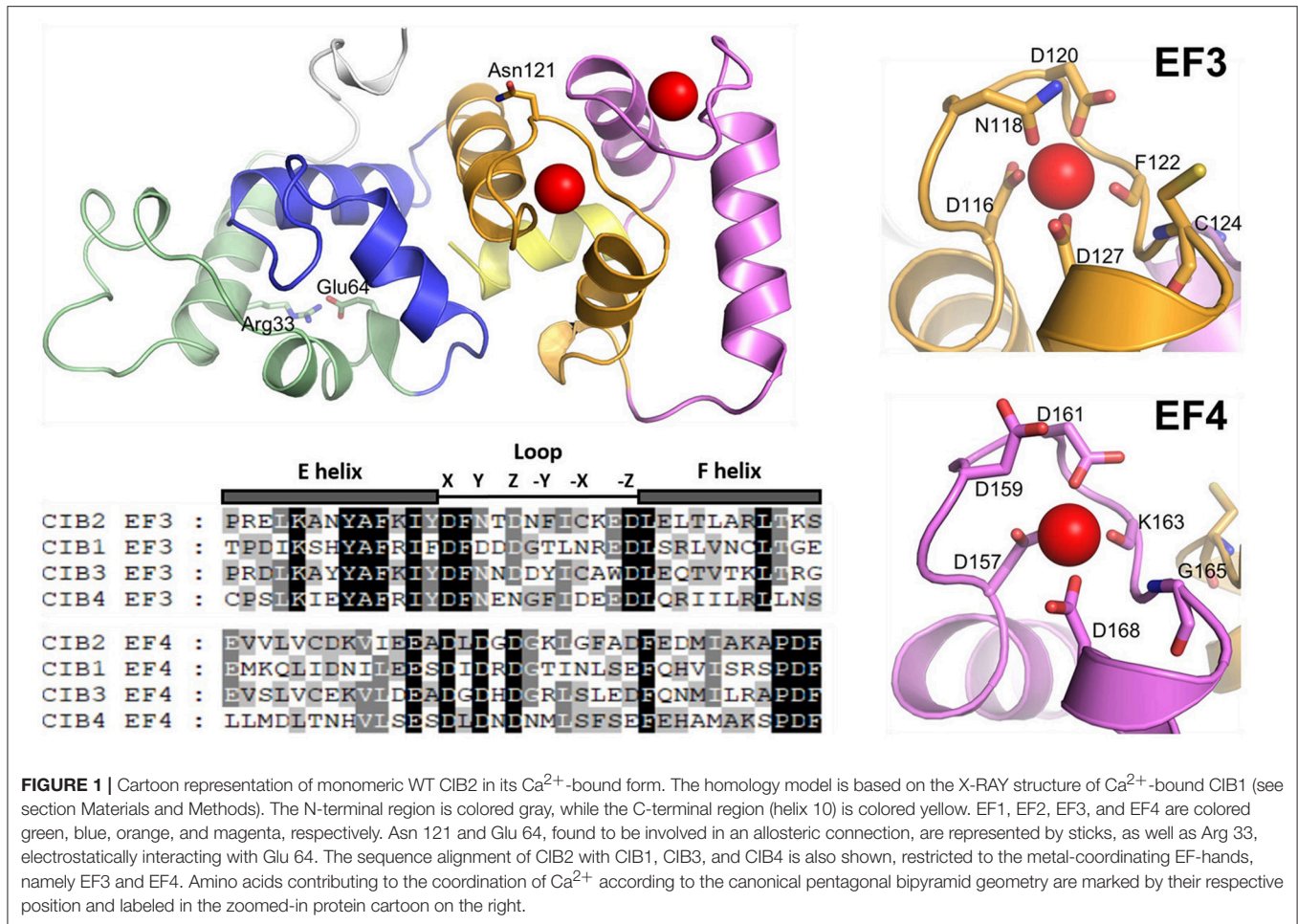
### Materials

QuikChange II Site-Directed Mutagenesis kit was purchased from Agilent. The Bradford reagent was purchased from Bio-Rad. Chromatographic columns were purchased from GE Healthcare, and synthetic oligonucleotides were from Eurofins. All other chemicals were purchased from Sigma Aldrich. All purchased chemicals were of the highest commercially available purity grade.

### Expression and Purification of Human Wild Type and E64D CIB2

The cDNA of human CIB2 isoform 1 (Uniprot entry 075838-1) was cloned into a pET24a(+) vector (Genscript) containing a 6xHis-tag at the N-terminal, followed by Tobacco Etch Virus (TEV) cleavage site. The plasmid was used to transform BL21 DE3 cells. Cells were grown in LB medium or in M9 minimal medium supplemented with  $^{15}\text{NH}_4\text{Cl}$  ( $1\text{ g L}^{-1}$ ) as a sole nitrogen source for NMR studies, at  $37^\circ\text{C}$  until the  $\text{OD}_{600}$  reached a value around 0.4. Flasks were then cooled down and, after induction by  $0.5\text{ mM}$  IPTG at  $\text{OD}_{600} = 0.6$ , bacteria were grown at  $15^\circ\text{C}$  for 20 h. After centrifugation at  $5,500\text{ g}$  (20 min at  $4^\circ\text{C}$ ) the obtained pellets were suspended in lysis buffer (20 mM TRIS pH = 7.5, 0.5 M NaCl, 20 mM imidazole, 1 mM DTT, 5 U/mL DNase, 0.1 mg/mL lysozyme, 1 mM PMSF, 2.5 mM  $\text{MgCl}_2$ ) and incubated at  $25^\circ\text{C}$  for 30 min. In addition, 10–12 sonication cycles on ice, 10 s each, were performed. Soluble and insoluble fractions were separated by centrifugation at  $16,000\text{ g}$ ,  $4^\circ\text{C}$  for 30 min. WT CIB2 was found in high amount in the soluble phase and it was directly loaded in a 5 mL His-trap FF Crude column (GE Healthcare) previously equilibrated with loading buffer (20 mM TRIS, pH = 7.5, 0.5 M NaCl, 1 mM DTT, 20 mM imidazole). A one-step elution by 500 mM imidazole was chosen after initial tests with a gradient. In order to remove the imidazole excess to allow for TEV-protease activity, His-CIB2 was dialyzed against 50 mM TRIS pH 8, 150 mM NaCl, 1 mM DTT and then incubated with a previously prepared His-tagged TEV-protease (Dal Cortivo et al., 2018) (ratio 1:30) overnight at  $8^\circ\text{C}$ . Tag-free CIB2 was purified from His-TEV and cleaved His-tails by reloading into a His-trap column and collecting the flow-through. Protein concentration was measured by a Bradford assay optimized for homolog calcium sensor proteins or by using the predicted molar extinction coefficient ( $\epsilon_{280} = 6,400\text{ M}^{-1}\text{cm}^{-1}$ , <http://protcalc.sourceforge.net/>) and the purity was verified by SDS-PAGE to be at least 90%. Purified WT CIB2 was washed in 20 mM TRIS pH 7.5, 150 mM KCl, 1 mM DTT, using an Amicon concentrator. Protein aliquots were then flash-frozen and stored at  $-80^\circ\text{C}$  until use.

The E64D point mutation was obtained by site-directed mutagenesis on the complete cDNA of CIB2 using a forward



primer (5'-ATCATTCAAATGCCGGACCTGCGTGAGAACCCTT-3') and a reverse primer (5'-AACGGGTTCTCACGAGGTCCGGCATTGGAATGAT-3'). Protein expression was performed as for the WT but the mutant protein was found to concentrate in the insoluble fraction, thus requiring purification from the inclusion bodies. After cell lysis, the insoluble pellets were suspended in the unfolding buffer (20 mM TRIS pH 7.5, 0.5 M NaCl, 6M guanidine hydrochloride, 20 mM imidazole, 1 mM DTT) and incubated overnight at 4°C. Unfolded CIB2 was loaded into a His-trap column and then renatured by a gradient from 0 to 100% of refolding buffer (unfolding buffer guanidine hydrochloride-free) setting the flow rate to 1 mL/min (100 mL total volume). After elution with 500 mM imidazole E64D CIB2 was treated as the WT protein.

## Peptides

The peptide corresponding to the membrane proximal segment of the cytoplasmic domain of  $\alpha 7\text{B}$  integrin (Uniprot entry: Q13683) comprised between residues 1101–1116 ( $\alpha 7\text{B}_\text{M}$ , Ac-LLLWKMGFFKRAKHPE-NH<sub>2</sub>) and a scrambled peptide obtained by shuffling the  $\alpha 7\text{B}_\text{M}$  sequence (Scrb, Ac-KEFWGLHAKPRLKLMF-NH<sub>2</sub>) were

synthesized by GenScript USA Inc. (New Jersey, 144 USA). The purity of peptides, estimated by HPLC, was  $\geq 95\%$  and concentration was determined using the predicted molar extinction coefficient ( $\epsilon_{280} = 5,690 \text{ M}^{-1}\text{cm}^{-1}$ , <http://protcalc.sourceforge.net/>).

## Circular Dichroism Spectroscopy and Thermal Denaturation Profiles

Secondary and tertiary structures of WT and E64D CIB2 and thermal denaturation profiles were investigated by using a Jasco J-710 spectropolarimeter equipped with a Peltier type cell holder, using protocols previously described (Astegno et al., 2014; Marino et al., 2014, 2015a,b; Vocke et al., 2017). Briefly, near UV (320–250 nm) and far UV (250–200 nm) spectra of  $\sim 30 \mu\text{M}$  and  $12 \mu\text{M}$  CIB2 respectively were collected at 37°C after consecutive additions of 0.5 mM EDTA, 1 mM  $\text{Mg}^{2+}$  and 1 mM  $\text{Ca}^{2+}$ . Quartz cuvettes were used both for near UV (1 cm) and far UV (0.1 cm). Solvent spectra were recorded and considered as a blank.

Thermal denaturation profiles were collected in the same conditions as for far UV spectra by monitoring ellipticity signal at 222 nm in a temperature range between 4 and 70°C (scan rate 90°C/h).

Titration experiments were designed starting from the apo WT and E64D CIB2 in order to estimate an apparent  $K_d$  value ( $K_d^{app}$ ) for calcium and magnesium binding, similar to what was done previously for calmodulin (Maune et al., 1992). The dichroic signal (in terms of molar ellipticity per residue (MRE) at  $\Theta = 222$  nm, indicative of typical acquirement of secondary structure, was followed as a function of the concentration of free  $Mg^{2+}$  or  $Ca^{2+}$ . In order to obtain a controlled free ion concentration under well-defined pH and salt conditions, the MaxChelator software (<http://maxchelator.stanford.edu/>) was used. Each titration point represents an independent sample where 0.5  $\mu$ L of a  $Ca^{2+}$  or  $Mg^{2+}$  stock solution at the appropriate concentration was added to the fixed volume (200  $\mu$ L) of 12  $\mu$ M CIB2 aliquots in the presence of 1 mM EGTA. After 3 min incubation at 25°C, three replicas of each spectrum were collected.

## Fluorescence Spectroscopy

Fluorescence spectra were obtained with a Jasco FP750 spectrofluorimeter. The interaction of WT CIB2 with  $\alpha 7B\_M$  and Scrb peptides and that of E64D with  $\alpha 7B\_M$  was studied by monitoring the peptide intrinsic fluorescence. The only Trp residue of both peptides was selectively excited at 295 nm and fluorescence emission was recorded from 300 to 400 nm, setting 5 nm excitation and emission bandwidths. Two scan averaged spectra were recorded.  $\alpha 7B\_M$  (4  $\mu$ M) was titrated with increasing concentrations of WT or E64D CIB2 in 20 mM Hepes, 150 mM KCl, 1 mM DTT pH 7.5 at 37°C in the presence of 1 mM  $Mg^{2+}$  and 1 mM  $Ca^{2+}$ . Titration experiments were performed by monitoring the change (blue-shift) in wavelength ( $\lambda$ ) of the peptide emission peak on the fluorescence spectrum. The apparent equilibrium dissociation constant ( $K_d$ ) was calculated by using the following equation:

$$y = y_0 + ax/(K_d + x) \quad (1)$$

where  $y_0$  is the wavelength of the peptide emission peak in the absence of WT/E64D CIB2,  $a$  is the difference between the maximum and minimum ( $1/\lambda$ )  $\times 10^5$  values of the peptide emission peak as a function of  $x$ , the concentration of CIB2. The intrinsic fluorescence emission of the single Trp of the Scrb peptide (4  $\mu$ M) was measured in the same buffer at 37°C, in the presence of 2, 4, and 8  $\mu$ M WT CIB2.

8-Anilino-naphthalene-1-sulfonic acid (ANS) fluorescence was used to probe the changes in hydrophobicity of WT and E64D CIB2 upon  $Mg^{2+}$  and  $Ca^{2+}$  binding. Two micromolar of WT or E64D CIB2 in 20 mM Hepes pH 7.5, 150 mM KCl, 1 mM DTT, was incubated with 30  $\mu$ M ANS and fluorescence was measured after the addition of 0.5 mM EDTA, 1 mM  $Mg^{2+}$  and 1 mM  $Ca^{2+}$ . ANS fluorescence spectra were recorded at 37°C in the 400–650 nm range after excitation at 380 nm, with 5 nm bandwidths. Three scan averaged spectra were recorded.

## Size Exclusion Chromatography

The molecular weight (MW) of the  $Ca^{2+}$ -free,  $Mg^{2+}$ -bound and  $Mg^{2+}/Ca^{2+}$ -bound states of WT and E64D CIB2 was determined by size exclusion chromatography (SEC) in an

ÅKTA FPLC system using a Superose 12 column (10/300GL, GE Healthcare). Standard proteins for calibration were: carbonic anhydrase (29 kDa), alcohol dehydrogenase (150 kDa),  $\beta$ -amylase (200 kDa), and cytochrome *c* (12.4 kDa). The column was equilibrated with a buffer containing 20 mM Tris pH 7.5, 150 mM KCl, 1 mM DTT with either 3 mM EGTA or 2 mM EGTA + 3 mM  $Mg^{2+}$  or 3 mM  $Mg^{2+}$  + 2 mM  $Ca^{2+}$  added. WT (100  $\mu$ M) or E64D (70  $\mu$ M) CIB2 were incubated with 3 mM EGTA or 2 mM EGTA + 3 mM  $Mg^{2+}$  or 3 mM  $Mg^{2+}$  + 2 mM  $Ca^{2+}$  at 25°C for 5 min before being applied to the column. The protein elution profile was recorded at 280 nm; elution volumes  $V_e$  were determined and the distribution coefficient  $K_d$  was calculated according to the equation:

$$K_d = (V_e - V_0)/(V_t - V_0) \quad (2)$$

in which  $V_t$  is the total column volume and  $V_0$  is the void volume. Molecular weights were determined from a calibration plot of  $\log(MW)$  vs.  $K_d$ .

## Native Page

In order to investigate CIB2 oligomeric state with another approach, the Ferguson plot technique (Ferguson, 1964) was used. Three continuous gels (lacking a stacking phase) under non-denaturing conditions were polymerized at increasing acrylamide concentration (10%, 12%, 15%) using two different BSA concentrations as standards (0.25, 0.41 mgmL<sup>-1</sup>). Twenty micromolar of CIB2 was incubated at room temperature with EGTA (4.5 mM),  $Mg^{2+}$  (3 mM EGTA + 4.5 mM  $Mg^{2+}$ ) or both  $Ca^{2+}$  and  $Mg^{2+}$  (3 mM  $Ca^{2+}$ , 4.5 mM  $Mg^{2+}$ ) in the presence of 1 mM DTT for 20 min. Samples were loaded in each gel and let run as in a normal electrophoresis experiment for 40 min, 200 V at room temperature. Bands were visualized by Coomassie Blue staining. Data analysis was performed as explained in (Ferguson, 1964).

## Dynamic Light Scattering

Dynamic light scattering (DLS) measurements were performed with a Zetasizer Nano-S (Malvern Instruments) and polystyrene low volume disposable sizing cuvettes (ZEN0112) using a general setup optimized previously (Sulmann et al., 2014; Marino et al., 2015a, 2017; Vocke et al., 2017). Viscosity and refractive index were set to 0.6864 cP and 1.33 (default values for water), respectively; the temperature was set to 37°C, with 2 min equilibration time. The measurement angle was 173° backscatter, and the analysis model was set to multiple narrow modes. For each measurement, 12 determinations were performed, each consisting of 14–16 repetitions. DLS measurements were performed on the samples of dimeric WT or E64D CIB2 in 20 mM Tris-HCl pH 7.5, 150 mM KCl, 1 mM DTT with 3 mM EGTA or 2 mM EGTA + 3 mM  $Mg^{2+}$  or 3 mM  $Mg^{2+}$  + 2 mM  $Ca^{2+}$ , immediately after their purification by SEC. Each measurement was run for 5 h. The samples were filtered through an Anotop 10 filter (Whatman, 0.02  $\mu$ m) before each measurement.



## Nuclear Magnetic Resonance Experiments and Data Analysis

NMR spectra were acquired on a Bruker Avance III spectrometer (Bruker, Karlsruhe, Germany) operating at 600.13 MHz proton Larmor frequency, and equipped with a cryogenic probe. The spectra were recorded at 25°C, the samples were at protein concentration of 320  $\mu$ M (unless otherwise specified) in 20 mM Hepes, 100 mM KCl, 1 mM DTT, pH 7.5 and 7% D<sub>2</sub>O.

A standard <sup>1</sup>H-<sup>15</sup>N heteronuclear single-quantum coherence (HSQC) pulse sequence was used, with pulsed field gradients for suppression of the solvent signal and cancellation of artifacts. <sup>1</sup>H-<sup>15</sup>N HSQC spectra were acquired with a data matrix consisting of 2K (F<sub>2</sub>, <sup>1</sup>H)  $\times$  256 (F<sub>1</sub>, <sup>15</sup>N) complex points, spectral windows of 8417.509 Hz (<sup>1</sup>H)  $\times$  2189.44 Hz (<sup>15</sup>N), 8 transients, and 1.5 s relaxation delay.

NMR titration experiments were run on 320  $\mu$ M <sup>15</sup>N-WT CIB2 with Ca<sup>2+</sup> ion added stepwise from a concentrated stock solution. The following protein/ligand ratios were analyzed by <sup>1</sup>H-<sup>15</sup>N HSQC spectra: 1:1, 1:3, 1:5, 1:7, 1:10, 1:15, 1:20. Intensity perturbations were computed as:  $I/I_{max}$ , where  $I$  is the signal intensity at titration step analyzed, and  $I_{max}$  is the maximum signal intensity at the last titration point.

The  $K_d$  values were obtained by fitting the NMR isotherms to a singlestep one-site binding model (Equation 3; **Figures 5D,F**) or to a single step with Hill slope binding model (Equation 4; **Figure 5E**), using GraphPad software according to the following equations:

$$I/I_{max} = ((K_d + [L]_t + [P]_t) - ((K_d + [L]_t + [P]_t)^2 - 4[L]_t[P]_t)^{0.5})/2[P]_t; \quad (3)$$

$$I/I_{max} = B_{max}[L]^h/(K_d^{apph} + [L]^h) \quad (4)$$

where  $I/I_{max}$  is the relative intensity observed at each titration point,  $[P]_t$  and  $[L]_t$  represent the total protein and ligand concentration, respectively,  $[L]$  is approximated by  $[L]_t$  and  $K_d$  is the dissociation constant of the complex.

For Equation (4)  $K_d^{app}$  is the apparent equilibrium dissociation constant,  $h$  is the Hill slope, and  $B_{max}$  is the maximum intensity observable. All data were processed and analyzed using TOPSPIN 3.2 (Bruker, Karlsruhe, Germany) and CARA software.

## Building of WT CIB2 Homology Model

The homology model of WT CIB2 monomer was built using the MODWEB-MODBASE server version r189 (Pieper et al., 2014). Briefly, 4 out of 189 structural models were selected based on the MPQS, TSVMOD, LONGEST\_DOPE and DOPE criteria. The most reliable model, covering the 13–187 region of the full protein sequence, was built based on the X-ray structure of human CIB1 [PDB entry: 1XO5 (Gentry et al., 2005) chain A], which shares 39% sequence identity with CIB2. Ca<sup>2+</sup> ions were manually positioned in EF3 and EF4 binding sites based on the experimental coordinates of the Ca<sup>2+</sup>-loaded CIB1 structure (1XO5.pdb) (Gentry et al., 2005). The structure was energy-minimized in two steps, first with the steepest descent and then with the conjugate gradients algorithm, keeping in both cases

the position of the backbone atoms restricted, according to a previous protocol used for other Ca<sup>2+</sup> sensor proteins (Marino et al., 2015b; Marino and Dell'Orco, 2016).

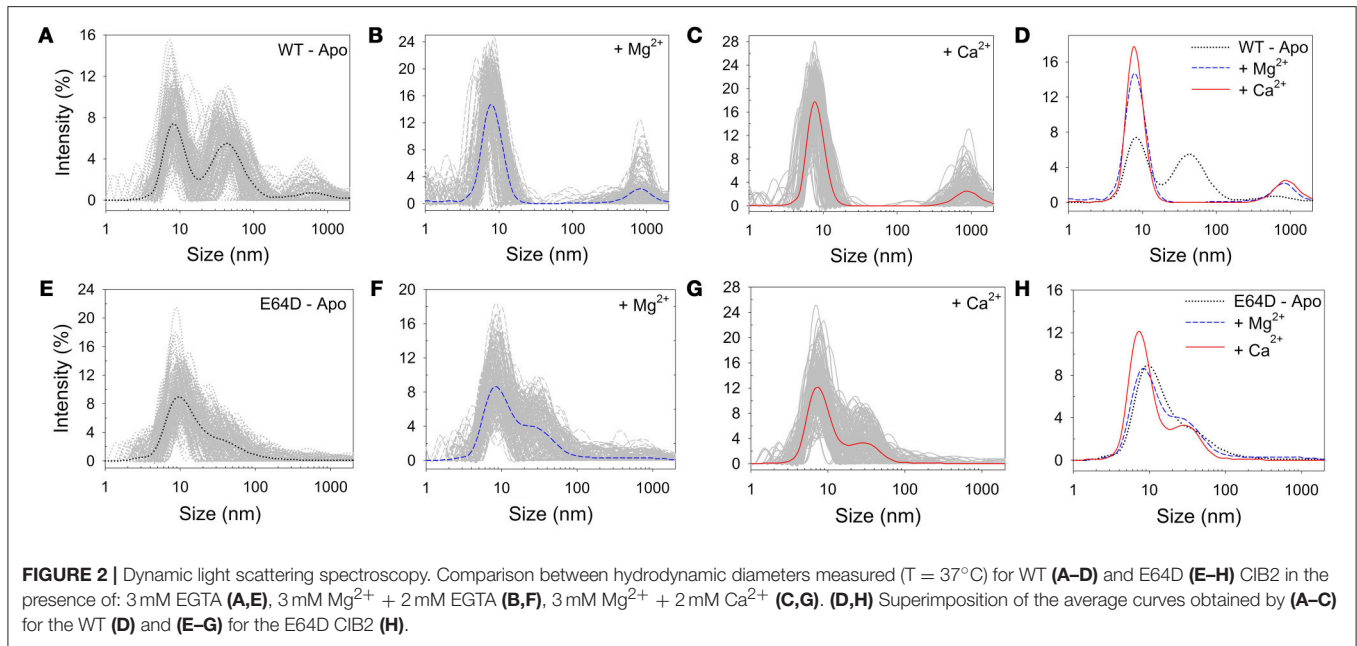
## RESULTS

### Wild-Type and E64D CIB2 Form Non-covalent Dimers With Different Colloidal Properties

We investigated the oligomeric state of both WT and E64D CIB2 by three different approaches, namely PolyAcrylamide Gel Electrophoresis under non-denaturing conditions (native-PAGE), analytical SEC and DLS. **Figure S1a** shows that, under denaturing conditions (SDS-PAGE), the electrophoretic mobility of CIB2 is compatible with that of a 21.6 kDa protein, although the band is shifted to a slightly higher molecular weight, as previously observed in other studies (Blazejczyk et al., 2009; Huang et al., 2012). Gels obtained under non-denaturing conditions show that in the presence of a reducing agent (1 mM DTT) both apo (lane 2) and Ca<sup>2+</sup>-bound (lane 4) CIB2 run as single bands (**Figure S1b**). However, multiple bands were observed in the absence of DTT independent of the presence of Ca<sup>2+</sup> (lanes 1 and 3). This is compatible with the formation of covalent oligomers due to disulfide bridges resulting from the oxidation of thiol groups in either of the four Cys residues.

In order to investigate the nature of the single bands observed in the native-PAGE experiments, we performed analytical SEC of both WT and E64D CIB2 in the apo form as well as in the presence of Mg<sup>2+</sup> and Ca<sup>2+</sup>/Mg<sup>2+</sup> and determined the molecular weight (MW) by using a calibration curve shown in **Figure S2**. As previously observed for other Ca<sup>2+</sup>/Mg<sup>2+</sup> sensor proteins (Sulmann et al., 2014; Marino et al., 2015a; Astegno et al., 2016, 2017; Vallone et al., 2016) the elution profile was sensitive to the metal ion loading state (**Figure S2**) and resulted in an apparent lower MW for the Ca<sup>2+</sup>/Mg<sup>2+</sup> bound form of CIB2 compared to the apo-form (**Table S1**). Under reducing conditions, the elution profiles for both WT and E64D CIB2 variants in the Ca<sup>2+</sup>/Mg<sup>2+</sup> form (MW = 37–39 kDa, **Table S1**) were compatible with a dimer and incompatible with a monomer (MW ~22 kDa). The dimeric nature of CIB2 under all the tested conditions was further confirmed by Ferguson plots, which estimated a MW in the 51–53 kDa range for both WT and E64D variants independent on the cation loading state (**Table S1**).

Samples from SEC experiments were further analyzed by DLS immediately after elution. Results are reported in **Figure 2**. The DLS intensity profile of WT CIB2 in the absence of Ca<sup>2+</sup> and Mg<sup>2+</sup> showed multiple peaks and a generally high polydispersity (**Figure 2A**), with two not-well separated prevailing peaks. However, the addition of Mg<sup>2+</sup> (**Figure 2B**) or Ca<sup>2+</sup> (**Figure 2C**) led to a general improvement of the colloidal properties and a single prominent peak was distinguished in both cases, which allowed the determination of the hydrodynamic diameter ( $d^{Mg} = 8.43 \pm 0.12$  nm and  $d^{Ca} = 8.18 \pm 0.01$  nm, respectively; see **Figure 2D**). The E64D CIB2 variant instead showed less satisfactory colloidal properties, as under no tested condition, apo (**Figure 2E**), Mg<sup>2+</sup> (**Figure 2F**), or Ca<sup>2+</sup> (**Figure 2G**) could



a single, prevailing peak be observed in the intensity profile. The constant presence of higher-size aggregates and the overlapping of peaks (Figure 2H) prevented an estimate of the hydrodynamic diameter to be made for this CIB2 variant.

The differences observed in the DLS profiles of WT and E64D CIB2 under the tested conditions prompted us to analyze the time-dependent properties of the dispersions. The mean count rate (MCR) of the samples, which can be indicative of time-dependent protein aggregation, was thus followed over time for 5 h (Figure S3). Interestingly, for WT CIB2 (Figure S3a) no trend was observed under the investigated conditions, but significant fluctuations in the MCR were observed especially in the apo conditions (150–600 kcps), in line with a partly reversible protein aggregation process. Less prominent but still significant MCR fluctuations were observed in the presence of  $\text{Ca}^{2+}$  or  $\text{Mg}^{2+}$  (150–300 kcps). A somewhat different pattern was detected for E64D CIB2 (Figure S3b). Both in apo conditions and in the presence of  $\text{Ca}^{2+}$  and  $\text{Mg}^{2+}$  a slow, constantly increasing trend in MCR was observed. In the sole presence of  $\text{Mg}^{2+}$ , significantly broad fluctuations of MCR (150–400 kcps) were detected, which also showed a slowly increasing trend.

### Apo, $\text{Mg}^{2+}$ - and $\text{Ca}^{2+}$ -Loaded WT and E64D CIB2 Show Different Levels of Folding

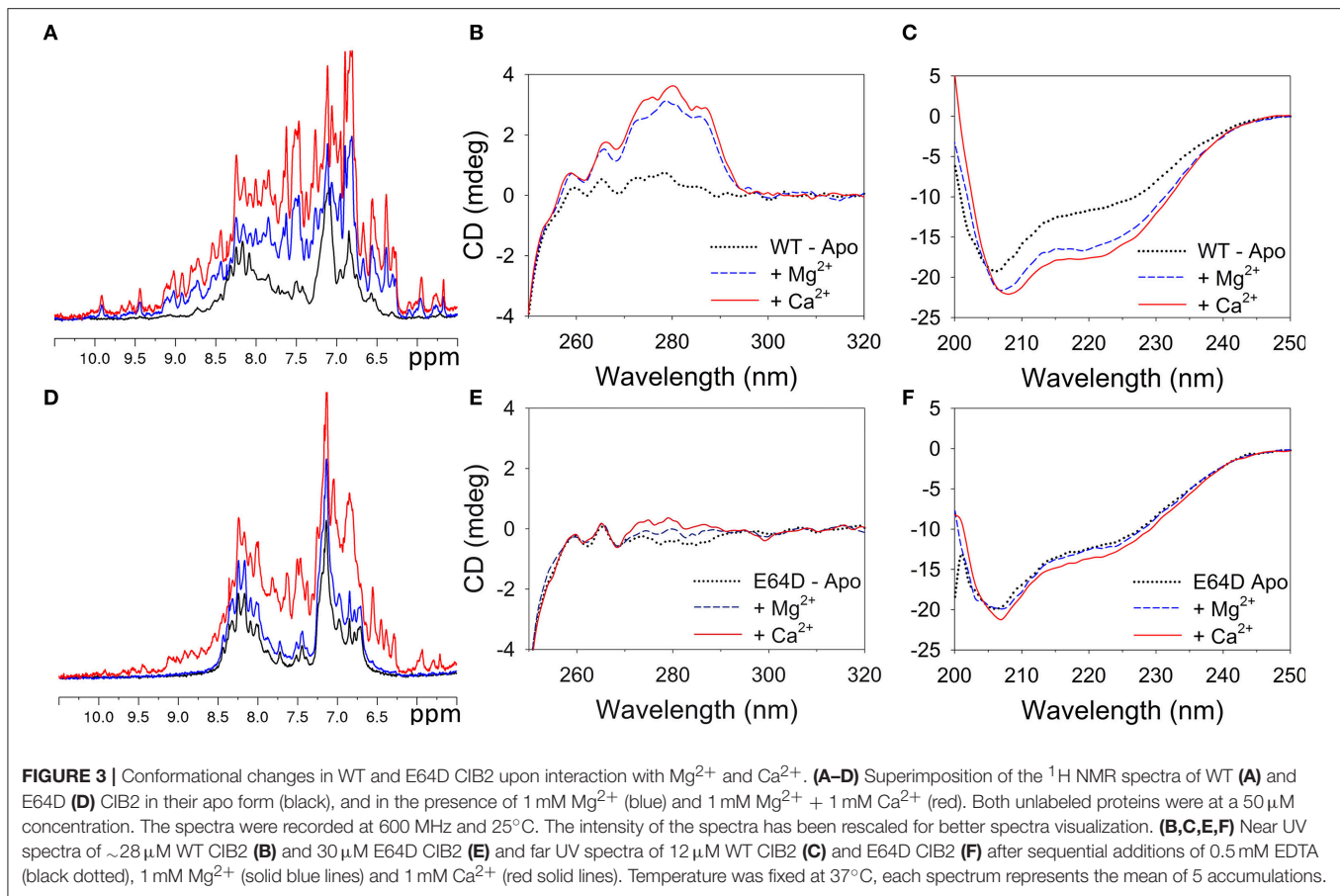
One-dimensional (1D)  $^1\text{H}$  NMR spectroscopy and far/near UV CD spectroscopy were used to monitor the folding state of WT and E64D CIB2 under different conditions (Figure 3).

1D  $^1\text{H}$  NMR spectroscopy is a fast and powerful technique that can provide information on the global fold of a protein. In 1D  $^1\text{H}$  NMR spectra, the signal dispersion in the regions of the amide (6–10 ppm), and methyl (–0.5 to 1.5 ppm) protons provides indications on the folded globular state of the proteins.

Moreover calcium binding proteins show typical downfield-shifted NMR peaks at  $\sim 10.5$  ppm belonging to residues of the EF-hands upon binding of divalent metals (Huang et al., 2012). The 1D  $^1\text{H}$  NMR spectrum of WT CIB2 in the absence of metal ions displayed evidence of chemical shift dispersion but also line broadening in the amide region (Figure 3A, black line). Addition of 1 mM  $\text{Mg}^{2+}$  promoted a large change in the WT CIB2 spectrum (Figure 3A, blue line); the signals appeared more disperse and sharp indicating the ability of the protein to assume a globular folded structure upon binding of the metal cation. Further addition of 1 mM  $\text{Ca}^{2+}$  (Figure 3A, red line) caused slight changes in the 1D  $^1\text{H}$  NMR spectrum, indicating a low degree of structural rearrangement upon binding of the second ion.

The NMR data recorded on samples of E64D CIB2 drive to different conclusions. The 1D  $^1\text{H}$  NMR spectrum of the E64D CIB2 in the absence of metal ions displayed narrow signal dispersion throughout the spectrum and especially in the region of amide protons (Figure 3D, black line). The addition of 1 mM  $\text{Mg}^{2+}$  (Figure 3D, blue line) did not promote changes in the NMR spectrum clearly indicating the inability of the E64D CIB2 to bind  $\text{Mg}^{2+}$ . Upon subsequent addition of  $\text{Ca}^{2+}$  the NMR signals appeared more disperse as a consequence of the binding of the metal ion, however the 1D spectrum suggests that the protein still retains a certain degree of flexibility and it is not characterized by a rigid tertiary structure (Figure 3D, red line).

Near UV (250–320 nm) CD spectroscopy provides information as to the microenvironment of the aromatic amino acids Phe, Tyr, and Trp, which contribute to the stabilization of protein tertiary structure. CIB2 lacks Trp, therefore near UV CD spectra represent a fingerprint of the possible variations in tertiary structure in the Tyr (5 residues) and Phe (16 residues) microenvironments upon metal cation binding. Monitoring the CD signal in the far UV region (200–250 nm) provides instead information as to



variations of the protein secondary structure. The near UV CD spectrum of WT CIB2 in the absence of metal cations was almost flat (**Figure 3B**, black dotted line), nevertheless some helical content was clearly observed in the far UV region (**Figure 3C**), thus suggesting that apo CIB2 forms a molten globule state, in line with NMR findings. Addition of 1 mM  $Mg^{2+}$  led to a significant response both in the Phe and Tyr bands (**Figure 3B**, blue dashed line) and to a remarkable increase in the helical content as observed in the far UV region (**Figure 3C**). Notably, upon addition of physiological concentrations of  $Mg^{2+}$  the far UV spectrum acquired the typical  $\alpha$ -helix minima at 208 and 222 nm, while the first minimum was shifted to 206 nm in the apo form (black dotted line). Further addition of 1 mM  $Ca^{2+}$  refined the near UV CD spectrum especially in the Tyr region (**Figure 3B**, solid red line) and further increased the intensity of the far UV spectrum (**Figure 3C**).

The behavior of E64D CIB2 was substantially different. When exposed to the same  $Mg^{2+}$  and  $Ca^{2+}$  conditions, E64D CIB2 showed only minor variations in the near UV region, in line with a substantial conservation of the molten globule conformation independent of the metal cation (**Figure 3E**). Only a slight response to  $Ca^{2+}$  was observed in the far UV region (**Figure 3F**), however the first minimum at 206 nm did not shift to 208 nm upon addition of  $Mg^{2+}$  or  $Ca^{2+}$ , at odds with the WT variant.

## Hydrophobicity and Thermal Denaturation Profiles of WT and E64D CIB2

In their apo form, both WT and E64D CIB2 present a partially folded, molten globule conformation, thus suggesting a significant solvent-exposition of hydrophobic patches. We investigated the surface hydrophobicity of CIB2 by using the fluorescent probe ANS, whose fluorescent properties will change as it binds to hydrophobic regions on the protein surface. Results are shown in **Figure S4**. Both ANS fluorescence spectra of WT and E64D CIB2 highlight a significant hydrophobicity of the protein surface under all the tested conditions, as clearly displayed by the remarkable blue-shift of the fluorescence emission maximum (27 nm for WT CIB2, 31 nm for E64D CIB2, in the apo state, **Table S2**) and the relative increase in fluorescence intensity as compared to the emission of ANS alone (2.6- to 2.8-fold, in the apo state, **Table S2**). Addition of 1 mM  $Mg^{2+}$  or 1 mM  $Ca^{2+}$  slightly reduced the blue-shift (1–2 nm, depending on the CIB2 variant, **Table S2**), however the change in relative fluorescence ( $F^{max}/F^{ref}$ ) was higher for WT (2.1–2.2 vs. 2.6) than for E64D CIB2 (2.5–2.6 vs. 2.8). Overall, fluorescence data confirm that both WT and E64D CIB2 are highly hydrophobic and the pathogenic variant maintains higher hydrophobicity in the presence of  $Mg^{2+}$  or  $Ca^{2+}$  compared to the WT.

The thermal stability of WT and E64D CIB2 in the 4–70°C range was investigated by monitoring the dichroic signal at

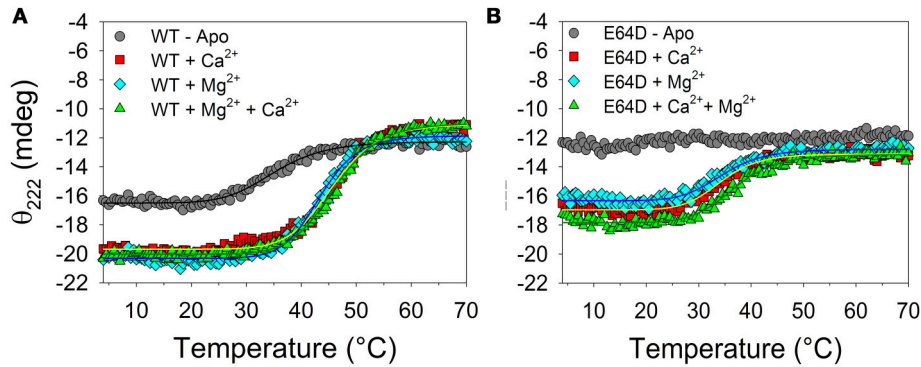


**FIGURE 4 |** Thermal denaturation of WT and E64D CIB2. Thermal denaturation profiles were recorded between 4 and 70°C with 12  $\mu$ M WT CIB2 **(A)** and E64D CIB2 **(B)** in the presence of 0.5 mM EDTA (gray circles), 1 mM  $\text{Ca}^{2+}$  (red squares), 1 mM  $\text{Mg}^{2+}$  (light blue diamonds) and 1 mM  $\text{Ca}^{2+}$  + 1 mM  $\text{Mg}^{2+}$  (green triangles). Data fitting was performed using a Hill 4 parameter function, results are shown by solid lines and parameters are reported in **Table S2**.

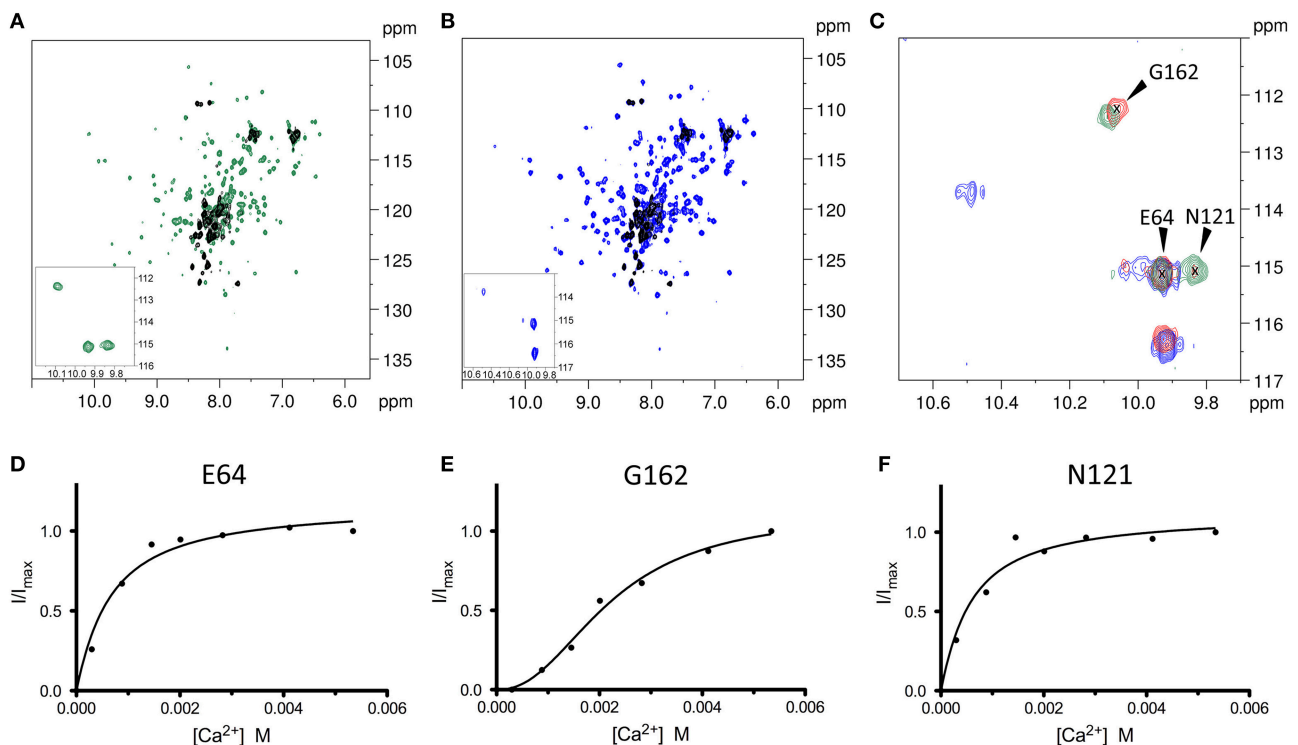


**FIGURE 5 |**  $^1\text{H}$ - $^{15}\text{N}$  HSQC NMR spectra of WT CIB2 in its apo form and in the presence of  $\text{Mg}^{2+}$  and  $\text{Ca}^{2+}$  highlight an allosteric communication between E64 and N121. **(A)** Superimposition of the two-dimensional  $^1\text{H}$ - $^{15}\text{N}$  HSQC NMR spectra of the apo- (black), and  $\text{Ca}^{2+}$ -bound (green)  $^{15}\text{N}$ -WT CIB2. **(B)** Superimposition of the HSQC spectra of apo (black), and  $\text{Mg}^{2+}$ -bound (blue)  $^{15}\text{N}$ -WT CIB2. In the insets, zoom of the HSQC spectra of the downfield peaks of the metal-bound forms of  $^{15}\text{N}$ -WT CIB2. Metal ions were present at a protein:metal ratio of 1:15. **(C)** Superimposition of downfield region of the  $^1\text{H}$ - $^{15}\text{N}$  HSQC NMR spectra recorded on  $^{15}\text{N}$ -WT CIB2 containing 15 equivalents of  $\text{Mg}^{2+}$  (blue), 15 eq  $\text{Mg}^{2+}$  + 15 eq  $\text{Ca}^{2+}$  (red), and 15 eq  $\text{Ca}^{2+}$  (green). **(D–F)** Variation of  $^1\text{H}$ - $^{15}\text{N}$  HSQC peak intensities of WT CIB2 as a function of  $\text{Ca}^{2+}$  concentration. The peak intensities were normalized with respect to the maximum value. The continuous lines represent the data fitted against equations as indicated in section Materials and Methods. The plots refer to the amide peaks of residues E64 **(D)**, G162 **(E)**, and N121 **(F)**. All the spectra were recorded at 600 MHz and 25°C. All samples were at protein concentration of 320  $\mu$ M in 20 mM Hepes, 100 mM KCl, 1 mM DTT, pH 7.5.

222 nm, where a minimum was observed in the far UV CD spectrum (**Figure 3**). Thermal denaturation profiles are reported in **Figure 4**. Apo WT CIB2 was found to be rather unstable, having a melting temperature of 35.1°C (**Table S2**). Addition of

$\text{Mg}^{2+}$  increased the thermal stability of  $\sim 11^\circ\text{C}$ , and a similar effect was observed for addition of 1 mM  $\text{Ca}^{2+}$ , although the stabilization was lower ( $\sim 8^\circ\text{C}$ ). In the presence of both cations the thermal stability resembled that of  $\text{Mg}^{2+}$  ( $T_m = 45.9^\circ\text{C}$ ,

**Table S2).** The transition was faster in the metal-bound states compared to the apo-state ( $H_c = 11\text{--}12.5$  vs.  $7.5$ , **Table S2**). The persistent CD signal at  $222\text{ nm}$  (**Figure 4A**) suggests that the transition ended in a still partially folded structure, independent of the presence of  $Mg^{2+}$  or  $Ca^{2+}$ . Interestingly, the thermal profile of apo E64D CIB2 was unperturbed in the scanned range of temperature, as no transition was observed (**Figure 4B**). Addition of  $Mg^{2+}$  resulted in a  $T_m$ -value  $\sim 11.5^\circ\text{C}$  lower than that of WT CIB2, and a very similar effect was observed after the addition of  $1\text{ mM}$   $Ca^{2+}$  (**Table S2**). Only the co-presence of both cations slightly increased the thermal stability of E64D CIB2, which however was  $\sim 9^\circ\text{C}$  lower than the respective WT case (**Table S2**). All the transitions observed for E64D CIB2 were significantly slower compared to the respective cases in WT CIB2 (compare the  $H_c$  values, **Table S2**).

### Mg<sup>2+</sup> and Ca<sup>2+</sup> Binding to WT CIB2 Explored by NMR Spectroscopy Reveals an Inter-domain Allosteric Switch

Two-dimensional  $^1\text{H}$ - $^{15}\text{N}$  HSQC NMR spectra are often employed to investigate protein structural changes. The NMR chemical shift of the signals belonging to all HN groups of the protein is a sensitive reporter of the local and global structure rearrangements occurring upon ligand binding events. The NMR signals of the  $^1\text{H}$ - $^{15}\text{N}$  HSQC spectrum of the apo  $^{15}\text{N}$  WT CIB2 were broad and poorly dispersed in line with the previous observation that apo CIB2 forms a molten globule state.

In line with previously reported data (Huang et al., 2012), the  $^1\text{H}$ - $^{15}\text{N}$  HSQC spectrum changed dramatically upon addition of either  $Ca^{2+}$  or  $Mg^{2+}$  ions; the NMR signals became more disperse and sharp and new downfield peaks appeared, indicative of metal binding (**Figures 5A–C**).

In order to investigate at a deeper level the structural mechanisms associated with  $Ca^{2+}$  binding, NMR titration experiments of  $Ca^{2+}$  into  $^{15}\text{N}$ -WT CIB2 have been performed collecting a series of  $^1\text{H}$ - $^{15}\text{N}$  HSQC spectra. Notably, the variation of the intensity of the peaks belonging to residues E64, which belongs to the kinked H3b helix in the non-functional EF1 motif and N121 of EF3 loop appeared to be correlated (**Figures 5D,F**), thus indicating that these amino acid residues belong to the same allosteric network. The NMR titration data were fitted assuming a simple one-site binding model which better describes a hyperbolic shape of the curve and  $K_d$  values of  $0.55 \pm 0.13$  and  $0.48 \pm 0.15\text{ mM}$  were obtained for E64 and N121, respectively.

Moreover, we were able to follow the peculiar behavior of the G162 belonging to the EF4 loop, upon addition of increasing amount of  $Ca^{2+}$  (**Figure 5E**). Interestingly, the intensity variation upon addition of  $Ca^{2+}$  had a sigmoidal shape, indicative of positive cooperativity of the binding mechanism. From the fitting of the data a  $K_d^{\text{app}}$  value of  $2.22 \pm 0.25\text{ mM}$  and a Hill coefficient  $h = 2.27 \pm 0.38$  were obtained. The data of the two sites with different affinities for the  $Ca^{2+}$  ion are consistent with the analysis of the  $^1\text{H}$ - $^{15}\text{N}$  HSQC spectra of the protein in the early steps of titration (data not shown). When only the peaks of E64 and N121 are visible, the protein already adopts a well-folded

structure, further addition of  $Ca^{2+}$  promotes only small changes in the spectrum, thus confirming that the binding of  $Ca^{2+}$  into the first site triggers the structural rearrangement of WT CIB2.

NMR spectroscopy was also employed to investigate whether WT CIB2 had a preferential binding capability toward  $Ca^{2+}$  or  $Mg^{2+}$ . To this aim we recorded a  $^1\text{H}$ - $^{15}\text{N}$  HSQC spectrum of  $^{15}\text{N}$ -WT CIB2 after addition of a solution containing equal concentration of the two cations (**Figure 5C**) and we analyzed the downfield peaks as indicators of the binding site occupancy. Interestingly, WT CIB2 displayed a preferential binding site for  $Mg^{2+}$  in the EF3 loop and for  $Ca^{2+}$  in the EF4 loop. This observation was confirmed by analyzing the  $^1\text{H}$ - $^{15}\text{N}$  HSQC spectra of the protein in the presence of different ratios of  $Ca^{2+}$  or  $Mg^{2+}$  (**Figure S5**). As expected, when  $Mg^{2+}$  was in excess we could observe the peak of N121 at the chemical shift of the  $Mg^{2+}$  bound form, and the peak of G162, although with low intensity, as a reporter of  $Ca^{2+}$  bound to the EF4 loop. Notably, when  $Ca^{2+}$  was in excess the protein still retained its capability to bind  $Mg^{2+}$  in EF3 and we could still observe the peak of N121, typical of the  $Mg^{2+}$  bound form, while EF4 became occupied by  $Ca^{2+}$ .

### The Affinity of WT and E64D CIB2 for Ca<sup>2+</sup> Is Incompatible With a Role as a Physiological Ca<sup>2+</sup> Sensor

NMR experiments suggest that the affinity of WT CIB2 for  $Ca^{2+}$  is in the submillimolar range. We sought to quantify the affinity for  $Ca^{2+}$  and  $Mg^{2+}$  of both WT and E64D CIB2 in a comparative fashion in order to assess the potential role of CIB2 as a sensor protein under physiological and USH1J-related conditions. Titration experiments were performed by monitoring the CD signal at  $222\text{ nm}$ , under very carefully determined pH and free cation ( $Ca^{2+}$  or  $Mg^{2+}$ ) conditions spanning over their known physiological range. Although the method does not allow attributing the macroscopic association constant to each individual EF-hand, it provides an estimate of the cation concentration at which the conformational change, starting from the apo-state, is half maximal ( $K_d^{\text{app}}$ ). Therefore, it is a useful approach for comparisons of the two CIB2 variants over a physiological range of cation stimuli. Results are reported in **Figure 6** and **Table 1**.

In line with the data from NMR titrations, the measured apparent affinity for  $Ca^{2+}$  of both WT ( $500\text{ }\mu\text{M}$ ) and E64D ( $2\text{ mM}$ ) CIB2 was extremely low, thus excluding a possible role of CIB2 as a  $Ca^{2+}$  sensor under physiological conditions (see the section Discussion for further details). An alternative well-established spectroscopic method based on the competition with the chromophoric chelator  $5,5'$ -Br<sub>2</sub>-BAPTA was applied for WT CIB2, but it failed to detect any individual macroscopic binding constant in the low  $\mu\text{M}$  range (results not shown), thus confirming the overall low affinity for  $Ca^{2+}$ . Interestingly, WT CIB2 showed a relatively high affinity for  $Mg^{2+}$  ( $290\text{ }\mu\text{M}$ ), compatible with a fully loaded state under physiological conditions. On the contrary, E64D CIB2 is likely incapable of detecting  $Mg^{2+}$  under physiological conditions due to the low affinity ( $K_d^{\text{app}} = 1.5\text{ mM}$ ).

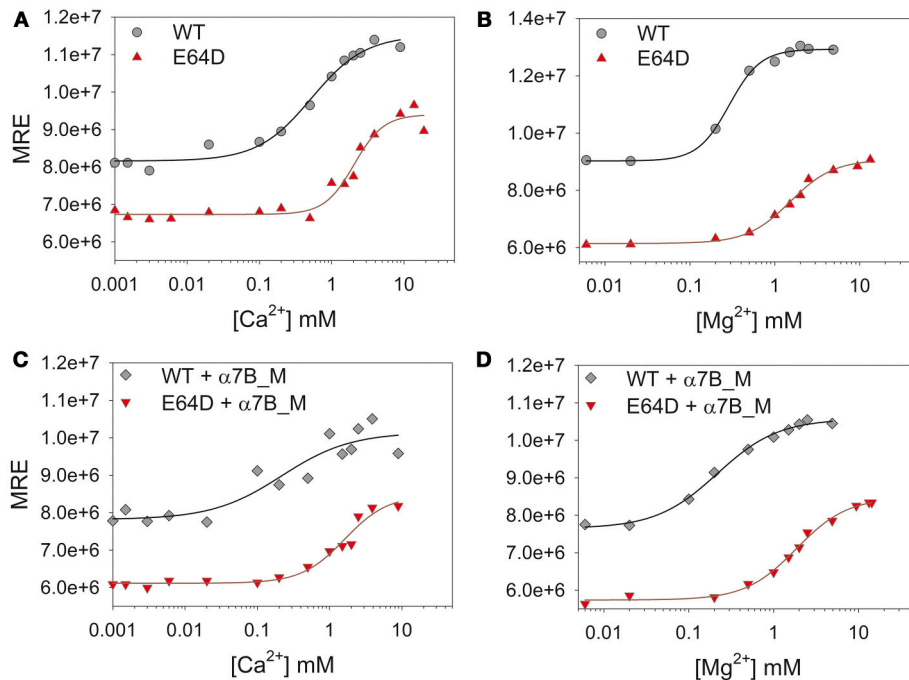


**FIGURE 6** |  $\text{Ca}^{2+}$  and  $\text{Mg}^{2+}$  titrations of CIB2 in the presence or in the absence of target peptide  $\alpha 7\text{B\_M}$ . **(A,B)** WT (circles) and E64D (triangles) CIB2 were titrated with  $\text{Ca}^{2+}$  **(A)** and  $\text{Mg}^{2+}$  **(B)** starting from the apo-form (1 mM free EGTA). **(C,D)**  $\text{Ca}^{2+}$  **(C)** and  $\text{Mg}^{2+}$  **(D)** titrations of WT (diamonds) and E64D (downwards triangles) CIB2 in the presence of  $\alpha 7\text{B\_M}$  peptide. Ions concentration ranged between 1  $\mu\text{M}$  and 10 mM, the obtained data were fitted using the Hill 4 parameters function. Data were normalized on protein concentration (MRE). Titrations were performed at 25°C, each point represents the mean of 3 accumulations.

All the titration curves could be fitted to a Hill sigmoid function (**Figure 6**), thus suggesting in some cases a cooperative effect of the cation binding on the structural transition. Interestingly, while  $\text{Ca}^{2+}$  binding to WT CIB2 was substantially non-cooperative ( $H_c = 1.1$ , **Table 1**), binding of  $\text{Mg}^{2+}$  showed evidence of positive cooperativity ( $H_c = 2.3$ , **Table 1**). As for E64D CIB2, data suggest positive cooperativity both in the case of  $\text{Mg}^{2+}$  ( $H_c = 1.7$ , **Table 1**) and  $\text{Ca}^{2+}$  binding ( $H_c = 2.2$ , **Table 1**).

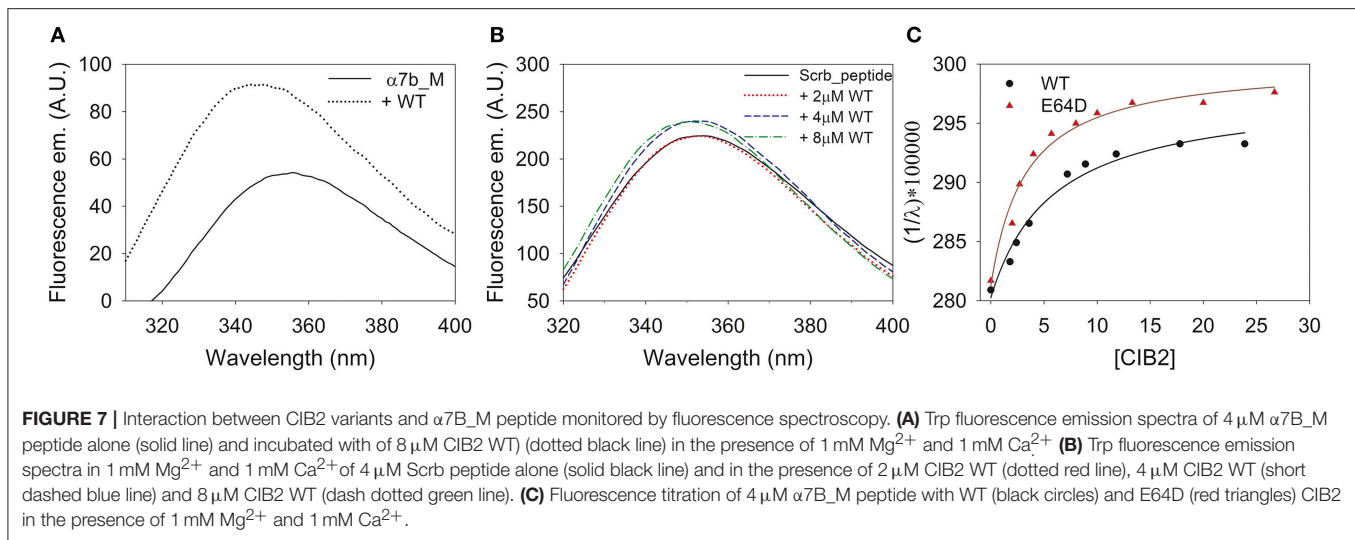
The fact that we detected for E64D CIB2 a significantly low affinity for both  $\text{Ca}^{2+}$  and  $\text{Mg}^{2+}$  (**Table 1**) made us wonder if higher concentration of cations could trigger a WT-like conformation. Near UV-CD spectra were thus recorded following sequential additions of increasing  $\text{Ca}^{2+}$  or  $\text{Mg}^{2+}$  (**Figure S6**). In line with the results from far UV-CD spectroscopy and titration experiments, our data show that at a  $\text{Ca}^{2+}$  concentration up to 5 mM E64D CIB2 did not switch to a WT-like three-dimensional conformation; however, at 10 mM  $\text{Ca}^{2+}$  the near UV spectra became similar (compare **Figure S6a** with **Figure 3B**). Interestingly, the same finding did not apply to  $\text{Mg}^{2+}$ . Even at 10 mM  $\text{Mg}^{2+}$  the near UV CD spectrum did not reach the shape and the intensity observed for the WT case (compare **Figure S6b** with **Figure 3E**). Therefore, our data are overall consistent with the inability of E64D CIB2 to sense  $\text{Mg}^{2+}$  under physiological conditions, and even under conditions that exceed the intracellular levels.

**TABLE 1** | Apparent affinity for  $\text{Ca}^{2+}$  and  $\text{Mg}^{2+}$  of WT and E64D CIB2 assessed by CD titrations.

	$\text{Mg}^{2+}$		$\text{Ca}^{2+}$	
	$K_d^{\text{app}}$ (mM)	$H_c$	$K_d^{\text{app}}$ (mM)	$H_c$
<b>WT CIB2</b>	$0.29 \pm 0.02$	$2.3 \pm 0.3$	$0.5 \pm 0.1$	$1.1 \pm 0.3$
<b>WT + <math>\alpha 7\text{B\_M}</math></b>	$0.49 \pm 0.03$	$1.4 \pm 0.1$	$0.2 \pm 0.2$	$0.9 \pm 0.6$
<b>E64D CIB2</b>	$1.5 \pm 0.1$	$1.7 \pm 0.2$	$2.0 \pm 0.2$	$2.2 \pm 0.6$
<b>E64D + <math>\alpha 7\text{B\_M}</math></b>	$1.8 \pm 0.2$	$1.4 \pm 0.2$	$1.5 \pm 0.3$	$1.4 \pm 0.3$

### $\alpha 7\text{B}$ Integrin Is a Specific Target of Both WT and E64D CIB2

We asked whether E64D CIB2 was still capable of interacting with specific targets of WT CIB2. Based on the results of previous work (Huang et al., 2012), we focused on a peptide ( $\alpha 7\text{B\_M}$ ) covering the membrane-proximal CIB2-specific sequence of recognition of the integrin  $\alpha 7\text{B}$  cytosolic domain. As a negative control, we generated a scrambled peptide (Scrb) by shuffling the  $\alpha 7\text{B\_M}$  sequence, thus conserving general physicochemical properties such as net charge and hydrophilicity while losing biological specificity. Both peptides have a single Trp residue, which allowed us to exploit their fluorescence for studying the interaction with both WT and E64D CIB2, which lack Trp residues (see section Materials and Methods). Results from fluorescence experiments are reported in **Figure 7**.



The interaction between WT CIB2 and the  $\alpha 7B\_M$  peptide was apparent, as assessed from the 1.7-fold increase in the maximal fluorescence emission and the 12 nm blueshift (Figure 7A) indicative of an augmented hydrophobicity of the peptide Trp residue upon interaction with the protein. On the contrary, no significant change in either the fluorescence emission intensity and the relative maximum wavelength was observed when the experiments were performed with the ScrB peptide, even when the concentration of WT CIB2 was brought up to  $8 \mu M$ , thus indicating the lack of specific binding (Figure 7B). Similar results were obtained for the E64D CIB2 variant (results not shown).

Titration experiments were performed to estimate the stoichiometry of interaction between WT/E64D CIB2 and  $\alpha 7B\_M$  peptide and to assess the apparent affinity. Results are reported in Figure 7C. The curves showed that both WT and E64D CIB2 interact with the target peptide with a 2:1 stoichiometry, that is, a CIB2 dimer binds a single peptide. The estimated affinities are similar ( $K_d^{app} = 4.99 \pm 1.01 \mu M$  for WT CIB2;  $K_d^{app} = 3.1 \pm 0.2 \mu M$  for E64D CIB2; mean  $\pm$  s.d. of 4 and 3 repetitions, respectively), therefore the USH1J-related variant is still capable of binding the  $\alpha 7B\_M$  target peptide, with even higher affinity compared to the WT case.

In order to assess if the binding of the target peptide could influence the sensing of  $Ca^{2+}$  or  $Mg^{2+}$  and the protein conformation, far UV CD spectra were recorded and titration experiments performed in the same conditions as with the protein alone. Figure S7 clearly shows that the peptide does not possess any secondary structure and that its incubation with WT CIB2 led to the same spectral properties observed in response to additions of  $Ca^{2+}$  for the protein alone (compare with Figure 3C). Therefore, we conclude that the interaction with the  $\alpha 7B\_M$  peptide does not induce any appreciable structural change in WT CIB2. Moreover, the interaction with the  $\alpha 7B\_M$  peptide had a relatively small effect on the  $Ca^{2+}$  or  $Mg^{2+}$  sensing abilities of CIB2. While a 1.6-fold increase in the  $K_d^{app}$  was observed for  $Mg^{2+}$  binding to WT CIB2 (Table 1 and Figure 6),

a slightly increased affinity for  $Ca^{2+}$  was detected, although the  $K_d^{app}$  was still quite high for physiological relevance ( $0.2 \text{ mM}$ , Table 1). Minor differences were observed in the variation of  $K_d^{app}$  in the presence of  $\alpha 7B\_M$  peptide for E64D CIB2 (1.2-fold increase for  $Mg^{2+}$  and 1.2-fold decrease for  $Ca^{2+}$ ; Figure 6 and Table 1).

## DISCUSSION

The ubiquitous expression of CIB2 in various tissues suggests that it may exert yet unknown biological functions in a broad range of biochemical processes. Besides being involved in hearing physiology and pathology (Riazuddin et al., 2012; Jan, 2013; Patel et al., 2015; Seco et al., 2016; Wang et al., 2017), CIB2 has been indeed found to play a role in congenital muscular dystrophy type 1A (Häger et al., 2008), in the N-methyl-D-aspartate receptor-mediated  $Ca^{2+}$  signaling in cultured hippocampal neurons (Blazejczyk et al., 2009), in the promotion of HIV-viral infection (Godinho-Santos et al., 2016), and very recently it was found to act as a negative regulator of sphingosine kinase 1-mediated oncogenic signaling in ovarian cancer (Zhu et al., 2017). Available mechanistic studies focusing on the  $Ca^{2+}$  and  $Mg^{2+}$  sensing properties of CIB2 are just a few, and a comprehensive characterization of the protein in comparison to its disease-associated variants was missing. Indeed, so far much of the molecular interpretation of the processes in which CIB2 is involved has been based on the significantly better explored structure-function properties of the homologous protein CIB1 (Leisner et al., 2016), although the relatively low sequence identity and similarity call for particular caution when inferring common functions for the two proteins.

In this work, we present a thorough characterization of two variants of human CIB2, namely the WT form and the E64D mutant associated with USH1J. It should be reported that a recent study disqualified CIB2 as a USH1J-related gene, however the E64D variant was found to be associated with autosomal recessive non-syndromic hearing loss (Booth et al., 2018). Our biochemical

and biophysical study highlights a number of clear structural and functional differences with CIB1, which may thus pose the molecular basis for understanding the malfunctioning of CIB2 in USH1J and possibly other genetic diseases causing hearing loss.

While the general topology of CIB2 is similar to that of CIB1 (**Figure 1**), a first clear difference between CIB1 and CIB2 resides in their oligomeric states. While analytical SEC experiments performed with CIB1 detected a monomeric protein independently on the presence of  $\text{Ca}^{2+}$  and target peptide (Gentry et al., 2005), our SEC data, electrophoresis experiments under non-denaturing conditions (**Figure S2** and **Table S1**) and DLS experiments (**Figure 2**) all converge to CIB2 forming non-covalent dimers both in the apo and in  $\text{Ca}^{2+}/\text{Mg}^{2+}$ -bound conditions. The oligomeric state of CIB2 is particularly relevant for its interaction with biological targets. Although we cannot exclude different situations with different targets, fluorescence titration experiments (**Figure 7**) point to a 1:1 stoichiometry for a CIB2 dimer: $\alpha 7\text{B}_M$  peptide complex, at odds with the results observed for CIB1: $\alpha\text{IIB}$  peptide complex, where the 1:1 stoichiometry involved a monomeric protein (Gentry et al., 2005).

The stability of the oligomeric state of WT CIB2 was found to be significantly affected by the presence of metal cations and by the presence of the E64D point mutation. DLS spectroscopy highlighted how, in order to achieve a substantially monodisperse protein solution, the saturation with  $\text{Ca}^{2+}$  or  $\text{Mg}^{2+}$  was necessary, as the apo-form was observed to dynamically fluctuate between oligomers of different size (**Figure 2** and **Figure S3**). Surprisingly, the USH1J-associated E64D mutation, that does not change the physicochemical properties of the substituted amino acid, still leads to a dimeric protein (**Figure S2**), which is however more prone to form heterogeneous aggregates over time independent of the presence of  $\text{Ca}^{2+}$  or  $\text{Mg}^{2+}$  (**Figure 2** and **Figure S3**).

Important differences between WT and E64D CIB2 were found in their cation-dependent folding state. A general agreement between  $^1\text{H}$  NMR and near and far UV-CD spectra was obtained for both protein variants (**Figure 3**). Indeed, WT CIB2 was found to respond to both  $\text{Ca}^{2+}$  and  $\text{Mg}^{2+}$  by adopting a similar secondary (**Figure 3C**) and tertiary structure (**Figures 3A,B**), at odds with the E64D variant, for which 1 mM  $\text{Mg}^{2+}$  was not enough to trigger any detectable switch (**Figures 3D–F**). Further addition of 1 mM  $\text{Ca}^{2+}$  led to a detectable increase in E64D CIB2's tertiary structure (**Figures 3D,E**) although the change was significantly lower compared to that observed for the WT. Besides showing a lower structural responsiveness to  $\text{Ca}^{2+}$  and  $\text{Mg}^{2+}$  compared to the WT, E64D CIB2 was found to have a significantly lower thermal stability under all the tested conditions (**Figure 4** and **Table S2**), and its apo-form apparently maintains a more hydrophobic surface that persists upon exposition to  $\text{Ca}^{2+}$  and  $\text{Mg}^{2+}$  (**Figure S4**). This could also explain while no transition was observed for apo E64D CIB2 upon thermal denaturation in the 4–70°C range (**Figure 4B**), this form being particularly unstable and unstructured.

2D HSQC NMR experiments shed light on the mechanisms related to  $\text{Ca}^{2+}$  and  $\text{Mg}^{2+}$  binding to WT CIB2 (**Figure 5**). While confirming the molten globule conformation of the apo form, NMR highlighted that the  $\text{Ca}^{2+}$ - and  $\text{Mg}^{2+}$ -bound states of WT CIB2 have a rather similar three-dimensional structure. The analysis of the downfield regions permits the distinction of specific  $\text{Ca}^{2+}$ - or  $\text{Mg}^{2+}$ -related fingerprints in the observed pattern. In particular, by performing  $\text{Ca}^{2+}$  titrations we observed that the intensity of the peak attributed to N121, which is located in the sixth position of the EF3 metal binding loop (**Figure 1**) shows a very similar trend compared to that of E64, the residue substituted by Asp in USH1J, which is located in the N-terminal domain, far from the metal binding loops (**Figure 1**). This surprising finding suggests that an inter-domain allosteric communication occurs between the EF3 binding loop and E64, which according to the homology model based on the structure of CIB1, forms an electrostatic interaction with R33 (**Figure 1**) and is therefore likely contributing to the stability of the EF1 subdomain. The titration patterns observed by NMR (**Figures 5D–F**) further confirm that EF3 is the first EF-hand to be occupied by  $\text{Ca}^{2+}$ , followed by EF4, whose structural probe is the G162 residue in the sixth position of the loop (**Figure 5E**). Our data support a model, in which under physiological conditions EF3 is never occupied by  $\text{Ca}^{2+}$  but is instead always  $\text{Mg}^{2+}$ -bound (**Figure S5**).  $\text{Ca}^{2+}$  will however bind to the EF4 loop under conditions of particularly high  $\text{Ca}^{2+}$  concentration. Moreover, no replacement of  $\text{Mg}^{2+}$  was observed in EF3 following additions of equal amounts of  $\text{Ca}^{2+}$  into  $\text{Mg}^{2+}$ -bound WT CIB2 (**Figure 5C**).

These findings appear particularly relevant for their physiological implications when considered together with the estimated affinities for  $\text{Ca}^{2+}$  and  $\text{Mg}^{2+}$  of WT and E64D CIB2 (**Figure 6** and **Table 1**). The intracellular concentration of free  $\text{Ca}^{2+}$  oscillates in the 0.1–10  $\mu\text{M}$  range (Berridge et al., 1998, 2000) and it is even lower in the outer segments of photoreceptor cells, where a fine regulation of the phototransduction cascade by  $\text{Ca}^{2+}$  and cGMP operates (Koch and Dell'Orco, 2013, 2015). The level of free  $\text{Mg}^{2+}$  in most cells, however, is relatively constant and ranges in the 0.5–1 mM interval (Romani and Scarpa, 1992, 2000). While a 290  $\mu\text{M}$  apparent affinity for  $\text{Mg}^{2+}$  (**Table 1**) is consistent with the binding of  $\text{Mg}^{2+}$  to WT CIB2 under physiological conditions, the affinity measured for the E64D variant (1.5 mM) is too low for ensuring sensing capabilities under normal conditions. Moreover, neither WT nor E64D CIB2 could possibly work as  $\text{Ca}^{2+}$  sensors with the apparent affinities detected in our study (500  $\mu\text{M}$  and 2 mM, respectively). It should be noticed that other authors (Blazejczyk et al., 2009) previously determined a much higher affinity for  $\text{Ca}^{2+}$  for GST-fused CIB2 by using a TNS fluorescence assay (apparent  $K_d = 0.14 \mu\text{M}$ ). Such a high affinity is in contrast with our data based on three different experimental approaches, namely NMR and CD spectroscopic titrations and competition experiments with the 5,5'-Br<sub>2</sub>-BAPTA chromophoric chelator. This latter approach excluded apparent  $K_d$  values below 6  $\mu\text{M}$  (results not shown) and was instead able to detect binding of  $\text{Ca}^{2+}$  to CIB1 (Yamniuk et al., 2008). We don't have an explanation for such discrepancy, except for pointing out that all our experiments



were performed with unlabeled and untagged human proteins, while those in Blazejczyk et al. used a TNS-labeled rat CIB2 fused with GST, which might introduce artifacts when probing the protein sensing capabilities.

The lower affinity for  $\text{Ca}^{2+}$  is one of the elements distinguishing CIB2 from CIB1, which binds  $\text{Ca}^{2+}$  with high affinity in EF4 ( $K_d = 0.5 \mu\text{M}$ ) and with lower affinity in EF3 ( $K_d = 1.9 \mu\text{M}$ ); binding of  $\text{Mg}^{2+}$  is instead limited to EF3 ( $K_d = 120 \mu\text{M}$ ) (Yamniuk et al., 2004, 2007). A closer look at the sequence alignment of the EF3 and EF4  $\text{Ca}^{2+}$ -binding motifs (**Figure 1**) explains, at least in part, such difference. The high affinity of the EF4 loop for  $\text{Ca}^{2+}$  in CIB1 can be attributed to the optimal pentagonal bipyramid geometry of the  $\text{Ca}^{2+}$ -coordinating oxygens, also due to the presence of an Asn residue (N169) in the -X position and especially to a Glu residue in the -Z position (E172). This latter constitutes a bidentate ligand providing the highly conserved coordination via the two  $\gamma$ -carboxyl groups to the  $\text{Ca}^{2+}$  ion (Gagné et al., 1997; Grabarek, 2011). In CIB2, positions -X and -Z are occupied respectively by G165, lacking contributions from the side chain, and D168, which does not possibly act as a bidentate ligand (**Figure 1**). Moreover, the position occupied by the side chain of D159 in the structural model of CIB2 does not seem optimal for contributing to  $\text{Ca}^{2+}$  coordination even after energy-minimization, at odds with that of the aligned residue D163 in CIB1 (**Figure 1**). Overall, the geometry of the  $\text{Ca}^{2+}$ -coordinating oxygens in the EF4 loop of CIB2 is thus likely distorted with respect to the canonical one, hence leading to a low affinity for  $\text{Ca}^{2+}$ . Differences in the sequence of the EF3 loop also distinguish CIB2 from CIB1, which may explain the lower affinity for  $\text{Ca}^{2+}$  shown by the first protein. Position Y in CIB1 is occupied by the negatively charged D118, which is substituted by N118 in CIB2, moreover the -X position, again occupied by an Asn (N124) in CIB1 is occupied by a Cys (C124) in CIB2. Interestingly, CIB1 like CIB2 does not have a Glu at position -Z, but has an Asp instead (D127), thus explaining the lower affinity for  $\text{Ca}^{2+}$ -compared to EF4.

The fact that all four CIBs have an Asp instead of a Glu residue at position -Z (**Figure 1**) suggests that EF3 can serve as a  $\text{Mg}^{2+}$ -binding specific motif. Previous mutagenesis studies showed that the replacement of the Asp residue in the 12th position (-Z) of an EF-hand metal binding loop with a Glu increases the affinity for  $\text{Ca}^{2+}$  and abolishes binding of  $\text{Mg}^{2+}$ , rendering the site calcium-specific, probably due to the reduced ability of side chains to change conformation (da Silva et al., 1995). We are therefore tempted to generalize that EF3 is the  $\text{Mg}^{2+}$ -specific binding motif among the CIB family, while  $\text{Ca}^{2+}$  might bind to EF4 under physiological conditions, although this is clearly not the case for CIB2. The conformational switch from a molten globule to a well-defined tertiary structure is likely governed by the acidic residue in the 12th position (-Z) of an EF-hand (Gifford et al., 2007), therefore  $\text{Mg}^{2+}$  seems to be the initiator of the functional switch among the CIB family.

We have also studied the potential effect of a CIB2-specific target on the protein metal cation-sensing ability. Although our investigation has been limited to one of the many

possible binding targets of CIB2, namely a peptide covering the membrane-proximal sequence of the integrin  $\alpha 7\text{B}$  cytosolic domain, our data show that the interaction with the target doubles the apparent affinity of CIB2 for  $\text{Ca}^{2+}$  (**Table 1**), however the detected  $K_d^{\text{app}}$  is still incompatible with a physiological capability of  $\text{Ca}^{2+}$  sensing. We cannot exclude, however, that in specific cell compartments and/or under specific conditions related to disease and/or cell death, the increased intracellular  $\text{Ca}^{2+}$  and the concomitant presence of a specific target would render CIB2 capable of  $\text{Ca}^{2+}$  sensing, therefore providing specific functions. This is however not possibly the case of E64D CIB2, which showed a mM affinity for  $\text{Ca}^{2+}$  under all the tested conditions, including the presence of the target peptide (**Table 1** and **Figure 6**).

Both WT and E64D CIB2 were shown to bind specifically the  $\alpha 7\text{B}_M$  target peptide with a low  $\mu\text{M}$  affinity comparable to that shown for CIB1- $\alpha\text{IIb}$  interaction ( $K_d = 1.41\text{--}1.02 \mu\text{M}$ , in the presence of  $\text{Ca}^{2+}$  and  $\text{Mg}^{2+}$ , respectively) (Shock et al., 1999; Yamniuk and Vogel, 2005). Future studies will be necessary to further elucidate the binding thermodynamics of CIB2 to its putative targets, including those belonging to the Usher interactome. A broader set of conditions including different cation concentrations and models that account for the dimeric nature of CIB2 shall be specifically tested. Nevertheless, our data seem sufficient to exclude that the principal dysfunction of the USH1J-associated E64D CIB2 be related to the lack of recognition of specific targets. Instead, our data point clearly to the incapability of this CIB2 mutant to switch to its native,  $\text{Mg}^{2+}$ -bound conformation (**Figures 3, 5, 6**). E64D CIB2 was indeed observed to maintain, under physiological levels of  $\text{Mg}^{2+}$ , a partially unfolded conformation that makes it significantly less stable and prone to aggregation compared to the WT (**Figure 2** and **Figure S3**).

The switch that allows WT CIB2 to acquire a functional conformation at physiological  $\text{Mg}^{2+}$  appears to be finely regulated by an allosteric, long-range communication connecting EF1 with EF3. Our data are inconsistent with mutations in CIB2 disrupting auditory hair cell calcium homeostasis (Jan, 2013) as with such a low affinity not even the WT protein is expected to be involved in  $\text{Ca}^{2+}$  sensing under physiological conditions. Instead, we propose that the inability to bind  $\text{Mg}^{2+}$  of E64D CIB2 prevents the allosteric regulation that makes the protein switch to the native conformation required for its normal function.

## AUTHOR CONTRIBUTIONS

RV, GD, MD, and DD planned the experiments and analyzed the results. RV, GD, and MD performed the experiments. DD wrote the manuscript with contributions from all the authors.

## FUNDING

This work was supported by the research grant Ricerca di Base 2015—project UMBUSH from the University of Verona (to DD).

## ACKNOWLEDGMENTS

The Centro Piattaforme Tecnologiche (CPT) of the University of Verona is acknowledged for providing facilities and technical assistance.

## REFERENCES

- Astegno, A., Bonza, M. C., Vallone, R., La Verde, V., D'Onofrio, M., Luoni, L., et al. (2017). Arabidopsis calmodulin-like protein CML36 is a calcium ( $\text{Ca}^{2+}$ ) sensor that interacts with the plasma membrane  $\text{Ca}^{2+}$ -ATPase isoform ACA8 and stimulates its activity. *J. Biol. Chem.* 292, 15049–15061. doi: 10.1074/jbc.M117.787796
- Astegno, A., La Verde, V., Marino, V., Dell'Orco, D., and Dominici, P. (2016). Biochemical and biophysical characterization of a plant calmodulin: role of the N- and C-lobes in calcium binding, conformational change, and target interaction. *Biochim. Biophys. Acta* 1864, 297–307. doi: 10.1016/j.bbapap.2015.12.003
- Astegno, A., Maresi, E., Marino, V., Dominici, P., Pedroni, M., Piccinelli, F., et al. (2014). Structural plasticity of calmodulin on the surface of CaF2 nanoparticles preserves its biological function. *Nanoscale* 6, 15037–15047. doi: 10.1039/C4NR04368E
- Berridge, M. J., Bootman, M. D., and Lipp, P. (1998). Calcium—a life and death signal. *Nature* 395, 645–648. doi: 10.1038/27094
- Berridge, M. J., Lipp, P., and Bootman, M. D. (2000). The versatility and universality of calcium signalling. *Nat. Rev. Mol. Cell. Biol.* 1, 11–21. doi: 10.1038/35036035
- Blazejczyk, M., Sobczak, A., Debowska, K., Wisniewska, M. B., Kirilenko, A., Pikula, S., et al. (2009). Biochemical characterization and expression analysis of a novel EF-hand  $\text{Ca}^{2+}$  binding protein calmyrin2 (Cib2) in brain indicates its function in NMDA receptor mediated  $\text{Ca}^{2+}$  signaling. *Arch. Biochem. Biophys.* 487, 66–78. doi: 10.1016/j.abb.2009.05.002
- Booth, K. T., Kahrizi, K., Babanejad, M., Daghagh, H., Bademci, G., Arzhang, S., et al. (2018). Variants in CIB2 cause DFNB48 and not USH1J. *Clin. Genet.* 93, 812–821. doi: 10.1111/cge.13170
- da Silva, A. C., Kendrick-Jones, J., and Reinach, F. C. (1995). Determinants of ion specificity on EF-hands sites. Conversion of the  $\text{Ca}^{2+}$  / $\text{Mg}^{2+}$  site of smooth muscle myosin regulatory light chain into a  $\text{Ca}^{2+}$ -specific site. *J. Biol. Chem.* 270, 6773–6778. doi: 10.1074/jbc.270.12.6773
- Dal Cortivo, G., Wagner, G. E., Cortelletti, P., Padmanabha Das, K. M., Zangger, K., Speghini, A., et al. (2018). Luminescent and paramagnetic properties of nanoparticles shed light on their interactions with proteins. *Sci. Rep.* 8:3420. doi: 10.1038/s41598-018-21571-y
- Ferguson, K. A. (1964). Starch-gel electrophoresis—application to the classification of pituitary proteins and polypeptides. *Metabolism* 13(Suppl. 2), 985–1002. doi: 10.1016/S0026-0495(64)80018-4
- Gagné, S. M., Li, M. X., and Sykes, B. D. (1997). Mechanism of direct coupling between binding and induced structural change in regulatory calcium binding proteins. *Biochemistry* 36, 4386–4392. doi: 10.1021/bi963076+
- Gentry, H. R., Singer, A. U., Betts, L., Yang, C., Ferrara, J. D., Sondek, J., et al. (2005). Structural and biochemical characterization of CIB1 delineates a new family of EF-hand-containing proteins. *J. Biol. Chem.* 280, 8407–8415. doi: 10.1074/jbc.M411515200
- Gifford, J. L., Walsh, M. P., and Vogel, H. J. (2007). Structures and metal-ion-binding properties of the  $\text{Ca}^{2+}$ -binding helix-loop-helix EF-hand motifs. *Biochem. J.* 405, 199–221. doi: 10.1042/BJ20070255
- Godinho-Santos, A., Hance, A. J., Goncalves, J., and Mammano, F. (2016). CIB1 and CIB2 are HIV-1 helper factors involved in viral entry. *Sci. Rep.* 6:30927. doi: 10.1038/srep30927
- Grabarek, Z. (2011). Insights into modulation of calcium signaling by magnesium in calmodulin, troponin C and related EF-hand proteins. *Biochim. Biophys. Acta* 1813, 913–921. doi: 10.1016/j.bbapap.2011.01.017
- Häger, M., Bigotti, M. G., Meszaros, R., Carmignac, V., Holmberg, J., Allamand, V., et al. (2008). Cib2 binds integrin  $\alpha 7\beta 1$  and is reduced in laminin  $\alpha 2$  chain-deficient muscular dystrophy. *J. Biol. Chem.* 283, 24760–24769. doi: 10.1074/jbc.M801166200

## SUPPLEMENTARY MATERIAL

The Supplementary Material for this article can be found online at: <https://www.frontiersin.org/articles/10.3389/fnmol.2018.00274/full#supplementary-material>

- Huang, H., Bogstie, J. N., and Vogel, H. J. (2012). Biophysical and structural studies of the human calcium- and integrin-binding protein family: understanding their functional similarities and differences. *Biochem. Cell. Biol.* 90, 646–656. doi: 10.1139/o2012-021
- Huang, H., Ishida, H., Yamniuk, A. P., and Vogel, H. J. (2011). Solution structures of  $\text{Ca}^{2+}$ -CIB1 and  $\text{Mg}^{2+}$ -CIB1 and their interactions with the platelet integrin  $\alpha\text{IIb}$  cytoplasmic domain. *J. Biol. Chem.* 286, 17181–17192. doi: 10.1074/jbc.M110.179028
- Jan, A. (2013). Mutations in CIB2 calcium and integrin-binding protein disrupt auditory hair cell calcium homeostasis in Usher syndrome type 1J and non-syndromic deafness DFNB48. *Clin. Genet.* 83, 317–318. doi: 10.1111/cge.12100
- Koch, K. W., and Dell'Orco, D. (2013). A calcium-relay mechanism in vertebrate phototransduction. *ACS Chem. Neurosci.* 4, 909–917. doi: 10.1021/cn400027z
- Koch, K. W., and Dell'Orco, D. (2015). Protein and signaling networks in vertebrate photoreceptor cells. *Front. Mol. Neurosci.* 8:67. doi: 10.3389/fnmol.2015.00067
- Leisner, T. M., Freeman, T. C., Black, J. L., and Parise, L. V. (2016). CIB1: a small protein with big ambitions. *FASEB J.* 30, 2640–2650. doi: 10.1096/fj.201500073R
- Marino, V., Astegno, A., Pedroni, M., Piccinelli, F., and Dell'Orco, D. (2014). Nanodevice-induced conformational and functional changes in a prototypical calcium sensor protein. *Nanoscale* 6, 412–423. doi: 10.1039/C3NR04978G
- Marino, V., Borsatto, A., Vocke, F., Koch, K. W., and Dell'Orco, D. (2017). CaF2 nanoparticles as surface carriers of GCAP1, a calcium sensor protein involved in retinal dystrophies. *Nanoscale* 9, 11773–11784. doi: 10.1039/C7NR03288A
- Marino, V., and Dell'Orco, D. (2016). Allosteric communication pathways routed by  $\text{Ca}^{2+}$  / $\text{Mg}^{2+}$  exchange in GCAP1 selectively switch target regulation modes. *Sci. Rep.* 6:34277. doi: 10.1038/srep34277
- Marino, V., Scholten, A., Koch, K. W., and Dell'Orco, D. (2015a). Two retinal dystrophy-associated missense mutations in GUCA1A with distinct molecular properties result in a similar aberrant regulation of the retinal guanylate cyclase. *Hum. Mol. Genet.* 24, 6653–6666. doi: 10.1093/hmg/ddv370
- Marino, V., Sulmann, S., Koch, K. W., and Dell'Orco, D. (2015b). Structural effects of  $\text{Mg}^{2+}$  on the regulatory states of three neuronal calcium sensors operating in vertebrate phototransduction. *Biochim. Biophys. Acta* 1853, 2055–2065. doi: 10.1016/j.bbapap.2014.10.026
- Maune, J. F., Beckingham, K., Martin, S. R., and Bayley, P. M. (1992). Circular dichroism studies on calcium binding to two series of  $\text{Ca}^{2+}$  binding site mutants of *Drosophila melanogaster* calmodulin. *Biochemistry* 31, 7779–7786. doi: 10.1021/bi00149a006
- Patel, K., Giese, A. P., Grossheim, J. M., Hegde, R. S., Delio, M., Samanich, J., et al. (2015). A novel C-terminal CIB2 (Calcium and Integrin Binding Protein 2) mutation associated with non-syndromic hearing loss in a hispanic family. *PLoS ONE* 10:e0133082. doi: 10.1371/journal.pone.0133082
- Pieper, U., Webb, B. M., Dong, G. Q., Schneidman-Duhovny, D., Fan, H., Kim, S. J., et al. (2014). ModBase, a database of annotated comparative protein structure models and associated resources. *Nucleic Acids Res* 42, D336–D346. doi: 10.1093/nar/gkt1144
- Riazuddin, S., Belyantseva, I. A., Giese, A. P., Lee, K., Indzhykulia, A. A., Nandamuri, S. P., et al. (2012). Alterations of the CIB2 calcium- and integrin-binding protein cause Usher syndrome type 1J and nonsyndromic deafness DFNB48. *Nat. Genet.* 44, 1265–1271. doi: 10.1038/ng.2426
- Romani, A., and Scarpa, A. (1992). Regulation of cell magnesium. *Arch. Biochem. Biophys.* 298, 1–12. doi: 10.1016/0003-9861(92)90086-C
- Romani, A. M., and Scarpa, A. (2000). Regulation of cellular magnesium. *Front. Biosci.* 5, D720–734. doi: 10.2741/Romani
- Seco, C. Z., Giese, A. P., Shafique, S., Schraders, M., Oonk, A. M., Grossheim, M., et al. (2016). Novel and recurrent CIB2 variants, associated with nonsyndromic deafness, do not affect calcium buffering and localization in hair cells. *Eur. J. Hum. Genet.* 24, 542–549. doi: 10.1038/ejhg.2015.157

- Seki, N., Hattori, A., Hayashi, A., Kozuma, S., Ohira, M., Hori, T., et al. (1999). Structure, expression profile and chromosomal location of an isolog of DNA-PKcs interacting protein (KIP) gene. *Biochim. Biophys. Acta* 1444, 143–147. doi: 10.1016/S0167-4781(98)00253-X
- Shock, D. D., Naik, U. P., Brittain, J. E., Alahari, S. K., Sondek, J., and Parise, L. V. (1999). Calcium-dependent properties of CIB binding to the integrin alphaIIb cytoplasmic domain and translocation to the platelet cytoskeleton. *Biochem. J.* 342(Pt 3), 729–735. doi: 10.1042/bj3420729
- Sulmann, S., Dell'orco, D., Marino, V., Behnen, P., and Koch, K. W. (2014). Conformational changes in calcium-sensor proteins under molecular crowding conditions. *Chemistry* 20, 6756–6762. doi: 10.1002/chem.201402146
- Vallone, R., La Verde, V., D'Onofrio, M., Giorgetti, A., Dominici, P., and Astegno, A. (2016). Metal binding affinity and structural properties of calmodulin-like protein 14 from *Arabidopsis thaliana*. *Protein Sci.* 25, 1461–1471. doi: 10.1002/pro.2942
- Vocke, F., Weisschuh, N., Marino, V., Malfatti, S., Jacobson, S. G., Reiff, C. M., et al. (2017). Dysfunction of cGMP signalling in photoreceptors by a macular dystrophy-related mutation in the calcium sensor GCAP1. *Hum. Mol. Genet.* 26, 133–144. doi: 10.1093/hmg/ddw374
- Wang, Y., Li, J., Yao, X., Li, W., Du, H., Tang, M., et al. (2017). Loss of CIB2 causes profound hearing loss and abolishes mechano-electrical transduction in mice. *Front Mol. Neurosci.* 10:401. doi: 10.3389/fnmol.2017.00401
- Yamniuk, A. P., Gifford, J. L., Linse, S., and Vogel, H. J. (2008). Effects of metal-binding loop mutations on ligand binding to calcium- and integrin-binding protein 1. evolution of the EF-hand? *Biochemistry* 47, 1696–1707. doi: 10.1021/bi701494m
- Yamniuk, A. P., Ishida, H., and Vogel, H. J. (2006). The interaction between calcium- and integrin-binding protein 1 and the alphaIIb integrin cytoplasmic domain involves a novel C-terminal displacement mechanism. *J. Biol. Chem.* 281, 26455–26464. doi: 10.1074/jbc.M603963200
- Yamniuk, A. P., Nguyen, L. T., Hoang, T. T., and Vogel, H. J. (2004). Metal ion binding properties and conformational states of calcium- and integrin-binding protein. *Biochemistry* 43, 2558–2568. doi: 10.1021/bi035432b
- Yamniuk, A. P., Silver, D. M., Anderson, K. L., Martin, S. R., and Vogel, H. J. (2007). Domain stability and metal-induced folding of calcium- and integrin-binding protein 1. *Biochemistry* 46, 7088–7098. doi: 10.1021/bi700200z
- Yamniuk, A. P., and Vogel, H. J. (2005). Calcium- and magnesium-dependent interactions between calcium- and integrin-binding protein and the integrin alphaIIb cytoplasmic domain. *Protein Sci.* 14, 1429–1437. doi: 10.1110/ps.041312805
- Zhu, W., Jarman, K. E., Lokman, N. A., Neubauer, H. A., Davies, L. T., Gliddon, B. L., et al. and Pitson, S.M. (2017). CIB2 negatively regulates oncogenic signaling in ovarian cancer via sphingosine kinase 1. *Cancer Res.* 77, 4823–4834. doi: 10.1158/0008-5472.CAN-17-0025

**Conflict of Interest Statement:** The authors declare that the research was conducted in the absence of any commercial or financial relationships that could be construed as a potential conflict of interest.

Copyright © 2018 Vallone, Dal Cortivo, D'Onofrio and Dell'Orco. This is an open-access article distributed under the terms of the Creative Commons Attribution License (CC BY). The use, distribution or reproduction in other forums is permitted, provided the original author(s) and the copyright owner(s) are credited and that the original publication in this journal is cited, in accordance with accepted academic practice. No use, distribution or reproduction is permitted which does not comply with these terms.

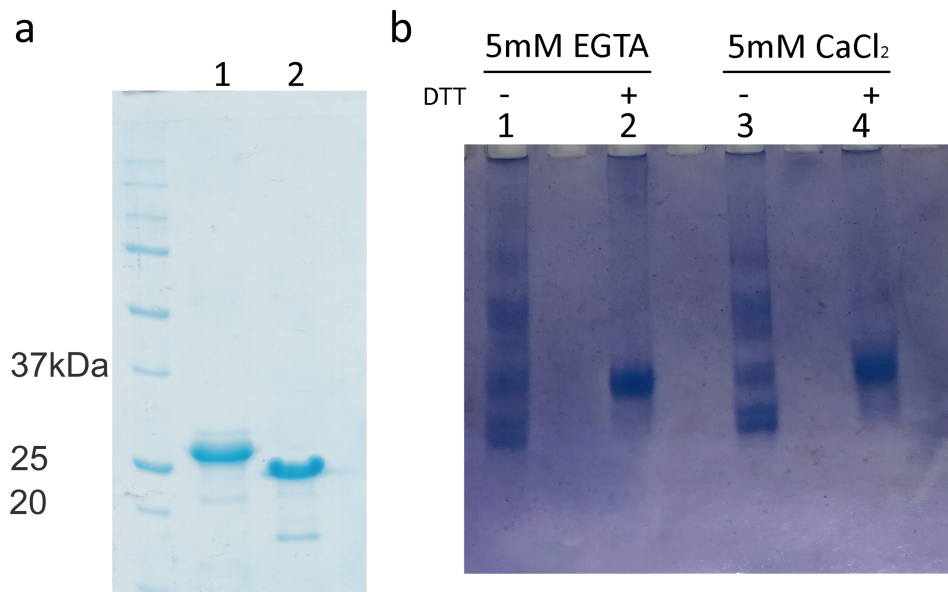
## Supplementary Material

### Preferential binding of $Mg^{2+}$ over $Ca^{2+}$ to CIB2 triggers an allosteric switch impaired in Usher Syndrome type 1J

Rosario Vallone, Giuditta Dal Cortivo, Mariapina D'Onofrio and Daniele Dell'Orco\*

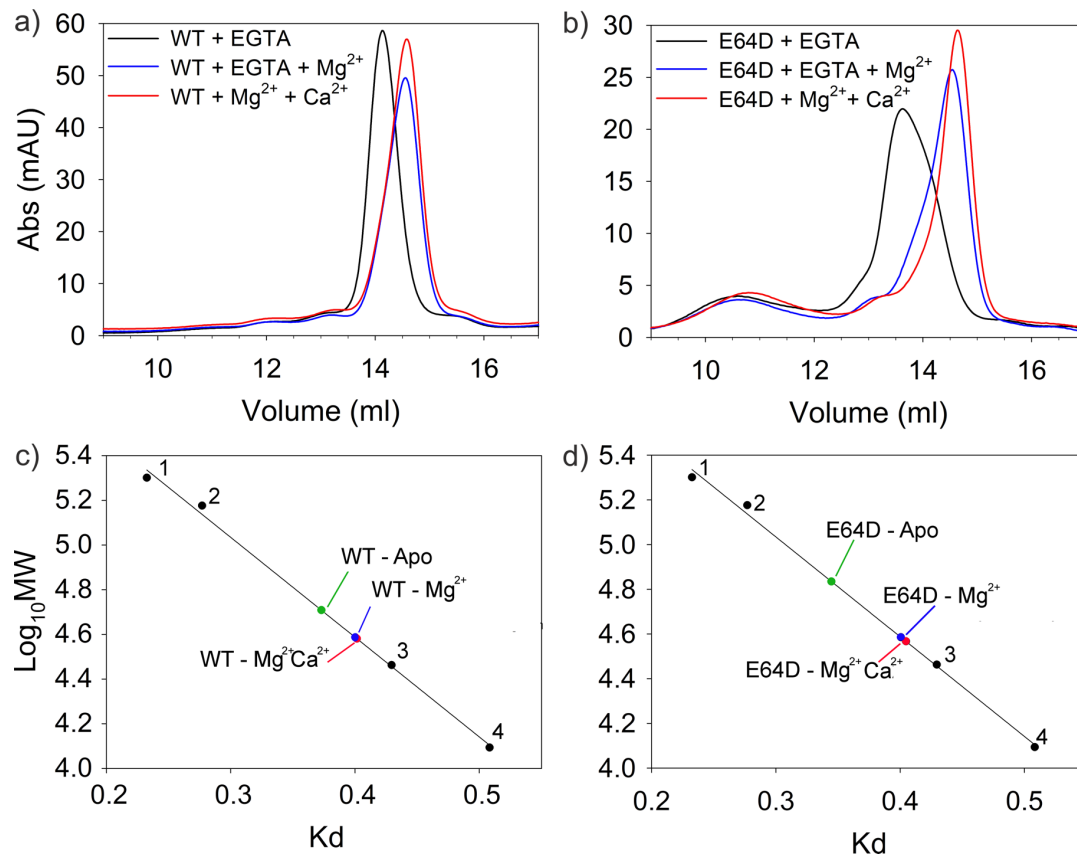
\* Correspondence: daniele.dellorco@univr.it

Figure S1



**Figure S1:** SDS and Native-PAGE of CIB2. **a)** SDS-PAGE of 20 $\mu$ M CIB2 before (lane 1) and after (lane 2) TEV-cleavage of the His-tag in the presence of 1mM DTT. **b)** Continuous native-PAGE (12% acrylamide/bis- acrylamide) of 14 $\mu$ M CIB2 in the presence of 5mM EGTA (lanes 1-2) or 5mM  $Ca^{2+}$  (lanes 3-4). 1mM DTT was added in lanes 2 and 4.

**Figure S2**



**Figure S2:** SEC analysis. Gel filtration elution profiles under reducing conditions of : **a)** WT CIB2 and **b)** E64D CIB2 in the presence of 3 mM EGTA (black line), 3 mM Mg<sup>2+</sup> + 2 mM EGTA (blue line) and 3 mM Mg<sup>2+</sup> + 2 mM Ca<sup>2+</sup> (red line). **c-d)** Determination of MW for apo-, Mg<sup>2+</sup> and Ca<sup>2+</sup> - bound WT and E64D CIB2. Calibration curve prepared by plotting the Log<sub>10</sub> MW value for each standard protein versus its corresponding K<sub>d</sub> value. 1. β-amylase; 2. Alcohol Dehydrogenase; 3. Carbonic anhydrase; 4. Cytochrome c. Chromatograms in a) and b) were used to determine the MW for apo-, Mg<sup>2+</sup> and Ca<sup>2+</sup> -bound WT CIB2 and E64D CIB2, respectively (Table S1).

**Figure S3**

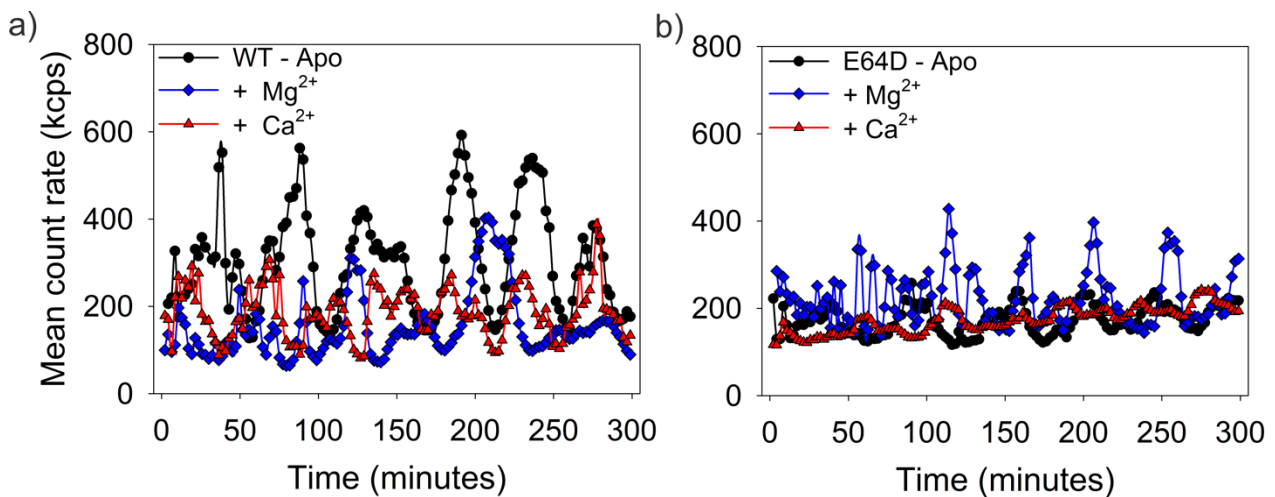


**Figure S3:** Time-resolved dynamic light scattering. Mean count rate time-course of **a)** WT and **b)** E64D CIB2 in the presence of 3 mM EGTA (black line), 3 mM Mg<sup>2+</sup> + 2 mM EGTA (blue line) and 3 mM Mg<sup>2+</sup> + 2 mM Ca<sup>2+</sup> (red line).

**Figure S4**

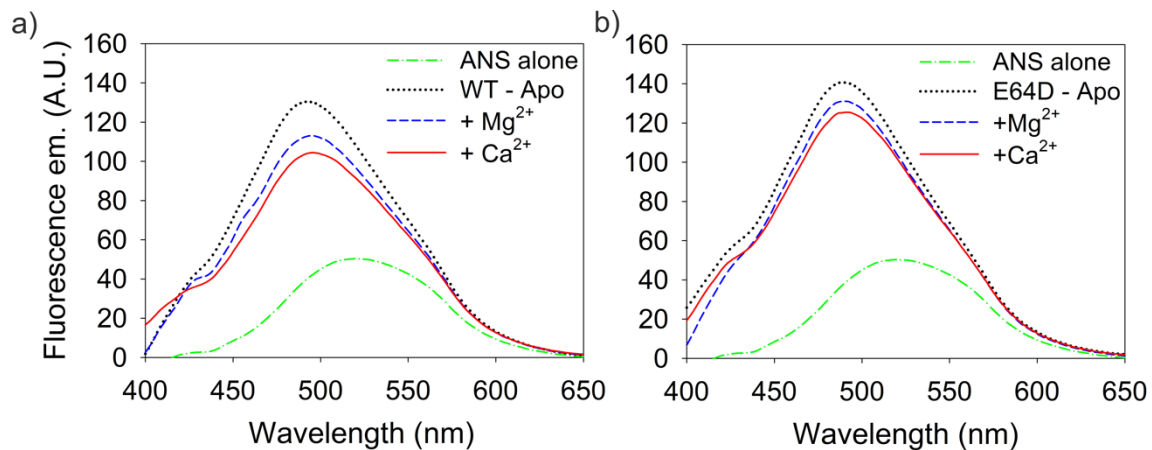


**Figure S4: ANS fluorescence spectroscopy.** ANS fluorescence spectra of: **a)** WT CIB2 and **b)** E64D CIB2 in the presence of 0.5 mM EDTA (dotted black line), 1 mM Mg<sup>2+</sup> (short dashed blue line) and 1 mM Mg<sup>2+</sup> + 1 mM Ca<sup>2+</sup> (solid red line). The fluorescence spectrum of ANS alone is also shown (dash dotted green line).

**Figure S5**

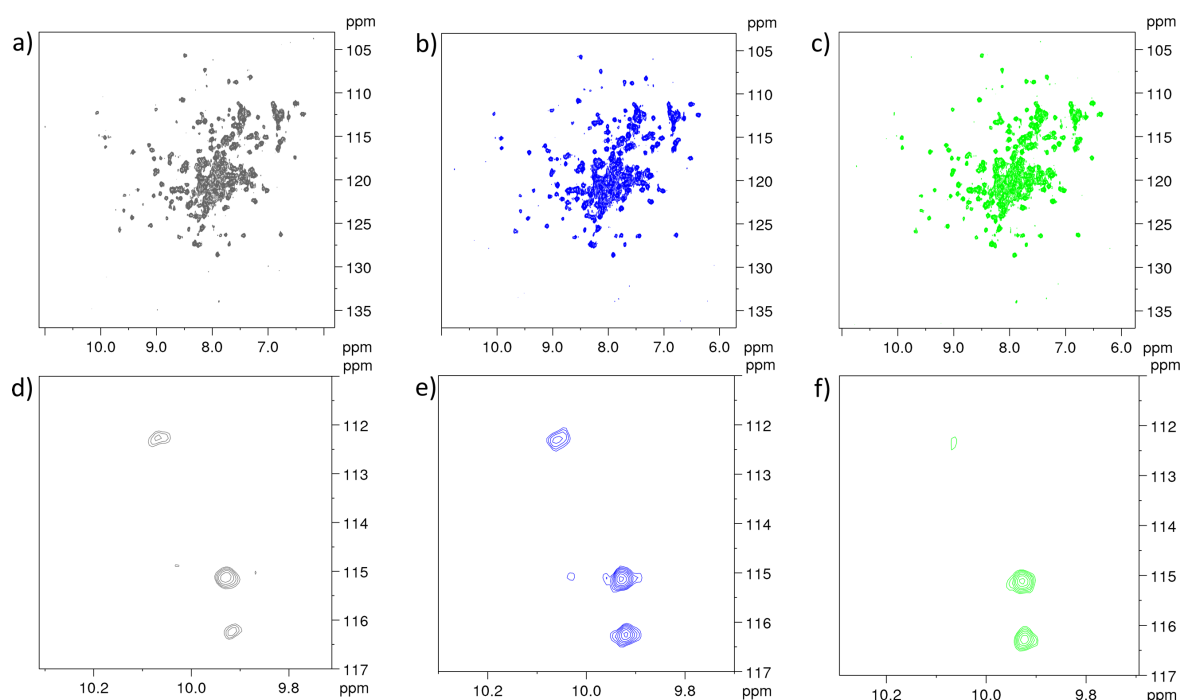


**Figure S5: 2D NMR spectra.** Two-dimensional  $^1\text{H}$ - $^{15}\text{N}$  HSQC NMR spectra of  $^{15}\text{N}$ -WT CIB2 with addition of 3 mM  $\text{Mg}^{2+}$  + 7 mM  $\text{Ca}^{2+}$  (panels **a**, **d**), 5 mM  $\text{Mg}^{2+}$  + 5 mM  $\text{Ca}^{2+}$  (panels **b**, **e**), 7 mM  $\text{Mg}^{2+}$  + 3 mM  $\text{Ca}^{2+}$  (panels **c**, **f**). The complexes were obtained by adding to the protein different solutions containing both  $\text{Mg}^{2+}$  and  $\text{Ca}^{2+}$  ions yielding the same overall ionic strength. The spectra were recorded at 600 MHz and 25°C, the samples were at protein concentration of 150  $\mu\text{M}$  in 20 mM HEPES, 100 mM KCl, 1 mM DTT, pH 7.5 and 7%  $\text{D}_2\text{O}$ .

**Figure S6**

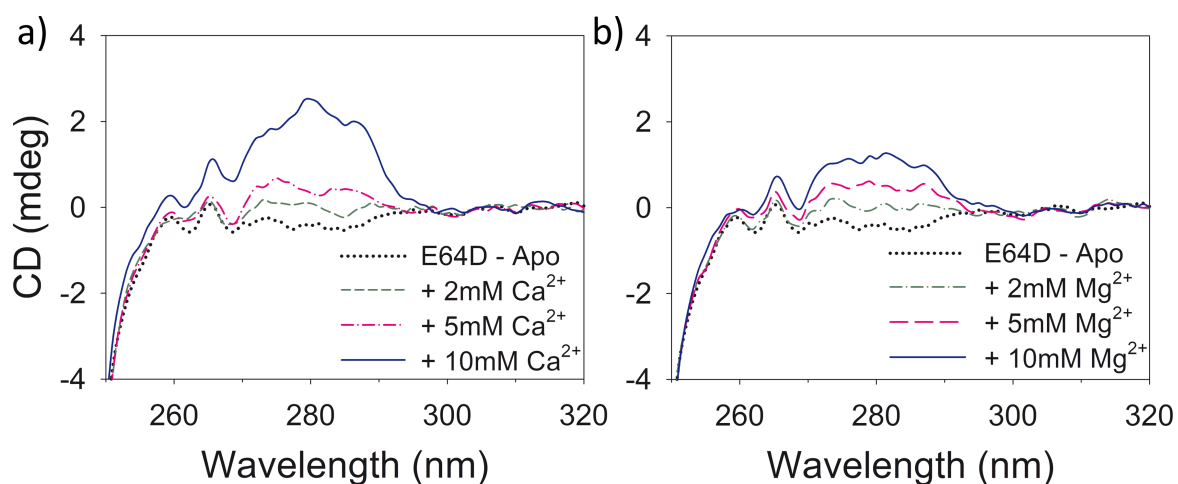


**Figure S6: Near UV CD spectra** of E64D CIB2 after sequential additions of increasing concentrations of: **a)**  $\text{Ca}^{2+}$  and: **b)**  $\text{Mg}^{2+}$  in the 2-10 mM range. The experimental conditions were the same as those of *Figure 3e*.

**Figure S7**

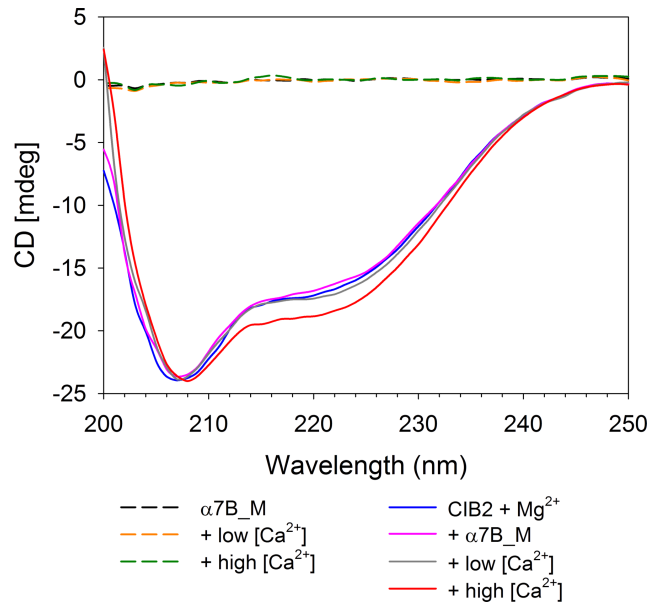


**Figure S7: Effect of the  $\alpha 7B\_M$  peptide on the secondary structure of WT CIB2.**  $12\mu M$   $Mg^{2+}$  bound-WT CIB2 was incubated at  $37^\circ C$  in the presence of  $6\mu M$   $\alpha 7B\_M$  peptide (ratio 2:1). Spectra were collected in the presence of low ( $100\mu M$ , grey line) and high ( $1mM$ , red line)  $Ca^{2+}$  concentration. Spectra obtained for the  $\alpha 7B\_M$  peptide in the absence of CIB2 are also shown (dashed lines).



**Table S1: Molecular weight of WT and E64D CIB2 estimated by Analytical SEC and Ferguson Plots**

	MW <sup>SEC</sup> (KDa)	MW <sup>FP</sup> (KDa)
<b>WT -apo</b>	51.1	51
<b>+ Mg<sup>2+</sup></b>	38.6	52
<b>+Mg<sup>2+</sup>+ Ca<sup>2+</sup></b>	38.1	53
<b>E64D -apo</b>	68.4	53
<b>+ Mg<sup>2+</sup></b>	38.5	53
<b>+Mg<sup>2+</sup>+ Ca<sup>2+</sup></b>	36.9	53

**Table S2: Analysis of ANS fluorescence and CD thermal denaturation data for WT and E64D CIB2**

	blue shift (nm) <sup>1</sup>	F <sup>max</sup> /F <sup>ref</sup>	T <sub>m</sub> (°C)	H <sub>c</sub>
<b>WT -apo</b>	27	2.6	35.1	7.5
<b>+ Mg<sup>2+</sup></b>	25	2.2	45.7	11
<b>+ Ca<sup>2+</sup></b>	25	2.1	43.4	12.5
<b>+Mg<sup>2+</sup>/Ca<sup>2+</sup></b>	-	-	45.9	11.2
<b>E64D -apo</b>	31	2.8	-	-
<b>+ Mg<sup>2+</sup></b>	30	2.6	34.2	9.5
<b>+ Ca<sup>2+</sup></b>	29	2.5	34.5	8.6
<b>+Mg<sup>2+</sup>/Ca<sup>2+</sup></b>	-	-	36.7	8.9

<sup>1</sup> Blue shift refers to the observed shift of the wavelength of maximum emission of the protein + ANS mixture upon excitation at 380 nm as referred to that of ANS alone.

<sup>2</sup> F<sup>max</sup>/F<sup>ref</sup> refers to the ratio between maximal fluorescence emission of the protein + ANS mixture and that of ANS alone.

<sup>3</sup> T<sub>m</sub> and H<sub>c</sub> represent, respectively, the melting temperature and the Hill coefficient obtained by data fitting in thermal denaturation profiles.

OPEN

# Oligomeric state, hydrodynamic properties and target recognition of human Calcium and Integrin Binding protein 2 (CIB2)

Giuditta Dal Cortivo<sup>1</sup>, Valerio Marino<sup>1,2</sup>, Claudio Iacobucci<sup>3</sup>, Rosario Vallone<sup>1,4</sup>, Christian Arlt<sup>3</sup>, Anne Rehkamp<sup>3</sup>, Andrea Sinz<sup>3</sup> & Daniele Dell'Orco<sup>1\*</sup>

Calcium- and Integrin-Binding protein 2 (CIB2) is a small and ubiquitously expressed protein with largely unknown biological function but ascertained role in hearing physiology and disease. Recent studies found that CIB2 binds  $\text{Ca}^{2+}$  with moderate affinity and dimerizes under conditions mimicking the physiological ones. Here we provided new lines of evidence on CIB2 oligomeric state and the mechanism of interaction with the  $\alpha 7\text{B}$  integrin target. Based on a combination of native mass spectrometry, chemical cross-linking/mass spectrometry, analytical gel filtration, dynamic light scattering and molecular dynamics simulations we conclude that CIB2 is monomeric under all tested conditions and presents uncommon hydrodynamic properties, most likely due to the high content of hydrophobic solvent accessible surface. Surface plasmon resonance shows that the interaction with  $\alpha 7\text{B}$  occurs with relatively low affinity and is limited to the cytosolic region proximal to the membrane, being kinetically favored in the presence of physiological  $\text{Mg}^{2+}$  and in the absence of  $\text{Ca}^{2+}$ . Although CIB2 binds to an  $\alpha 7\text{B}$  peptide in a 1:1 stoichiometry, the formation of the complex might induce binding of another CIB2 molecule.

Calcium- and Integrin-Binding protein 2 (CIB2) is a small (21.7 kDa)  $\text{Ca}^{2+}$  and  $\text{Mg}^{2+}$ -binding protein initially discovered as a DNA-dependent protein kinase interacting protein<sup>1</sup>. It is a member of the CIB family, which contains homolog EF-hand proteins showing evolutionary relationship with the class of neuronal calcium sensor proteins<sup>2</sup>. Its broad expression levels in a variety of tissues suggests the direct involvement of CIB2 in a heterogeneous group of physiological and disease-associated processes, which include congenital muscular dystrophy type 1A<sup>3</sup>, promotion of HIV-viral infection<sup>4</sup>, N-methyl-D-aspartate receptor-mediated  $\text{Ca}^{2+}$  signaling in cultured hippocampal neurons<sup>5</sup>, and very recently sphingosine kinase 1-mediated oncogenic signaling in ovarian cancer<sup>6</sup>. While its physiological role remains largely unknown, some general functional features of CIB2 have been established: (i) CIB2 can bind  $\text{Ca}^{2+}$  and  $\text{Mg}^{2+}$  ions via two functional EF-hand motifs, namely EF3 and EF4, therefore switching to a specific conformation<sup>7,8</sup>; (ii) CIB2 specifically binds to the cytoplasmic domain of integrin  $\alpha 7\text{B}$ <sup>3,7</sup>, as well as to  $\alpha \text{IIb}$  integrin<sup>7</sup>, thus being presumably involved in a variety of signal transduction processes.

In spite of its evidently broad biological role, recent findings suggest that CIB2 is deeply involved in hearing physiology. CIB2 knockout mice showed abolished mechano-electrical transduction in auditory cells leading to profound hearing loss<sup>9</sup>, moreover missense mutations in the gene encoding for CIB2 have been found to be associated with hereditary non-syndromic deafness (DFNB48) and possibly Usher Syndrome type 1J, a genetic disorder characterized by hearing loss and progressive blindness<sup>10,11</sup>. Altogether, these recent findings suggest that CIB2 is an essential component for the normal development of hair cells.

In a recent study<sup>8</sup> we investigated the capability of CIB2 to bind  $\text{Ca}^{2+}$  and  $\text{Mg}^{2+}$  thereby switching to a functionally distinct structural state. By integrating several biochemical and biophysical techniques we could establish that in the absence of any cation CIB2 forms a molten globule state that essentially lacks tertiary structure.

<sup>1</sup>Department of Neurosciences, Biomedicine and Movement Sciences, Section of Biological Chemistry, University of Verona, Verona, Italy. <sup>2</sup>Department of Translational Research and New Technologies in Medicine and Surgery, University of Pisa, Pisa, Italy. <sup>3</sup>Department of Pharmaceutical Chemistry and Bioanalytics, Institute of Pharmacy, Charles Tanford Protein Center, Martin Luther University Halle-Wittenberg, Halle, Germany. <sup>4</sup>Structural Biology and Biophysics Unit, Fondazione Ri.MED, Palermo, Italy. \*email: [daniele.dellorco@univr.it](mailto:daniele.dellorco@univr.it)

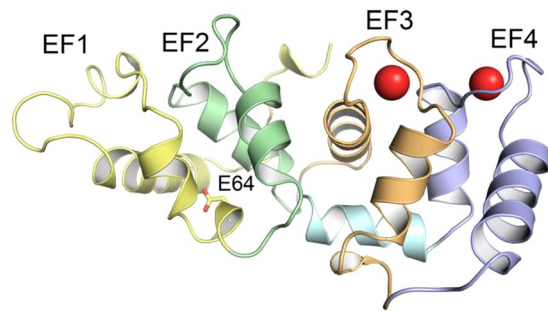


**Figure 1.** Three-dimensional structure of the homology model of  $\text{Ca}^{2+}$ -bound human CIB2. Protein secondary structure is shown as cartoons, EF1 is colored in yellow, EF2 is colored in green, EF3 is colored in orange, EF4 is colored in blue, the C-terminal helix is colored in cyan and  $\text{Ca}^{2+}$  ions are shown as red spheres. Residue E64 is shown as sticks. The structural model is from ref.<sup>8</sup> (see Methods).

Binding of either  $\text{Ca}^{2+}$  or  $\text{Mg}^{2+}$  leads to a highly similar tertiary structure although the apparent affinity for  $\text{Ca}^{2+}$  ( $K_d^{\text{app}} = 0.5 \text{ mM}$ ) was found to be significantly lower compared to that for  $\text{Mg}^{2+}$  ( $K_d^{\text{app}} = 290 \mu\text{M}$ ). This is quite unusual for  $\text{Ca}^{2+}$ -sensor proteins, but it could be explained by the relatively low sequence similarity in key functional regions when comparing CIB2 with the homologue CIB1 and other members of the CIB family<sup>8</sup>. We also found that the binding of cations to the functional motif EF3 at the C-terminal domain (Fig. 1) triggers a conformational transition that puts the EF3 loop in allosteric communication with the N-terminal domain, specifically with residue E64, that has been found mutated into an aspartic acid in Usher Syndrome type 1J<sup>11</sup>. Surprisingly, the apparently conservative E64D mutation abolishes the conformational switch and significantly lowers the affinity for both cations<sup>8</sup>, indicating that even a small difference such as the presence or absence of a methylene bridge between acidic amino acids can be critical to whether an essential interaction can take place or not. Both wild type (WT) and E64D-CIB2 were found to recognize and bind a peptide from the known target integrin  $\alpha 7\text{B}^{3,7}$  with similar affinity in the micromolar range, and based on analytical size exclusion chromatography (SEC), dynamic light scattering (DLS) and non-denaturing electrophoresis assays we concluded that CIB2 is dimeric, in line with independent previous observations<sup>11,12</sup>.

In an attempt to define the structural features of the CIB2 dimeric interface and its interaction with putative target peptides by employing cross-linking/mass spectrometry<sup>13–15</sup>, we found evidence of monomeric CIB2, but surprisingly no evidence of dimers. In this work we therefore sought to thoroughly characterize the oligomeric state of CIB2 and the interaction with its established target. A variety of mass spectrometry (MS)-based techniques, including native ESI-MS, MALDI-TOF-MS, and cross-linking/MS (XL-MS) experiments of the intact protein, were integrated with novel SEC and DLS experiments based on a more accurate selection of the heterogeneous components of the elution bands. The analysis of the newly assessed hydrodynamic properties of CIB2, in comparison with those of two other  $\text{Ca}^{2+}$ -sensors, namely calmodulin (CaM) and recoverin (Rec), helped explaining the misinterpretation in our previous results as to the dimeric nature of CIB2, thus calling for particular caution when using analytical SEC for assessing the apparent molecular weight of  $\text{Ca}^{2+}$ -sensor proteins. The MS-based techniques as well as surface plasmon resonance (SPR) analysis exclude dimerization of CIB2 over the broad range of conditions tested in this study, and highlight a specific interaction only with the membrane proximal segment of the cytoplasmic domain of  $\alpha 7\text{B}$  integrin, in line with previous results by us<sup>8</sup> and others<sup>7</sup>, revealing no significant interaction with the C-terminus proximal region.

## Results and Discussion

**Native Mass Spectrometry and XL-MS analyses do not show evidence of CIB2 dimers.** Native electrospray ionization (ESI)-MS served to investigate the oligomeric state of CIB2. Figure 2A shows that under native pH conditions CIB2 appears in the three main charge states 8+ to 10+ with signals at  $m/z$  2178, 2420, and 2722. Deconvolution of the mass spectrum yielded a molecular mass of 21,767 Da, which is in perfect agreement with the mass of 21.7 kDa. Strikingly, no signals of CIB2 dimers, nor higher order oligomers were detected in native MS experiments.

In addition, CIB2 was subjected to chemical cross-linking with DSBU (disuccinimidyl dibutyric urea) in the presence of the two peptides  $\alpha 7\text{B}_\text{M}$  and  $\alpha 7\text{B}_\text{Scrb}$  (Fig. 2B,C). While peptide  $\alpha 7\text{B}_\text{M}$  is supposed to bind to CIB2, the scrambled peptide  $\alpha 7\text{B}_\text{Scrb}$  should not show complex formation with CIB2. CIB2 appears in the MALDI-TOF mass spectrum at  $m/z$  21,770 (Fig. 2B, black line). With increasing amount of peptide  $\alpha 7\text{B}_\text{M}$ , a 1:1 CIB2/peptide complex appears in the mass spectra, as is visible from the signals between  $m/z \sim 24,000$  and 26,000 (Fig. 2B). The calculated mass of a 1:1 CIB2/peptide complex with one cross-linker molecule is 23,964 Da. The mass spectrum indicates the additional attachment of two to five cross-linker molecules to the 1:1 complex where the cross-linker DSBU has either reacted at both sides or is partially hydrolyzed. A weak signal for a 1:2 CIB2/ $\alpha 7\text{B}_\text{M}$  peptide complex is also visible in the mass spectrum (signals between  $m/z$  26,500 and 28,000). Moreover, CIB2 was detected without peptide, but decorated with one to five DSBU cross-linker molecules. As such, the signal at  $m/z$  21,967 corresponds to CIB2 that is intramolecularly cross-linked with one DSBU molecule ( $\Delta m = 196 \text{ u}$ ).

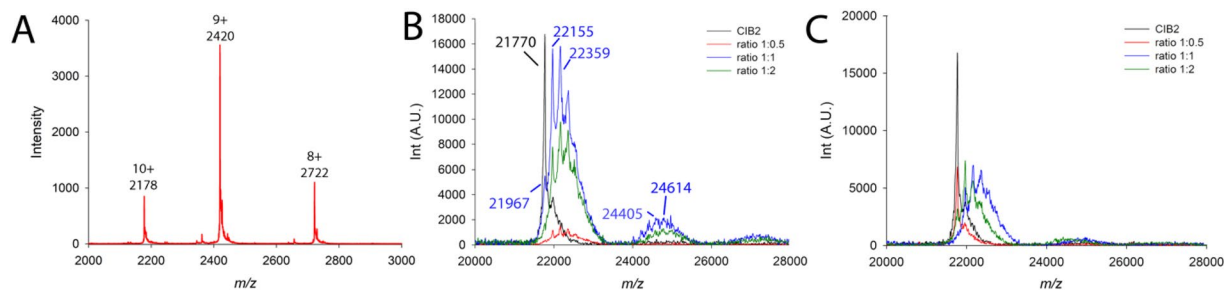


**Figure 2.** Results from MS experiments. (A) Native ESI mass spectra collected in the presence of 14  $\mu\text{M}$  CIB2 in 200 mM ammonium acetate, pH 6.8. Collision energy was set to 60 V. (B,C) MALDI-TOF-MS measurements of cross-linked CIB2 samples with peptides  $\alpha 7\text{B}_\text{M}$  (B) and  $\alpha 7\text{B}_\text{Scrb}$  (C). 10  $\mu\text{M}$  CIB2 was cross-linked with 50-fold molar excess of DSBU with increasing concentrations (5  $\mu\text{M}$ , red line; 10  $\mu\text{M}$ , blue line; 20  $\mu\text{M}$ , green line) of  $\alpha 7\text{B}_\text{M}$  (B) and  $\alpha 7\text{B}_\text{Scrb}$  (C) peptides in the presence of 1 mM  $\text{Mg}^{2+}$  and 2 mM  $\text{Ca}^{2+}$ . Between 1000 to 3000 laser shots were accumulated to one MALDI-TOF mass spectrum. CIB2 without DSBU cross-linker was included as internal control (black line).

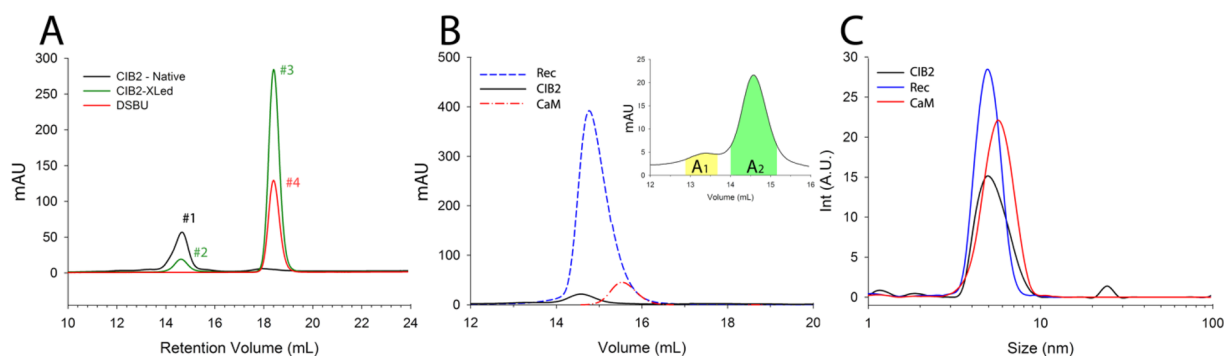


**Figure 3.** Investigation of apparent MW of CIB2 including other two  $\text{Ca}^{2+}$ -sensor proteins by analytical SEC (A,B) and DLS (C). (A) MW investigation of CIB2 before (black line) and after (green line) modification with DSBU. One reaction was performed in the presence of sole DSBU (red line). (B) CIB2 ( $\sim 70 \mu\text{M}$ ), Rec ( $\sim 80 \mu\text{M}$ ) and CaM ( $\sim 110 \mu\text{M}$ ) were loaded into an analytical SEC column previously equilibrated with 20 mM HEPES pH 7.4, 150 mM KCl, 1 mM DTT, 1 mM  $\text{Mg}^{2+}$ , 2 mM  $\text{Ca}^{2+}$ . The inset shows the zoom of CIB2 elution profile that was collected in two different fractions, represented by the colored areas. (C) The hydrodynamic diameters of the eluted peaks were assessed by DLS: 15 to 30 measurements were collected for each sample at 37  $^\circ\text{C}$ , consisting in at least 13–15 repetitions. The presented curves represent the average distribution. The protein concentration in the eluted fractions was found to be: 11  $\mu\text{M}$  (Rec), 7.4  $\mu\text{M}$  (CaM) and 1.8  $\mu\text{M}$  (CIB2).

In contrast, cross-linking between CIB2 and peptide  $\alpha 7\text{B}_\text{Scrb}$  showed only minor signals for a 1:1 complex (Fig. 2C), but CIB2 was mainly found to be modified with one to five DSBU molecules (signals between  $m/z \sim 22,000$  and  $23,000$ ).

Given that native ESI-MS only showed a CIB2 monomer and furthermore, in cross-linking experiments, a 2:1 CIB2 and peptide  $\alpha 7\text{B}_\text{M}$  complex was never observed, this clearly points to monomeric rather than dimeric CIB2.

### Analytical size exclusion chromatography and dynamic light scattering of CIB2, CaM and Rec highlight different hydrodynamic properties.

Previous analytical SEC experiments of CIB2 under reducing conditions displayed elution profiles corresponding to an apparent MW in the 37–39 kDa range in different cation-bound states, thus compatible with a dimer and incompatible with a monomer<sup>8</sup>. Moreover, DLS experiments performed with the samples collected immediately after elution from the SEC column measured a relatively high hydrodynamic diameter ( $d^{\text{Mg}} = 8.43 \text{ nm}$  and  $d^{\text{Ca}} = 8.18 \text{ nm}$ ), which was also interpreted as an evidence of a dimeric protein<sup>8</sup>. Since the present MS-based data appear to be in clear contradiction with previous findings, we repeated both analytical SEC and DLS using identical conditions as for the XL-MS experiments. Results are reported in Fig. 3.

In the presence of 1 mM  $\text{Mg}^{2+}$ , 2 mM  $\text{Ca}^{2+}$  and DSBU cross-linker (same conditions as those used in XL-MS experiments) CIB2 showed a SEC elution profile (Fig. 3A, green curve) that substantially overlapped with that of the protein without cross-linker (Fig. 3A, black curve) when the first elution peak is concerned (see peaks #1 and #2). According to a calibration curve obtained with globular proteins of known MW, these bands would correspond to an apparent MW ( $M^{\text{WSEC}}$ ) of 35.9 kDa in the absence and of 36.7 kDa in the presence of the cross-linker, thus very similar to those obtained in our previous work under slightly different conditions. The second prominent peak at higher elution times observed for cross-linked CIB2 (Fig. 3A, green curve, peak #3) corresponds to

	HydroPro $\Phi$ (nm)	Gyration radius (nm)	DLS $\Phi$ [n] (nm) <sup>a</sup>	Hydrophobic SAS area (nm <sup>2</sup> )	Hydrophilic SAS area (nm <sup>2</sup> )	Total SAS area (nm <sup>2</sup> )	MW (kDa)	MW <sup>SEC</sup> (kDa)
CIB2 (13–184) <sup>b</sup>	4.736	1.88	5.4 ± 0.2 [15]	59.94	55.34	115.38	21.3	37.8 (A <sub>2</sub> band)
Rec (1–201) <sup>b</sup>	5.112	1.94	5.0 <sup>a</sup> ± 0.1 [18]	62.54	64.68	127.23	23.3	33.5
CaM (1–149) <sup>b</sup>	5.076	2.22	5.8 ± 0.1 [30]	50.28	54.97	105.26	16.8	20.5

**Table 1.** Comparison of the hydrodynamic properties of CIB2, CaM and Rec. <sup>a</sup>Data are reported as mean ± SEM; n represents the number of measurements used for the calculation. <sup>b</sup>Sequence coverage of the structural models used for hydrodynamic diameter calculation.

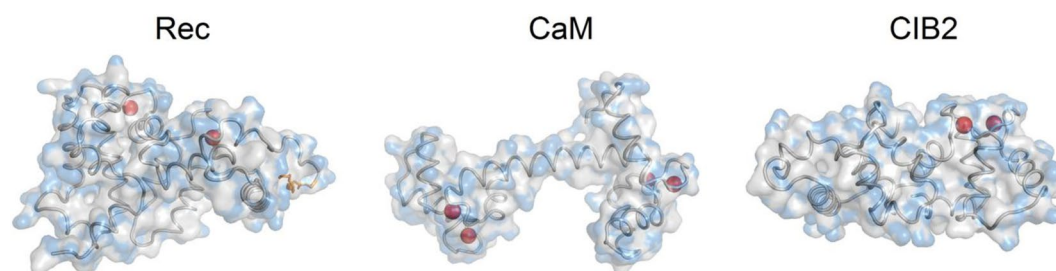


**Figure 4.** Three-dimensional structures of bovine Rec (left), human CaM (center) and human CIB2 (right) used for hydrodynamic diameter estimation. Proteins secondary structure is shown as grey tubes, Ca<sup>2+</sup> ions are represented as red spheres, myristoyl group is shown as orange sticks, hydrophilic and hydrophobic solvent accessible surfaces are represented in transparency as blue and grey surfaces, respectively.

the elution of DSBU compounds, as proved by the complete overlapping with the band obtained when eluting DSBU alone (red curve, peak #4). The chemical nature of the eluate was further confirmed by NMR spectroscopy (data not shown). Therefore, although an MW<sup>SEC</sup> of 37–39 kDa previously drove us to the conclusion that a protein with actual MW of 21.6 kDa eluted as a dimer, our MS and XL-MS results clearly show that the interpretation was not correct in the case of CIB2, which remained monomeric in all tested conditions.

To further investigate the nature of the misleading result we performed analytical SEC of two other Ca<sup>2+</sup>-sensors of similar size in the same conditions in which CIB2 was shown to elute with a significantly higher MW than that expected for a monomer. For this purpose, we used CaM (16.8 kDa) and Rec (23.3 kDa), which are both well characterized, Ca<sup>2+</sup>-sensor proteins. The three-dimensional structure of the three proteins was also used to estimate the theoretical value of the hydrodynamic diameter by the HydroPro software<sup>16</sup> and compare it with that measured by DLS right after the elution from the SEC column. Quantitative results are reported in Table 1.

SEC elution profiles (Fig. 3B) showed a main elution peak for each Ca<sup>2+</sup>-sensor, which corresponds to an MW<sup>SEC</sup> of 37.8 kDa for CIB2, 33.5 kDa for Rec and 20 kDa for CaM (Table 1). A closer look at the elution profile of CIB2, however, showed the presence of a lower intensity shoulder at lower elution time (Fig. 3B; inset). This shoulder (here denominated A<sub>1</sub>) was collected together with the main peak (A<sub>2</sub>) in our previous work<sup>8</sup>. In contrast, the two fractions were separately collected and analyzed in the present study. Interestingly, the effect of A<sub>1</sub>, with a predicted MW<sup>SEC</sup> of 81.3 kDa was that of rendering the colloidal suspension analyzed by DLS more disperse and to confer CIB2 an apparently higher hydrodynamic radius. Indeed, when A<sub>2</sub> was analyzed by DLS as separated from A<sub>1</sub> (Figs 3C and S1), a lower hydrodynamic diameter was determined (5.4 ± 0.2 nm; Table 1 and Fig. S1), which was similar to that of Rec (5.0 ± 0.1 nm; Table 1 and Fig. S1) and CaM (5.8 ± 0.1 nm; Table 1 and Fig. S1), and significantly lower compared to that previously measured for CIB2 when both A<sub>1</sub> and A<sub>2</sub> were collected in one sample (d<sup>Mg</sup> = 8.4)<sup>8</sup>. We thus conclude that our inferences as to the dimeric nature of CIB2 based on previous DLS experiments were affected by the presence of the A<sub>1</sub> band, as current DLS data based on a more accurate selection of the elution peak confirm the monomeric form of CIB2.

An apparent joint feature of Rec and CIB2 is that their estimated MW<sup>SEC</sup> is significantly higher than that of a monomer (Table 1). Although Rec has been shown to dimerize in the presence of Ca<sup>2+</sup><sup>17</sup>, dimers were clearly isolated at protein concentrations above 100 μM, so we assume that in our experiments Rec was mostly monomeric. We speculate that this fact could be related to the significantly higher hydrophobic solvent-accessible surface of Rec and CIB2 compared to that of CaM (60–62 nm<sup>2</sup> vs 50 nm<sup>2</sup>, Table 1; Fig. 4). Solvation of their large hydrophobic surfaces might influence the interaction of CIB2 and Rec with the column matrix and result in lower retention time, that is higher MW<sup>SEC</sup> compared to CaM. On the other hand, DLS data show a significantly better correlation between the measured and the theoretical hydrodynamic diameter estimated by HydroPro, especially considering that the structural model used for CIB2 was missing the first 12 residues (Table 1). The size measured by DLS seems to correlate to some extent with the radius of gyration of the protein, which accounts for molecular geometry and shape and the space distribution of amino acids. In spite of its lower MW, due to its elongated

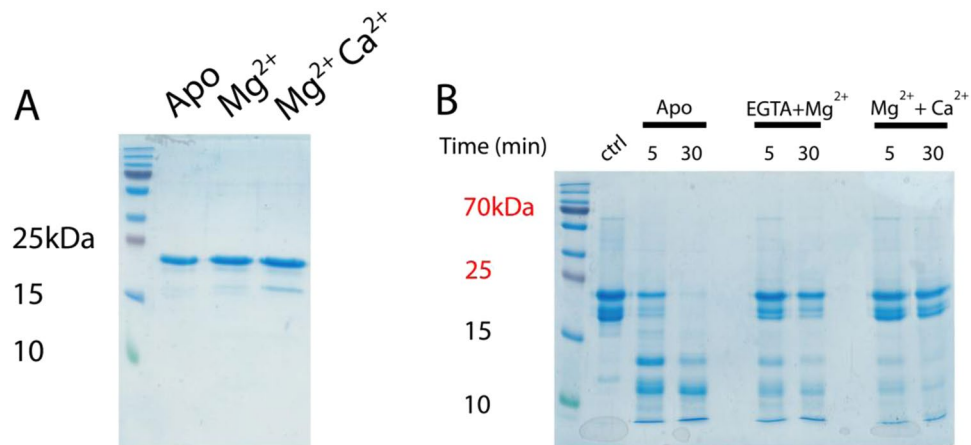


**Figure 5.** CIB2 limited proteolysis. (A) 10  $\mu\text{M}$  CIB2 was incubated at 25  $^{\circ}\text{C}$  in the presence of 1 mM EDTA (Apo), 500  $\mu\text{M}$  EGTA + 1 mM  $\text{Mg}^{2+}$  ( $\text{Mg}^{2+}$ ) and 1 mM  $\text{Mg}^{2+}$  + 2 mM  $\text{Ca}^{2+}$  for 10 minutes at 25  $^{\circ}\text{C}$ . Samples were boiled and loaded in a 18% SDS polyacrylamide gel. (B) Limited proteolysis was performed incubating trypsin with 25  $\mu\text{M}$  CIB2 in the same concentrations of ions used for (A) (protein:enzyme ratio was 100:1). Samples were collected at different times, boiled and loaded on a 18% SDS-PAGE. Both gels run for 45–50 min, then they were Coomassie Blue-stained. The figure results from two separate gels, which have been reported in full length in Fig. S6.

form (Fig. 4) CaM has a significantly higher radius of gyration (2.22 nm) compared to Rec (1.94 nm) and CIB2 (1.88 nm), which is reflected by a significantly higher size detected by DLS (Table 1).

Although analytical SEC has been widely used to determine the molecular weight of proteins by comparing elution volume parameters with those of different known calibration standards, the elution profile of proteins is closer to their Stokes radius rather than to their effective molecular weight, and particular care should be taken when the shape of the protein is different from the generally globular shape of the standards<sup>18</sup>. For  $\text{Ca}^{2+}$ -sensor proteins, that significantly change their conformation as well as their solvation properties upon  $\text{Ca}^{2+}$  binding<sup>19–21</sup>, this aspect appears to be especially relevant. When a comparison of the hydrodynamic properties was made for a single  $\text{Ca}^{2+}$ -sensor protein in the presence of several point mutations, a significant correlation between SPR, DLS, and SEC data was observed<sup>21</sup>, but comparisons cannot be easily extended to different proteins with different shapes and hydration shells due to different hydrophobic SAS. In conclusion, one should be extremely careful when using analytical SEC for assessing  $\text{MW}^{\text{SEC}}$  based on a standard of unrelated proteins and should always look for other independent estimates.

**$\text{Ca}^{2+}$  and  $\text{Mg}^{2+}$  binding stabilize CIB2 tertiary structure.** It was previously shown by NMR spectroscopy that saturation with either  $\text{Mg}^{2+}$  or  $\text{Ca}^{2+}$  makes CIB2 switch from a molten globule state to a structurally-folded state with very similar tertiary structure<sup>7,8</sup>. We performed limited proteolysis experiments to assess the sensitivity of CIB2 structural states to protease digestion. It is indeed known that binding of specific ligands may significantly affect the accessibility of proteins to proteases, thus providing useful information as to protein flexibility<sup>22</sup>.

Incubation of CIB2 with trypsin showed a clear time-dependent proteolytic pattern, which was found to depend on the cation-bound state (Fig. S2). We chose to further analyze the proteolytic pattern after 5 minutes and 30 minutes for apo-CIB2, as well as for the protein in the presence of 1 mM  $\text{Mg}^{2+}$  and after the further addition of 2 mM  $\text{Ca}^{2+}$  (Fig. 5).

Even without the addition of trypsin, CIB2 showed some propensity to degradation, as shown by the faint band appearing after 10 minutes at 25  $^{\circ}\text{C}$  under all tested conditions (Fig. 5A). The band was impossible to eliminate completely with the purification procedure and was observed previously before and after the cleavage of the His-tag<sup>8</sup>. MALDI experiments confirmed the presence of 16–17 kDa fragments (results not shown). The fact that the intensity of this band increased significantly in the time frame of the proteolysis experiments (Fig. 5B, control lane) supports its presumed nature.

Limited proteolysis clearly showed that after 30 min incubation with trypsin the native band of apo-CIB2 was completely lost, and several proteolytic fragments at lower molecular weight appeared. Interestingly, incubation with either  $\text{Mg}^{2+}$  or  $\text{Ca}^{2+}$  and  $\text{Mg}^{2+}$  permitted the detection of the native CIB2 band even after 30 min, although some smaller proteolytic fragments of comparable MW as to the ones for apo-CIB2 were clearly detected (Fig. 5B). Thus,  $\text{Mg}^{2+}$  and  $\text{Ca}^{2+}$  seem to exert a protective role in terms of accessibility to the protease, as a result of more rigid conformation, in line with previous observations<sup>7,8</sup>. It should be pointed, however, that some flexible regions remain even in the cation-complexed state, as clearly shown by the smaller MW bands.

In order to investigate the nature of the most flexible regions observed in cation-complexed CIB2, we performed 400 ns Molecular Dynamics (MD) simulations of  $\text{Ca}^{2+}$ -CIB2 and computed the Root Mean-Squared Fluctuation index (RMSF) of  $\text{C}\alpha$  atoms. RMSF provides information as to the average displacement of selected atoms with respect to the initial position during the time course of the simulation, thus providing information

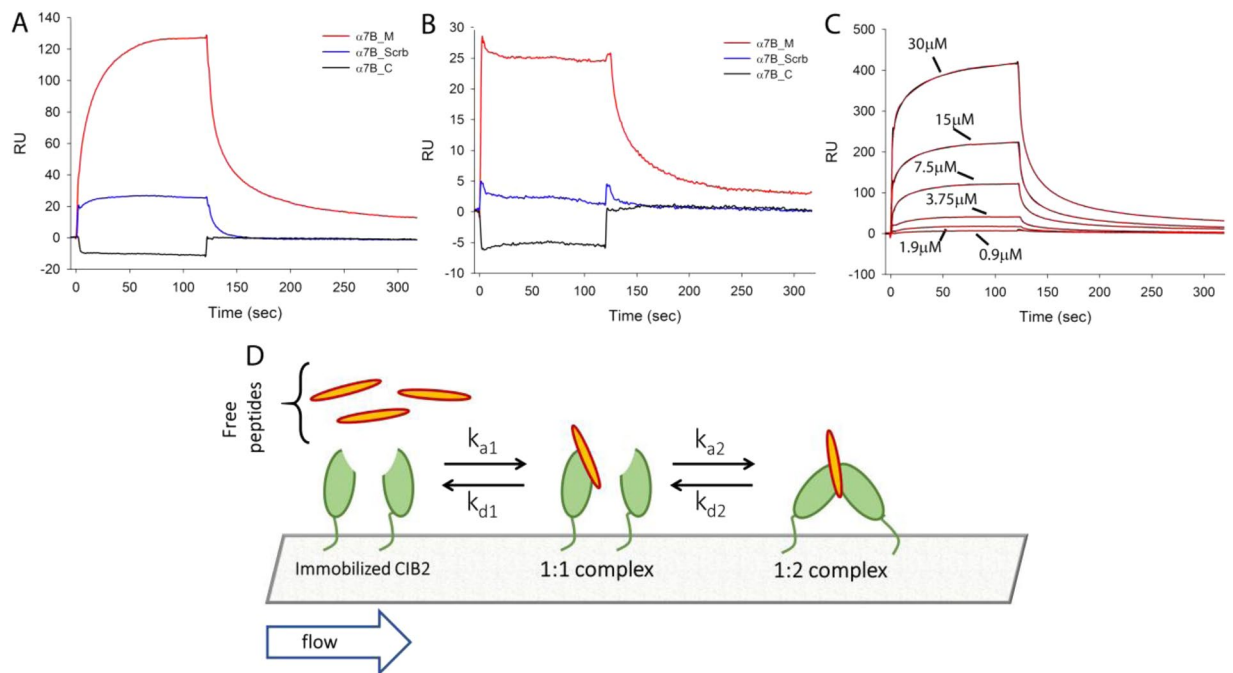


**Figure 6.** SPR measurements of CIB2-peptide interaction. (A) Either  $\alpha 7B\_M$ ,  $\alpha 7B\_Scrb$  or  $\alpha 7B\_C$  peptides ( $7.5 \mu M$ ) were injected over His-CIB2 homogeneously immobilized by His-tag on the chip surface. (B)  $30 \mu M$  of the same peptides were injected over untagged CIB2 previously immobilized on the surface of a COOH5 chip via amine coupling. (C) Increasing concentrations of  $\alpha 7B\_M$  peptide were injected on His-CIB2 immobilized as in (A). Experimental data (black curves) were fitted to a bivalent analyte kinetic model (red curves). All the experiments were performed using 20 mM HEPES pH 7.5, 150 mM KCl, 1 mM DTT, 1 mM  $Mg^{2+}$ , 2 mM  $Ca^{2+}$ , 50  $\mu M$  EDTA, 0.005% Tween as buffer. Two minutes injections were performed using a flow rate of  $20 \mu L \text{ min}^{-1}$ , dissociations were followed for 200 seconds. (D) A possible scheme of CIB2- $\alpha 7B\_M$  interaction compatible with the kinetic model. The interaction of a CIB2 monomer immobilized on the chip (green) with a peptide (orange) can lead to the binding of another CIB2 molecule; all steps are fully reversible.

on protein flexibility. The RMSF profile of  $Ca^{2+}$ -saturated CIB2 (Fig. S3) is that of a somewhat flexible protein, as other WT  $Ca^{2+}$ -sensors that underwent the same MD simulation procedure displayed significantly lower RMSF distributions<sup>23–26</sup>. The structural regions that showed higher flexibility are the pseudo EF1 motif (yellow segment, Figs 1 and S3), the loop linking EF3 and EF4 (orange and blue), the end of the exiting helix in EF4 and the C-terminus (blue and cyan). We speculate that these regions could be those that remain accessible to trypsin even when CIB2 is bound to  $Ca^{2+}$ , due to their high intrinsic flexibility.

**Surface plasmon resonance points to monomeric CIB2 and highlights a low-affinity interaction with the membrane proximal segment of  $\alpha 7B$  integrin.** SPR is a powerful and versatile technique to detect at real time biomolecular interactions, and it can be applied to study protein oligomerization, in particular dimerization, when care is taken to immobilize on the surface of a sensor chip low amounts of proteins under controlled conditions<sup>27–29</sup>. Two independent experiments were run following low levels of amine-coupling of CIB2 (130 RU and 226 RU, respectively) on the surface of a sensor chip. In no case was a signal detected when injecting uncoupled CIB2 in the 92 nM – 46  $\mu M$  range in the presence of  $Ca^{2+}$  and  $Mg^{2+}$  (results not shown). Hence, SPR did not detect dimerization for CIB2 over a broad range of concentrations.

SPR was also used to study quantitatively the interaction of CIB2 with one of its established targets, namely the cytoplasmic domain of integrin  $\alpha 7B$ <sup>3,7</sup>. Three different peptides were used in the interaction experiments. A peptide corresponding to the membrane proximal segment of the cytoplasmic domain of  $\alpha 7B$  integrin ( $\alpha 7B\_M$ ), another peptide with the same amino acid content, but randomized sequence ( $\alpha 7B\_Scrb$ ) and a peptide covering the C-terminal region of the cytoplasmic domain of  $\alpha 7B$  integrin ( $\alpha 7B\_C$ ). Three different approaches were used. In a first approach, His-tagged CIB2 was initially coupled to the surface of a His-cap sensor chip (see Methods), thus ensuring homogeneous site-specific orientation, and then blocked via standard amine coupling. Near-UV CD spectroscopy (Fig. S4) confirmed that the His-tagged CIB2 had substantially the same tertiary structure of the untagged protein, and identically responded to  $Mg^{2+}$  and  $Ca^{2+}$ . The minor differences in the spectra at the level of the phenylalanine band can be ascribed to the TEV-protease recognition site (ENLYFQ), uncleaved in the His-tagged protein. In a second approach, the  $\alpha 7B\_M$  peptide was immobilized on the surface of a sensor chip by amine coupling at levels comparable to those for CIB2 in the former approach (2250 RU). In a third approach, we used the same low levels of CIB2 immobilization via amine coupling described in the experiments to probe CIB2 dimerization (100–200 RU) and flowed the three peptides. Examples of the obtained sensorgrams are reported in Fig. 6.

	$k_{a1}$ ( $M^{-1}s^{-1}$ ) <sup>a</sup>	$k_{a2}$ ( $RU^{-1}s^{-1}$ )	$k_{d1}$ ( $s^{-1}$ )	$k_{d2}$ ( $s^{-1}$ )	$K_D^{app1}$ ( $\mu M$ ) <sup>b</sup>	$K_D^{appTOT}$ ( $\mu M$ ) <sup>c</sup> (N = 28)
1 mM $Mg^{2+}$ (N = 16)	$(3.1 \pm 0.1) \times 10^4$	$(1.9 \pm 0.4) \times 10^{-3}$	$(3.6 \pm 0.5) \times 10^{-1}$	$(2.0 \pm 1.7) \times 10^{-2}$	$11.6 \pm 1.8$	$210 \pm 20$
1 mM $Mg^{2+}$ 2 mM $Ca^{2+}$ (N = 15)	$(1.6 \pm 0.2) \times 10^4$	$(4.2 \pm 0.5) \times 10^{-4}$	$(4.0 \pm 0.3) \times 10^{-1}$	$(5.3 \pm 0.5) \times 10^{-2}$	$25 \pm 5$	$154 \pm 8$

**Table 2.** Results from Surface Plasmon Resonance analysis of CIB2- $\alpha 7B\_M$  interaction. <sup>a</sup>Kinetic constants were determined according to a bivalent analyte model as explained in Methods. N refers to the number of independently analyzed sensorgrams. Results refer to average  $\pm$  SEM. <sup>b</sup>Apparent affinity for the first binding event, determined by the ratio  $k_{d1}/k_{a1}$ . <sup>c</sup>Apparent affinity constant accounting for avidity, determined by steady state analysis, measured by taking the maximum response  $RU^{max}$  for a series of 4 repetitions of 7 injections of  $\alpha 7B\_M$  at increasing concentrations.

The second approach (direct peptide immobilization) led to very low signals and unreproducible results and was not pursued any further. Interestingly, both homogenous and site-specific coupling of CIB2 via its His-tag (approach 1) and heterogeneous coupling via non-specific amine coupling (approach 2) showed sensorgrams incompatible with a typical 1:1 Langmuir adsorption process. The two experiments showed clearly different association kinetics, and yet very similar dissociation kinetics incompatible with a monophasic exponential profile (Fig. 6A,B). In spite of such differences, which might reflect both the heterogeneity of the surface and the different chemistry of immobilization, interaction results were consistent with one another. Indeed, both experiments confirmed that  $\alpha 7B\_M$  binds to CIB2 significantly stronger than the control peptide  $\alpha 7B\_Scrb$ , which was shown to interact with low affinity also in MALDI experiments (Fig. 2B,C), where a band was detected in the same stoichiometric conditions, although with lower intensity. Moreover, the assays could not detect any interaction with the  $\alpha 7B\_C$  peptide over the whole range of tested conditions. In this respect, our results are in line with those by Huang *et al.*<sup>7</sup>, who by fluorescence spectroscopy detected a much stronger interaction of CIB2 with the membrane-proximal region of the cytosolic tail of  $\alpha 7B$  integrin (corresponding to  $\alpha 7B\_M$ ), and a much weaker interaction with the C-terminal region, corresponding to the  $\alpha 7B\_C$  peptide, at odds with Häger *et al.*<sup>3</sup>, who tested and detected interaction with the C-terminal region of  $\alpha 7B$ . It should be noted that both Huang *et al.*<sup>7</sup> and Häger *et al.*<sup>3</sup> used peptides from mouse integrin, while we used the corresponding human sequences, which in the case of  $\alpha 7B\_C$  lacks the tryptophan residue present in the mouse sequence. It is not uncommon that fluorescence spectroscopy interaction studies based on the peptide intrinsic fluorescence (CIB2 has no tryptophan residue) reveal some non-specific binding, especially when a highly hydrophobic protein such as CIB2 is the ligand. Indeed, in our previous work we observed some non-specific signal when titrating CIB2 with  $\alpha 7B\_Scrb$ , although fluorescence variation upon titration with  $\alpha 7B\_M$  was much higher<sup>8</sup>. It cannot be excluded that a similar phenomenon occurred for murine  $\alpha 7B\_C$  in the work by Häger *et al.*<sup>3</sup>. Our present results, based on accurate, label-free interaction studies clearly identify the region covered by  $\alpha 7B\_M$  as the preferential binding site of CIB2 with  $\alpha 7B$  integrin.

SPR titrations of  $\alpha 7B\_M$  over homogeneously coupled CIB2 (approach 1) gave very reproducible results and were performed both in the presence of 1 mM  $Mg^{2+}$  and in the co-presence of 1 mM  $Mg^{2+}$  and 2 mM  $Ca^{2+}$ . Peptide concentration was varied in the 230 nM–30  $\mu M$  range. An example of such titration is reported in Fig. 6C. As anticipated, sensorgrams could not fit to a 1:1 binding model, and the kinetic model that better fit the data was a bivalent analyte model (see Methods), in which one  $\alpha 7B\_M$  peptide could bind to two CIB2 molecules. According to this scheme, binding of the peptide to the first CIB2 molecule would direct the binding to the second one, thus resulting in two sets of kinetic constants. Data fitting to this model was very good over the broad range of concentrations tested (Fig. 6C) and resulted in the kinetic parameters reported in Table 2. The same table also shows the results from steady state analysis, which allows an estimate of the total apparent affinity  $K_D^{appTOT}$  accounting for avidity effects, as compared to that determined by the first binding event (one peptide to one CIB2 molecule,  $K_D^{app1}$ ).

Our data suggest that CIB2 binds the  $\alpha 7B\_M$  peptide with a relatively low affinity and that the formation of a protein-peptide complex may drive the binding of a second CIB2 molecule. Since CIB2 *per se* is monomeric, our data cannot exclude that binding of a target peptide induced dimerization of CIB2 on the chip, which would explain the high maximal response in terms of RU obtained in our binding experiments (Fig. 6C). Whether this process has a physiological meaning remains to be clarified. Interestingly, both the association process of  $\alpha 7B\_M$  to the first CIB2 molecule, and then the association of the complex with a second CIB2 molecule occurred faster in the sole presence of  $Mg^{2+}$  compared to the co-presence of  $Ca^{2+}$  (2-fold for the first and 5-fold for the second binding event, respectively; Table 2). The dissociation process was not found to significantly depend on the cation conditions, the only significant difference being the 2.5 times faster dissociation of the second CIB2 molecule in the co-presence of  $Mg^{2+}$  and  $Ca^{2+}$ . In conclusion, the presence of  $Ca^{2+}$  seems to affect the recognition process of CIB2 and  $\alpha 7B$  in a complex way: it induces slower association and a slightly faster dissociation of the first CIB2-peptide complex, thus resulting in roughly half affinity compared to  $Mg^{2+}$  alone ( $K_D^{app1} = 25 \mu M$  vs  $11.6 \mu M$ ), however when the whole binding process is considered avidity comes into play and the apparent affinity in the presence of both  $Mg^{2+}$  and  $Ca^{2+}$  ( $K_D^{appTOT} = 154 \mu M$ ) seems to be slightly higher compared to that measured in the sole presence of  $Mg^{2+}$  ( $K_D^{appTOT} = 210 \mu M$ ).

To our knowledge, no other kinetic study was performed so far for CIB2-target recognition, the only possible comparison is thus with previous SPR experiments performed with the homolog CIB1 protein interacting with a peptide from  $\alpha IIb$  integrin<sup>30</sup>, which according to a 1:1 binding model revealed a very similar apparent



affinity ( $K_D^{\text{app}} = 12 \mu\text{M}$ ) without significant dependency on  $\text{Ca}^{2+}$ . It should be noted, however, that sequence and presumably structural/functional features of CIB2 could significantly differ from those of CIB1<sup>8</sup> and that even for the same system different studies reported quite different affinities, probably due to the heterogeneous set of experimental techniques used (see ref.<sup>31</sup> for a review).

**Interaction between CIB2 and  $\alpha 7\text{B}_\text{M}$  and structural rearrangement.** SPR data suggest a relatively low affinity interaction of CIB2 with the  $\alpha 7\text{B}_\text{M}$  peptides, and results from MALDI experiments seem to support this finding (Fig. 2B).

Near-UV CD spectroscopy was used to study the structural effects of the binding of  $\alpha 7\text{B}_\text{M}$  peptide to CIB2 in the presence and in the absence of cations (Fig. S5). The isolated peptide was unfolded in all the tested cases, but interestingly, when incubated with CIB2 some structural effects could be observed both for 1:1 and 2:1 peptide:protein conditions. For apo-CIB2, although the spectrum was still compatible with a molten globule state (Fig. S5A), peptide induced a finer spectrum in the phenylalanine and tyrosine bands, thus suggesting interaction between CIB2 and  $\alpha 7\text{B}_\text{M}$  even in the absence of cations. When the incubation was done in the presence of  $\text{Mg}^{2+}$  as well as in the co-presence of  $\text{Ca}^{2+}$ , the intensity of the resulting spectrum was lower compared to that of CIB2 without the peptide (Fig. S5A,B) and the decrease was proportional to the stoichiometric peptide:protein ratio, being especially apparent for the 2:1 ratio. A closer inspection showed mild alterations of the spectrum especially of the level of the phenylalanine band, with some smoothening of the tyrosine region in the case of incubation with only  $\text{Mg}^{2+}$ , however no clear signal was visible in the typical 285–305 nm tryptophan region. Since  $\alpha 7\text{B}$  has one tryptophan and CIB2 has none, the lack of signal following incubation suggests that the peptide did not acquire a defined structure upon interaction, at least not completely. If this was the case, the effect would have been likely visible, such as in the case of calmodulin-target interaction<sup>32,33</sup>. The decrease in the intensity of near-UV CD spectrum, more prominent for the case of  $\text{Mg}^{2+}$  alone, could then be attributed to some global effect such as increased flexibility and/or solvent accessibility of CIB2 upon interaction with the peptide, or even a dimerization of CIB2 induced by the bound peptide, which would lead to enhanced exposure of aromatic residues to the solvent.

## Conclusions

$\text{Ca}^{2+}$ -binding proteins belonging to the EF-hand superfamily may exist in a variety of conformational states<sup>34</sup> and many were found to form dimers depending on their cation-loading state and concentration<sup>35</sup>. CIB2 has been found to form dimers in previous studies, where it was fused with GFP<sup>11,12</sup> and tdTomato fluorescent protein<sup>11</sup> and studied in FRET and co-immunoprecipitation experiments. Our previous work with untagged purified CIB2 also concluded that CIB2 is dimeric<sup>8</sup>. We now provide new lines of evidence that allow us to reconsider some of the previous findings in the light of MS and SPR data. Based on our extensive analysis performed in a variety of conditions and over a broad range of concentrations we can conclude that CIB2 is *per se* monomeric, but presents uncommon hydrodynamic properties likely due to the high content of hydrophobic solvent accessible surface, which may lead to the erroneous appearance of a dimer. This feature, together with the possible interaction between fusion-proteins or tags and the highly hydrophobic surface of CIB2 calls for special care when assessing its oligomeric state.

Interaction with  $\alpha 7\text{B}$  occurs in the region proximal to the membrane and not close to the C-terminus of the cytosolic domain of the integrin. The recognition between CIB2 and the  $\alpha 7\text{B}$  target is kinetically favored in the presence of physiological  $\text{Mg}^{2+}$  and in the absence of  $\text{Ca}^{2+}$  and it might induce binding of another CIB2 molecule. This hypothesis seems to be in line with our previous fluorescence data where CIB2 was shown to interact with the target peptide with a 2:1 stoichiometry<sup>8</sup>. However, CIB2 *per se* binds a single peptide as a monomer, and the complex could then induce CIB2 dimerization, where the dimer is bridged by the target. Considering the largely unknown biological function of CIB2 and that the homolog protein CIB1 allows a high degree of promiscuity in target recognition<sup>31</sup>, this putative mechanism of target-induced dimerization might play a role in integrin signaling. Whether this intriguing scenario may have any physiological consequence needs to be further investigated.

## Methods

**Protein and peptide preparation and purification.** Recombinant human CIB2 was obtained exactly as explained in our previous work<sup>8</sup>. Untagged protein was used for all experiments except for one case of SPR interaction where the TEV protease recognition site and the Histag were kept. Human CaM and bovine Rec were expressed and purified as described in previous work<sup>36,37</sup>.

Peptides were purchased from Genscript and had the following sequence:  $\alpha 7\text{B}_\text{M}$  LLLWKMGFFKRAKHPE (HPLC purity = 96.7%),  $\alpha 7\text{B}_\text{S}$  KEFWGLHAKPRLKLMF (HPLC = 96.3%),  $\alpha 7\text{B}_\text{C}$  LAADGHPGLGPDGHPGPTA (HPLC = 98.8%). Both  $\alpha 7\text{B}_\text{M}$  and  $\alpha 7\text{B}_\text{S}$  were C-terminal amidated and N-terminal acetylated, while  $\alpha 7\text{B}_\text{C}$  was N-terminal acetylated. All peptides were initially resuspended in pure water and then diluted at final concentration in the working buffer.

**Cross-linking reactions.** CIB2 samples were cross-linked with DSBU in the presence of peptide  $\alpha 7\text{B}_\text{M}$  or  $\alpha 7\text{B}_\text{S}$  as described in ref.<sup>14</sup> Briefly,  $10 \mu\text{M}$  CIB2 was diluted in 20 mM HEPES, pH 7.5, 1 mM DTT, 1 mM  $\text{Mg}^{2+}$  and 2 mM  $\text{Ca}^{2+}$  and incubated with increasing peptide concentrations (5  $\mu\text{M}$ , 10  $\mu\text{M}$ , and 20  $\mu\text{M}$ ) for 10 min at room temperature. Then, 50-fold molar excess of DSBU was added and the reactions were conducted for 20 min at room temperature. As control, CIB2 was treated with DSBU without peptide. Reactions were blocked by adding ammonium bicarbonate to a final concentration of 20 mM.

**Mass spectrometry.** Cross-linked CIB2 samples were desalted via ZipTip C4 tips (Millipore) before MALDI-TOF-MS analysis (Ultraflex III MALDI-TOF/TOF mass spectrometer, Bruker Daltonik, Bremen) was

conducted using sinapinic acid as matrix. For further details see Supplementary Methods. Baseline subtraction and spectra smoothing were performed.

For native ESI-MS analyses (High-Mass Q-TOF II mass spectrometer, Waters/MSVision), CIB2 was prepared in 200 mM ammonium acetate, pH 6.8.

**Analytical size exclusion chromatography.** The molecular weight (MW) of the proteins was determined before and after DSBU-modification as previously described<sup>7</sup> in the same buffer (20 mM HEPES, pH 7.5, 1 mM DTT, 1 mM Mg<sup>2+</sup> and 2 mM Ca<sup>2+</sup>). Protein concentration was determined by Bradford Assay and was found to be 113 μM for CaM and between 70–80 μM for CIB2 and Rec. Standard calibration curve for MW estimation was the same used in our previous study<sup>8</sup>.

**DLS experiments.** DLS measurements were performed using Zetasizer Nano-S (Malvern Instruments) at 37 °C by setting the same parameters for hydrodynamic diameter estimation as in ref.<sup>26</sup>. The estimation was based on 15–30 measurements, each consisting of at least 13 repetitions; data in Table 1 are reported as mean ± standard error of mean (SEM). DLS samples for each protein are the same collected in the Analytical Size Exclusion Chromatography. Protein concentration was measured by Bradford Assay for Rec, CaM and CIB2 and was found to be 11 μM, 7.4 μM and 1.8 μM respectively.

**Circular dichroism spectroscopy.** CIB2 tertiary structure was investigated by using a Jasco J-710 spectropolarimeter equipped with a Peltier type cell holder as previously described<sup>37</sup>. Briefly: near-UV (250–320 nm) CD spectra of 20 μM of sole CIB2 or CIB2/α7B\_M complexes (1:1 and 1:2 ratios) were collected in the presence of 500 μM EGTA and after sequential additions of 1 mM Mg<sup>2+</sup> and 2 mM free Ca<sup>2+</sup>. A 1 cm quartz cuvette was used, temperature was set at 37 °C, integration time and data pitch were set to 4 s and 1 nm, respectively. Each spectrum represents the average of 5 accumulations.

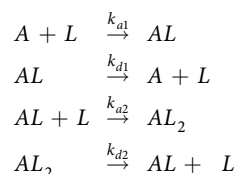
**Limited proteolysis experiments.** Limited proteolysis experiments were performed incubating 25 μM CIB2 in the presence of Trypsin (Sigma) in a ratio 1:100 enzyme:CIB2 at 25 °C. Three conditions were tested: 1 mM EDTA, 500 μM EGTA + 1 mM Mg<sup>2+</sup> and 1 mM Mg<sup>2+</sup> + 2 mM Ca<sup>2+</sup>. Time-resolved proteolysis patterns are reported in Supplementary Materials (Fig. S2), results shown in Fig. 5 refer to reactions stopped after 5 min and 30 min. Proteolysis products were loaded on a 15% or 18% SDS gel, as indicated.

**Molecular dynamics simulations.** The homology model of Ca<sup>2+</sup>-bound human CIB2 was built using the X-ray structure (resolution: 1.99 Å) of human CIB1 as a template (PDB entry: 1XO5)<sup>2</sup>, which shares 39% sequence identity with CIB2. Modeling details are provided in our previous work<sup>8</sup>. The PDB file of the model is available upon request for research purposes. MD simulations of Ca<sup>2+</sup>-bound CIB2 were performed using GROMACS 2016.1 simulation package<sup>38</sup> and CHARMM36m<sup>39</sup> all-atom force field (system size 47780 atoms). All simulation details were the same as in previous work<sup>25,40</sup>. Root-Mean Square Fluctuation of Cα along the 400-ns trajectory was calculated with respect to the equilibrated structure using “gmx rmsf” function included in GROMACS 2016.1 as previously explained<sup>23</sup>.

**Hydrodynamic diameter estimation.** Estimation of the hydrodynamic diameter was performed using Hydropro<sup>16</sup> on the structure of bovine Rec after removal of the GRK1 peptide<sup>41</sup>, and human CIB2<sup>8</sup>. Details on the preparation of human CaM structure as well as on the determination of the hydrodynamic diameter are given in the Supplementary Information.

**Surface plasmon resonance.** Details of the protein and peptide immobilization procedures and experimental settings are elucidated in the Supplementary Information.

Kinetic data were fitted according to a bivalent analyte model, where a CIB2 monomer (L) can bind an α7B\_M peptide (A), and the resulting complex (AL) can bind to a second CIB2 molecule (AL<sub>2</sub>), with all processes being possibly reversible, as follows:



The following set of ordinary differential equations can be numerically solved to determine the kinetic parameters:

$$\begin{aligned}
 \frac{d[L]}{dt} &= -(k_{a1} \cdot [A] \cdot [L] - k_{d1} \cdot [AL]) - (k_{a2} \cdot [AL] \cdot [L] - k_{d2} \cdot [AL_2]) \\
 \frac{d[AL]}{dt} &= (k_{a1} \cdot [A] \cdot [L] - k_{d1} \cdot [AL]) - (k_{a2} \cdot [AL] \cdot [L] - k_{d2} \cdot [AL_2]) \\
 \frac{d[AL_2]}{dt} &= k_{a2} \cdot [AL] \cdot [L] - k_{d2} \cdot [AL_2] \\
 L(0) &= R_{max}; AL(0) = AL_2(0) = 0
 \end{aligned}$$

where  $[A](t)$  is the molar concentration of  $\alpha 7B\_M$  peptide at time  $t$ ;  $L$  is the available CIB2 immobilized;  $[AL](t)$  is the concentration of the CIB2- $\alpha 7B\_M$  complex at time  $t$ ;  $[AL_2](t)$  is the concentration of the CIB2- $\alpha 7B\_M$ -CIB2 complex at time  $t$ ;  $k_{a1}$  is the association rate constant for the CIB2- $\alpha 7B\_M$  complex ( $M^{-1}s^{-1}$ );  $k_{d1}$  is the dissociation rate constant for the CIB2- $\alpha 7B\_M$  complex ( $s^{-1}$ );  $k_{a2}$  is the association rate constant for the CIB2- $\alpha 7B\_M$ -CIB2 complex ( $RU^{-1}s^{-1}$ ), driven by the first association;  $k_{d2}$  is the dissociation rate constant for the CIB2- $\alpha 7B\_M$ -CIB2 complex ( $s^{-1}$ ).

Data fitting was performed using the software QDAT (Pall FortéBio, LCC 2016).

Received: 2 August 2019; Accepted: 12 September 2019;

Published online: 21 October 2019

## References

1. Seki, N. *et al.* Structure, expression profile and chromosomal location of an isolog of DNA-PKcs interacting protein (KIP) gene. *Biochim Biophys Acta* **1444**, 143–147 (1999).
2. Gentry, H. R. *et al.* Structural and biochemical characterization of CIB1 delineates a new family of EF-hand-containing proteins. *J Biol Chem* **280**, 8407–8415, <https://doi.org/10.1074/jbc.M411515200> (2005).
3. Hager, M. *et al.* Cib2 binds integrin  $\alpha 7B\beta 1D$  and is reduced in laminin  $\alpha 2$  chain-deficient muscular dystrophy. *J Biol Chem* **283**, 24760–24769, <https://doi.org/10.1074/jbc.M801166200> (2008).
4. Godinho-Santos, A., Hance, A. J., Goncalves, J. & Mammano, F. CIB1 and CIB2 are HIV-1 helper factors involved in viral entry. *Sci Rep* **6**, 30927, <https://doi.org/10.1038/srep30927> (2016).
5. Blazejczyk, M. *et al.* Biochemical characterization and expression analysis of a novel EF-hand  $Ca^{2+}$  binding protein calmyrin2 (Cib2) in brain indicates its function in NMDA receptor mediated  $Ca^{2+}$  signaling. *Arch Biochem Biophys* **487**, 66–78, <https://doi.org/10.1016/j.abb.2009.05.002> (2009).
6. Zhu, W. *et al.* CIB2 Negatively Regulates Oncogenic Signaling in Ovarian Cancer via Sphingosine Kinase 1. *Cancer Res* **77**, 4823–4834, <https://doi.org/10.1158/0008-5472.CAN-17-0025> (2017).
7. Huang, H., Bogstie, J. N. & Vogel, H. J. Biophysical and structural studies of the human calcium- and integrin-binding protein family: understanding their functional similarities and differences. *Biochem Cell Biol* **90**, 646–656, <https://doi.org/10.1139/o2012-021> (2012).
8. Vallone, R., Dal Cortivo, G., D'Onofrio, M. & Dell'Orco, D. Preferential Binding of  $Mg(2+)$  Over  $Ca(2+)$  to CIB2 Triggers an Allosteric Switch Impaired in Usher Syndrome Type 1J. *Front Mol Neurosci* **11**, 274, <https://doi.org/10.3389/fnmol.2018.00274> (2018).
9. Wang, Y. *et al.* Loss of CIB2 Causes Profound Hearing Loss and Abolishes Mechanoelectrical Transduction in Mice. *Front Mol Neurosci* **10**, 401, <https://doi.org/10.3389/fnmol.2017.00401> (2017).
10. Patel, K. *et al.* A Novel C-Terminal CIB2 (Calcium and Integrin Binding Protein 2) Mutation Associated with Non-Syndromic Hearing Loss in a Hispanic Family. *PLoS One* **10**, e0133082, <https://doi.org/10.1371/journal.pone.0133082> (2015).
11. Riazuddin, S. *et al.* Alterations of the CIB2 calcium- and integrin-binding protein cause Usher syndrome type 1J and nonsyndromic deafness DFNB48. *Nat Genet* **44**, 1265–1271, <https://doi.org/10.1038/ng.2426> (2012).
12. Giese, A. P. J. *et al.* CIB2 interacts with TMC1 and TMC2 and is essential for mechanotransduction in auditory hair cells. *Nat Commun* **8**, 43, <https://doi.org/10.1038/s41467-017-00061-1> (2017).
13. Sinz, A. Cross-Linking/Mass Spectrometry for Studying Protein Structures and Protein-Protein Interactions: Where Are We Now and Where Should We Go from Here? *Angew Chem Int Ed Engl* **57**, 6390–6396, <https://doi.org/10.1002/anie.201709559> (2018).
14. Iacobucci, C. *et al.* A cross-linking/mass spectrometry workflow based on MS-cleavable cross-linkers and the MeroX software for studying protein structures and protein-protein interactions. *Nat Protoc* **13**, 2864–2889, <https://doi.org/10.1038/s41596-018-0068-8> (2018).
15. Piotrowski, C. & Sinz, A. Structural Investigation of Proteins and Protein Complexes by Chemical Cross-Linking/Mass Spectrometry. *Adv Exp Med Biol* **1105**, 101–121, [https://doi.org/10.1007/978-981-13-2200-6\\_8](https://doi.org/10.1007/978-981-13-2200-6_8) (2018).
16. Ortega, A., Amoros, D. & Garcia de la Torre, J. Prediction of hydrodynamic and other solution properties of rigid proteins from atomic- and residue-level models. *Biophys J* **101**, 892–898, <https://doi.org/10.1016/j.bpj.2011.06.046> (2011).
17. Myers, W. K. *et al.* Double electron-electron resonance probes  $Ca(2+)$ -induced conformational changes and dimerization of recoverin. *Biochemistry* **52**, 5800–5808, <https://doi.org/10.1021/bi400538w> (2013).
18. La Verde, V., Dominici, P. & Astegno, A. Determination of Hydrodynamic Radius of Proteins by Size Exclusion Chromatography. *Bio-Protocol* **7**, e2230 (2017).
19. Dell'Orco, D., Muller, M. & Koch, K. W. Quantitative detection of conformational transitions in a calcium sensor protein by surface plasmon resonance. *Chem Commun (Camb)* **46**, 7316–7318, <https://doi.org/10.1039/c0cc02086a> (2010).
20. Dell'Orco, D., Sulmann, S., Linse, S. & Koch, K. W. Dynamics of conformational  $Ca^{2+}$  -switches in signaling networks detected by a planar plasmonic device. *Anal Chem* **84**, 2982–2989, <https://doi.org/10.1021/ac300213j> (2012).
21. Sulmann, S., Dell'Orco, D., Marino, V., Behnen, P. & Koch, K. W. Conformational changes in calcium-sensor proteins under molecular crowding conditions. *Chemistry* **20**, 6756–6762, <https://doi.org/10.1002/chem.201402146> (2014).
22. Fontana, A. *et al.* Probing protein structure by limited proteolysis. *Acta Biochim Pol* **51**, 299–321, 035001299 (2004).
23. Marino, V. *et al.* A novel p.(Glu11Val) missense mutation in GUCA1A associated with cone-rod dystrophy leads to impaired calcium sensing and perturbed second messenger homeostasis in photoreceptors. *Hum Mol Genet* **27**, 4204–4217, <https://doi.org/10.1093/hmg/ddy311> (2018).
24. Marino, V., Scholten, A., Koch, K. W. & Dell'Orco, D. Two retinal dystrophy-associated missense mutations in GUCA1A with distinct molecular properties result in a similar aberrant regulation of the retinal guanylate cyclase. *Hum Mol Genet* **24**, 6653–6666, <https://doi.org/10.1093/hmg/ddv370> (2015).
25. Marino, V., Sulmann, S., Koch, K. W. & Dell'Orco, D. Structural effects of  $Mg(2+)$  on the regulatory states of three neuronal calcium sensors operating in vertebrate phototransduction. *Biochim Biophys Acta* **1853**, 2055–2065, <https://doi.org/10.1016/j.bbapap.2014.10.026> (2015).
26. Vocke, F. *et al.* Dysfunction of cGMP signalling in photoreceptors by a macular dystrophy-related mutation in the calcium sensor GCAP1. *Hum Mol Genet* **26**, 133–144, <https://doi.org/10.1093/hmg/ddw374> (2017).
27. Anggayasti, W. L., Mancera, R. L., Bottomley, S. & Helmerhorst, E. The effect of physicochemical factors on the self-association of HMGB1: A surface plasmon resonance study. *Biochim Biophys Acta* **1864**, 1620–1629, <https://doi.org/10.1016/j.bbapap.2016.07.008> (2016).
28. Anggayasti, W. L., Mancera, R. L., Bottomley, S. & Helmerhorst, E. Optimization of surface plasmon resonance experiments: Case of high mobility group box 1 (HMGB1) interactions. *Anal Biochem* **499**, 43–50, <https://doi.org/10.1016/j.ab.2015.12.024> (2016).
29. Singh, A. *et al.* Analysis of AKAP7gamma Dimerization. *J Signal Transduct* **2015**, 371626, <https://doi.org/10.1155/2015/371626> (2015).
30. Vallar, L. *et al.* Divalent cations differentially regulate integrin  $\alpha IIb$  cytoplasmic tail binding to  $\beta 3$  and to calcium- and integrin-binding protein. *J Biol Chem* **274**, 17257–17266, <https://doi.org/10.1074/jbc.274.24.17257> (1999).

31. Leisner, T. M., Freeman, T. C., Black, J. L. & Parise, L. V. CIB1: a small protein with big ambitions. *FASEB J* **30**, 2640–2650, <https://doi.org/10.1096/fj.201500073R> (2016).
32. Astegno, A., La Verde, V., Marino, V., Dell'Orco, D. & Dominici, P. Biochemical and biophysical characterization of a plant calmodulin: Role of the N- and C-lobes in calcium binding, conformational change, and target interaction. *Biochim Biophys Acta* **1864**, 297–307, <https://doi.org/10.1016/j.bbapap.2015.12.003> (2016).
33. Astegno, A. *et al.* Structural plasticity of calmodulin on the surface of CaF<sub>2</sub> nanoparticles preserves its biological function. *Nanoscale* **6**, 15037–15047, <https://doi.org/10.1039/c4nr04368e> (2014).
34. Yap, K. L., Ames, J. B., Swindells, M. B. & Ikura, M. Diversity of conformational states and changes within the EF-hand protein superfamily. *Proteins* **37**, 499–507 (1999).
35. Ames, J. B. Dimerization of Neuronal Calcium Sensor Proteins. *Front Mol Neurosci* **11**, 397, <https://doi.org/10.3389/fnmol.2018.00397> (2018).
36. Dal Cortivo, G. *et al.* Luminescent and paramagnetic properties of nanoparticles shed light on their interactions with proteins. *Sci Rep* **8**, 3420, <https://doi.org/10.1038/s41598-018-21571-y> (2018).
37. Marino, V., Astegno, A., Pedroni, M., Piccinelli, F. & Dell'Orco, D. Nanodevice-induced conformational and functional changes in a prototypical calcium sensor protein. *Nanoscale* **6**, 412–423, <https://doi.org/10.1039/c3nr04978g> (2014).
38. Abraham, M. J. *et al.* GROMACS: High performance molecular simulations through multi-level parallelism from laptops to supercomputers. *SoftwareX* **1**, 19–25, <https://doi.org/10.1016/j.softx.2015.06.001> (2015).
39. Huang, J. *et al.* CHARMM36m: an improved force field for folded and intrinsically disordered proteins. *Nat Methods* **14**, 71–73, <https://doi.org/10.1038/nmeth.4067> (2017).
40. Marino, V. & Dell'Orco, D. Allosteric communication pathways routed by Ca(2+)/Mg(2+) exchange in GCAP1 selectively switch target regulation modes. *Sci Rep* **6**, 34277, <https://doi.org/10.1038/srep34277> (2016).
41. Marino, V. & Dell'Orco, D. Evolutionary-Conserved Allosteric Properties of Three Neuronal Calcium Sensor Proteins. *Front Mol Neurosci* **12**, 50, <https://doi.org/10.3389/fnmol.2019.00050> (2019).

## Acknowledgements

SPR, MD simulations, and part of the MALDI-TOF-MS measurements were performed at the Spectroscopy, Computational and Mass Platform of the Centro Piattaforme Tecnologiche of University of Verona.

## Author contributions

G.D.C. expressed and purified the proteins, contributed to all spectroscopic and biochemical experiments and analyses, performed limited proteolysis experiments and contributed to SPR experiments. V.M. performed molecular modeling, MD simulations and analysis of hydrodynamic properties; C.I. contributed to MS experiments and data analysis; R.V. contributed to protein expression and purification and SPR experiments; C.A. and A.R. helped with MS experiments; A.S. coordinated MS experiments and analyses; D.D.O. conceived the study, performed SPR experiments and kinetic analyses and wrote the manuscript with contributions from all authors.

## Competing interests

The authors declare no competing interests.

## Additional information

**Supplementary information** is available for this paper at <https://doi.org/10.1038/s41598-019-51573-3>.

**Correspondence** and requests for materials should be addressed to D.D.

**Reprints and permissions information** is available at [www.nature.com/reprints](http://www.nature.com/reprints).

**Publisher's note** Springer Nature remains neutral with regard to jurisdictional claims in published maps and institutional affiliations.



**Open Access** This article is licensed under a Creative Commons Attribution 4.0 International License, which permits use, sharing, adaptation, distribution and reproduction in any medium or format, as long as you give appropriate credit to the original author(s) and the source, provide a link to the Creative Commons license, and indicate if changes were made. The images or other third party material in this article are included in the article's Creative Commons license, unless indicated otherwise in a credit line to the material. If material is not included in the article's Creative Commons license and your intended use is not permitted by statutory regulation or exceeds the permitted use, you will need to obtain permission directly from the copyright holder. To view a copy of this license, visit <http://creativecommons.org/licenses/by/4.0/>.

© The Author(s) 2019

## Supporting Information

### **Oligomeric state, hydrodynamic properties and target recognition of human Calcium and Integrin Binding protein 2 (CIB2)**

by

Giuditta Dal Cortivo, Valerio Marino, Claudio Iacobucci, Rosario Vallone, Christian Arlt, Anne Rehkamp, Andrea Sinz and Daniele Dell'Orco

### **Supplementary Methods**

#### **Cross-linking reactions and Mass Spectrometry**

Cross-linking reactions were performed with 10  $\mu$ M CIB2 (in 20 mM HEPES pH 7.5, 150 mM KCl, 1 mM DTT, 1 mM  $Mg^{2+}$ , 2 mM  $Ca^{2+}$ ) and increasing concentrations of peptides  $\alpha$ 7B\_M and  $\alpha$ 7B\_Scrb, ranging from 0.5:1 to 2:1 peptide:protein ratios. After incubating the samples for 10 minutes at room temperature, DSBU (freshly prepared solution, dissolved in neat DMSO) was added to the mixture at 50-fold molar excess compared to CIB2 concentration. As the final volume of the reaction mixture was 50  $\mu$ L, 1  $\mu$ L of 25 mM DSBU was added to each sample. After 20 minutes, the cross-linking reactions were quenched by adding ammonium bicarbonate to a final concentration of 20 mM. Samples were incubated for 10 minutes before SDS-PAGE analysis was performed (data not shown). Samples for MALDI-TOF-MS measurements were desalted by ZipTip C4 (Millipore) and desalted protein was eluted with 70% (v/v) acetonitrile / 1% (v/v) formic acid. Each sample was mixed with a saturated solution of sinapinic acid (in 50% (v/v) methanol / 0.1% (v/v) TFA) at 1:1 ratio and spotted onto the MALDI target.

#### **Hydrodynamic diameter estimation**

Since human CaM (pdb 1CLL)<sup>1</sup> was lacking the first 4 residues at the N-term, they were modeled using pdb structure 4e53 as template.<sup>2</sup> After superimposition of the  $C\alpha$  of residues 4-8, residues 1-7 of 4e53 were fused with residues 8-148 from 1CLL. Analogously, the missing Lys 149 at the C-term was modeled using the pdb structure 4djc<sup>3</sup> as a template by fusion of residues 146-149 of 4djc with residues 1-145 of 1CLL after superimposition of residues 146-148  $C\alpha$ .

Hydrodynamic diameter was estimated using default values for radius of atomic elements (2.84 Å), solvent density (1 g/ml) and solvent viscosity (0.01 poise), temperature was set to 25 °C and the mode was set to shell-model from atomic level. Specific volume for each protein structure was calculated

by summing the volume of each residue and correcting the final volume for electrostriction as explained in Ref.<sup>4</sup>, therefore the specific volume for Rec, CaM and CIB2 were 0.712, 0.694 and 0.715 cm<sup>3</sup>/g respectively. The molecular weight used for the estimation of hydrodynamic diameter was calculated based on the effective protein sequence of each pdb file using Protein Calculator 3.4 (<http://protcalc.sourceforge.net/>).

### Surface plasmon resonance analysis

A SensiQ Pioneer surface plasmon resonance instrument (FortéBio Pall) was employed for the investigation of the CIB2 dimerization and for the real-time monitoring of its interaction with selected peptides. For studies of on-chip CIB2 dimerization, HBS buffer (20 mM HEPES, pH 7.5, 150 mM KCl, 1 mM MgCl<sub>2</sub>, 50 μM EDTA, 0.005% Tween 20), was used both as immobilization and running buffer, with the addition of fresh 1 mM DTT just before each experiment.

CIB2 was immobilized on the surface of a COOH5 sensor chip (FortéBio Pall) coated with a carboxylated polysaccharide hydrogel spacer. Carboxyl groups were mobilized with sequential injections (5 μl min<sup>-1</sup> flow rate) of 60 μl of 10 mM H<sub>3</sub>PO<sub>4</sub>, 60 μl HBS, 60 μl 10 mM NaOH and 2 × 60 μl HBS. The sensor chip surface was then activated with a 7 min injection of a mixture of 10 mM *N*-hydroxysuccinimide (NHS) and *N*-ethyl-*N'*-(dimethylaminopropyl)carbodiimide (EDC) at a flow rate of 5 μl min<sup>-1</sup>. Previously frozen samples of untagged CIB2 in HBS were thawed and diluted to a final concentration of 50 nM in Na-acetate buffer (pH 3.1), 1.52 pKa units below its isoelectric point. Amine coupling of CIB2 was achieved with a slow and prolonged sequential injection of protein at flow rate of 10 μl min<sup>-1</sup> leading to a final amount of 130 RU in one case and 226 RU in another experiment (1 RU = 1 pg mm<sup>-2</sup>). The surface was blocked via injection of 70 μl 1M ethanolamine hydrochloride-NaOH, pH 8.5. In all SPR experiments, one of the three flow cells was activated and then blocked without protein immobilization, and was used as a reference. CIB2 was diluted to final concentrations of 92 nM – 46 μM and injected at a flow rate of 20 μl min<sup>-1</sup> (2 min injection) resulting in all cases in flat sensorgrams, except for some non-specific bulk effect.

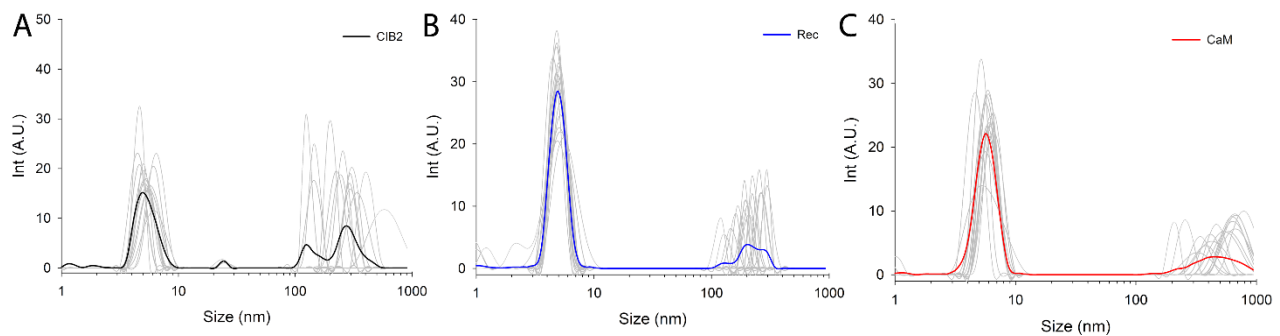
In the experiments concerning the interaction with peptides, the same chips with amine-coupled CIB2 were used and the three peptides α7B\_M, α7B\_Scrb and α7B\_C were diluted to a final concentration of 7.5 – 30 μM in HBS and injected in the same conditions (20 μl min<sup>-1</sup>, 2 min injection); experiments were repeated 4 times.

CIB2 was also homogeneously immobilized at higher levels using the capture-coupling technique, where His-tagged CIB2 is first site-specifically driven on the surface of a His-Cap sensor chip (FortéBio Pall), based on a three-dimensional non-dextran hydrogel polymer modified with Nitrilotriacetic acid (NTA) functional groups that chelate Nickel ions for the selective capture of 6X

His-tagged proteins, and then blocked via amine coupling as explained above. Preparation of the sensor chip and immobilization followed the instructions from the manufacturer and resulted in approximately 2250 RU of CIB2 immobilized. In binding experiments, peptide concentration was varied in the 230 nM- 30  $\mu$ M range for both  $\alpha$ 7B\_M, and  $\alpha$ 7B\_C, and experiments were repeated 4 times, both with the HBS buffer described above (containing 1 mM MgCl<sub>2</sub>) and with further addition of 2 mM CaCl<sub>2</sub>. Flow rate was set to 20  $\mu$ l min<sup>-1</sup> in all binding experiments, and the dissociation process was followed for 240 s, resulting in complete protein-peptide dissociation.

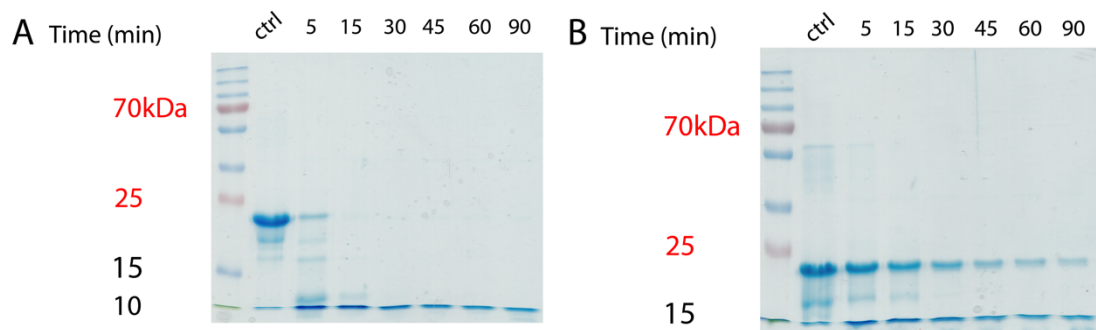
## Supplementary figures

**Figure S1**

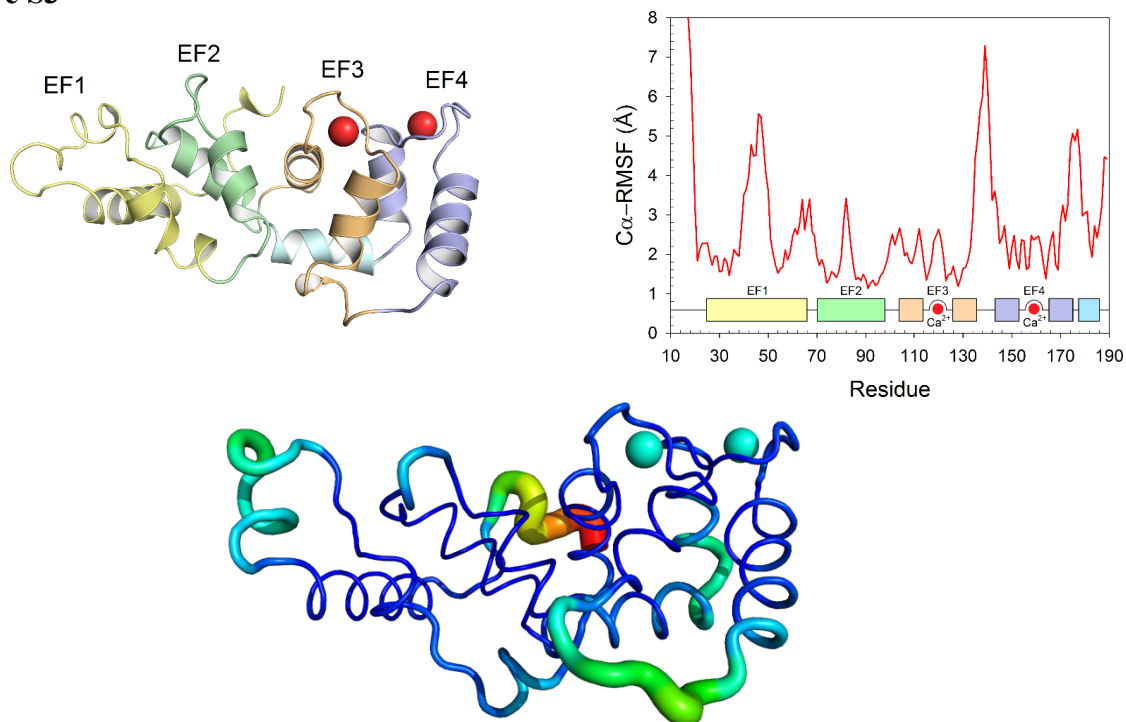


**Figure S1: DLS measurements of the SEC collected peaks.** CIB2 band A<sub>2</sub> (A), Rec (B) and CaM (C). Each data set consisted of 15-30 measurements (grey lines), with 13-15 repetitions each. Colored lines are referred to the average distribution. Temperature was set to 37°C and samples were equilibrated for 2 min before measurements.

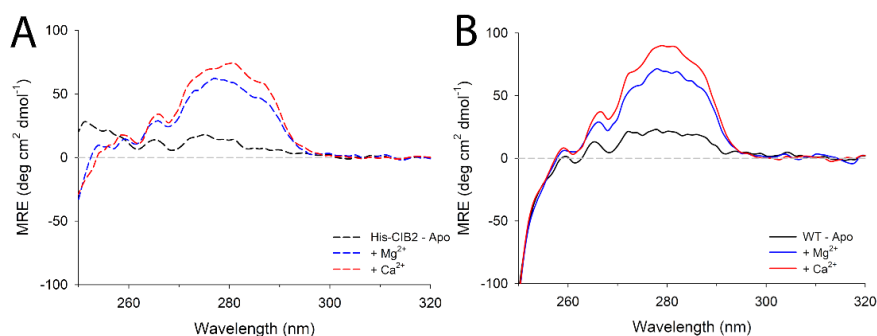
**Figure S2**



**Figure S2: Time-resolved proteolysis experiments.** 25  $\mu$ M CIB2 was incubated with Trypsin (1:100 enzyme:CIB2 ratio) in the presence of 1 mM EDTA (A) or 500  $\mu$ M EGTA + 1 mM Mg<sup>2+</sup> (B) for 90 minutes, samples were collected at different times. Temperature was set to 25°C and CIB2 without enzyme was used as control. Reaction products were loaded on a 15% SDS-PAGE.

**Figure S3**

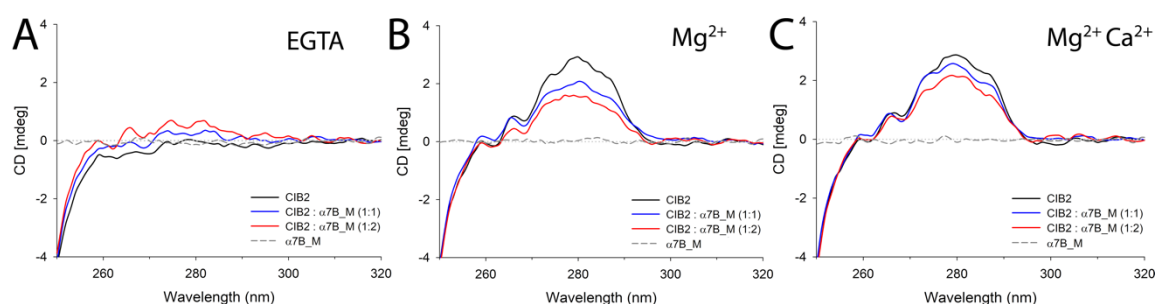
**Figure S3: Analysis of MD simulations.** Three-dimensional structure of the homology model of  $\text{Ca}^{2+}$ -bound human CIB2 (top left), protein secondary structure is shown as cartoons, EF1 is colored in yellow, EF2 is colored in green, EF3 is colored in orange, EF4 is colored in blue, C-term helix is colored in cyan and  $\text{Ca}^{2+}$  ions are shown as red spheres. Root-Mean Square Fluctuation of  $\text{C}\alpha$  (top right) calculated over 400 ns MD simulations, inset shows protein secondary structure where EF hands and  $\text{Ca}^{2+}$  ions are colored according to the left panel. Projection of the  $\text{C}\alpha$ -RMSF (bottom) on the three-dimensional structure of CIB2,  $\text{Ca}^{2+}$  ions are shown as spheres, protein is shown as cartoons, both are colored in a blue-to-red scale according to their  $\text{C}\alpha$ -RMSF, ranging from 1.1 to 13.9 Å. Thickness of the cartoon is also proportional to the  $\text{C}\alpha$ -RMSF.

**Figure S4**

**Figure S4: Structural comparison of His-CIB2 (A) and CIB2 (B).** Near-UV CD spectra (250-320 nm) of 20-30  $\mu\text{M}$  CIB2 were collected at 37°C in a quartz cuvette with 1 cm length path. Sequential additions of 500  $\mu\text{M}$  EGTA (black), 1 mM  $\text{Mg}^{2+}$  (blue) and 2 mM  $\text{Ca}^{2+}$  (red) were performed. Near-UV CD spectra of the buffer (20 mM HEPES pH 7.5, 150 mM KCl, 1 mM DTT) was considered as blank and subtracted. Each spectrum represents the mean of 5 accumulations. Data were normalized according to the protein concentration and the number of residues (Molar Residue Ellipticity, MRE).

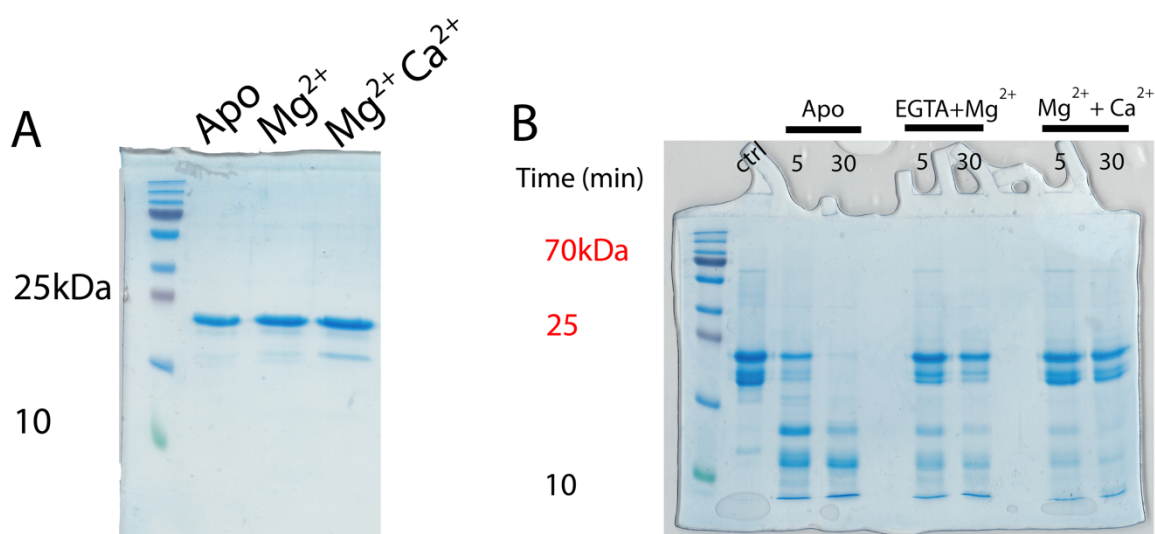


Figure S5



**Figure S5: Near-UV CD spectra of CIB2 in the presence of different stoichiometric ratios of alpha7B\_M peptide.** Near-UV CD spectra (250-320nm) of 20  $\mu$ M CIB2 in the absence of peptide (black lines) and in the presence of two different protein/peptide ratios (1:1 blue lines; 1:2 red lines) collected at 37°C in the presence of 500  $\mu$ M EGTA (A) and after sequential additions of 1 mM  $Mg^{2+}$  (B) and 2 mM free  $Ca^{2+}$  (C). The spectrum of alpha7B\_M peptide in the absence of CIB2 is shown in dashed grey lines.

Figure S6



**Figure S6. CIB2 limited proteolysis.** A) 10  $\mu$ M CIB2 was incubated at 25°C in the presence of 1 mM EDTA (Apo), 500  $\mu$ M EGTA + 1 mM  $Mg^{2+}$  ( $Mg^{2+}$ ) and 1 mM  $Mg^{2+}$  + 2 mM  $Ca^{2+}$  for 10 minutes at 25°C. Samples were boiled and loaded in a 18% SDS polyacrylamide gel. B) Limited proteolysis was performed incubating trypsin with 25  $\mu$ M CIB2 in the same concentrations of ions used for (A) (protein:enzyme ratio was 100:1). Samples were collected at different times, boiled and loaded on a 18% SDS-PAGE. Both gels run for 45-50 min, then they were Coomassie Blue-stained. Uncropped

## Supplementary References

1. Chattopadhyaya, R.; Meador, W. E.; Means, A. R.; Quioco, F. A., Calmodulin structure refined at 1.7 Å resolution. *J Mol Biol* **1992**, *228* (4), 1177-92.
2. Kumar, V.; Chichili, V. P.; Zhong, L.; Tang, X.; Velazquez-Campoy, A.; Sheu, F. S.; Seetharaman, J.; Gerges, N. Z.; Sivaraman, J., Structural basis for the interaction of unstructured neuron specific substrates neuromodulin and neurogranin with Calmodulin. *Sci Rep* **2013**, *3*, 1392.
3. Sarhan, M. F.; Tung, C. C.; Van Petegem, F.; Ahern, C. A., Crystallographic basis for calcium regulation of sodium channels. *Proc Natl Acad Sci U S A* **2012**, *109* (9), 3558-63.
4. Harpaz, Y.; Gerstein, M.; Chothia, C., Volume changes on protein folding. *Structure* **1994**, *2* (7), 641-9.

## GENERAL ARTICLE

# A novel p.(Glu111Val) missense mutation in *GUCA1A* associated with cone-rod dystrophy leads to impaired calcium sensing and perturbed second messenger homeostasis in photoreceptors

Valerio Marino<sup>1,2,#</sup>, Giuditta Dal Cortivo<sup>1,#</sup>, Elisa Oppici<sup>1</sup>, Paolo Enrico Maltese<sup>3</sup>, Fabiana D'Esposito<sup>4,5,6</sup>, Elena Manara<sup>5</sup>, Lucia Ziccardi<sup>7</sup>, Benedetto Falsini<sup>8,9</sup>, Adriano Magli<sup>10</sup>, Matteo Bertelli<sup>3,5</sup> and Daniele Dell'Orco<sup>1,\*</sup>

<sup>1</sup>Department of Neurosciences, Biomedicine and Movement Sciences, Section of Biological Chemistry, University of Verona, Verona, Italy, <sup>2</sup>Department of Translational Research and of New Surgical and Medical Technologies, University of Pisa, Pisa, Italy, <sup>3</sup>MAGI'S Lab s.r.l., Rovereto, Italy, <sup>4</sup>Imperial College Ophthalmic Research Unit, Western Eye Hospital, Imperial College Healthcare NHS Trust, London, UK, <sup>5</sup>MAGI Euregio, Bolzano, Italy, <sup>6</sup>Eye Clinic, Department of Neurosciences, Reproductive Sciences and Dentistry, Federico II University, Naples, Italy, <sup>7</sup>IRCCS-Fondazione Bietti, Rome, Italy, <sup>8</sup>Institute of Ophthalmology, Università Cattolica del Sacro Cuore, Rome, Italy, <sup>9</sup>Fondazione Policlinico Universitario "A. Gemelli", IRCCS, Rome, Italy, <sup>10</sup>Department of Pediatric Ophthalmology, University of Salerno, Fisciano (SA), Italy

\*To whom correspondence should be addressed at: Department of Neurosciences, Biomedicine and Movement Sciences, Section of Biological Chemistry, University of Verona, Strada le Grazie 8, 37134, Verona, Italy. Tel: +39-045-802-7637; Email: daniele.dellorco@univr.it

## Abstract

Guanylate Cyclase-Activating Protein 1 (GCAP1) regulates the enzymatic activity of the photoreceptor guanylate cyclases (GC), leading to inhibition or activation of the cyclic guanosine monophosphate (cGMP) synthesis depending on its Ca<sup>2+</sup>- or Mg<sup>2+</sup>-loaded state. By genetically screening a family of patients diagnosed with cone-rod dystrophy, we identified a novel missense mutation with autosomal dominant inheritance pattern (c.332A>T; p.(Glu111Val); E111V from now on) in the *GUCA1A* gene coding for GCAP1. We performed a thorough biochemical and biophysical investigation of wild type (WT) and E111V human GCAP1 by heterologous expression and purification of the recombinant proteins. The E111V substitution disrupts the coordination of the Ca<sup>2+</sup> ion in the high-affinity site (EF-hand 3, EF3), thus significantly decreasing the ability of GCAP1 to sense Ca<sup>2+</sup> (~80-fold higher K<sub>d</sub><sup>app</sup> compared to WT). Both WT and E111V GCAP1 form dimers independently on the presence of cations, but the E111V Mg<sup>2+</sup>-bound form is prone to severe aggregation over time. Molecular dynamics simulations suggest a significantly increased flexibility of both the EF3 and EF4 cation binding loops for the Ca<sup>2+</sup>-bound

#The authors wish it to be known that, in their opinion, the first two authors should be regarded as joint First Authors.

Received: July 31, 2018. Revised: August 23, 2018. Accepted: August 24, 2018

© The Author(s) 2018. Published by Oxford University Press. All rights reserved.

For Permissions, please email: journals.permissions@oup.com

form of E111V GCAP1, in line with the decreased affinity for  $\text{Ca}^{2+}$ . In contrast, a more rigid backbone conformation is observed in the  $\text{Mg}^{2+}$ -bound state compared to the WT, which results in higher thermal stability. Functional assays confirm that E111V GCAP1 interacts with the target GC with a similar apparent affinity ( $\text{EC}_{50}$ ); however, the mutant shifts the GC inhibition out of the physiological  $[\text{Ca}^{2+}]$  ( $\text{IC}_{50}^{\text{E111V}} \sim 10 \mu\text{M}$ ), thereby leading to the aberrant constitutive synthesis of cGMP under conditions of dark-adapted photoreceptors.

## Introduction

Phototransduction is the first biochemical cascade in photoreceptors, which triggers the visual process. The underlying signaling machinery is complex and requires adaptation and shut-off mechanisms that are finely regulated by  $\text{Ca}^{2+}$  and cyclic guanosine monophosphate (cGMP), which work as strictly interconnected second messengers (1–3). The concentration of  $\text{Ca}^{2+}$  in the photoreceptor outer segments is precisely controlled, and during the phototransduction cascade, it drops from several hundred nanomolar  $\text{Ca}^{2+}$  in the dark to below 100 nM in the light (4,5). Guanylate Cyclase-Activating Protein 1 (GCAP1) is a neuronal calcium sensor expressed in both rods and cones, which is crucial for phototransduction regulation. GCAP1 indeed detects subtle changes in  $\text{Ca}^{2+}$  concentration and responds by adopting conformations that control the activity of the target membrane-bound guanylate cyclases (GC) responsible for the cGMP synthesis. At high  $[\text{Ca}^{2+}]$ , GCAP1 adopts a  $\text{Ca}^{2+}$ -loaded state that inhibits GC activity, while it switches to a slightly different,  $\text{Mg}^{2+}$ -bound conformation following the drop in  $[\text{Ca}^{2+}]$  (6–8), thus stimulating the synthesis of cGMP by GC to rapidly restore dark-adapted cell conditions (3,9).

In recent years, an increasing number of point mutations (18 up to date) have been identified in *GUCA1A*, the gene coding for GCAP1, in patients suffering from autosomal dominant retinal dystrophies (10–21). These forms of vision-threatening diseases including cone dystrophy (COD), cone-rod dystrophy (CORD) and macular dystrophy (MACD) are all characterized by central vision loss, impaired color vision and photophobia. In the case of CORD and MACD, early and important changes in the macula are followed by progressive loss in peripheral vision, when the primary cone dysfunction is followed by rod degeneration (22–24). Biochemical investigations of some of the pathogenic GCAP1 variants allowed the elucidation of some common features of the GCAP1-related retinal dystrophies (20,25–30); however, detailed biophysical investigations showed that clinically similar phenotypes may result from very different molecular features of the affected GCAP1 variant (31), thus calling for the importance of a thorough characterization of each individual disease-associated variant. Photoreceptor degeneration is probably triggered by apoptosis (28,32), although different mechanisms have been proposed (33). It is well established, however, that a dysregulation of the homeostasis of  $\text{Ca}^{2+}$ , and consequently of cGMP, is deeply implicated in retinal degeneration (10,34,35).

We identified a novel c.332A>T missense mutation in *GUCA1A* with autosomal dominant inheritance pattern in a family of patients diagnosed with CORD. The clinical phenotype calls for a severe form of the disease, characterized by congenital nystagmus, photophobia, marked decrease in visual acuity progressing to central scotoma and central outer retinal dysfunction progressing to atrophy. The effect of the point mutation c.332A>T at the protein level [p.(Glu111Val), from now on E111V] is the substitution of a highly conserved glutamic acid directly involved in the coordination of  $\text{Ca}^{2+}$  at the high affinity binding site (EF-hand 3, EF3) with a hydrophobic residue;

therefore, we investigated whether the cation sensing capability, the structure and thus the function of the resulting E111V GCAP1 were compromised.

We report a detailed biochemical and biophysical characterization of wild type (WT) and E111V GCAP1 variants integrating *in vitro* experiments and molecular dynamics (MD) simulations. Our data suggest that the CORD-associated E111V GCAP1 is incapable of sensing  $\text{Ca}^{2+}$  and inhibiting the target GC under physiological conditions, but it rather adopts a conformationally rigid, aggregation-prone  $\text{Mg}^{2+}$ -bound form that constitutively activates GC even in dark-adapted conditions. The resulting excessive synthesis of cGMP in the absence of light stimuli is thought to trigger cell-death mechanisms responsible for the degeneration process.

## Results

### Clinical phenotype and genetic characterization

Our proband was a male patient, aged 53 at the time of our observation. He reported a congenital nystagmus, relatively improved over time, photophobia and low vision since early childhood. His visual acuity was 1.3 LogMAR (not improving with pinhole or lens correction) in both eyes (Table 1). Fundus imaging and optical coherence tomography (OCT) (data not shown) led us to confirm the initial clinical diagnosis of COD. When defining the pedigree (Fig. 1C), the patient reported to have three daughters, two of them suffering from the same condition (aged 22 and 16). We therefore asked to examine them and confirmed they were affected too. Indeed, their phenotype matched their father's one, being just slightly less severe due to the lesser duration of the disease. We confirmed that the middle daughter and the patient's mother were unaffected, while the deceased father was reported to be unaffected, but no ophthalmological records were available. At this stage, electrophysiologic testing was performed in all patients in order to define precisely the different components of the dysfunction.

Layouts of dark- and light-adapted electroretinogram (ERG) signals from the proband and his family members are reported in Figure 1B. Electrophysiological testing showed markedly reduced a- and b-wave amplitudes of the dark-adapted ERGs and increased a- and b-wave implicit times as compared to age-matched controls. The light-adapted responses showed reduced amplitude and increased implicit time values as well. The traces were, however, detectable with good level of reproducibility (Fig. 1B). This led us to redefine the condition as a CORD, although the symptoms of the cone dysfunction (low vision acuity and photophobia) were prevalent and no nyctalopia was reported.

The pedigree showed a clear dominant mode of transmission. Following patient's written consent, a genetic testing of our proband has been undertaken through next generation sequencing (NGS) of a panel of candidate genes. The NGS coverage of targeted bases was 291.87 X with 95.54% covered to at least 25 X. Genetic testing showed that the proband was heterozygous

**Table 1.** Clinical phenotype of patients with the GUCA1A mutation c.332A>T / p.(Glu111Val)

Patient ID	Age	First symptoms and course	VA (logMAR)	Visual field	Light-/dark-adapted/ ERG amplitudes // implicit time	EOG	OCT	Anterior segment
II:1	53	Cong. Nys. Low VA, minor progression, photophobia	1.3 (NI)	Central scotoma	Severely reduced (cone = rod) // Delayed (cone = rod)	Normal	CNA	Normal
III:1	22	Cong. Nys. Low VA, minor progression photophobia	1.08	Central scotoma	Severely reduced (cone > rod) // Delayed (cone = rod)	Normal	CNA	Normal
III:3	16	Low VA, minor progression, photophobia	0.79	Central scotoma	Severely reduced (cone > rod) // Delayed (cone = rod)	Normal	CNA	Normal

VA: visual acuity, ERG: electroretinogram, EOG: electrooculogram, OCT: optical coherence tomography, CNA: Central neuroretinal atrophy.

for the variant GUCA1A: NM\_000409: c.332A>T: p.(Glu111Val) (Supplementary Material, Fig. S1A). The variant is new since it is not listed in any public database and was predicted to be disease-causing, deleterious and probably damaging by *in silico* pathogenicity prediction software. This missense variation changes the negatively charged glutamate into a hydrophobic valine. The GUCA1A glutamate in position 111 seems to be highly conserved during evolution (Supplementary Material, Fig. S1B; see Discussion). Sanger sequencing confirmed the presence of the identified variant in the two affected daughters, so confirming the pathogenicity through segregation.

### Functional assays: regulation of the target GC by WT and E111V GCAP1

The capability of WT and E111V GCAP1 to regulate the target GC over  $Ca^{2+}$  levels spanning the physiological range pertinent to phototransduction was tested. For this purpose, recombinant human GCAP1 was expressed, purified and reconstituted with membranes from Human Embryonic Kidney flip cells 293 (HEK293) stably expressing human ROS-GC1 (GC) (HEK293-GC). Results are summarized in Figure 2 and Table 2. Both WT and E111V GCAP1 activated the target GC at low  $[Ca^{2+}]$  at similar levels; however, while the WT form induced a substantially complete inhibition of cGMP synthesis at high  $[Ca^{2+}]$ , E111V GCAP1 induced an important residual activation (~60%) of the target (Fig. 2A). The incapability of E111V GCAP1 to fully inhibit the target GC was also confirmed by the remarkably high  $IC_{50}$  values ( $[Ca^{2+}]$  at which GC activation was half-maximal) observed in the GC activation profiles in experiments where the concentration of the GCAP1 variant was kept fixed ( $IC_{50}^{WT} = 0.26 \mu M$ ,  $IC_{50}^{E111V} = 10 \mu M$ , Fig. 2C; Table 2). The dysregulation of the  $Ca^{2+}$ -dependent catalytic activity of the target, however, did not depend on changes in apparent affinity for GCAP1, as clearly proven by the very similar  $EC_{50}$  values obtained for WT (3.2  $\mu M$ ) and E111V (3.5  $\mu M$ ) GCAP1 (Fig. 2B and Table 2). Moreover, no significant alterations in the X-fold activation of the target enzyme were detected (X-fold = 16.0 for the WT; 15.7 for E111V).

### Oligomeric state and aggregation propensity of WT and E111V GCAP1

It was recently established that bovine GCAP1 is a functional dimer (36); therefore, we investigated whether the oligomeric state of human GCAP1 is the same under conditions corresponding to the GC-activating/inhibiting states. We used a combination of analytical size exclusion chromatography (SEC) and dynamic light scattering (DLS), which allowed us to study the time evolution of the detected average hydrodynamic size of the protein dispersion.

SEC profiles (Supplementary Material, Fig. S2A and B) showed a major elution band for both WT and E111V persisting almost unaltered in the presence of either  $Mg^{2+}$  or  $Mg^{2+}$  and  $Ca^{2+}$ . The molecular mass (Table 3) assessed by the elution peaks ranged from 43.7 kDa to 47.8 kDa independent of the cations, thus clearly indicating that both WT and E111V human GCAP1 are dimeric (the theoretical molecular mass of the monomer is 22.9 kDa, <https://www.uniprot.org/uniprot/P43080>).

Results from DLS spectroscopy were in line with those from SEC (Supplementary Material, Fig. S2C and D) and displayed relatively monodisperse samples. At 25°C, the estimated hydrodynamic diameter in the presence of  $Mg^{2+}$  was slightly smaller for E111V ( $5.98 \pm 0.05$  nm) compared to WT GCAP1 ( $6.33 \pm 0.03$  nm), but no significant difference could be observed in the hydrodynamic diameter of either variant upon addition of  $Ca^{2+}$  (Table 3). Moreover, the mean count rate (MCR) also remained substantially stable.

In order to probe whether the detected dimeric state of WT and E111V GCAP1 persisted at physiologically relevant temperature, DLS experiments were repeated at 37°C. Interestingly, under conditions of co-presence of physiological levels of  $Mg^{2+}$  (1 mM) and saturating  $Ca^{2+}$ , the colloidal properties of the WT and E111V dispersions were substantially unaltered and the proteins kept dimeric; however, the absence of  $Ca^{2+}$  led to very different behaviors (Fig. 3). The MCR of WT GCAP1, which in the first 4 h was on average unperturbed, started to increase with a constant slope and oscillatory behavior, consistent with a relatively slow aggregation process that led to ~4-fold increase

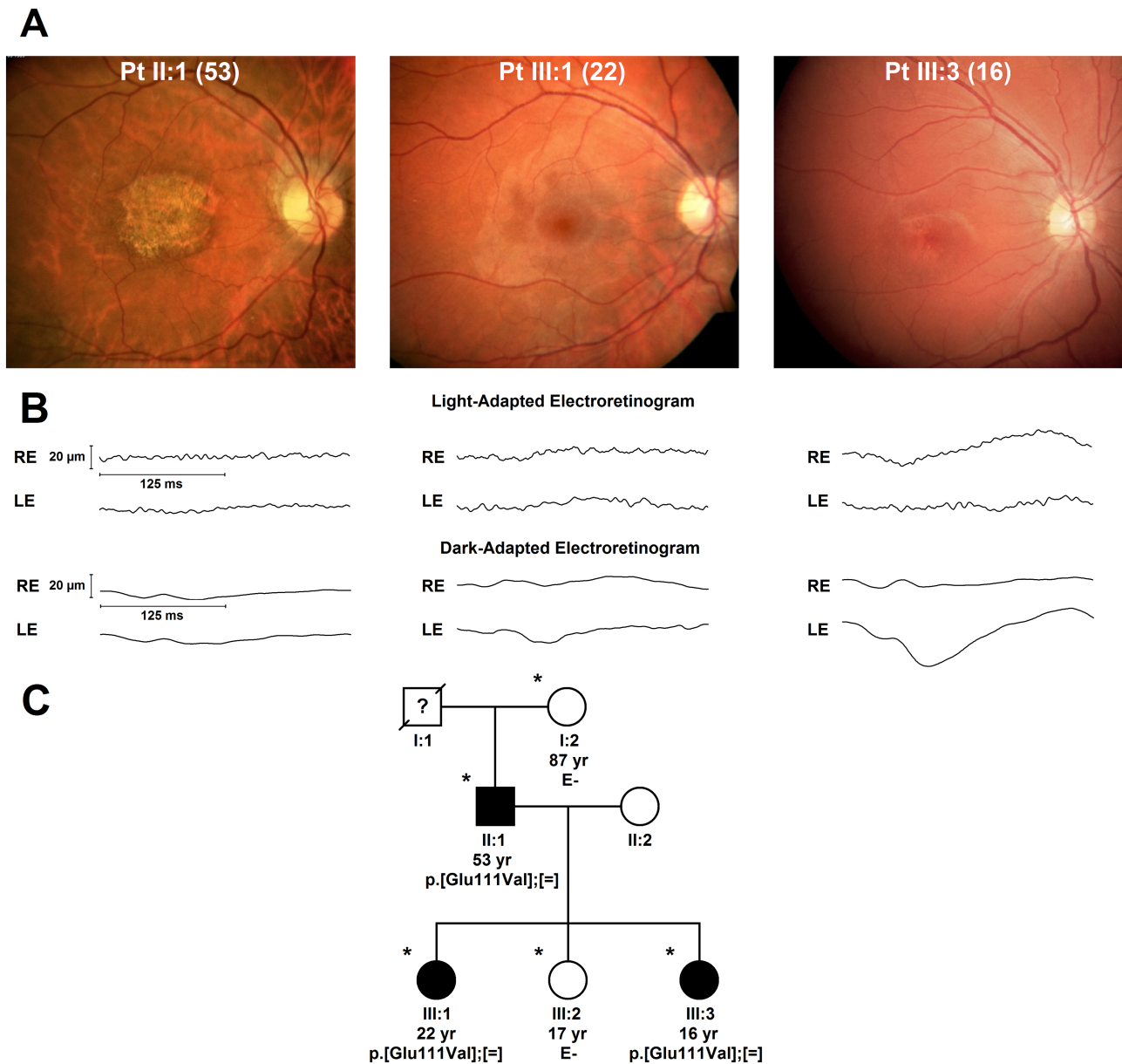


**Figure 1.** Clinical, genetic and electrophysiological data. (A) Color fundus image of the right eye of patients II:1 (age 53, left), III:1 (age 22, center) and III:3 (age 16, right). (B) Layouts of dark- and light-adapted electroretinographic signals from patients II:1, III:1 and III:3 showing severely reduced a-, b-wave amplitudes and delayed implicit times. (C) Family tree showing the matching genotype–phenotype segregation of the mutant allele of GUCA1A harboring the c. 332A>T transition causing the substitution E111V. Legend: square, male subject; circle, female subject; black symbol, affected subject; white symbol, healthy subject; \* Documented clinical evaluation; yr, subject age at last clinical evaluation; P, proband; E-, negative to genetic test; square brackets ([;];[;]),maternal and paternal chromosome; =, no change.

in the average MCR after 16 h. The MCR of E111V GCAP1 instead started to increase linearly from the beginning and doubled from ~200 kcps to ~400 kcps in the first 4 h. It then followed an even steeper rise, which led to a ~10-fold increase of MCR compatible with a severe, constant protein aggregation process.

#### Hydrophobic properties of WT and E111V GCAP1 probed by ANS fluorescence

Time-resolved DLS experiments suggested that the E111V GCAP1 variant could show altered surface properties compared to the WT, which may give rise to the observed aggregation in

the absence of  $\text{Ca}^{2+}$ . To investigate whether the substitution of a hydrophilic glutamic acid for a hydrophobic valine could lead to appreciable changes in surface properties, we performed fluorescence experiments using the hydrophobic probe 8-Anilino-naphthalene-1-sulfonic acid (ANS) (see Methods), whose fluorescence emission changes upon binding to hydrophobic patches on the protein surface. Results reported in [Supplementary Material, Figure S3A and B](#) confirm that both apo WT and E111V were somewhat hydrophobic, as clearly showed by the blue-shift and increased intensity in fluorescence emission of the ANS dye compared to the case in the absence of proteins ([Supplementary Material, Table S1](#)). Addition of  $\text{Mg}^{2+}$  generated a 7-nm red shift in the case of WT GCAP1 and a

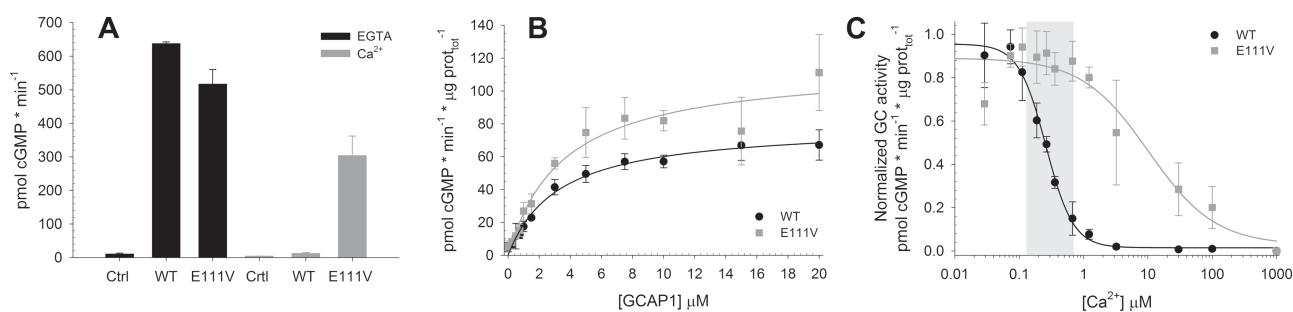


**Figure 2.** Guanylate cyclase 1 (GC) regulation by WT and E111V GCAP1. (A) Membranes containing GC were reconstituted with 5- $\mu\text{M}$  WT or E111V GCAP1 and <19-nM  $\text{Ca}^{2+}$  (black) or  $\sim 30\text{-}\mu\text{M}$  free  $\text{Ca}^{2+}$  (grey); membranes with no GCAP1 were used as control. (B) GC activity as a function of WT (black) or E111V (grey) GCAP1 concentration (0–20  $\mu\text{M}$ ) in the presence of <19-nM free  $\text{Ca}^{2+}$ ; activation was half-maximal ( $\text{EC}_{50}$ , Table 2) at 3.2  $\mu\text{M}$  and 3.5  $\mu\text{M}$ , respectively. (C) GC activity as a function of  $\text{Ca}^{2+}$  concentration (<19 nM – 1 mM) of 5- $\mu\text{M}$  WT (black) or E111V (grey) GCAP1; activation was half-maximal ( $\text{IC}_{50}$ , Table 2) at 0.26  $\mu\text{M}$  and 10  $\mu\text{M}$ , respectively. The physiological window of variation in  $\text{Ca}^{2+}$  concentration during the phototransduction cascade is shaded in grey.

**Table 2.** Results of GC regulation and  $\text{Ca}^{2+}$  binding experiments

	$\text{IC}_{50}^{\text{a}}$ ( $\mu\text{M}$ ) <sup>a</sup>	$h^{\text{b}}$	$\text{EC}_{50}$ ( $\mu\text{M}$ ) <sup>c</sup>	X-fold <sup>d</sup>	$\log K_1^{\text{e}}$	$\log K_2^{\text{e}}$	$K_{\text{d}}^{\text{app}}$ ( $\mu\text{M}$ ) <sup>f</sup>
WT	$0.26 \pm 0.01$	$2.05 \pm 0.21$	$3.2 \pm 0.3$	16.0	$7.07 \pm 0.13$	$5.55 \pm 0.19$	0.49
E111V	$10 \pm 5$	$0.83 \pm 0.27$	$3.5 \pm 0.9$	15.7	$4.3 \pm 1.1$	$4.5 \pm 1.6$	$\sim 40$

<sup>a</sup>  $\text{IC}_{50}$  is the half-maximal activating  $\text{Ca}^{2+}$  concentration.

<sup>b</sup>  $h$  is the Hill Coefficient.

<sup>c</sup>  $\text{EC}_{50}$  is the half-maximal activating GCAP1 concentration.

<sup>d</sup> X-fold activation is  $(\text{GC}_{\text{max}} - \text{GC}_{\text{min}})/\text{GC}_{\text{min}}$ .

<sup>e</sup> Decimal logarithm of the macroscopic  $\text{Ca}^{2+}$ -binding constants after fitting data to a two independent binding sites model with CalLigator (57).

<sup>f</sup> Apparent affinity is the average of the significant  $\log K_i$  (see Materials and Methods for details).

**Table 3.** Results of DLS and SEC experiments

	$\text{Pdl} \pm \sigma (10^{-1})$	$d \pm \sigma (\text{nm})$	$n [r]$	$\text{MCR} \pm \sigma (\text{kcps})$	SEC MW (kDa)
WT					
$\text{Mg}^{2+}$	$1.7 \pm 0.05$	$6.33 \pm 0.03$	32 [15]	$244.6 \pm 1.2$	45.9
$\text{Mg}^{2+} \text{ Ca}^{2+}$	$1.5 \pm 0.03$	$6.47 \pm 0.03$	36 [15]	$249.6 \pm 2.1$	47.8
E111V					
$\text{Mg}^{2+}$	$1.8 \pm 0.03$	$5.98 \pm 0.05$	77 [6]	$148.1 \pm 1.0$	45.9
$\text{Mg}^{2+} \text{ Ca}^{2+}$	$2.0 \pm 0.05$	$6.08 \pm 0.04$	74 [6]	$142.4 \pm 0.6$	43.7

Pdl: polydispersity index,  $\sigma$ : standard error,  $d$ : hydrodynamic diameter,  $n$ : number of measurements, each consisting of  $r$  runs, MCR: mean count rate, SEC MW, estimated molecular weight from analytical SEC using calibration curve from ref. (60).

6-nm red shift in the case of E111V GCAP1, together with a decrease in fluorescence emission. Addition of  $\text{Ca}^{2+}$  on top did not significantly change the observed patterns, leading for both variants to a minimal increase in fluorescence emission without appreciable wavelength shifts. In conclusion, the prominent aggregation observed for E111V GCAP1 in the presence of  $\text{Mg}^{2+}$  cannot be attributed to significantly different hydrophobic properties of the two variants.

### Changes in secondary and tertiary structure of WT and E111V GCAP1 in the presence of $\text{Ca}^{2+}$

GCAP1 is a relatively small protein formed by the assembly of four  $\alpha$  helix-loop- $\alpha$  helix motifs called EF-hands (Fig. 4A), three of which (EF2, EF3 and EF4) have the correct consensus sequence to bind cations (37). The overall fold of GCAP1 is that of an all- $\alpha$  helix protein; therefore, any change of its secondary structure can be ideally monitored by circular dichroism (CD) spectroscopy, which in the far UV range (200–250 nm) is particularly sensitive to the fold of the main chain.

Far UV CD spectra of both WT and E111V GCAP1 showed the expected  $\alpha$  helix pattern, with minima at 208 and 222 nm

(Supplementary Material, Fig. S3). Addition of 1-mM  $\text{Mg}^{2+}$  to the apo-proteins did not significantly change the spectra of the WT (Supplementary Material, Table S2), as shown by the unaltered ( $\theta_{222}/\theta_{208}$ ) ratio (0.94), while a small but significant change in the spectral shape could be appreciated for E111V ( $\theta_{222}/\theta_{208} = 0.92$  in the apo form, 0.93 in the presence of  $\text{Mg}^{2+}$ ). The addition of saturating  $\text{Ca}^{2+}$  led to a  $\sim 6\%$  increase of signal for the WT and to a smaller increase for E111V ( $\sim 4\%$ ). While the shape of the spectrum was slightly changed for the WT ( $\theta_{222}/\theta_{208}$  shifted from 0.94 to 0.96), no appreciable spectral changes could be observed for the mutant (Supplementary Material, Table S2).

The strong signal in the far UV allowed us to monitor the stability of both GCAP1 variants upon thermal denaturation in the 20–96°C range (Fig. 4B). While the stabilizing presence of saturating  $\text{Ca}^{2+}$  prevented a clear structural transition to be observed for either variant (Fig. 4B), in the sole presence of  $\text{Mg}^{2+}$  a clear difference could be observed, since E111V displayed a  $\sim 5.5^\circ\text{C}$  higher melting temperature compared to the WT ( $T_{\text{m}} = 49.0^\circ\text{C}$  for WT GCAP1 compared to  $54.5^\circ\text{C}$  for E111V, Supplementary Material, Table S2). Magnesium has therefore a significantly increased stabilizing effect on E111V GCAP1 compared to the WT form.

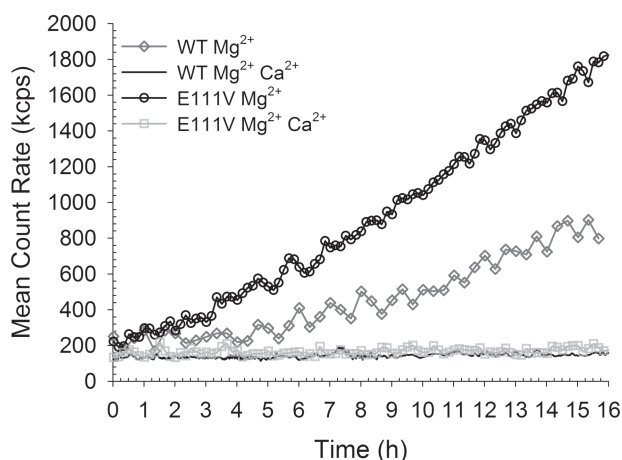


**Figure 3.** Results from dynamic light scattering experiments. Mean count rate evolution over 16 h of  $\sim 20\text{-}\mu\text{M}$  WT GCAP1 in 20-mM Tris-HCl pH 7.5, 150-mM KCl, 1-mM DTT, in the presence of 500- $\mu\text{M}$  EGTA and 1-mM  $\text{Mg}^{2+}$  (grey diamonds), or 1-mM  $\text{Mg}^{2+}$  and 500- $\mu\text{M}$   $\text{Ca}^{2+}$  (black line), and  $\sim 20\text{-}\mu\text{M}$  E111V in the presence of 500- $\mu\text{M}$  EGTA and 1-mM  $\text{Mg}^{2+}$  (black circles), or 1-mM  $\text{Mg}^{2+}$  and 500- $\mu\text{M}$   $\text{Ca}^{2+}$  (light grey squares). Measurements were collected at 37°C approximately every minute; each measurement was an accumulation of six runs.

CD spectra recorded in the near UV region (250–320 nm) provide information as to the local environment of the aromatic residues, namely Phe, Tyr and Trp, and therefore on protein tertiary structure. Near UV CD spectra of apo and  $\text{Mg}^{2+}$ -bound WT GCAP1 were almost indistinguishable from one another (Fig. 4C), indicative of no major conformational change occurring upon  $\text{Mg}^{2+}$  binding. When saturating  $\text{Ca}^{2+}$  was added an increase of intensity of the signal was observed, with significant changes especially in the Phe and Tyr bands. Interestingly, the near UV CD spectrum of apo E111V GCAP1 was more intense compared to the WT and displayed a completely positive ellipticity. A significant decrease in the spectral intensity was observed in the whole near UV range upon addition of  $\text{Mg}^{2+}$ , and major changes were displayed upon addition of saturating  $\text{Ca}^{2+}$ , especially in the Phe and Tyr bands. Overall, the presence of cations seems to induce more appreciable changes in the tertiary structure of E111V GCAP1 compared to the WT, although the comparison between both far and near UV CD spectra points to fairly modest structural variations.

### Binding of $\text{Ca}^{2+}$ to WT and E111V GCAP1

Since no major structural change was observed for E111V GCAP1 compared to the WT, nor was a substantial difference in protein surface hydrophobicity detected under condition of saturating  $\text{Ca}^{2+}$ , we investigated whether the E111V substitution affected GCAP1  $\text{Ca}^{2+}$  sensitivity. In order to probe the  $\text{Ca}^{2+}$  sensing properties of the CORD-related variant in comparison with the WT, we used two different approaches. Figure 5A shows results from gel mobility shift assays. The mobility of WT GCAP1 on SDS-PAGE was typically shifted toward lower apparent molecular weight (MW) in the presence of saturating  $\text{Ca}^{2+}$ , as observed previously with the bovine ortholog (38). The same experiment performed with E111V GCAP1 highlighted significantly slower electrophoretic mobility for the mutant in the presence of saturating  $\text{Ca}^{2+}$ , indicative of a less pronounced  $\text{Ca}^{2+}$ -induced effect

on the conformation of the mutant suggestive of decreased affinity for  $\text{Ca}^{2+}$ .

$\text{Ca}^{2+}$ -titration experiments performed with the chromophoric chelator 5,5'-dibromo-BAPTA (Fig. 5B and Table 2) in the presence of 1-mM  $\text{Mg}^{2+}$  confirmed the significantly compromised  $\text{Ca}^{2+}$  sensing ability of E111V GCAP1. A high affinity  $\text{Ca}^{2+}$ -binding site ( $K_1$ , low nM range) and a moderate affinity site ( $K_2$ , low  $\mu\text{M}$  range) were detected for WT GCAP1, resulting in a physiologically relevant apparent affinity ( $K_d^{\text{app}} = 490\text{ nM}$ ; Table 2). The titration profile of E111V GCAP1 was instead compatible with two very low affinity sites ( $K_1$  and  $K_2$ , high  $\mu\text{M}$  range). The resulting extremely low apparent affinity (estimated  $K_d^{\text{app}} \sim 40\text{ }\mu\text{M}$ ; Table 2) appears inconsistent with physiological  $\text{Ca}^{2+}$  sensing for E111V GCAP1.

### Dynamic structural properties of WT and E111V GCAP1: insights from MD simulations

Major conformational changes associated with the E111V substitution were excluded by CD spectroscopy; however, a number of structure-related differences remained to be clarified, namely (i) the significant propensity of the mutant to form aggregates; (ii) its higher thermal stability in the presence of physiological  $\text{Mg}^{2+}$ ; and (iii) its compromised  $\text{Ca}^{2+}$  sensing. In order to shed light on such subtle differences, we performed 200-ns all-atom MD simulations of both WT and E111V GCAP1 in their  $\text{Ca}^{2+}$ -loaded states (all three EF-hands binding a  $\text{Ca}^{2+}$  ion, corresponding to GC-inhibiting state) and EF2- $\text{Mg}^{2+}$  states (a  $\text{Mg}^{2+}$  ion bound to EF2, corresponding to the GC-activating state). Although the overall  $C_\alpha$  root-mean square fluctuation (RMSF) was comparatively similar for WT and E111V under both tested conditions, some important local differences could be noticed, highlighting a substantially altered flexibility of specific protein structural regions far apart from the EF2 motif, where the cation was bound (Supplementary Material, Fig. S4, top panels). Interestingly, the  $\text{Mg}^{2+}$ -bound form of E111V displayed an overall lower RMSF compared to the WT. The flexibility of the WT was in fact significantly higher for residues belonging to the entering helix and cation-binding loop of the EF3 motif as well as parts of the EF4 exiting helix (Fig. 6A). The dynamically more rigid conformation of  $\text{Mg}^{2+}$ -bound E111V also resulted in a distortion of the EF3 loop, which shortened of approximately 4 Å the distance between the  $C_\alpha$  atoms of residues 111 and V101, located at the N-terminal extreme of the EF3 loop (Supplementary Material, Fig. S4C). In contrast, placing three  $\text{Ca}^{2+}$  ions in the respective EF-hands of E111V GCAP1 led to significant structural fluctuations of the EF3 and EF4 binding loops, as highlighted by the prominent RMSF values in these regions compared to the WT case (Fig. 6A and Supplementary Material, S4B). MD simulations highlighted how forcing the binding of  $\text{Ca}^{2+}$  to EF3 in the absence of the bidentate coordinator provided by the side chain carboxyl group of Glu111 results in severe instability of the loop conformation and loss of optimal coordination of the  $\text{Ca}^{2+}$  ion, which was also characterized by high flexibility (Fig. 6A). Interestingly, the structural perturbation induced by the point mutations extended to the neighbor EF4 motif, whose cation binding loop and relative  $\text{Ca}^{2+}$  ion also showed remarkably higher flexibility compared to the WT case (Fig. 6A and Supplementary Material, S4B).

The irreversible distortion of the EF3 loop, responsible for the apparent loss of affinity for  $\text{Ca}^{2+}$  of the mutant became apparent when analyzing the distance between residue 111 and Val 101 (Fig. 6B and Supplementary Material, S4D). While



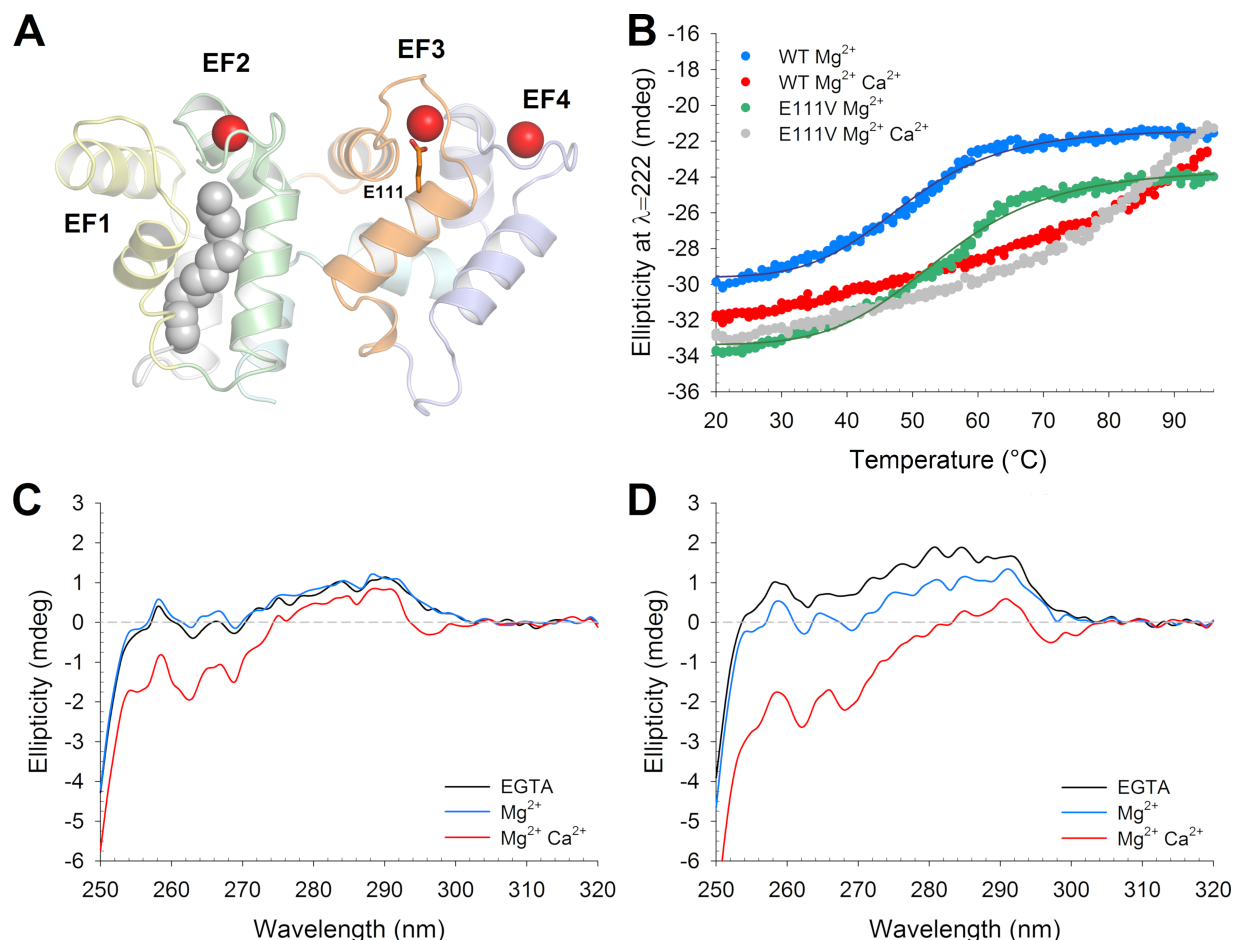


**Figure 4.** Structural and stability changes occurring in WT and E111V GCAP1 upon ion binding monitored by circular dichroism spectroscopy. (A) Cartoon representation of the three-dimensional homology model of  $\text{Ca}^{2+}$ -loaded human GCAP1; EF1 is colored in yellow, EF2 in green, EF3 in orange and EF4 in light blue. N- and C-terminal are represented in light grey and light cyan, respectively; the myristoyl group is represented in grey spheres,  $\text{Ca}^{2+}$  ions are shown as red spheres and residue E111 is shown as sticks. (B) Thermal denaturation profiles of  $\sim 10\text{-}\mu\text{M}$  WT GCAP1 in the presence of  $300\text{-}\mu\text{M}$  EGTA and  $1\text{-mM}$   $\text{Mg}^{2+}$  (blue), or  $1\text{-mM}$   $\text{Mg}^{2+}$  and  $300\text{-}\mu\text{M}$   $\text{Ca}^{2+}$  (red), and  $\sim 10\text{-}\mu\text{M}$  E111V in the presence of  $300\text{-}\mu\text{M}$  EGTA and  $1\text{-mM}$   $\text{Mg}^{2+}$  (green), or  $1\text{-mM}$   $\text{Mg}^{2+}$  and  $300\text{-}\mu\text{M}$   $\text{Ca}^{2+}$  (grey). Thermal denaturation was performed in  $20\text{-mM}$  Tris-HCl pH 7.5,  $150\text{-mM}$  KCl by following the decrease in ellipticity at  $\lambda = 222$  nm over the  $20\text{-}96^\circ\text{C}$  temperature range. When possible, data were fitted to a four-parameter Hill sigmoid; estimation of the  $T_m$  is reported in Supplementary Material, Table S2. Near UV CD spectra of  $\sim 35\text{-}\mu\text{M}$  WT (C) and E111V (D) GCAP1 in the presence of  $500\text{-}\mu\text{M}$  EGTA (black) and after sequential additions of  $1\text{-mM}$   $\text{Mg}^{2+}$  (blue) and  $500\text{-}\mu\text{M}$  free  $\text{Ca}^{2+}$  (red). CD spectra were recorded at  $37^\circ\text{C}$  in  $20\text{-mM}$  Tris-HCl pH 7.5,  $150\text{-mM}$  KCl,  $1\text{-mM}$  DTT.

in  $\text{Ca}^{2+}$ -loaded WT GCAP1 the optimal packing of the EF3 motif ensured a constant distance of  $\sim 6$  Å between the  $\text{C}_\alpha$  carbons, the cation binding loop opened up in the case of E111V, resulting in an almost doubled distance between the same atoms (Fig. 6B and Supplementary Material, S4D).

## Discussion

CORD is a severe vision-threatening disease, affecting 1/30,000 to 1/40,000 individuals (22). Several genes encoding for proteins involved in the phototransduction cascade have been found to be associated with CORD, and among them, 19 mutations, including the one presented in this study, were found in *GUCA1A* (10–21). It is important to notice that, while the first *GUCA1A* mutation associated with retinal dystrophy (p.(Tyr99Cys)) was discovered almost 20 years ago (19), 9 out of these 19 mutations have been found in the last 5 years. The number of CORD-associated mutations is probably going to increase due to higher attention to molecular diagnostics and to the significant improvement

of sequencing techniques. Defining precisely the genotype of patients affected by CORD and other retinal dystrophies seems to be an essential step to move towards personalized medicine. Previous biochemical and biophysical investigations performed on COD/CORD-associated *GUCA1A* variants, on the other hand, showed that specific molecular phenotypes do not necessarily correlate with the clinical disease phenotype, thus pointing to an urgency for highly defined molecular characterization of the effect of each individual point mutation at the protein level as well as at the system level (10,39,40).

In this work, we identified a novel mutation in *GUCA1A* affecting a highly conserved glutamate residue (Supplementary Material, Fig. S1B), which is essential for the correct coordination of the  $\text{Ca}^{2+}$  ion in the high affinity site EF3 (Fig. 6B). The family study involved four members of the proband's family, including his mother and three daughters. In line with the autosomal dominant model of Mendelian inheritance, the *GUCA1A* variant was only found in the two affected daughters and not in the other two healthy relatives (Fig. 1B), showing that the disease

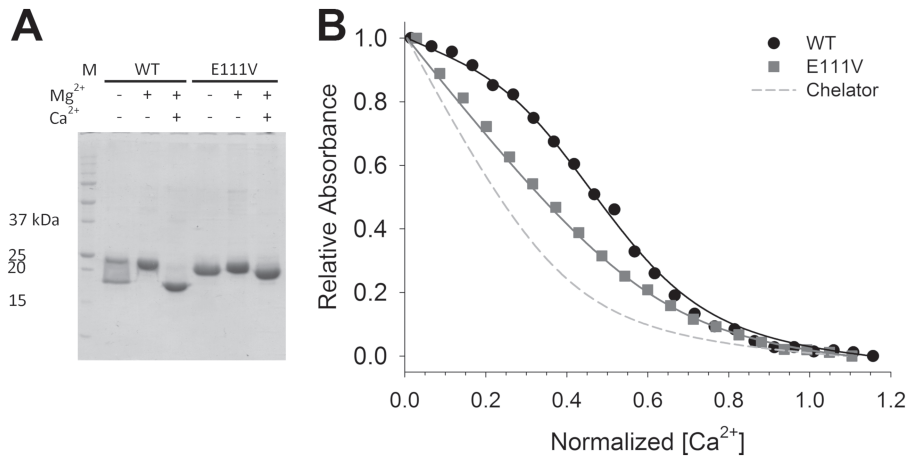


**Figure 5.** Ca<sup>2+</sup>-sensitivity of WT and E111V GCAP1 monitored by gel mobility shift SDS-PAGE and absorption spectroscopy. (A) 15% SDS-PAGE of ~30- $\mu$ M WT or E111V GCAP1 in the absence of ions (5-mM EDTA), in the presence of Mg<sup>2+</sup> (5-mM EGTA and 1-mM free Mg<sup>2+</sup>) and in the presence of Mg<sup>2+</sup> and Ca<sup>2+</sup> (1-mM Mg<sup>2+</sup> and 5-mM Ca<sup>2+</sup>). (B) Normalized Ca<sup>2+</sup> titration curves obtained by a competition assay with the chromophoric 5,5'-Br<sub>2</sub>-BAPTA of WT (black circles) and E111V GCAP1 (grey squares) in the presence of 1-mM Mg<sup>2+</sup>. Ca<sup>2+</sup> concentrations include dilution effects upon titration; normalization details are reported in the Methods section. Experimental data are shown together with the optimal curve obtained by computer fitting (black and grey solid lines, respectively) and the theoretical (Chelator) curve simulating the titration of the chelator (grey dashed line); estimation of log K<sub>1</sub> is reported in Table 2.

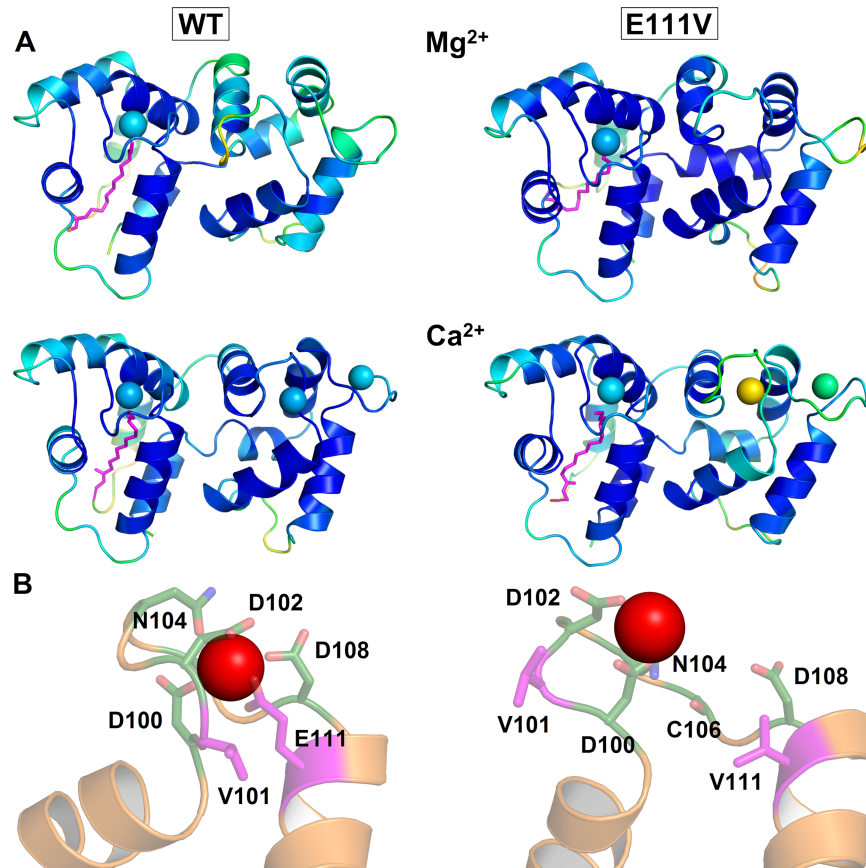


**Figure 6.** Structural insights from MD simulations. Final conformations after 200-ns MD simulations (A) of WT (right panels) and E111V (left panels) GCAP1 in their EF2-Mg<sup>2+</sup> (top panels) and Ca<sup>2+</sup>-loaded forms (bottom panels). Proteins are shown as cartoons, the myristoyl group is represented as magenta sticks, ions are shown as spheres and proteins and ions are colored in a blue-to-red scale according to their C <sub>$\alpha$</sub> -RMSF, ranging from 0.5 to 4.2 Å (Supplementary Material, Fig. S4). (B) Detail of the Ca<sup>2+</sup>-binding loop of EF3 of Ca<sup>2+</sup>-loaded WT (left) and E111V (right); helices are shown as cartoons colored according to Figure 4A, Ca<sup>2+</sup> coordinating residues are represented as sticks where C atoms are green, N atoms are blue and O atoms are red. Residues V101 and E/V111 are represented as magenta sticks; Ca<sup>2+</sup> ion is shown as a red sphere.

gene is fully penetrant in this family. The clinical phenotype was severe in all patients at the congenital presentation (nystagmus, photophobia) and suggestive of further progressive retinal

degeneration of both cone and rod elements when comparing the younger family members to the older proband, who showed evolution to macular atrophy (Fig. 1, Table 1).

Our detailed biochemical and biophysical characterization comparing human WT GCAP1 and the CORD-associated E111V variant permits to elucidate some hallmarks of the pathogenic variant. While the molecular features of the WT form, including the sensitivity to  $\text{Ca}^{2+}$  and the oligomeric properties as well as the induced regulation of the target GC, were all compatible with a physiological function, E111V GCAP1 displayed important differences. Although the point mutation did not significantly alter protein secondary and tertiary structures (Fig. 4, Supplementary Material, Table S2, Fig. S3), the substitution significantly stabilized the  $\text{Mg}^{2+}$ -bound, GC-activating state, as highlighted by thermal denaturation studies (Fig. 4B). MD simulations supported this finding and suggested a more rigid conformation of the mutant compared to the WT in the  $\text{Mg}^{2+}$ -bound state (Fig. 6). The less flexible conformation acquired at low  $\text{Ca}^{2+}$  induced a severe aggregation for E111V GCAP1 (Fig. 3), which could have important functional consequences.

In terms of alteration in protein structure, our data clearly show that the E111V substitution leads to important distortion of the EF3 loop, as well as to an increased flexibility of the EF4 loop (Fig. 6), which in the WT case hosts the first  $\text{Ca}^{2+}$  dissociating from GCAP1 during GC activation (6–8–41). Such structurally important perturbations are reflected into a significantly decreased affinity for  $\text{Ca}^{2+}$  of the mutant (Fig. 5B, Table 2). The  $\sim 40\text{-}\mu\text{M}$  apparent affinity for  $\text{Ca}^{2+}$  measured for E111V GCAP1 appears to be incompatible with the changes of intracellular  $\text{Ca}^{2+}$  in photoreceptor outer segments during the phototransduction cascade, which all occur in the sub-micromolar range of  $[\text{Ca}^{2+}]$  (1,4,5). Interestingly, the impressive difference in affinity for  $\text{Ca}^{2+}$  of E111V GCAP1 compared to the WT ( $\sim 80$ -fold) did not impact the apparent affinity of GCAP1 for the target GC, as shown by the very similar  $\text{EC}_{50}$  values (Table 2, Fig. 2B). However, a dramatic effect of the point mutation was detected in the regulation of the catalytic activity of the GC target (Fig. 2). As expected, WT GCAP1 was found to regulate the switch between maximal and minimal GC enzymatic activity over the physiological range of  $[\text{Ca}^{2+}]$  ( $\text{IC}_{50} = 0.26\ \mu\text{M}$ ). In contrast, the  $\text{IC}_{50}$  value measured for E111V GCAP1 was  $\sim 40$ -fold higher ( $\text{IC}_{50} = 10\ \mu\text{M}$ ), thus shifting the GC-inhibiting capability of the mutant GCAP1 to non-physiological, extremely high  $[\text{Ca}^{2+}]$  levels. In other words, at sub-micromolar physiological  $[\text{Ca}^{2+}]$  typical of the phototransduction processes, E111V GCAP1 would keep the target GC in a constitutively active state (Fig. 2, Table 2), which would result in aberrant synthesis of cGMP in the absence of light stimulus, therefore severely perturbing the homeostasis of both second messengers (10).

Although it might be tempting to associate a reduced affinity for  $\text{Ca}^{2+}$  with a severe dysregulation of the target GC, this is not always the case. Previous studies demonstrated that most of the COD/CORD-related GCAP1 mutants indeed showed reduced affinity for  $\text{Ca}^{2+}$  and  $\text{IC}_{50}$  values for the GC activity shifted to non-physiologically high  $\text{Ca}^{2+}$  levels (15,20,25,30,31); however, cases have been found in which the  $\text{Ca}^{2+}$  sensing was substantially unaltered with respect to the WT case, and yet a constitutive regulation of the target GC was observed (31). The subtle effects of COD/CORD point mutations should therefore be considered in the context of altered molecular communication between the GCAP1 protein and its molecular target, which is highly dependent on the cation-loaded state (42). However, other factors have been established to modulate the activity of GC especially in cones (43,44), the first photoreceptors affected in COD/COD, which renders the GCAP1-GC complex a highly modular and finely regulated signaling network unit (45).

System-level analyses performed on the biochemical data available for some COD/CORD-associated GCAP1 mutants suggest that the severity of the disease in terms of deregulation of the second messenger homeostasis eventually depends on the deregulation of the GC-GCAP enzymatic complex (46). In particular, in the case of high expression levels of pathogenic GCAP1 mutants with extremely high  $\text{IC}_{50}$  values, GCAP1 would not possibly contribute to shaping the cGMP rate synthesis, therefore the GC enzymatic activity would become dynamically regulated solely by the other present  $\text{Ca}^{2+}$  sensor GCAP2, for which no COD/COD associated mutation is known so far.

The aberrant regulation of GC by pathogenic GCAP1 could be potentially overcome by the compensatory effect of other GCAPs. This possibility would come as a direct consequence of the calcium-relay mechanism, which finely regulates the activity of GC and ensures the correct physiological control of cGMP synthesis by GC (1). As to date, no cure exists for COD/CORD; this is an interesting concept for the development of protein therapy-based approaches aimed at the delivery of controlled amounts of functional GCAP1 in the photoreceptors. Although at their infancy (47,48), these approaches could constitute promising starting points for the development of effective therapies for COD/CORD in the future.

## Materials and Methods

### Patients studies

This study is a retrospective case series description that does not require ethics committee approval. Written, informed consent was obtained from adult patients or both parents for the minor patient, prior to their inclusion in this study and after full explanation of the clinical and instrumental procedures. The informed consent forms include consent for the use of anonymized genetic results for scientific publications. All research procedures described in this work adhered to the tenets of the Declaration of Helsinki.

### Clinical and instrumental ophthalmological examinations

Ophthalmological characterization included visual acuity evaluation (expressed in LogMAR), ocular motility evaluation, dilated funduscopy and multicolour imaging. Furthermore, in order to complete phenotype definition, we performed spectral domain OCT, Blue autofluorescence (Spectralis HRA+, Heidelberg Engineering, Heidelberg, Germany) and OCT angiography (OptovueAngioVue System, Optovue Inc, Fremont, CA) (Imaging not shown).

### Genetic testing

Genetic testing was performed for diagnostic purposes following genetic counselling. The DNA of all patients was extracted from peripheral blood using a commercial kit (E.Z.N.A. Blood DNA kit Omega Bio-tek; Norcross, GA, USA).

The proband's DNA underwent NGS on an Illumina MiSeq instrument (PE  $2 \times 150$  bp protocol) with a custom panel designed for a suspected diagnosis of COD. The panel comprised the following genes: CNGA3 (OMIM \*600053), RAB28 (OMIM \*612994), GUCY2D (OMIM \*600179), C8orf37 (OMIM \*614477), PROM1 (OMIM \*604365), GUCA1A (OMIM \*600364), CERKL (OMIM \*608381), CACNA1F (OMIM \*300110), SEMA4A (OMIM \*607292), CRX (OMIM \*602225), AIPL1 (OMIM \*604392), RGRIP1 (OMIM \*605446),

ABCA4 (OMIM \*601691), PITPNM3 (OMIM \*608921), PRPH2 (OMIM \*179605), CNGB3 (OMIM \*605080), ADAM9 (OMIM \*602713), RPGR (OMIM \*312610), CDHR1 (OMIM \*609502), RIMS1 (OMIM \*606629) and RAX2 (OMIM \*610362).

The sequences were mapped on the human reference sequence GRCh38. The in-house bioinformatics pipeline comprises sequence variant calling using VarScan (version v2.3), Bcftools of SAMTools (version 0.1.19-44428cd), GATK Unified Genotyper and filter-based annotation using Annovar software with online databases such as dbSNP (<http://www.ncbi.nlm.nih.gov/projects/SNP>), 1000 Genomes (<http://www.1000genomes.org>) and Exome Variant Server (evs.gs.washington.edu/EVS). Pathogenic variations were sought in HumsVar (<http://omictools.com/humsavar-tool>) and Human Gene Mutation Database (HGMD professional). In silico prediction softwares such as Mutation Taster (<http://www.mutationtaster.org/>) and the Ensembl Variant Effect Predictor tool (<http://www.ensembl.org/Tools/VEP>) were used to assess the pathogenicity of each variant.

Sanger sequencing (CEQ8800 Sequencer, Beckman Coulter) was used to confirm NGS variants and for target sequencing in the family genotype–phenotype segregation study.

## Materials

QuikChange II Site-Directed Mutagenesis Kit was purchased from Agilent; Bradford reagent was purchased from Bio-Rad. DMEM, fetal bovine serum, penicillin, streptomycin and geneticin were purchased from Thermofisher–Life Technologies. Chromatographic columns (Superose 12 10/300 GL, HiPrep Q HP 16/10 and HiPrep 26/60 Sephacryl S-200 HR) were purchased from GE healthcare; HPLC column (LiChrospher 100 RP-18) was purchased from Sigma Aldrich. Synthetic oligonucleotides were purchased by Eurofins. All other chemicals were of the highest commercially available purity grade and purchased from Sigma Aldrich.

## Electrophysiological recordings

Electrophysiological assessment was executed by Retimax apparatus (CSO, Firenze, Italy).

Full-Field ERGs were obtained from both eyes, after full pupil dilatation by 1% tropicamide eye drops. Prior to any ERG recordings, subjects underwent a preadaptation period to the stimulus/background mean luminance (20 min of preadaptation to a steady background of 0 cd/m<sup>2</sup> for dark-adapted ERG and to 30 cd/m<sup>2</sup> for light-adapted ERG).

Ganzfeld-rod and cone ERG were recorded following the ISCEV standards (49), under the constant monitoring of an external observer. The stimulus for dark-adapted ERG was a dim white flash of 0.01 cd/(s m<sup>2</sup>), with a minimum interval of 2 s between flashes. For photopic ERGs, white 50-ms stimuli with an intensity of 3 cd/(s m<sup>2</sup>) were presented on a steady white background of 30 cd/m<sup>2</sup>. The interstimulus interval was 1 s. ERGs were recorded by skin electrodes. Silver chloride electrodes (0.8 mm) were taped on the skin of the lower eyelids after coating the electrode surface with saline electroconductive gel, just 2.5 mm below the inferior lid rim, in the vertical axis passing through the corneal apex. A similar electrode on the lower eyelid of the contralateral patched eye was used as reference to minimize potential artefacts due to blink and conjugate eye movement (50). Signals were amplified (50 K), filtered (0.3–300 Hz), digitized at 2 KHz and averaged (40 events) with automatic artefact rejection. Two runs were typically performed

for each eye. The peak-to-peak noise level was estimated in line with the sum of events and odd events obtained for the averaging process.

The amplitude and implicit times of the a- and b-waves were measured as previously described (51,52). Dark and light-adapted ERG a-wave amplitudes were measured from prestimulus baseline to first negative trough. The scotopic and photopic ERG b-wave amplitudes were measured from the negative peak of the a-wave to the positive peak of the b-wave.

## Cloning, protein expression and purification of human WT and E111V GCAP1

The cDNA of human GCAP1-E6S (Uniprot: P43080) was cloned into a pET-11a using NdeI and NheI as restriction sites (GenScript). The E6S mutation was inserted to generate the consensus sequence for posttranslational N-terminal myristoylation by *Saccharomyces cerevisiae* N-myristoyl transferase (yNMT) (53). Sequence variant c.332A>T (leading to the E111V substitution) was created by polymerase chain reaction site-directed mutagenesis using QuikChange II Site-Directed Mutagenesis Kit (Agilent), primers (forward: 5'-TGCATCGATCGCGACGACTGCTG ACCATTATC-3', reverse: 5'-GATAATGGTCAGCAGTACGTCGGAT CGATGCA-3') and DNA sequencing were provided by Eurofins.

Heterologous expression of GCAP1 forms was performed in BL21 *Escherichia coli* cells after co-transformation with pBB131-yNMT. Proteins were purified from the insoluble fraction by a combination of Size Exclusion and Anionic Exchange Chromatography as described before (27,31,53), with the only difference of the presence of 2-mM Ca<sup>2+</sup> in all purification buffers for improved resolution and protein stability. Methods for the determination of protein purity and concentration were the same as previously reported (27,31,53). Proteins were aliquoted in 20-mM Tris-HCl pH 7.5, 150-mM KCl, 1-mM DTT, flash-frozen and kept at –80°C until use. Alternatively, some aliquots of the proteins were washed against decalcified NH<sub>4</sub>HCO<sub>3</sub> buffer and lyophilized for use in competition chelator assays.

## Cell culture and assays of GC enzymatic activity

Recombinant human ROS-GC1 (GC) was stably expressed in HEK flip 293 cells, and the so obtained HEK293-GC cells were cultured in DMEM medium supplemented with fetal bovine serum (10%, v/v), penicillin (100 units/ml), streptomycin (100 µg/ml) and geneticin (500 µg/ml), as previously described (54). GC activity was measured as previously described (20,54,55) after reconstitution of cell membranes and GCAP1 forms. The maximal and minimal GC activation of GCAP1 forms was measured by incubation of 5-µM WT or E111V GCAP1 with either <19 nM or ~30-µM free Ca<sup>2+</sup>. The Ca<sup>2+</sup> concentration at which GC activation is half-maximal (IC<sub>50</sub>) was measured by incubation of 5-µM WT or E111V GCAP1 at different [Ca<sup>2+</sup>] levels (<19 nM–1 mM) using Ca<sup>2+</sup>-EGTA buffer solutions (54–56). The GCAP1 concentration at which GC activation is half-maximal (EC<sub>50</sub>) was measured by incubation of increasing concentrations of WT or E111V GCAP1 (0–20 µM) in the presence of <19-nM free Ca<sup>2+</sup>. X-fold activation was expressed as (GC<sub>max</sub> – GC<sub>min</sub>)/GC<sub>min</sub>, where GC<sub>max</sub> and GC<sub>min</sub> are the GC activity in the presence of 1-mM Mg<sup>2+</sup> at <19 nM and 1-mM free Ca<sup>2+</sup>, respectively. Reported activity values are expressed as mean ± standard deviation of at least three data sets.

## Ca<sup>2+</sup>-binding assays

Calcium affinity of GCAP1 variants was estimated using a method based on the competition with a chromophoric chelator (57,58) as described in previous work (25), with the only difference consisting of the experimental decalcified buffer (20-mM Tris-HCl pH 7.5, 150-mM KCl, 1-mM DTT initial free [Ca<sup>2+</sup>] = 0.9–1.5 μM). Briefly, decalcified lyophilized proteins were dissolved in the experimental buffer containing the chromophoric chelator 5,5'-Br<sub>2</sub>-BAPTA (24–25 μM) at a concentration of 9.5–12 μM. The concentration of protein stocks was determined by Bradford assays (59) optimized for GCAP1 based on determination of precise protein content by amino acid analysis of initial stocks (Alphalyze).

Absorbance decrease upon Ca<sup>2+</sup>-titration was monitored at λ = 263 nm and fitted using CaLigator (57) to estimate individual macroscopic binding constants (log K<sub>i</sub>, Table 2) and subsequently apparent affinity values (K<sub>d</sub><sup>app</sup> = 10<sup>-(log K<sub>1</sub> + log K<sub>2</sub>)/2</sup>, Table 2). Data fitting to a three-independent binding sites model resulted in a highly unreliable estimation of the lowest affinity binding site for the WT (log K<sub>i</sub> <<4), while for the E111V variant results were not substantially different from data fitting to a two-independent binding sites model.

Presented data was normalized as follows:

$$y = \frac{A_{\max} - A_{263}}{A_{\max} - A_{\min}} \quad \text{Normalized } [Ca^{2+}] = \frac{[Ca^{2+}]}{[Q] + 3[P]}$$

where A<sub>263</sub> is the absorbance at λ = 263 nm, A<sub>max</sub> and A<sub>min</sub> are the maximal and the minimal absorbance values, [Ca<sup>2+</sup>] is the total Ca<sup>2+</sup> concentration, [Q] is the 5,5'-Br<sub>2</sub>-BAPTA concentration and [P] is the protein concentration.

## CD spectroscopy and thermal denaturation profiles

CD spectra were recorded in 20-mM Tris-HCl pH 7.5, 150-mM KCl, 1-mM DTT buffer with a Jasco J-1500 spectropolarimeter equipped with a Peltier thermostated cell holder set at 37°C with a scan rate of 50 ns/min, 1-nm bandwidth, 4-s response time. Each spectrum was the average of five accumulations. Far UV CD spectra and thermal denaturation profiles were recorded in a 0.1-cm quartz cuvette with a protein concentration of ~10 μM in the presence of 300-μM EGTA, 300-μM EDTA and 1-mM Mg<sup>2+</sup> or 1-mM Mg<sup>2+</sup> and 300-μM Ca<sup>2+</sup>. Near UV CD spectra were recorded in a 1-cm quartz cuvette with a protein concentration of ~40 μM in the presence of 500-μM EGTA and after sequential additions of 1-mM Mg<sup>2+</sup> and 500-μM free Ca<sup>2+</sup>. Thermal denaturation data were collected from 20 to 96°C at λ = 222 nm, with a scan rate of 1.5°C/min, data pitch 0.1°C, response time 4 s and fitted to a four-parameter Hill sigmoid as follows:

$$y = e_f + \frac{|e_f - e_u| T^H}{T_m + T^H}$$

where e<sub>f</sub> is the ellipticity of the folded state, e<sub>u</sub> is the ellipticity of the unfolded state, T is the temperature, H is the Hill coefficient and T<sub>m</sub> is the melting temperature.

## DLS experiments

DLS measurements were performed at 25°C with a Zetasizer Nano-S (Malvern Instruments) with the same parameters for hydrodynamic diameter estimation as in ref. (20). Aggregations

studies were performed at 37°C collecting data every minute for ~16 h. The number of measurements for hydrodynamic diameter estimation was at least 32, each consisting of at least 6 repetitions; data are reported as mean ± standard error. All proteins were dissolved at a concentration of ~40 μM in 20-mM Tris-HCl pH 7.5, 150-mM KCl, 1-mM DTT buffer and either 500-μM EGTA and 1-mM Mg<sup>2+</sup> or 1-mM Mg<sup>2+</sup> and 500-μM Ca<sup>2+</sup>, then centrifuged at 4°C for 15 min at 18000 x g and finally filtered using 0.02-μm Anotop 10 filter (Whatman) before DLS analysis.

## Analytical SEC

The MW of WT and E111V GCAP1 was determined by SEC using a Superose 12 10/300 GL column (GE Healthcare) using the same calibration curve as in ref. (60). The column was equilibrated with 20-mM Tris-HCl pH 7.5, 150-mM KCl, 1-mM DTT buffer and either 500-μM EGTA and 1-mM Mg<sup>2+</sup> or 1-mM Mg<sup>2+</sup> and 500-μM Ca<sup>2+</sup>. Approximately 40-μM proteins were incubated in the same running buffers for 5 min, then centrifuged at 4°C for 15 min at 18000 x g before loading. Protein elution profiles were recorded at λ = 280 nm, retention volumes R<sub>v</sub> were determined and the distribution coefficient K<sub>d</sub> was calculated as follows:

$$K_d = \frac{R_v - V_0}{V_t - V_0}$$

where V<sub>t</sub> is the column volume and V<sub>0</sub> is the void volume. MWs were calculated from a calibration plot of log (MW) versus K<sub>d</sub>.

## Fluorescence spectroscopy

ANS fluorescence was used to monitor hydrophobicity changes in WT and E111V GCAP1 upon Mg<sup>2+</sup> and Ca<sup>2+</sup> binding. Proteins were diluted in 20-mM Tris-HCl pH 7.5, 150-mM KCl, 1-mM DTT buffer at ~2-μM concentration and incubated for 2 min with 30-μM ANS and 500-μM EDTA or 1-mM Mg<sup>2+</sup> and after addition of 1-mM Ca<sup>2+</sup>. Three accumulations of ANS fluorescence spectra were recorded at 37°C in the 400–650 nm range after excitation at λ = 380 nm with excitation and emission bandwidths of 5 nm.

## Gel mobility shift assays

SDS-PAGE on a 15% acrylamide gel was performed to monitor the differential mobility in denaturing conditions of WT and E111V GCAP1 upon Mg<sup>2+</sup> and Ca<sup>2+</sup> binding. Proteins were diluted in 20-mM Tris-HCl pH 7.5, 150-mM KCl, 1-mM DTT buffer at 30-μM concentration and incubated at 25°C for 5 min with 5-mM EDTA or 5-mM EGTA and 1.2-mM Mg<sup>2+</sup> or 1-mM Mg<sup>2+</sup> and 5-mM Ca<sup>2+</sup>.

## MD simulation and analyses

The homology model of human GCAP1 was obtained from the chicken GCAP1 structure template (37) using the procedure elucidated in ref. (25). Mutation E111V was inserted by *in silico* mutagenesis of WT human GCAP1 by selecting the most probable rotamer proposed by the 'mutate residue' function of the Maestro (Schrodinger) suite. MD simulations and analyses were run on GROMACS 2016.1 simulation package (61) using CHARMM36m all-atom force field (62), in which parameters for myristoylated-Gly were generated manually (available upon request). All settings for MD simulations were taken from ref. (6),

in which details are provided. Protocols for energy minimization, system equilibration and production phase were the same as in ref. (42). The 200-ns trajectories were subjected to RMSF and distance analyses, calculated on the  $C_{\alpha}$  atoms with the 'gmx rmsf' and 'gmx distance' functions of GROMACS 2016.1, respectively. RMSF, representing the time-averaged root-mean square deviation of bound ions and  $C_{\alpha}$  of all  $n$  residues with respect to the initial structure of the production, was calculated as follows:

$$\text{RMSF}(C_{\alpha})_n = \sqrt{\frac{1}{T} \sum_{t_i=1}^T |r_n(t_i) - r_n^{\text{ref}}|^2}$$

where  $T$  is the 200-ns timeframe,  $r_n(t_i)$  and  $r_n^{\text{ref}}$  are the  $C_{\alpha}$  coordinates of residue  $n$  at time  $t_i$  and in the reference structure, respectively.

## Supplementary Material

Supplementary Material is available at HMG online.

## Acknowledgements

Helpful technical suggestions on enzymatic assays from Dr Alexander Scholten are gratefully acknowledged. The authors thank Dr Paolo Esposito Veneruso for technical help in executing electrophysiological recordings and for collecting data. The contribution by Fondazione Bietti in this paper was supported by the Ministry of Health and Fondazione Roma. The financial support of Fondazione Telethon-Italy (grant no. GGP16010 to DDO) is gratefully acknowledged.

Conflict of Interest statement. None declared.

## References

- Koch, K.W. and Dell'Orco, D. (2013) A calcium-relay mechanism in vertebrate phototransduction. *ACS Chem. Neurosci.*, **4**, 909–917.
- Koch, K.W. and Dell'Orco, D. (2015) Protein and signaling networks in vertebrate photoreceptor cells. *Front. Mol. Neurosci.*, **8**, 67.
- Koch, K.W., Duda, T. and Sharma, R.K. (2010) Ca<sup>2+</sup>-modulated vision-linked ROS-GC guanylate cyclase transduction machinery. *Mol. Cell. Biochem.*, **334**, 105–115.
- Korenbrod, J.I. (2012) Speed, sensitivity, and stability of the light response in rod and cone photoreceptors: facts and models. *Prog. Retin. Eye Res.*, **31**, 442–466.
- Pugh, E.J. and Lamb, T. (2000) In Stavenga, D., DeGrip, W. and Pugh, E.J. (eds), *Handbook of Biological Physics*. Elsevier Science BV, Vol. 3, pp. 183–255.
- Marino, V., Sulmann, S., Koch, K.W. and Dell'Orco, D. (2015) Structural effects of Mg<sup>2+</sup> on the regulatory states of three neuronal calcium sensors operating in vertebrate phototransduction. *Biochim. Biophys. Acta*, **1853**, 2055–2065.
- Peshenko, I.V. and Dizhoor, A.M. (2004) Guanylyl cyclase-activating proteins (GCAPs) are Ca<sup>2+</sup>/Mg<sup>2+</sup> sensors: implications for photoreceptor guanylyl cyclase (RetGC) regulation in mammalian photoreceptors. *J. Biol. Chem.*, **279**, 16903–16906.
- Peshenko, I.V. and Dizhoor, A.M. (2006) Ca<sup>2+</sup> and Mg<sup>2+</sup>-binding properties of GCAP-1. Evidence that Mg<sup>2+</sup>-bound form is the physiological activator of photoreceptor guanylyl cyclase. *J. Biol. Chem.*, **281**, 23830–23841.
- Dizhoor, A.M., Olshevskaya, E.V. and Peshenko, I.V. (2010) Mg<sup>2+</sup>/Ca<sup>2+</sup> cation binding cycle of guanylyl cyclase activating proteins (GCAPs): role in regulation of photoreceptor guanylyl cyclase. *Mol. Cell. Biochem.*, **334**, 117–124.
- Behnen, P., Dell'Orco, D. and Koch, K.W. (2010) Involvement of the calcium sensor GCAP1 in hereditary cone dystrophies. *Biol. Chem.*, **391**, 631–637.
- Chen, X., Sheng, X., Zhuang, W., Sun, X., Liu, G., Shi, X., Huang, G., Mei, Y., Li, Y., Pan, X. et al. (2017) GUCA1A mutation causes maculopathy in a five-generation family with a wide spectrum of severity. *Genet. Med.*, **19**, 945–954.
- Huang, L., Li, S., Xiao, X., Jia, X., Sun, W., Gao, Y., Li, L., Wang, P., Guo, X. and Zhang, Q. (2013) Novel GUCA1A mutation identified in a Chinese family with cone-rod dystrophy. *Neurosci. Lett.*, **541**, 179–183.
- Jiang, L., Katz, B.J., Yang, Z., Zhao, Y., Faulkner, N., Hu, J., Baird, J., Baehr, W., Creel, D.J. and Zhang, K. (2005) Autosomal dominant cone dystrophy caused by a novel mutation in the GCAP1 gene (GUCA1A). *Mol. Vis.*, **11**, 143–151.
- Jiang, L., Wheaton, D., Bereta, G., Zhang, K., Palczewski, K., Birch, D.G. and Baehr, W. (2008) A novel GCAP1(N104K) mutation in EF-hand 3 (EF3) linked to autosomal dominant cone dystrophy. *Vision Res.*, **48**, 2425–2432.
- Kamenarova, K., Corton, M., Garcia-Sandoval, B., Fernandez-San Jose, P., Panchev, V., Avila-Fernandez, A., Lopez-Molina, M.I., Chakarova, C., Ayuso, C. and Bhattacharya, S.S. (2013) Novel GUCA1A mutations suggesting possible mechanisms of pathogenesis in cone, cone-rod, and macular dystrophy patients. *Biomed. Res. Int.*, **2013**, 517570.
- Manes, G., Mamouni, S., Herald, E., Richard, A.C., Senechal, A., Aouad, K., Bocquet, B., Meunier, I. and Hamel, C.P. (2017) Cone dystrophy or macular dystrophy associated with novel autosomal dominant GUCA1A mutations. *Mol. Vis.*, **23**, 198–209.
- Nishiguchi, K.M., Sokal, I., Yang, L., Roychowdhury, N., Palczewski, K., Berson, E.L., Dryja, T.P. and Baehr, W. (2004) A novel mutation (I143NT) in guanylate cyclase-activating protein 1 (GCAP1) associated with autosomal dominant cone degeneration. *Invest. Ophthalmol. Vis. Sci.*, **45**, 3863–3870.
- Nong, E., Lee, W., Merriam, J.E., Allikmets, R. and Tsang, S.H. (2014) Disease progression in autosomal dominant cone-rod dystrophy caused by a novel mutation (D100G) in the GUCA1A gene. *Doc. Ophthalmol.*, **128**, 59–67.
- Payne, A.M., Downes, S.M., Bessant, D.A., Taylor, R., Holder, G.E., Warren, M.J., Bird, A.C. and Bhattacharya, S.S. (1998) A mutation in guanylate cyclase activator 1A (GUCA1A) in an autosomal dominant cone dystrophy pedigree mapping to a new locus on chromosome 6p21.1. *Hum. Mol. Genet.*, **7**, 273–277.
- Vocke, F., Weisschuh, N., Marino, V., Malfatti, S., Jacobson, S.G., Reiff, C.M., Dell'Orco, D. and Koch, K.W. (2017) Dysfunction of cGMP signalling in photoreceptors by a macular dystrophy-related mutation in the calcium sensor GCAP1. *Hum. Mol. Genet.*, **26**, 133–144.
- Wilkie, S.E., Li, Y., Deery, E.C., Newbold, R.J., Garibaldi, D., Bateman, J.B., Zhang, H., Lin, W., Zack, D.J., Bhattacharya, S.S. et al. (2001) Identification and functional consequences of a new mutation (E155G) in the gene for GCAP1 that causes autosomal dominant cone dystrophy. *Am. J. Hum. Genet.*, **69**, 471–480.
- Hamel, C.P. (2007) Cone rod dystrophies. *Orphanet J. Rare Dis.*, **2**, 7.

23. Michaelides, M., Hardcastle, A.J., Hunt, D.M. and Moore, A.T. (2006) Progressive cone and cone-rod dystrophies: phenotypes and underlying molecular genetic basis. *Surv. Ophthalmol.*, **51**, 232–258.
24. Roosing, S., Thiadens, A.A., Hoyng, C.B., Klaver, C.C., den Hollander, A.I. and Cremers, F.P. (2014) Causes and consequences of inherited cone disorders. *Prog. Retin. Eye Res.*, **42**, 1–26.
25. Dell'Orco, D., Behnen, P., Linse, S. and Koch, K.W. (2010) Calcium binding, structural stability and guanylate cyclase activation in GCAP1 variants associated with human cone dystrophy. *Cell. Mol. Life Sci.*, **67**, 973–984.
26. Dizhoor, A.M., Boikov, S.G. and Olshevskaya, E.V. (1998) Constitutive activation of photoreceptor guanylate cyclase by Y99C mutant of GCAP-1. Possible role in causing human autosomal dominant cone degeneration. *J. Biol. Chem.*, **273**, 17311–17314.
27. Kitiratschky, V.B., Behnen, P., Kellner, U., Heckenlively, J.R., Zrenner, E., Jagle, H., Kohl, S., Wissinger, B. and Koch, K.W. (2009) Mutations in the GUCA1A gene involved in hereditary cone dystrophies impair calcium-mediated regulation of guanylate cyclase. *Hum. Mutat.*, **30**, E782–E796.
28. Olshevskaya, E.V., Calvert, P.D., Woodruff, M.L., Peshenko, I.V., Savchenko, A.B., Makino, C.L., Ho, Y.S., Fain, G.L. and Dizhoor, A.M. (2004) The Y99C mutation in guanylyl cyclase-activating protein 1 increases intracellular Ca<sup>2+</sup> and causes photoreceptor degeneration in transgenic mice. *J. Neurosci.*, **24**, 6078–6085.
29. Sokal, I., Dupps, W.J., Grassi, M.A., Brown, J. Jr., Affatigato, L.M., Roychowdhury, N., Yang, L., Filipek, S., Palczewski, K., Stone, E.M. et al. (2005) A novel GCAP1 missense mutation (L151F) in a large family with autosomal dominant cone-rod dystrophy (adCORD). *Invest. Ophthalmol. Vis. Sci.*, **46**, 1124–1132.
30. Sokal, I., Li, N., Surgucheva, I., Warren, M.J., Payne, A.M., Bhattacharya, S.S., Baehr, W. and Palczewski, K. (1998) GCAP1 (Y99C) mutant is constitutively active in autosomal dominant cone dystrophy. *Mol. Cell*, **2**, 129–133.
31. Marino, V., Scholten, A., Koch, K.W. and Dell'Orco, D. (2015) Two retinal dystrophy-associated missense mutations in GUCA1A with distinct molecular properties result in a similar aberrant regulation of the retinal guanylate cyclase. *Hum. Mol. Genet.*, **24**, 6653–6666.
32. Olshevskaya, E.V., Peshenko, I.V., Savchenko, A.B. and Dizhoor, A.M. (2012) Retinal guanylyl cyclase isozyme 1 is the preferential in vivo target for constitutively active GCAP1 mutants causing congenital degeneration of photoreceptors. *J. Neurosci.*, **32**, 7208–7217.
33. Arango-Gonzalez, B., Trifunovic, D., Sahaboglu, A., Kranz, K., Michalakis, S., Farinelli, P., Koch, S., Koch, F., Cottet, S., Janssen-Bienhold, U. et al. (2014) Identification of a common non-apoptotic cell death mechanism in hereditary retinal degeneration. *PLoS One*, **9**, e112142.
34. Comitato, A., Subramanian, P., Turchiano, G., Montanari, M., Becerra, S.P. and Marigo, V. (2018) Pigment epithelium-derived factor hinders photoreceptor cell death by reducing intracellular calcium in the degenerating retina. *Cell Death Dis.*, **9**, 560.
35. Kulkarni, M., Trifunovic, D., Schubert, T., Euler, T. and Paquet-Durand, F. (2016) Calcium dynamics change in degenerating cone photoreceptors. *Hum. Mol. Genet.*, **25**, 3729–3740.
36. Lim, S., Roseman, G., Peshenko, I., Manchala, G., Cudia, D., Dizhoor, A.M., Millhauser, G. and Ames, J.B. (2018) Retinal guanylyl cyclase activating protein 1 forms a functional dimer. *PLoS One*, **13**, e0193947.
37. Stephen, R., Bereta, G., Golczak, M., Palczewski, K. and Sousa, M.C. (2007) Stabilizing function for myristoyl group revealed by the crystal structure of a neuronal calcium sensor, guanylate cyclase-activating protein 1. *Structure*, **15**, 1392–1402.
38. Dell'Orco, D., Sulmann, S., Linse, S. and Koch, K.W. (2012) Dynamics of conformational Ca<sup>2+</sup>-switches in signaling networks detected by a planar plasmonic device. *Anal. Chem.*, **84**, 2982–2989.
39. Dell'Orco, D. and Koch, K.W. (2010) Systems biochemistry approaches to vertebrate phototransduction: towards a molecular understanding of disease. *Biochem. Soc. Trans.*, **38**, 1275–1280.
40. Mariani, S., Dell'Orco, D., Felling, A., Raimondi, F. and Fanelli, F. (2013) Network and atomistic simulations unveil the structural determinants of mutations linked to retinal diseases. *PLoS Comput. Biol.*, **9**, e1003207.
41. Peshenko, I.V. and Dizhoor, A.M. (2007) Activation and inhibition of photoreceptor guanylyl cyclase by guanylyl cyclase activating protein 1 (GCAP-1): the functional role of Mg<sup>2+</sup>/Ca<sup>2+</sup> exchange in EF-hand domains. *J. Biol. Chem.*, **282**, 21645–21652.
42. Marino, V. and Dell'Orco, D. (2016) Allosteric communication pathways routed by Ca(2+)/Mg(2+) exchange in GCAP1 selectively switch target regulation modes. *Sci. Rep.*, **6**, 34277.
43. Duda, T., Pertz, A. and Sharma, R.K. (2018) CO<sub>2</sub>/bicarbonate modulates cone photoreceptor ROS-GC1 and restores its CORD6-linked catalytic activity. *Mol. Cell. Biochem.* <https://doi.org/10.1007/s11010-018-3317-9>.
44. Duda, T., Pertz, A., Makino, C.L. and Sharma, R.K. (2016) Bicarbonate and Ca(2+) Sensing Modulators Activate Photoreceptor ROS-GC1 Synergistically. *Front. Mol. Neurosci.*, **9**, 5.
45. Sharma, R.K., Duda, T. and Makino, C.L. (2016) Integrative signaling networks of membrane guanylate cyclases: biochemistry and physiology. *Front. Mol. Neurosci.*, **9**, 83.
46. Dell'Orco, D., Sulmann, S., Zigel, P., Marino, V. and Koch, K.W. (2014) Impact of cone dystrophy-related mutations in GCAP1 on a kinetic model of phototransduction. *Cell. Mol. Life Sci.*, **71**, 3829–3840.
47. Asteriti, S., Dal Cortivo, G., Pontelli, V., Cangiano, L., Buffelli, M. and Dell'Orco, D. (2015) Effective delivery of recombinant proteins to rod photoreceptors via lipid nanovesicles. *Biochem. Biophys. Res. Commun.*, **461**, 665–670.
48. Marino, V., Borsatto, A., Vocke, F., Koch, K.W. and Dell'Orco, D. (2017) CaF<sub>2</sub> nanoparticles as surface carriers of GCAP1, a calcium sensor protein involved in retinal dystrophies. *Nanoscale*, **9**, 11773–11784.
49. McCulloch, D.L., Marmor, M.F., Brigell, M.G., Hamilton, R., Holder, G.E., Tzekov, R. and Bach, M. (2015) ISCEV Standard for full-field clinical electroretinography (2015 update). *Doc. Ophthalmol.*, **130**, 1–12.
50. Fiorentini, A., Maffei, L., Pirchio, M., Spinelli, D. and Porciatti, V. (1981) The ERG in response to alternating gratings in patients with diseases of the peripheral visual pathway. *Invest. Ophthalmol. Vis. Sci.*, **21**, 490–493.
51. Abed, E., Piccardi, M., Rizzo, D., Chiaretti, A., Ambrosio, L., Petroni, S., Parrilla, R., Dickmann, A., Riccardi, R. and Falsini, B. (2015) Functional loss of the inner retina in childhood optic gliomas detected by photopic negative response. *Invest. Ophthalmol. Vis. Sci.*, **56**, 2469–2474.
52. Esposito Veneruso, P., Ziccardi, L., Magli, G., Parisi, V., Falsini, B. and Magli, A. (2017) Early light deprivation effects on

- human cone-driven retinal function. *Acta Ophthalmol.*, **95**, 133–139.
53. Hwang, J.Y. and Koch, K.W. (2002) Calcium- and myristoyl-dependent properties of guanylate cyclase-activating protein-1 and protein-2. *Biochemistry*, **41**, 13021–13028.
  54. Zigel, P., Dell'Orco, D. and Koch, K.W. (2013) The dimerization domain in outer segment guanylate cyclase is a Ca<sup>2+</sup>(+)-sensitive control switch module. *Biochemistry*, **52**, 5065–5074.
  55. Koch, K.W. and Helten, A. (2008) In *Signal Transduction in the Retina*. Taylor and Francis CRC Press, pp. 121–143.
  56. Hwang, J.Y., Lange, C., Helten, A., Hoppner-Heitmann, D., Duda, T., Sharma, R.K. and Koch, K.W. (2003) Regulatory modes of rod outer segment membrane guanylate cyclase differ in catalytic efficiency and Ca<sup>2+</sup>-sensitivity. *Eur. J. Biochem.*, **270**, 3814–3821.
  57. Andre, I. and Linse, S. (2002) Measurement of Ca<sup>2+</sup>-binding constants of proteins and presentation of the CaLigator software. *Anal. Biochem.*, **305**, 195–205.
  58. Linse, S. (2002) Calcium binding to proteins studied via competition with chromophoric chelators. *Methods Mol. Biol.*, **173**, 15–24.
  59. Bradford, M.M. (1976) A rapid and sensitive method for the quantitation of microgram quantities of protein utilizing the principle of protein-dye binding. *Anal. Biochem.*, **72**, 248–254.
  60. Vallone, R., Dal Cortivo, G., D'Onofrio, M. and Dell'Orco, D. (2018) Preferential binding of Mg<sup>2+</sup> over Ca<sup>2+</sup> to CIB2 triggers an allosteric switch impaired in Usher Syndrome type 1J. *Front. Mol. Neurosci.*, **11**, 274.
  61. Abraham, M.J., Murtola, T., Schulz, R., Páll, S., Smith, J.C., Hess, B. and Lindahl, E. (2015) GROMACS: high performance molecular simulations through multi-level parallelism from laptops to supercomputers. *SoftwareX*, **1**, 19–25.
  62. Huang, J., Rauscher, S., Nawrocki, G., Ran, T., Feig, M., de Groot, B.L., Grubmuller, H. and MacKerell, A.D. Jr. (2017) CHARMM36m: an improved force field for folded and intrinsically disordered proteins. *Nat. Methods*, **14**, 71–73.



## SUPPLEMENTARY MATERIAL

### A novel p.(Glu111Val) missense mutation in *GUCA1A* associated with cone-rod dystrophy leads to impaired calcium sensing and perturbed second messenger homeostasis in photoreceptors

Valerio Marino, Giuditta Dal Cortivo, Elisa Oppici, Paolo Maltese, Fabiana D'Esposito, Elena Manara, Lucia Ziccardi, Benedetto Falsini, Adriano Magli, Matteo Bertelli, Daniele Dell'Orco\*

\* Corresponding Author: [daniele.dellorco@univr.it](mailto:daniele.dellorco@univr.it)

Figure S1

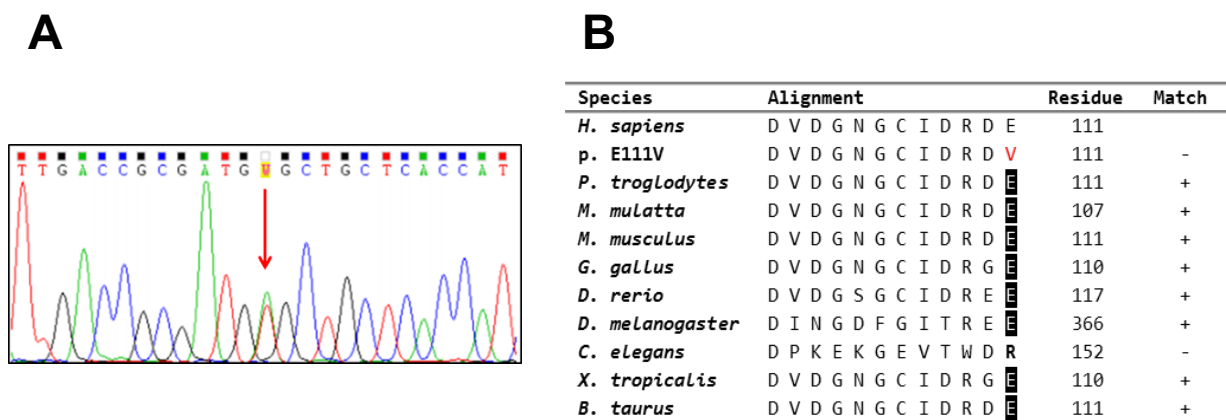
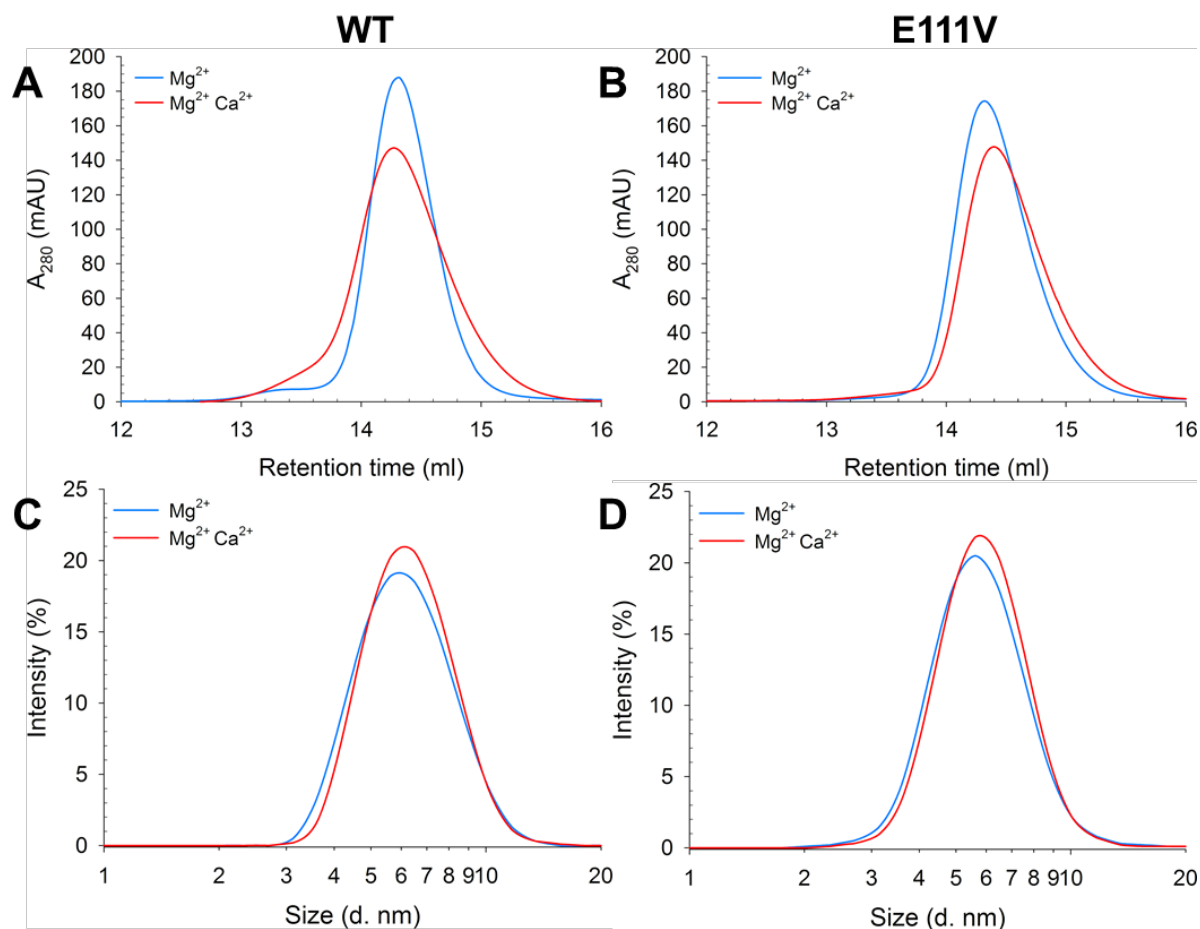


Figure S1

Example of sequence chromatogram (A) of the *GUCA1A*: NM\_000409: c.332A>T: p.(Glu111Val) variant identified in heterozygous state in the proband and in his affected daughters. Residue conservation of EF3 (B) Ca<sup>2+</sup>-binding loop across species of the novel *GUCA1A* variant showing that amino acid E111 of this protein is highly conserved due to its importance in Ca<sup>2+</sup>-coordination.

**Figure S2**



**Figure S2**

Results from Size Exclusion Chromatography and Dynamic Light Scattering experiments on WT (left panels) and E111V (right panels) GCAP1, performed in 20 mM Tris-HCl pH 7.5, 150 mM KCl, 1 mM DTT at 25 °C. Chromatograms of Size Exclusion Chromatography of ~40  $\mu$ M WT (A) and E111V (B) GCAP1 in the presence of 500  $\mu$ M EGTA and 1 mM  $Mg^{2+}$  (blue), or 1 mM  $Mg^{2+}$  and 500  $\mu$ M  $Ca^{2+}$  (red). Hydrodynamic diameter estimation of ~20  $\mu$ M WT (C) and E111V (D) GCAP1 in the presence of 500  $\mu$ M EGTA and 1 mM  $Mg^{2+}$  (blue), or 1 mM  $Mg^{2+}$  and 500  $\mu$ M  $Ca^{2+}$  (red). DLS measurements were collected approximately every minute, each measurement was an accumulation of 6 runs.

**Figure S3**

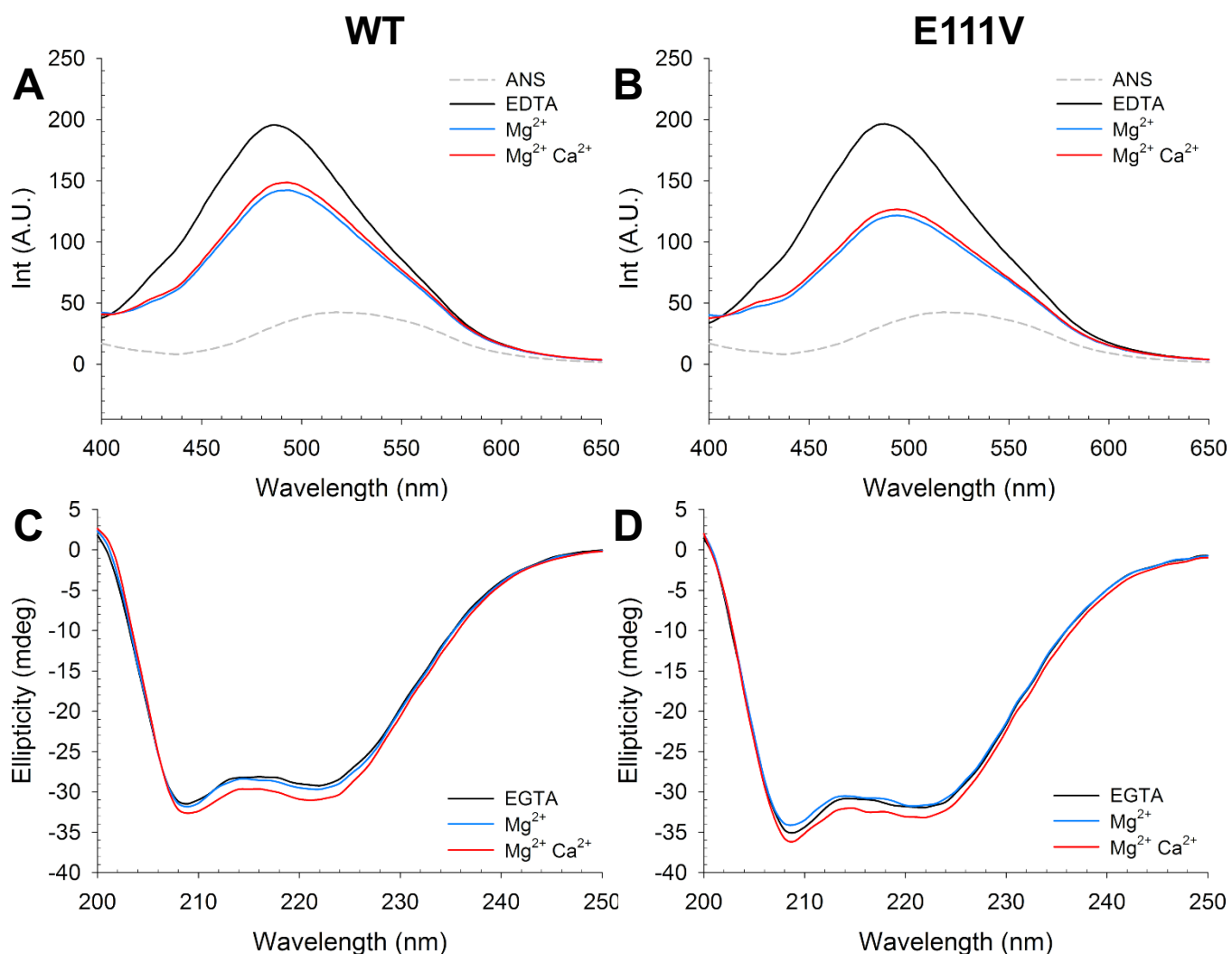


**Figure S3**

Results from ANS fluorescence and far UV CD spectroscopy experiments on WT (left panels) and E111V (right panels) GCAP1, performed in 20 mM Tris-HCl pH 7.5, 150 mM KCl, 1 mM DTT at 37 °C. Fluorescence emission spectra from 400 to 650 nm upon excitation at  $\lambda=380$  nm of  $\sim 2 \mu\text{M}$  WT (A) and E111V (B) GCAP1 in the presence of 30  $\mu\text{M}$  ANS and 500  $\mu\text{M}$  EDTA (black) and in the presence of 1 mM  $Mg^{2+}$  (blue) and after addition of 1 mM  $Ca^{2+}$  (red). The spectrum of ANS in the presence of 250  $\mu\text{M}$  EDTA is shown in dashed grey. Far UV CD spectra of  $\sim 10 \mu\text{M}$  WT (C) and E111V (D) GCAP1 in the presence of 300  $\mu\text{M}$  EGTA (black) and after additions of 1 mM  $Mg^{2+}$  (blue) and 300  $\mu\text{M}$  free  $Ca^{2+}$  (red).

**Figure S4**

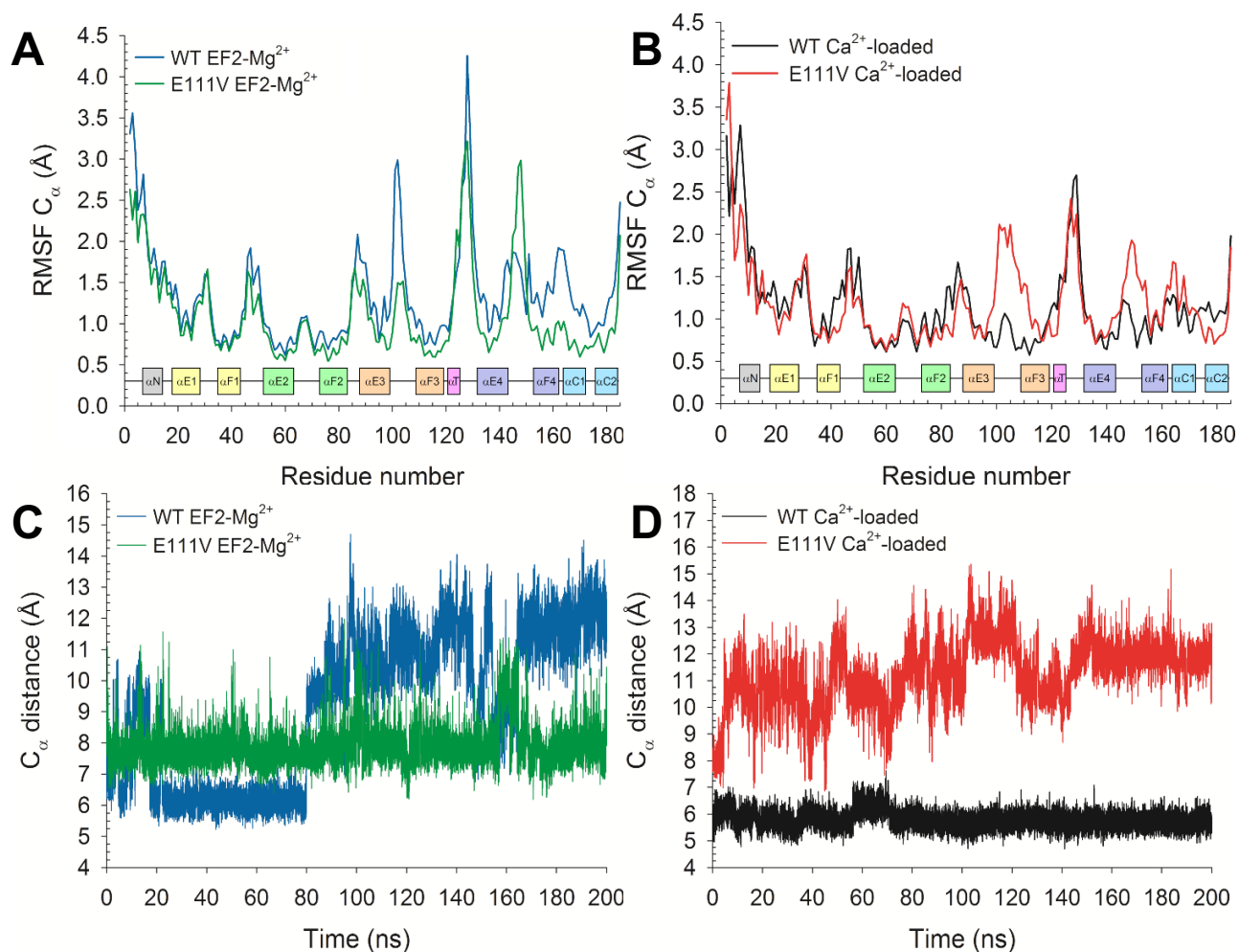


**Figure S4**

Analysis of MD simulations of WT and E111V GCAP1 in their Ca<sup>2+</sup> loaded and EF2-Mg<sup>2+</sup> forms. Root-mean square fluctuation calculated over 200 ns MD simulations on  $C_{\alpha}$  of WT and E111V GCAP1 in their (A) EF2-Mg<sup>2+</sup> and (B) Ca<sup>2+</sup> loaded forms. Insets show protein secondary structure, helices are colored according to Figure 4A. Time evolution over 200 ns of the distance between  $C_{\alpha}$  atoms of residues V101-E/V111 of WT and E111V GCAP1 in their (C) EF2-Mg<sup>2+</sup> and (D) Ca<sup>2+</sup> loaded forms. WT is shown in blue in panels A and C and in black in panels B and D, E111V is represented in green in panels A and C and in red in panels B and D.

**Supplementary Table T1.** Results from ANS measurements

	$I_{\max}$	$\lambda_{\max}$	$\Delta_{\text{int}}$	$\Delta_{\lambda}$
<i>ANS</i>				
<b>EDTA</b>	42.5	517		
<i>WT GCAPI</i>				
<b>EDTA</b>	195.7	486		31
<b>Mg<sup>2+</sup></b>	142.3	493	53.4	24
<b>Ca<sup>2+</sup></b>	148.7	493	47	24
<i>E111V GCAPI</i>				
<b>EDTA</b>	196.5	488		29
<b>Mg<sup>2+</sup></b>	121.6	494	74.9	23
<b>Ca<sup>2+</sup></b>	136.7	494	69.8	23

$I_{\max}$  is the maximal intensity at  $\lambda_{\max}$ ,  $\Delta_{\text{int}}$  is the intensity variation w.r.t the protein in the presence of EDTA,  $\Delta_{\lambda}$  is the variation of the maximal wavelength w.r.t. ANS alone.

**Supplementary Table T2.** Results from CD far UV spectroscopy and thermal denaturation profiles

	$\theta_{222}/\theta_{208}$	$\Delta\theta/\theta$	$T_m$ (°C)
<i>WT GCAPI</i>			
<b>EGTA</b>	0.94		
<b>Mg<sup>2+</sup></b>	0.94	0.02	49.0
<b>Mg<sup>2+</sup> Ca<sup>2+</sup></b>	0.96	0.06	>96
<i>E111V GCAPI</i>			
<b>EGTA</b>	0.92		
<b>Mg<sup>2+</sup></b>	0.93	-0.01	54.5
<b>Mg<sup>2+</sup> Ca<sup>2+</sup></b>	0.93	0.04	>96

$\theta_{222}/\theta_{208}$  is the intensity ratio at  $\lambda=222$  and  $\lambda=208$  nm,  $\Delta\theta/\theta$  is calculated as  $(\theta_{\text{ion}} - \theta_{\text{EGTA}}) / \theta_{\text{EGTA}}$  at  $\lambda=222$  nm,  $T_m$  is the transition temperature after fitting the signal at  $\lambda=222$  nm to a 4-parameter Hill sigmoid

OPEN

# Normal GCAPs partly compensate for altered cGMP signaling in retinal dystrophies associated with mutations in *GUCA1A*

Daniele Dell'Orco\* &amp; Giuditta Dal Cortivo

Missense mutations in the *GUCA1A* gene encoding guanylate cyclase-activating protein 1 (GCAP1) are associated with autosomal dominant cone/cone-rod (CORD) dystrophies. The nature of the inheritance pattern implies that a pool of normal GCAP proteins is present in photoreceptors together with the mutated variant. To assess whether human GCAP1 and GCAP2 may similarly regulate the activity of the retinal membrane guanylate cyclase GC-1 (GC-E) in the presence of the recently discovered E111V-GCAP1 CORD-variant, we combined biochemical and *in silico* assays. Surprisingly, human GCAP2 does not activate GC1 over the physiological range of  $\text{Ca}^{2+}$  whereas wild-type GCAP1 significantly attenuates the dysregulation of GC1 induced by E111V-GCAP1. Simulation of the phototransduction cascade in a well-characterized murine system, where GCAP2 is able to activate the GC1, suggests that both GCAPs can act in a synergic manner to mitigate the effects of the CORD-mutation. We propose the existence of a species-dependent compensatory mechanism. In murine photoreceptors, slight increases of wild-type GCAPs levels may significantly attenuate the increase in intracellular  $\text{Ca}^{2+}$  and cGMP induced by E111V-GCAP1 in heterozygous conditions. In humans, however, the excess of wild-type GCAP1 may only partly attenuate the mutant-induced dysregulation of cGMP signaling due to the lack of GC1-regulation by GCAP2.

The absorption of photons by visual pigments in retinal rod and cone cells triggers a complex signaling cascade known as phototransduction, which results in the electrical response of the cell and generates the visual stimulus<sup>1</sup>. A variety of protein-protein, protein-nucleotide and protein-ion interactions finely regulates the cascade<sup>2</sup>, whose dynamics depend on the interplay between  $\text{Ca}^{2+}$  and cyclic guanosine monophosphate (cGMP), the second messengers involved in the signaling process<sup>3,4</sup>. The core of the  $\text{Ca}^{2+}$ /cGMP signaling unit resides in the complex formed by the membrane retinal guanylate cyclase (GC1, also called ROS-GC1 or GC-E being the main cyclase in photoreceptor outer segments<sup>5</sup>) and guanylate cyclase-activating proteins (GCAPs). This supramolecular machinery ensures a precise control of the cGMP synthesis by GC1 as a consequence of the level of intracellular free  $\text{Ca}^{2+}$ , which drops from few hundred nanomolar in the dark to below 100 nM in the light<sup>1,6</sup>. Several GCAP isoforms exist in various species. In mouse<sup>7</sup> and in bovine<sup>8,9</sup> photoreceptors both GCAP1 and GCAP2 have been shown to regulate the target GC1, while in humans so far only GCAP1 has been directly shown to regulate the activity of GC1<sup>10,11</sup>.

GCAPs are neuronal calcium sensors that detect subtle changes in  $\text{Ca}^{2+}$  concentration and adopt specific conformations required for controlling the activity of the target GC1, *per se* unable to respond to  $\text{Ca}^{2+}$ . At high  $[\text{Ca}^{2+}]$ , GCAPs adopt a  $\text{Ca}^{2+}$ -loaded state that inhibits GC1 activity, but following the drop in intracellular  $[\text{Ca}^{2+}]$  during the light activation of the cascade, they switch to a  $\text{Mg}^{2+}$ -bound conformation<sup>12–15</sup> that stimulates GC1 to rapidly restore dark-adapted cell conditions by enhancing the synthesis of cGMP<sup>3,16</sup>.

To date, 20 missense mutations have been found in the *GUCA1A* gene encoding GCAP1, which have been associated with cone (COD) or cone-rod (CORD) dystrophies, severe forms of retinal dystrophy characterized by central vision loss, impaired color vision and photophobia<sup>17–19</sup>. No COD/CORD mutation in the gene encoding GCAP2 is known to date. When studied in reconstituted *in vitro* systems, most of the point mutations in *GUCA1A* resulted in GCAP1 variants that constitutively activate the GC1 over the physiological range of  $[\text{Ca}^{2+}]$ <sup>10,20–25</sup>. The

Department of Neurosciences, Biomedicine and Movement Sciences, Section of Biological Chemistry, University of Verona, I-37134, Verona, Italy. \*email: [daniele.dellorco@univr.it](mailto:daniele.dellorco@univr.it)

Y99C-GCAP1 mutation was the first one to have been discovered<sup>24</sup>, moreover it was the first one to be studied in a transgenic mouse line<sup>26</sup>. Other transgenic mouse lines were then generated to study similar COD/CORD-related phenotypes associated with mutations in GCAP1, namely the E155G-GCAP1<sup>27</sup> and L151F-GCAP1<sup>28</sup> models. The *in vivo* studies showed that the COD-related mutant caused photoreceptor degeneration due to an elevated  $[Ca^{2+}]$  in the rod outer segment. However, rod photoresponses from the Y99C-GCAP1 mice showed relatively little changes especially at bright flashes, indicating a partly preserved  $Ca^{2+}$ -regulated cGMP synthesis. Interestingly, the rate of photoreceptor cell loss increased with the level of Y99C-GCAP1 expression<sup>26</sup>.

For bovine and murine photoreceptors, it is well established that GCAP1 and GCAP2 are both capable of activating and inhibiting the target GC1 at similar levels in the physiological range of  $[Ca^{2+}]$ , however the two GCAPs differ from one another in some features: (i) GCAP1 has a slightly lower affinity for  $Ca^{2+}$  compared to GCAP2<sup>12</sup>; (ii) GCAP1 triggers the activation of GC1 earlier than GCAP2, that is at dimmer light conditions and/or when intracellular  $Ca^{2+}$  is still relatively high<sup>3</sup>; (iii) both GCAPs are myristoylated, but the myristoylation seems to exert a more prominent role for GCAP1 compared to GCAP2 in GC1 activation<sup>9</sup>. Moreover, in bovine cells the cellular concentration of GCAP1 and GCAP2 sums to the cellular concentration of GC1<sup>9</sup>. While it is clear that both GCAPs can regulate GC1 over the narrow physiological window of intracellular  $Ca^{2+}$ , quite different mechanisms have been proposed for the regulation. Some studies support distinct binding interfaces between GC1 and GCAP1/GCAP2, the first GCAP being located at the juxtamembrane region and the second prevalently bound to the catalytic-C terminal domain<sup>29–31</sup>, thus allowing the binding of GCAP1 and GCAP2 to either the same or distinct GC1 molecules, but always in different interfaces. On the other hand, other studies found a partly overlapped GC interface for GCAP1 and GCAP2<sup>32,33</sup>, suggesting a competition between GCAP1 and GCAP2 for GC1 activation in mouse cones<sup>34</sup> as well as in rods. Overall, GCAPs seem to operate in a “calcium-relay” mode, thus acting simultaneously on either the same or distinct GC1 molecules to induce gradual responses in terms of cGMP synthesis triggered by small changes in intracellular  $[Ca^{2+}]$ <sup>3,35</sup>. Their slightly different GC1-regulatory properties and  $Ca^{2+}$ -sensitivity would therefore be needed to achieve the complex temporal dynamics necessary for finely tuning the enzymatic activity of GC1 over the broad range of light stimuli typical of photoreceptors.

COD and CORD linked to mutations in *GUCA1A* are associated with autosomal dominant (ad) inheritance pattern, thus implying that one half of the GCAP1 molecules in the overall GCAP pool would carry the mutation in affected photoreceptors. Under the assumption that no other alteration beside the missense mutation occurs, a normal amount of GCAP2 molecules would be therefore still present, together with one half of normal GCAP1. In this work we present the results of biochemical assays of human GC1 catalytic activity performed with different amounts of human wild-type (WT)-GCAP1, GCAP2 and E111V-GCAP1, a recently discovered variant associated with a severe form of CORD<sup>10</sup>. Interestingly, we found that human GCAP2 is incapable of activating GC1 and therefore does neither co-act nor compete with GCAP1. On the other hand, increasing the amount of WT-GCAP1 with respect to E111V-GCAP1 led to a partial restoration of the  $Ca^{2+}$ -regulation of GC1 enzymatic activity, although a 3-fold excess of WT was not enough to restore a fully normal behavior. In order to predict the dysregulation of the  $Ca^{2+}$  and cGMP homeostasis in a rod cell under conditions mimicking different expression levels of mutated GCAP1, we transferred the quantitative results from the enzymatic assays to a comprehensive model of mouse phototransduction that showed capable of reproducing photoresponses under both dim and bright stimuli<sup>36,37</sup>. We observed a crucial role for GCAP2 in mouse in compensating the dysregulation induced by the disease-associated E111V-GCAP1 which cannot possibly occur in human cones due to the lack of activity on GC1.

## Results and Discussion

Regulation of the GC1 activity by  $Ca^{2+}$  via GCAPs represents an exemplary case, in which an enzyme (GC1) that *per se* is not sensitive to  $Ca^{2+}$  can be either inhibited or activated by the same molecule (GCAP) depending on the subtle changes in intracellular  $[Ca^{2+}]$ . The discovery of the highly cooperative negative feedback mechanism mediated by  $Ca^{2+}$  on the GC1 dates back to the late 80s<sup>38</sup>, and yet the fine mechanisms of its regulation are not completely understood. It has been established that the GCAP1/2-mediated  $Ca^{2+}$  feedback on GC1 activity is the only one that occurs at very dim light intensities, corresponding to the single photon response<sup>39</sup>. By integrating quantitative information arising from assays performed with recombinant systems and numerical simulations, we sought to clarify some mechanisms that are apparently perturbed in cases such as the severe CORD form recently associated with the E111V mutation in GCAP1<sup>10</sup>. To investigate the role of each GCAP variant, namely WT-GCAP1, E111V-GCAP1 and WT-GCAP2 in GC1 (dys)regulation, we performed biochemical assays both in the presence of individual GCAPs and in the co-presence of the variants, and measured quantitative parameters to describe the  $Ca^{2+}$ -dependence of the cGMP synthesis by GC1 and the apparent cooperativity of the process.

**Human GCAP2 does not activate human GC1.** Human GCAP1 (both WT and carrying the E111V mutation) and GCAP2 were heterologously expressed and purified at high purity levels. All GCAP variants responded to  $Ca^{2+}$  by switching to a different conformation that showed the typical increase in electrophoretic mobility (Fig. 1a), as observed in other calcium sensors<sup>40</sup>. The presence of smeared or multiple bands in SDS-PAGE gels is usual for calcium sensor proteins, and is related to the residual capability of the protein to bind  $Ca^{2+}$  in spite of the detergent-induced denaturation and the chelator present in the buffer<sup>12</sup>. Human GC1 was stably expressed in HEK cells and it concentrated in the membrane milieu (Fig. S1b), thus allowing the correct *in vitro* reconstitution of the GCAP-GC1 complex for biochemical assays.

While WT-GCAP1 was able to activate GC1 at low  $Ca^{2+}$ , as observed in previous studies<sup>10,11</sup>, GCAP2 was unable to exert any regulation of GC1 as in both low and high  $Ca^{2+}$  conditions the levels of cGMP synthesis were unaltered with respect to those of the control (Fig. 1b). When the enzymatic assays were performed with equal amounts of GCAP1 and GCAP2, at low  $Ca^{2+}$  a slight decrease in the GC1 activation was observed ( $n = 3$ ,  $p = 0.045$ ) with respect to the sole presence of GCAP1, thus indicating that the presence of GCAP2 only slightly

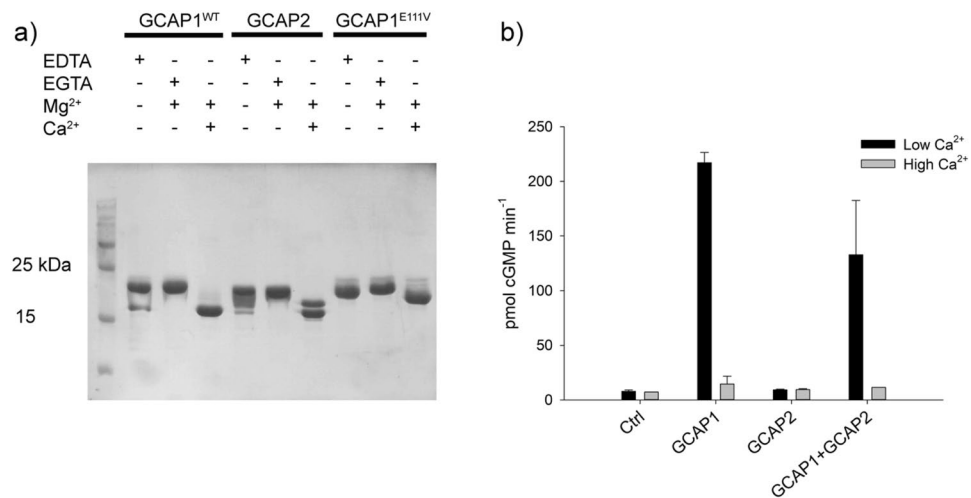


**Figure 1.** Purity of recombinant proteins, Ca<sup>2+</sup>-induced gel shifts and GC1 enzymatic assays. **(a)** SDS-PAGE of WT/E111V GCAP1 and GCAP2 in the presence of 5 mM EDTA, 4 mM EGTA + 1.4 mM Mg<sup>2+</sup> and 1 mM Mg<sup>2+</sup> + 4 mM Ca<sup>2+</sup>. Twenty micromolar WT-GCAP1, E111V-GCAP1 and WT-GCAP2 were incubated for 10 min at 30 °C in the presence or absence of ions and loaded in a 15% SDS-PAGE. Gel was Coomassie blue-stained. **(b)** GC1 enzymatic assays in the presence of 10 μM GCAP1, 10 μM GCAP2 and equal amounts of both (5 μM GCAP1 + 5 μM GCAP2) in the presence of less than 19 nM Ca<sup>2+</sup> (low Ca<sup>2+</sup>) or ~30 μM Ca<sup>2+</sup> (high Ca<sup>2+</sup>). Each bar represents the average of three replicas ± standard deviations (n = 3). Full-length gels are reported in Supplementary Fig. S1.

interferes with the activity of GCAP1, which was still capable of regulating GC1. No GCAP2-induced activation of GC1 was observed even when the experiments were performed at higher (12 mM) Mg<sup>2+</sup> (Fig. S2), thus indicating that the inability is intrinsic and not due to a low amount of Mg<sup>2+</sup>-bound GCAP2 in the assay.

The finding that human GCAP2 does not activate human GC1 might seem surprising, but in fact it is in line with previous work indicating that in human retinas, and similarly in monkey, GCAP2 localizes in cone inner segments, soma and synaptic terminal and only at very low levels in inner segments<sup>41</sup>. GCAP2 is crucial for maintaining the integrity of the photoreceptor synaptic terminal, likely mediating the effect of light on the morphological remodeling changes of synaptic ribbons<sup>42</sup> and even a single phosphorylation of GCAP2 has been shown to cause the complete retention of the protein in the inner segment<sup>43</sup>. Thus, while experiments with GCAPs<sup>-/-</sup> transgenic mice clearly established a role for GCAP2 in regulating the GCAP1-dominated GC1 activity<sup>39,44</sup>, and thorough *in vitro* investigations confirmed such capability<sup>7</sup>, in humans GCAP2 might have not-yet clear functions non-related with phototransduction.

**CORD-associated E111V-GCAP1 is dominant and leads to GC1-dysregulation.** Since GCAP2 did not contribute to the activation of human GC1, we monitored the Ca<sup>2+</sup>-dependent regulation of the cyclase in the co-presence of different amounts of WT-GCAP1 and E111V-GCAP1, with the goal to quantitatively assess the effects of the two variants on the same enzymatic target. Over the relatively narrow window of physiological variations of intracellular [Ca<sup>2+</sup>] (~10 nM–600 nM), WT-GCAP1 correctly switched from GC1-inhibitor to GC1-activator (Fig. 2, black curve). The IC<sub>50</sub> value, i.e. the [Ca<sup>2+</sup>] at which the synthesis of cGMP and therefore the activity of GC was half-maximal, was 251 ± 19 nM (n = 6) and the cooperativity of the process was high (h<sub>c</sub> = 2.60 ± 0.42; n = 6; Table 1).

Like many other COD/CORD-associated GCAP1 mutants, E111V-GCAP1 showed a dramatic shift of GC1 regulation to very high Ca<sup>2+</sup> levels, with IC<sub>50</sub><sup>E111V</sup> = 10 ± 5 μM (n = 4) and a significantly lower cooperativity (h<sub>c</sub> = 0.83 ± 0.27, n = 4; see red curve in Fig. 2)<sup>10</sup> compared to the WT, thus constitutively activating the GC1 target over a physiological range of [Ca<sup>2+</sup>]. Those biochemical assays, however, were performed in the sole presence of E111V-GCAP1. When the assay was performed by mixing equal amounts of WT and E111V-GCAP1, thus resembling the heterozygous WT/E111V case found in CORD patients, the situation led to a different scenario (Fig. 2, green curve). While no significant change in the cooperativity could be observed (Table 1), the IC<sub>50</sub> value shifted down to 694 ± 75 nM (n = 6) (Fig. 2, Table 1). Although this value is still insufficient to inhibit the GC1 at physiologically high [Ca<sup>2+</sup>], leading to ~55% of the maximal activity, it is definitely lower compared to the ~90% activity of E111V-GCAP1 alone.

WT-GCAP1 is thus capable of partly restoring the functional switch of GC1 in the presence of a mutant that would otherwise block the enzyme in a constitutively active state. A similar result was previously obtained by Dizhoor and co-workers<sup>21</sup>, who investigated in a bovine system the Y99C-GCAP1 variant associated with COD, and noticed that enzymatic assays in the co-presence of WT and mutated GCAP1 still led to constitutive GC1 activity. The authors also investigated the co-presence of Y99C-GCAP1 and WT-GCAP2, obtaining very similar results, and thus concluded that the mutant stimulates the cyclase in the presence of equimolar concentrations of



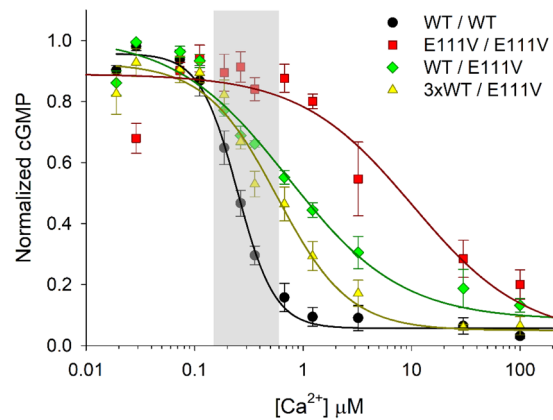


**Figure 2.**  $\text{Ca}^{2+}$ -dependence of GC1 activity in the presence of various GCAP1 variants. The GC1 activity as function of  $[\text{Ca}^{2+}]$  was measured in the presence of  $10\ \mu\text{M}$  WT-GCAP1 (black circles),  $5\ \mu\text{M}$  WT-GCAP1 +  $5\ \mu\text{M}$  E111V-GCAP1 (green diamonds) and  $15\ \mu\text{M}$  WT-GCAP1 +  $5\ \mu\text{M}$  E111V-GCAP1 (yellow triangles). E111V-GCAP1's activity profile is referred to the published data<sup>10</sup>. Each data set is relative to 4–6 replicas and data are normalized according to both total protein content in membranes and maximum and minimum GC1 activity recorded in each replica; error bars represent s.e.m. Solid lines represent the results of data fitting while the grey box represents the physiological  $\text{Ca}^{2+}$  fluctuations in rod photoreceptors.

	GCAP1 <sup>WT</sup> (n = 6)	GCAP1 <sup>E111V</sup> (n = 4)	GCAP1 <sup>WT/E111V</sup> (n = 6)	3XGCAP1 <sup>WT</sup> /GCAP1 <sup>E111V</sup> (n = 6)
IC <sub>50</sub> (nM)	251 ± 19 <sup>a</sup>	(10 ± 5) × 10 <sup>3</sup>	694 ± 75	497 ± 49
h <sub>c</sub>	2.60 ± 0.42	0.83 ± 0.27	0.87 ± 0.18	1.49 ± 0.35

**Table 1.** Results from enzymatic assays. Human GC1 activity as a function of free  $[\text{Ca}^{2+}]$ . <sup>(a)</sup> reported data are mean ± s.e.m. <sup>(b)</sup> data from ref. <sup>10</sup>.

either WT-GCAP1 or GCAP2<sup>21</sup>. However, those assays were performed in a bovine system, where GCAP2 plays a role in GC1 activation, at odds with our current findings referring to a human system.

Since human GCAP2 does not activate GC1, we sought to investigate whether the observed partial restoring capability of WT-GCAP1 to restore GC1 activity in the presence of E111V-GCAP1 could even increase in the presence of extra WT-GCAP1. The assays were performed with 3-fold excess of WT-GCAP1, while keeping the concentration of E111V unaltered with respect to the previous conditions. Interestingly, a statistically significant decrease of IC<sub>50</sub> was observed ( $497 \pm 49$  compared to  $694 \pm 75$ ; n = 6; one-tailed p = 0.029; Table 1). Although the residual activity of GC1 at physiologically high  $[\text{Ca}^{2+}]$  was still quite high (~45%; Fig. 1, yellow curve) the regulation profile became more cooperative, as shown by the increase in h<sub>c</sub> ( $1.49 \pm 0.35$  vs.  $0.87 \pm 0.18$ , n = 6). Therefore, although the switch was still non-optimal, the presence of 3-fold excess WT-GCAPs seems to slightly attenuate the dominant and detrimental effect caused by the E111V-GCAP1 mutation.

The observed results of GC1 activity in the presence of different amounts of GCAP1 and its E111V variant are not straightforward to interpret. Human WT-GCAP1 and E111V-GCAP1 have very similar apparent affinity (EC<sub>50</sub>) for GC1<sup>10</sup>, therefore it seems unlikely that the cause of the still dominant effect of the mutant in a situation of 3-fold excess of WT be attributed to the preferential formation of a complex with the GC1. A more realistic explanation could be the existence of different equilibria between the oligomeric states of WT-GCAP1 and E111V-GCAP1, which could result in different amounts of monomeric GCAP available for GC regulation. GCAP1 is known to form dimers<sup>10,45</sup> and under conditions mimicking the physiological ones E111V-GCAP1 was also found to be dimeric<sup>10</sup>. We cannot exclude that in the conditions of our *in vitro* assays the tendency of WT-GCAP1 to form dimers enhanced at the higher concentrations corresponding to the 3-fold excess experiments, *de facto* limiting the availability of monomers that could further improve the restoration of the GC1 regulation towards a physiological behavior.

### Expression levels of normal GCAPs set the homeostasis of $\text{Ca}^{2+}$ and cGMP in a computational model of E111V-GCAP1 mouse rod.

In order to evaluate the putative cellular consequences of the  $\text{Ca}^{2+}$ /cGMP dysregulation brought about by the E111V-GCAP1 mutation associated with CORN and the extent of a potential compensation by normal GCAPs, we used the parameters experimentally measured in the human system to predict the rate of cGMP synthesis in a mouse rod illuminated by flashes of increasing intensity. We used a comprehensive kinetic model of phototransduction that demonstrated very effective in reproducing experimental results from dim to bright light conditions<sup>37</sup>. In particular, we could directly probe the role of each GCAP, namely WT/E111V GCAP1 and GCAP2, in regulating the levels of second messengers by virtually tuning the contribution of each protein to GC1 regulation and simulating the dark-adapted state of the cell as well as the response to specific light stimuli, thus investigating the dynamic shaping of cGMP synthesis.

	GCAP1 <sup>WT/E111Va</sup>	GCAP1 <sup>E111V/E111V</sup>	3XGCAP1 <sup>WT</sup> /GCAP1 <sup>E111V</sup> + GCAP2	3XGCAP1 <sup>WT</sup> /GCAP1 <sup>E111V</sup> -GCAP2
X-fold [Ca <sup>2+</sup> <sub>free</sub> ]	3.1	12.5	1.4	3.0
X-fold [cGMP]	1.4	2.0	1.1	1.4

**Table 2.** Increase in dark levels of Ca<sup>2+</sup> and cGMP according to numerical simulations of a mouse rod outer segment compared to a wild-type case. <sup>a</sup>combination of individual weight factor  $f_i$  to simulate each condition are illustrated in the Methods.

The significant perturbation of the GC1 regulation induced by the E111V mutation in GCAP1 assessed *in vitro* was reflected by a substantial increase of the dark levels of Ca<sup>2+</sup> and cGMP (Table 2).

The simulation of the rod in the dark for a heterozygous WT/E111V mouse resembles the case of adCORD pattern in humans, in which half of the GCAP1 pool is made of WT molecules and the other half carries the E111V mutation. Under these conditions, a 3.1-fold increase in the level of intracellular Ca<sup>2+</sup> and 1.4-fold increase in that of cGMP was predicted by numerical simulations (Table 2). These results are substantially in line with the experimental measurements of intracellular [Ca<sup>2+</sup>] in Y99C-GCAP1 mice, where an increase of 1 to 2-fold depending on the expression levels of the mutant over a background of WT-GCAP1 was observed<sup>26</sup>. To probe the effects of different expression levels of mutant vs. WT-GCAP1, we performed numerical simulations of other putative cases, first one in which the whole pool of GCAP1 carried the E111V mutation in the co-presence of endogenous WT-GCAP2. The simulated increase of dark levels of Ca<sup>2+</sup> and cGMP was dramatic in this hypothetical E111V/E111V homozygosis case (12.5-fold and 2.0-fold, respectively; Table 2). In line with our *in vitro* experiments with human proteins, we also simulated the effects of a 3-fold excess of WT-GCAP1 over a background of constant E111V-GCAP1, both in the presence and in the absence of endogenous GCAP2. Interestingly, extra-delivery of WT-GCAP1 in the presence of GCAP2 restored an almost WT-like homeostasis of dark Ca<sup>2+</sup> and cGMP (1.4-fold and 1.1. fold, respectively; Table 2). However, the same delivery of WT-GCAP1 performed in the absence of endogenous GCAP2 did not restore a WT-like homeostasis for second messengers, and led to a dramatic increase of 3.0-fold dark Ca<sup>2+</sup> and 1.4-fold cGMP, similar to what was observed in the simulated heterozygous WT/E111V case (Table 2). Hence, simulations suggest that GC1 activation by GCAP2 is fundamental in mouse photoreceptor to set the normal levels of second messengers. In its absence, the normally dominant WT-GCAP1 although delivered in excess cannot compensate for the detrimental dysregulation of GC1 by the pathogenic E111V mutation.

**GCAP2 shapes cGMP synthesis in E111V-GCAP1 mouse photoresponses.** Perturbation of the second messenger homeostasis in the dark might lead to alterations in the photoresponse of the affected cells. To probe such potential variations, we simulated photoresponses from mouse rods expressing the same amounts of GCAPs investigated in the dark following the excitation of the phototransduction cascade by flashes of increasing intensity, from dim to saturating. The resulting dynamics of suppression of the dark current in a rod of a WT mouse and the respective cases for a heterozygous WT/E111V and a homozygous E111V/E111V-GCAP1 case are reported in Fig. 3a,b, respectively.

For all the tested flash intensities the photoresponses of the mutant cases were prolonged compared to the WT, with increased time to peak. The prolongation of the photoresponse apparently depends on the relative abundance of E111V-GCAP1 with respect to the WT and was in fact significantly more pronounced in the homozygous (Fig. 3b) compared to the heterozygous case (Fig. 3a). Similar results were experimentally measured in Y99C-GCAP1 mice<sup>26</sup>, although the effect was less prominent, probably due to the milder phenotype that developed COD and not COD as in the case of E111V-GCAP1.

Our computational implementation of the GC1 regulation by different GCAP variants allowed us to ideally dissect their individual contributions in shaping the rate of cGMP synthesis at different light stimuli. Figure 3c,d reports on the overall GCAPs contribution (black line) to the time course of cGMP synthesis as a sum of the contribution by GCAP1 variants (blue line) and WT-GCAP2 (red line). Clear differences could be observed between WT and WT/E111V heterozygous case. For WT rods, increasing the flash intensity led to an increasing contribution of GCAP2 in shaping the cGMP synthesis rate, which was less important for very dim flashes, but became predominant at bright intensities (Fig. 3c), in line with the Ca<sup>2+</sup>-relay mechanism<sup>3,35</sup>. In the case of WT/E111V heterozygous mouse, however, the unbalance in the contributions became apparent under dim light conditions, where GCAP1 variants dominated, while GCAP2 was still capable of shaping the rate at brighter flashes (Fig. 3d). It should be noticed that, in spite of the dramatic perturbation in the dark levels of Ca<sup>2+</sup> and cGMP (Table 2), our model predicts that the photoreceptor would still respond to light stimuli, with all in all minor perturbation of the photoresponse shape (Fig. 3a), thus fully in line with experimental observations<sup>26</sup>.

The major dysregulation of second messenger homeostasis observed in the hypothetical E111V/E111V homozygous case, where the whole GCAP1 pool carried the E111V mutation reflected in a dramatic perturbation of the photocurrent shapes, which became significantly prolonged and did not completely shut-off even after 5 s for brighter stimuli (Fig. 3b). Under dim flashes, GCAP2 did not contribute at all to the shaping of the cGMP synthesis rate, but at middle to bright light conditions, where GCAP1 was almost completely blocked in the GC1-constitutively activating state, GCAP2 provided most of the dynamic contribution (Fig. 3e).

Simulation of 3-fold WT-GCAP1 delivery over a background of E111V-GCAP1 variant suggested a scenario that strictly depends on the presence of the other endogenous GCAP2. Indeed, when endogenous GCAP2 was considered in the simulations, the mutant-induced prolongation of the photocurrent was reduced at all light intensities (Fig. 4a) and the dynamics of cGMP synthesis as well as the specific contributions of GCAPs (Fig. 4c)

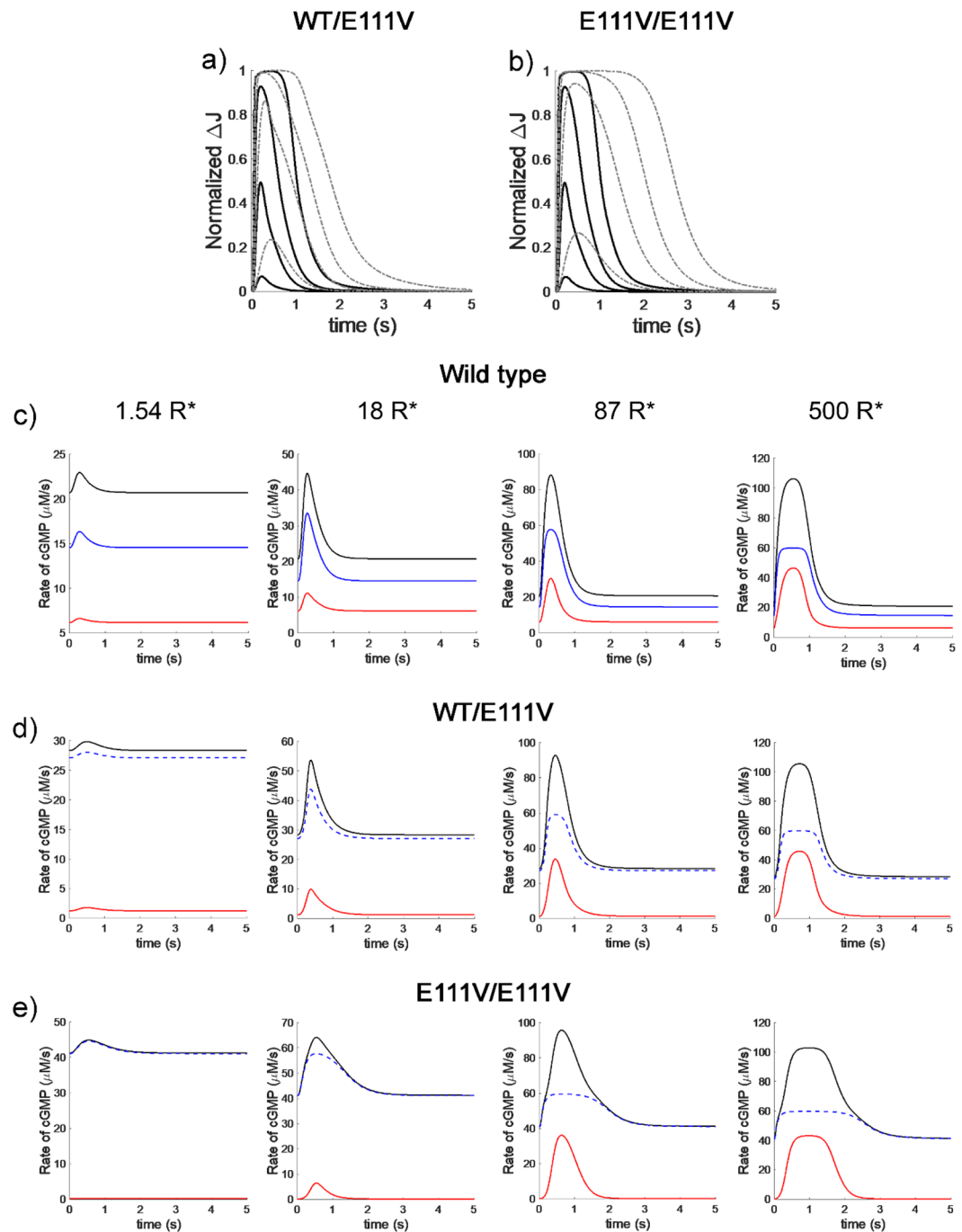


**Figure 3.** Simulation of flash responses and dynamics of cGMP synthesis in a mouse rod, from dim to bright light conditions. After equilibration of the rod outer segment in the dark, 24 ms flashes were delivered, leading to 1.54, 18, 87 and 500 photoisomerizations of rhodopsin; **(a,b)** Black traces: WT GCAPs-containing rods. Dash-dotted gray lines: photoresponses in a WT/E111V heterozygous case **(a)** and E111V/E111V homozygous case **(b)**. Photocurrents represent the suppression of the dark current at each light intensity and have been normalized. **(c–e)** Simulated time course of the rate of cGMP synthesis by GC1 in the same conditions as in **(a,b)**. Blue lines: contribution by WT-GCAP1 + E111V-GCAP1 (if present). Red lines: contribution by GCAP2. Black lines: overall GCAPs contribution obtained by adding up the former terms.

were overall fairly similar to the WT case (Fig. 3c). This suggests that under these conditions it would be in principle possible to partly restore a normal shaping of both the photocurrent and cGMP synthesis profile, thus minimizing the perturbation of the second messengers (Table 2). However, when the same delivery of 3-fold WT-GCAP1 was simulated in the absence of endogenous GCAP2, the prolongation of the photocurrents became significant under all light regimes (Fig. 4b), resembling that of heterozygous WT/E111V (Fig. 3a). Nevertheless, in this case the absence of GCAP2 led to a completely GCAP1 (WT and E111V)-driven cGMP synthesis, with

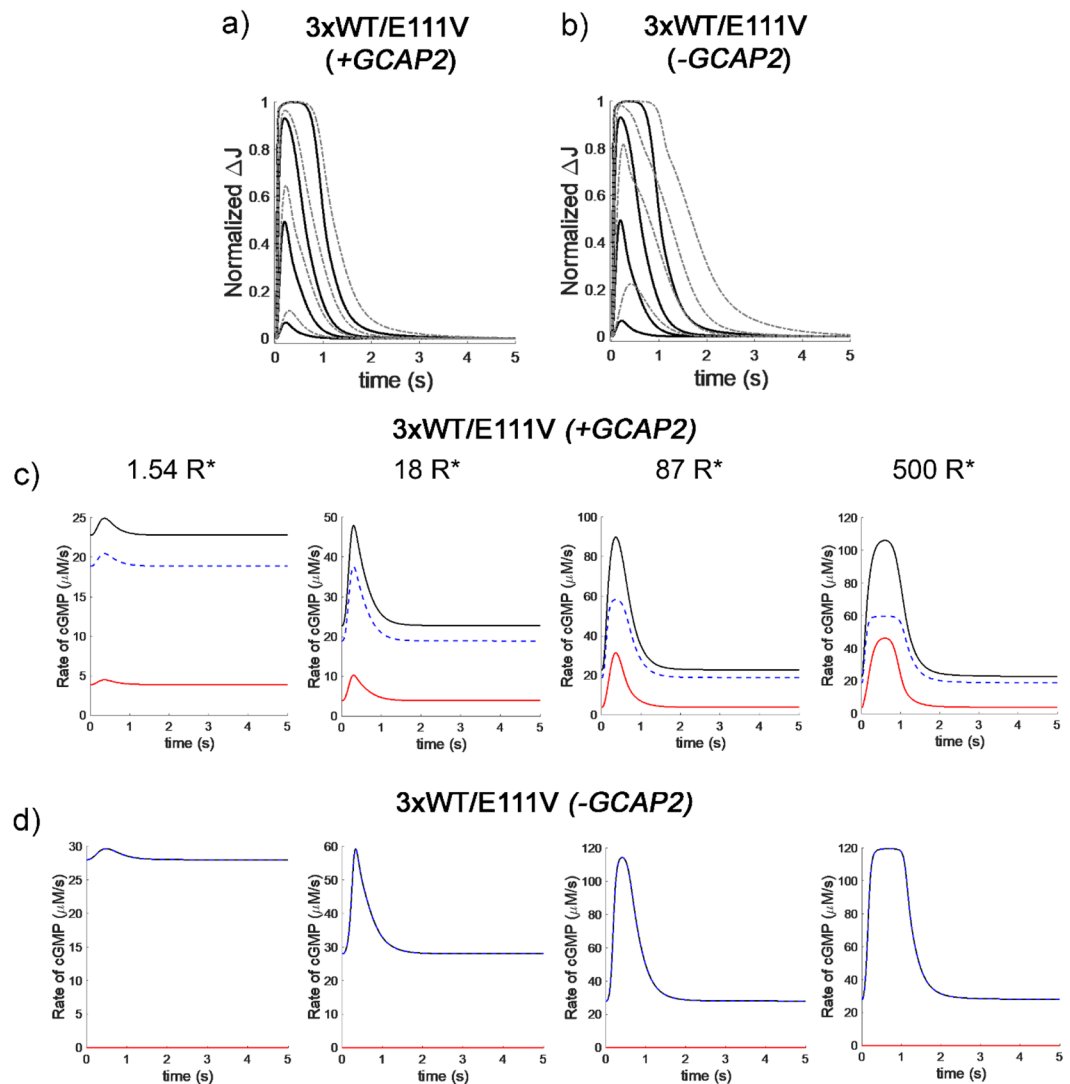


**Figure 4.** Simulation of flash responses and dynamics of cGMP synthesis in a mouse rod, from dim to bright light conditions, in the presence of 3-fold WT-GCAP1 with respect to E111V-GCAP1. Panels (a,c) refer to simulations in which endogenous GCAP2 was present. Panels (b,d) refer to simulations in the absence of endogenous GCAP2. All simulated conditions and symbols are the same of Fig. 3.

higher maximal levels of synthesis at each light intensity (Fig. 4d) compared to the heterozygous case (Fig. 3d). Hence, in spite of the dominant role of this GCAP1 isoform in the WT photoreceptor, the excess of GCAP1 alone is not sufficient to compensate for the absence of GCAP2 in mouse rods.

The crucial role of GCAP2 in compensating for the extreme perturbations of cGMP signaling induced by blocking GCAP1 into a GC1-constitutively active state was proposed by us for a bovine system based on comprehensive model of the phototransduction kinetics<sup>46</sup> and was then experimentally confirmed in a mouse cone system<sup>34</sup>.

## Conclusions

In conclusion, our findings support the view that the severity of COD/CORD phenotypes associated with point mutations in *GUCA1A* correlates both with the dysregulation of the cGMP signaling induced by the point mutation and with the levels of mutated GCAP1 over WT-GCAPs. Increasing the levels of WT-GCAP1 on a background of disease-associated mutants may partly attenuate the increased dark levels of  $\text{Ca}^{2+}$  and cGMP, which are ultimately associated to cell death<sup>47,48</sup> and reduce the perturbation of the photocurrent dynamics. Since promising strategies for the delivery of WT recombinant proteins to photoreceptors are under development<sup>49,50</sup>, our findings might be relevant for future protein therapies aimed at slowing retinal degenerations associated with *GUCA1A* mutants. However, our data also show that, while useful for the purpose, extra-WT-GCAP1 alone would probably not be sufficient to restore a normal regulation of GC1 in human retinas. The intricate  $\text{Ca}^{2+}$ -relay mechanism involving GC1 and the GCAPs might be substantially species-dependent, and whether other regulators in human photoreceptors may mimic the synergic activation of GCAP1 and GCAP2 on GC1 observed in mouse and bovine retinas remains to be clarified.

## Materials and Methods

**GCAPs expression and purification.** Synthetic genes (Genscript) corresponding to the cDNA of human GCAP1 (Uniprot: P43080) and GCAP2 (Uniprot: Q9UMX6) were cloned into pET-11a(+) vectors using NdeI and NheI as restriction site. Mutagenesis, protein expression and purification of myristoylated proteins were performed as described previously<sup>10,12</sup>. Briefly, cells were let grown at 37 °C until an OD<sub>600</sub> value of 0.4 was reached, then myristic acid (100 µg/mL, in 50% EtOH, pH 7.5) was added. After the induction with 1 mM IPTG, cells were let grown for 4 hours at 37 °C. Both WT and E111V-GCAP1 as well as GCAP2 were purified from inclusion bodies. After protein denaturation by 6 M guanidinium hydrochloride and refolding steps by dialysis, two subsequent chromatographic steps (size exclusion and anionic exchange chromatography) were performed. Proteins purity was tested by Polyacrylamide Gel Electrophoresis in the presence of Sodium-Dodecyl-Sulfate (SDS-PAGE) and was found to be at least 95% (see Fig. 1a). The efficiency of protein myristoylation was proven by HPLC and mass spectrometry. After buffer exchange (20 mM TRIS, 150 mM NaCl, 1 mM DTT), proteins were shock frozen and stored at -80 °C until use.

**GC expression and enzymatic assays.** A stable cell line expressing human guanylate cyclase isoform 1 (GC1) was obtained as explained previously<sup>10,51</sup> by transfecting HEK293 flp cells with pIRES-eGFP plasmid using Turbofect reagent. Transfected clones were selected based on the resistance to geneticin (G418). Cells were cultured in DMEM media containing fetal bovine serum (10% v/v), streptomycin (100 µg/mL), penicillin (100 units/mL) and geneticin (500 µg/mL). At 90% confluence the cells were harvested, washed with sterile PBS and stored at -80 °C. To perform enzymatic assays on isolated membranes cells pellets were suspended in lysis buffer (10 mM HEPES pH 7.4, 1 mM DTT, protease inhibitor cocktail 1X) and incubated for 20 min on ice. After 15 up-and-down cycles with a 1 mL syringe on ice, cells were centrifuged for 20 min at 10000 rpm. The obtained pellets were suspended in 50 mM HEPES pH 7.4, 50 mM KCl, 20 mM NaCl, 1 mM DTT.

First, GC1 activity was assessed incubating 10 µM GCAP1 or GCAP2 or a combination of both (5 µM GCAP1 + 5 µM GCAP2) in the absence (<19 nM) and in the presence (~30 µM) of Ca<sup>2+</sup>, obtained using 10 mM K<sub>2</sub>H<sub>2</sub>EGTA and K<sub>2</sub>CaEGTA buffers<sup>51</sup> respectively (Fig. 1b). Basal GC1 activity was assessed as internal control by replacing GCAPs with equal amount of the buffer used for protein storing. Then, the enzymatic activity as a function of [Ca<sup>2+</sup>] was measured as in previous work<sup>10</sup>, with minor changes explained in the following. Several combinations of GCAPs were tested, namely: (i) 10 µM WT-GCAP1; (ii) 5 µM WT-GCAP1 + 5 µM E111V-GCAP1; (iii) 15 µM WT-GCAP1 + 5 µM E111V-GCAP1. Data for E111V-GCAP1 alone are referred to our previous publication<sup>10</sup>. Ca<sup>2+</sup> concentration in each assay was carefully determined by combining the same K<sub>2</sub>H<sub>2</sub>EGTA and K<sub>2</sub>CaEGTA buffers previously mentioned. The assay consisted in incubating for 5 min at RT the diluted proteins with a fixed amount of extracted membranes, then reaction buffer (30 mM MOPS pH 7.2, 20 mM KCl, 10 mM, 4 mM NaCl, 1 mM DTT, 3.5 mM MgCl<sub>2</sub>, 1 mM GTP, 300 µM ATP, 160 µM Zaprinast) was added and the samples were incubated for 5 min at 30 °C. The reaction was blocked by the addition of 50 mM EDTA and incubating at 98 °C for 5 min. After centrifugation at 13000 rpm the supernatant was loaded in a C18 reverse phase column (Chromolith column, Millipore) previously equilibrated with 5 mM KH<sub>2</sub>PO<sub>4</sub>. Following a previously established protocol<sup>10</sup> on an HPLC apparatus (Jasco) the cGMP concentration was determined by acetonitrile gradient. Four to 6 repetitions of each assay were performed. Data have been normalized to the total protein content present in membranes used for the assay (amido black, Sigma) and on the minimum and maximum GC-activity. IC<sub>50</sub> and Hill coefficient (h<sub>c</sub>) values were determined for each assay by curve fitting to a 4-parameter Hill function (Sigma Plot 12.5) and mean, standard deviation and standard error of the mean (s.e.m.) were determined. All data distributions passed the Shapiro-Wilk normality test and the observed parameters IC<sub>50</sub> and h<sub>c</sub> were compared with one another by one-tailed t-test (SigmaPlot 12.5), rejecting in all cases the null hypothesis (p < 0.05).

**Numerical simulations of mouse photoresponses.** A previously developed comprehensive biochemical model of phototransduction in mouse rods was used for numerical simulations<sup>37</sup>. All parameters describing the phototransduction cascade were left unaltered, the only difference being the way the reaction describing the dynamic synthesis of cGMP by GC1 was implemented. In the present implementation, to account for specific contributions of GCAP variants to the cGMP synthesis in a mouse photoreceptor, each variant (GCAP<sub>i</sub>) was described to contribute by a specific fraction  $f_i$  to the maximal activation ( $\alpha_{max}$ ) of GC1:

$$\frac{d[cGMP]}{dt} = \sum_i \frac{f_i \times \alpha_{max}}{1 + \left(\frac{Ca_{free}^2}{IC_{50i}}\right)^{h_{c_i}}} \quad \text{where } \sum_i f_i = 1$$

The value for  $\alpha_{max}$ , assumed to be the same for each variant, was fixed to 120 µM/s, as in the previous model, while IC<sub>50</sub> and h<sub>c</sub> for WT-GCAP1 and GCAP2 were fixed to their experimentally measured values in mouse rod outer segments<sup>7</sup>. IC<sub>50</sub> and h<sub>c</sub> for E111V-GCAP1 were set to their relative values (-fold variation) compared to the wild type, according to the parameters experimentally measured for the human orthologs (Table 1). The use of different weight factors  $f_i$  is a convenient way to account for the specific contribution of each GCAP variant to the overall regulation of GC1, with the assumption of a similar apparent affinity between GCAP variants and GC1, so that the variants may compete for the target based solely on their concentration/expression levels. This condition has been demonstrated to be realistic for E111V and WT human GCAP1, for which substantially unaltered EC<sub>50</sub> values for human GC1 were measured<sup>10</sup>, as well as for murine GCAP1 and GCAP2, which showed almost identical EC<sub>50</sub> values for murine GC1 in rod outer segment membranes<sup>7</sup>.

With the above assumptions, by tuning the  $f_i$  terms one can simulate a broad variety of experimental conditions; for example, the situation of a heterozygous mouse E111V/WT, corresponding to the human adCORD case,

in which half of the GCAP1 molecules are WT and half carry the E111V mutations, in the presence of normal amounts of WT GCAP2 was modeled as follows:

$$\frac{d[cGMP]}{dt} = \frac{d[cGMP]^{GCAP1^{WT}}}{dt} + \frac{d[cGMP]^{GCAP1^{E111V}}}{dt} + \frac{d[cGMP]^{GCAP2^{WT}}}{dt}$$

$$= \alpha_{max} \times \left[ \frac{0.25}{1 + \left( \frac{Ca_{free}^{2+}}{IC_{50}^{GCAP1^{WT}}} \right)^{h_{GCAP1^{WT}}}} + \frac{0.25}{1 + \left( \frac{Ca_{free}^{2+}}{IC_{50}^{GCAP1^{E111V}}} \right)^{h_{GCAP1^{E111V}}}} \right]$$

$$+ \frac{0.5}{1 + \left( \frac{Ca_{free}^{2+}}{IC_{50}^{GCAP2^{WT}}} \right)^{h_{GCAP2^{WT}}}}$$

The case of homozygous mouse E111V/E111V in the presence of endogenous GCAP2 was simulated by setting  $f_{GCAP1^{WT}} = 0$ ;  $f_{GCAP1^{E111V}} = 0.5$ ;  $f_{GCAP2} = 0.5$ . Finally, the case of 3-fold excess of WT-GCAP1 over a background of E111V-GCAP1 and endogenous GCAP2 was obtained by setting:  $f_{GCAP1^{WT}} = 0.375$ ;  $f_{GCAP1^{E111V}} = 0.125$ ;  $f_{GCAP2} = 0.5$ , while the same excess in the absence of endogenous GCAP2 was simulated by:  $f_{GCAP1^{WT}} = 0.75$ ;  $f_{GCAP1^{E111V}} = 0.25$ ;  $f_{GCAP2} = 0$ . All numerical simulations were performed in Matlab as explained in earlier works<sup>36,37</sup>.

Received: 17 September 2019; Accepted: 12 December 2019;

Published online: 27 December 2019

## References

- Pugh, E. J. & Lamb, T. In Handbook of Biological Physics Vol. 3 (eds DG Stavenga, WJ DeGrip, & EN Jr Pugh) 183–255 (Elsevier Science BV, 2000).
- Koch, K. W. & Dell'Orco, D. Protein and Signaling Networks in Vertebrate Photoreceptor Cells. *Front Mol Neurosci* **8**, 67, <https://doi.org/10.3389/fnmol.2015.00067> (2015).
- Koch, K. W. & Dell'Orco, D. A calcium-relay mechanism in vertebrate phototransduction. *ACS Chem Neurosci* **4**, 909–917, <https://doi.org/10.1021/cn400027z> (2013).
- Koch, K. W., Duda, T. & Sharma, R. K. Ca(2+)-modulated vision-linked ROS-GC guanylate cyclase transduction machinery. *Mol Cell Biochem* **334**, 105–115, <https://doi.org/10.1007/s11010-009-0330-z> (2010).
- Sharon, D., Wimberg, H., Kinarty, Y. & Koch, K. W. Genotype-functional-phenotype correlations in photoreceptor guanylate cyclase (GC-E) encoded by GUCY2D. *Prog Retin Eye Res* **63**, 69–91, <https://doi.org/10.1016/j.preteyeres.2017.10.003> (2018).
- Korenbrod, J. I. Speed, sensitivity, and stability of the light response in rod and cone photoreceptors: facts and models. *Prog Retin Eye Res* **31**, 442–466, doi:S1350-9462(12)00039-0 [pii], 10.1016/j.preteyeres.2012.05.002 (2012).
- Peshenko, I. V. *et al.* Enzymatic properties and regulation of the native isoforms of retinal membrane guanylyl cyclase (RetGC) from mouse photoreceptors. *Biochemistry* **50**, 5590–5600, <https://doi.org/10.1021/bi200491b> (2011).
- Hwang, J. Y. & Koch, K. W. Calcium- and myristoyl-dependent properties of guanylate cyclase-activating protein-1 and protein-2. *Biochemistry* **41**, 13021–13028, doi:bi026618y [pii] (2002).
- Hwang, J. Y. *et al.* Regulatory modes of rod outer segment membrane guanylate cyclase differ in catalytic efficiency and Ca(2+)-sensitivity. *Eur J Biochem* **270**, 3814–3821, doi:3770 [pii] (2003).
- Marino, V. *et al.* A novel p.(Glu111Val) missense mutation in GUCA1A associated with cone-rod dystrophy leads to impaired calcium sensing and perturbed second messenger homeostasis in photoreceptors. *Hum Mol Genet* **27**, 4204–4217, <https://doi.org/10.1093/hmg/ddy311> (2018).
- Peshenko, I. V. *et al.* A G86R mutation in the calcium-sensor protein GCAP1 alters regulation of retinal guanylyl cyclase and causes dominant cone-rod degeneration. *J Biol Chem* **294**, 3476–3488, <https://doi.org/10.1074/jbc.RA118.006180> (2019).
- Dell'Orco, D., Sulmann, S., Linse, S. & Koch, K. W. Dynamics of conformational Ca2+-switches in signaling networks detected by a planar plasmonic device. *Anal Chem* **84**, 2982–2989, <https://doi.org/10.1021/ac300213j> (2012).
- Marino, V., Sulmann, S., Koch, K. W. & Dell'Orco, D. Structural effects of Mg2+ on the regulatory states of three neuronal calcium sensors operating in vertebrate phototransduction. *Biochim Biophys Acta* **1853**, 2055–2065, <https://doi.org/10.1016/j.bbamer.2014.10.026> (2015).
- Peshenko, I. V. & Dizhoor, A. M. Guanylyl cyclase-activating proteins (GCAPs) are Ca2+/Mg2+ sensors: implications for photoreceptor guanylyl cyclase (RetGC) regulation in mammalian photoreceptors. *J Biol Chem* **279**, 16903–16906, [https://doi.org/10.1074/jbc.C400065200C400065200\[pii\]](https://doi.org/10.1074/jbc.C400065200C400065200[pii]) (2004).
- Peshenko, I. V. & Dizhoor, A. M. Ca2+ and Mg2+ binding properties of GCAP-1. Evidence that Mg2+-bound form is the physiological activator of photoreceptor guanylyl cyclase. *J Biol Chem* **281**, 23830–23841, doi:M600257200 [pii] 10.1074/jbc.M600257200 (2006).
- Dizhoor, A. M., Olshevskaya, E. V. & Peshenko, I. V. Mg2+/Ca2+ cation binding cycle of guanylyl cyclase activating proteins (GCAPs): role in regulation of photoreceptor guanylyl cyclase. *Mol Cell Biochem* **334**, 117–124, <https://doi.org/10.1007/s11010-009-0328-6> (2010).
- Behnen, P., Dell'Orco, D. & Koch, K. W. Involvement of the calcium sensor GCAP1 in hereditary cone dystrophies. *Biol Chem* **391**, 631–637, <https://doi.org/10.1515/BC.2010.063> (2010).
- Jiang, L. & Baehr, W. GCAP1 mutations associated with autosomal dominant cone dystrophy. *Adv Exp Med Biol* **664**, 273–282, [https://doi.org/10.1007/978-1-4419-1399-9\\_31](https://doi.org/10.1007/978-1-4419-1399-9_31) (2010).
- Manes, G. *et al.* Cone dystrophy or macular dystrophy associated with novel autosomal dominant GUCA1A mutations. *Mol Vis* **23**, 198–209 (2017).
- Dell'Orco, D., Behnen, P., Linse, S. & Koch, K. W. Calcium binding, structural stability and guanylate cyclase activation in GCAP1 variants associated with human cone dystrophy. *Cell Mol Life Sci* **67**, 973–984, <https://doi.org/10.1007/s00018-009-0243-8> (2010).
- Dizhoor, A. M., Boikov, S. G. & Olshevskaya, E. V. Constitutive activation of photoreceptor guanylate cyclase by Y99C mutant of GCAP-1. Possible role in causing human autosomal dominant cone degeneration. *J Biol Chem* **273**, 17311–17314 (1998).

22. Kitiratschky, V. B. *et al.* Mutations in the GUCA1A gene involved in hereditary cone dystrophies impair calcium-mediated regulation of guanylate cyclase. *Hum Mutat* **30**, E782–796, <https://doi.org/10.1002/humu.21055> (2009).
23. Marino, V., Scholten, A., Koch, K. W. & Dell’Orco, D. Two retinal dystrophy-associated missense mutations in GUCA1A with distinct molecular properties result in a similar aberrant regulation of the retinal guanylate cyclase. *Hum Mol Genet* **24**, 6653–6666, <https://doi.org/10.1093/hmg/ddv370> (2015).
24. Payne, A. M. *et al.* A mutation in guanylate cyclase activator 1A (GUCA1A) in an autosomal dominant cone dystrophy pedigree mapping to a new locus on chromosome 6p21.1. *Hum Mol Genet* **7**, 273–277, doi:ddb036 [pii] (1998).
25. Vocke, F. *et al.* Dysfunction of cGMP signalling in photoreceptors by a macular dystrophy-related mutation in the calcium sensor GCAP1. *Hum Mol Genet* **26**, 133–144, <https://doi.org/10.1093/hmg/ddw374> (2017).
26. Olshevskaya, E. V. *et al.* The Y99C mutation in guanylyl cyclase-activating protein 1 increases intracellular Ca<sup>2+</sup> and causes photoreceptor degeneration in transgenic mice. *J Neurosci* **24**, 6078–6085, <https://doi.org/10.1523/JNEUROSCI.0963-04.200424/27/6078>[pii] (2004).
27. Buch, P. K. *et al.* Dominant cone-rod dystrophy: a mouse model generated by gene targeting of the GCAP1/Guca1a gene. *PLoS One* **6**, e18089, <https://doi.org/10.1371/journal.pone.0018089> (2011).
28. Jiang, L. *et al.* RNAi-mediated gene suppression in a GCAP1(L151F) cone-rod dystrophy mouse model. *PLoS One* **8**, e57676, <https://doi.org/10.1371/journal.pone.0057676> (2013).
29. Duda, T. *et al.* The calcium-sensor guanylate cyclase activating protein type 2 specific site in rod outer segment membrane guanylate cyclase type 1. *Biochemistry* **44**, 7336–7345, <https://doi.org/10.1021/bi050068x> (2005).
30. Lange, C., Duda, T., Beyermann, M., Sharma, R. K. & Koch, K. W. Regions in vertebrate photoreceptor guanylyl cyclase ROS-GC1 involved in Ca(2+)-dependent regulation by guanylyl cyclase-activating protein GCAP-1. *FEBS Lett* **460**, 27–31 (1999).
31. Rehkamp, A. *et al.* Molecular Details of Retinal Guanylyl Cyclase 1/GCAP-2 Interaction. *Front Mol Neurosci* **11**, 330, <https://doi.org/10.3389/fnmol.2018.00330> (2018).
32. Laura, R. P. & Hurley, J. B. The kinase homology domain of retinal guanylyl cyclases 1 and 2 specifies the affinity and cooperativity of interaction with guanylyl cyclase activating protein-2. *Biochemistry* **37**, 11264–11271, <https://doi.org/10.1021/bi9809674> (1998).
33. Peshenko, I. V., Olshevskaya, E. V. & Dizhoor, A. M. Evaluating the role of retinal membrane guanylyl cyclase 1 (RetGC1) domains in binding guanylyl cyclase-activating proteins (GCAPs). *J Biol Chem* **290**, 6913–6924, <https://doi.org/10.1074/jbc.M114.629642> (2015).
34. Vinberg, F., Peshenko, I. V., Chen, J., Dizhoor, A. M. & Kefalov, V. J. Guanylate cyclase-activating protein 2 contributes to phototransduction and light adaptation in mouse cone photoreceptors. *J Biol Chem* **293**, 7457–7465, <https://doi.org/10.1074/jbc.RA117.001574> (2018).
35. Makino, C. L. *et al.* Enzymatic relay mechanism stimulates cyclic GMP synthesis in rod photoresponse: biochemical and physiological study in guanylyl cyclase activating protein 1 knockout mice. *PLoS One* **7**, e47637, <https://doi.org/10.1371/journal.pone.0047637>[PONE-D-12-25181][pii] (2012).
36. Dell’Orco, D., Schmidt, H., Mariani, S. & Fanelli, F. Network-level analysis of light adaptation in rod cells under normal and altered conditions. *Mol Biosyst* **5**, 1232–1246, <https://doi.org/10.1039/b908123b> (2009).
37. Invergo, B. M., Dell’Orco, D., Montanucci, L., Koch, K. W. & Bertranpetit, J. A comprehensive model of the phototransduction cascade in mouse rod cells. *Mol Biosyst* **10**, 1481–1489, <https://doi.org/10.1039/c3mb70584f> (2014).
38. Koch, K. W. & Stryer, L. Highly cooperative feedback control of retinal rod guanylate cyclase by calcium ions. *Nature* **334**, 64–66, <https://doi.org/10.1038/334064a0> (1988).
39. Burns, M. E., Mendez, A., Chen, J. & Baylor, D. A. Dynamics of cyclic GMP synthesis in retinal rods. *Neuron* **36**, 81–91, [https://doi.org/10.1016/s0896-6273\(02\)00911-x](https://doi.org/10.1016/s0896-6273(02)00911-x) (2002).
40. Viviano, J., Krishnan, A., Wu, H. & Venkataraman, V. Electrophoretic mobility shift in native gels indicates calcium-dependent structural changes of neuronal calcium sensor proteins. *Anal Biochem* **494**, 93–100, <https://doi.org/10.1016/j.ab.2015.11.005> (2016).
41. Otto-Bruc, A. *et al.* Localization of guanylate cyclase-activating protein 2 in mammalian retinas. *Proc Natl Acad Sci USA* **94**, 4727–4732, <https://doi.org/10.1073/pnas.94.9.4727> (1997).
42. Lopez-del Hoyo, N. *et al.* Overexpression of guanylate cyclase activating protein 2 in rod photoreceptors *in vivo* leads to morphological changes at the synaptic ribbon. *PLoS One* **7**, e42994, <https://doi.org/10.1371/journal.pone.0042994> (2012).
43. Lopez-Begines, S., Plana-Bonamaiso, A. & Mendez, A. Molecular determinants of Guanylate Cyclase Activating Protein subcellular distribution in photoreceptor cells of the retina. *Sci Rep* **8**, 2903, <https://doi.org/10.1038/s41598-018-20893-1> (2018).
44. Mendez, A. *et al.* Role of guanylate cyclase-activating proteins (GCAPs) in setting the flash sensitivity of rod photoreceptors. *Proc Natl Acad Sci USA* **98**, 9948–9953, <https://doi.org/10.1073/pnas.171308998171308998>[pii] (2001).
45. Lim, S. *et al.* Retinal guanylyl cyclase activating protein 1 forms a functional dimer. *PLoS One* **13**, e0193947, <https://doi.org/10.1371/journal.pone.0193947> (2018).
46. Dell’Orco, D., Sulmann, S., Zagel, P., Marino, V. & Koch, K. W. Impact of cone dystrophy-related mutations in GCAP1 on a kinetic model of phototransduction. *Cell Mol Life Sci* **71**, 3829–3840, <https://doi.org/10.1007/s00018-014-1593-4> (2014).
47. Kulkarni, M., Trifunovic, D., Schubert, T., Euler, T. & Paquet-Durand, F. Calcium dynamics change in degenerating cone photoreceptors. *Hum Mol Genet* **25**, 3729–3740, <https://doi.org/10.1093/hmg/ddw219> (2016).
48. Power, M. *et al.* Cellular mechanisms of hereditary photoreceptor degeneration - Focus on cGMP. *Prog Retin Eye Res*, 100772, <https://doi.org/10.1016/j.preteyeres.2019.07.005> (2019).
49. Asteriti, S. *et al.* Effective delivery of recombinant proteins to rod photoreceptors via lipid nanovesicles. *Biochem Biophys Res Commun* **461**, 665–670, <https://doi.org/10.1016/j.bbrc.2015.04.088> (2015).
50. Marino, V., Borsatto, A., Vocke, F., Koch, K. W. & Dell’Orco, D. CaF<sub>2</sub> nanoparticles as surface carriers of GCAP1, a calcium sensor protein involved in retinal dystrophies. *Nanoscale* **9**, 11773–11784, <https://doi.org/10.1039/c7nr03288a> (2017).
51. Zagel, P., Dell’Orco, D. & Koch, K. W. The dimerization domain in outer segment guanylate cyclase is a Ca(2+)-sensitive control switch module. *Biochemistry* **52**, 5065–5074, <https://doi.org/10.1021/bi400288p> (2013).

## Acknowledgements

This work was funded by a grant from Fondazione Telethon–Italy (grant no. GGP16010 to DDO). We would like to thank Dr. Valerio Marino for helpful discussions and Anna Avesani for assistance with GCAP2 preparation.

## Author contributions

D.D.O. conceived the work, performed *in silico* simulations and wrote the manuscript. G.D.C. designed and performed all experimental assays and contributed in writing the manuscript.

## Competing interests

The authors declare no competing interests.

### Additional information

**Supplementary information** is available for this paper at <https://doi.org/10.1038/s41598-019-56606-5>.

**Correspondence** and requests for materials should be addressed to D.D.O.

**Reprints and permissions information** is available at [www.nature.com/reprints](http://www.nature.com/reprints).

**Publisher's note** Springer Nature remains neutral with regard to jurisdictional claims in published maps and institutional affiliations.



**Open Access** This article is licensed under a Creative Commons Attribution 4.0 International License, which permits use, sharing, adaptation, distribution and reproduction in any medium or format, as long as you give appropriate credit to the original author(s) and the source, provide a link to the Creative Commons license, and indicate if changes were made. The images or other third party material in this article are included in the article's Creative Commons license, unless indicated otherwise in a credit line to the material. If material is not included in the article's Creative Commons license and your intended use is not permitted by statutory regulation or exceeds the permitted use, you will need to obtain permission directly from the copyright holder. To view a copy of this license, visit <http://creativecommons.org/licenses/by/4.0/>.

© The Author(s) 2019



## Supporting information

# Normal GCAPs partly compensate for altered cGMP signaling in retinal dystrophies associated with mutations in *GUCA1A*

Daniele Dell'Orco<sup>1\*</sup> and Giuditta Dal Cortivo<sup>1</sup>

<sup>1</sup>Department of Neuroscience, Biomedicine and Movement Sciences, Section of Biological Chemistry, University of Verona, I-37134 Verona, Italy

\*to whom correspondence should be addressed. Telephone: +39-045-8027637; E-mail: [daniele.dellorco@univr.it](mailto:daniele.dellorco@univr.it)

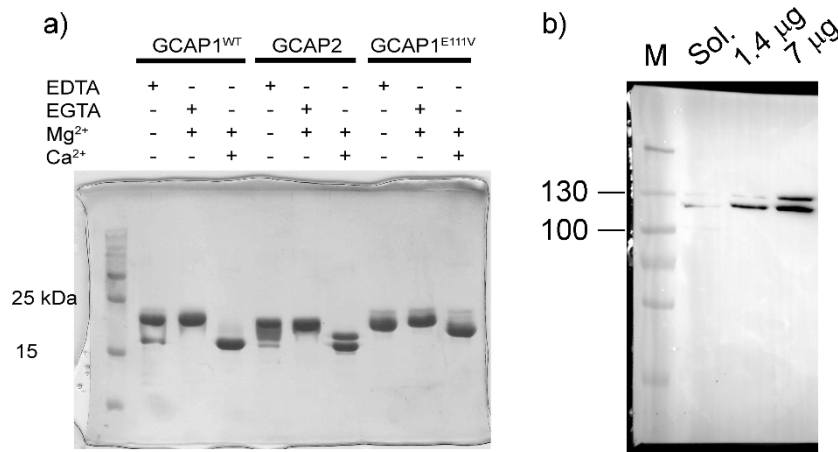


**Figure S1. Purity of recombinant proteins and GC1 enzymatic assay.** a) Full-length gel used for the preparation of Figure 1a. b) Western blot analysis of HEK293 soluble phase (Sol) and two different amounts (1.4 and 7 µg) of membrane proteins previously quantified by amido black. Anti-GC1#3 antibody (Ref. 51) was used (1:1000 dilution).

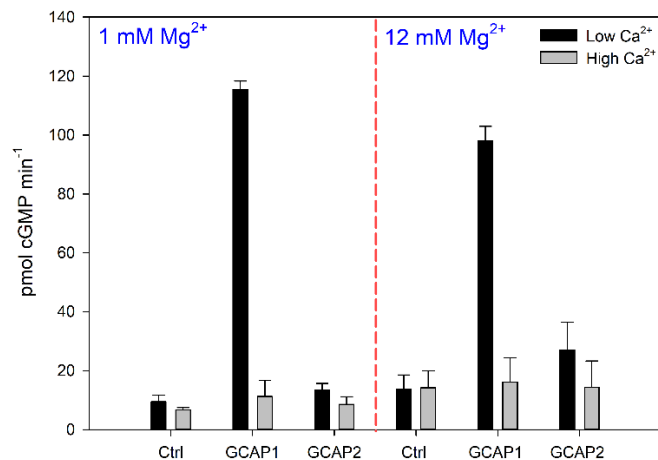


**Figure S2: GC assay at different Mg<sup>2+</sup> concentrations.** Guanylate Cyclase activity induced by GCAPs was analyzed at 1 mM (left) and 12 mM Mg<sup>2+</sup> (right), in the presence of low (< 19 nM) and high (~30 µM) Ca<sup>2+</sup> concentration. Each measurement represents the average of three replicas.

# SCIENTIFIC REPORTS



OPEN

## Luminescent and paramagnetic properties of nanoparticles shed light on their interactions with proteins

Giuditta Dal Cortivo<sup>1</sup>, Gabriel E. Wagner<sup>2</sup>, Paolo Cortelletti<sup>3</sup>, Krishna Mohan Padmanabha Das<sup>4</sup>, Klaus Zangger<sup>5</sup>, Adolfo Speghini<sup>3</sup>, Daniele Dell'Orco<sup>1</sup> & N. Helge Meyer<sup>6</sup>

Nanoparticles have been recognized as promising tools for targeted drug-delivery and protein therapeutics. However, the mechanisms of protein-nanoparticle interaction and the dynamics underlying the binding process are poorly understood. Here, we present a general methodology for the characterization of protein-nanoparticle interaction on a molecular level. To this end we combined biophysical techniques including nuclear magnetic resonance (NMR), circular dichroism (CD), resonance energy transfer (RET) and surface plasmon resonance (SPR). Particularly, we analyzed molecular mechanisms and dynamics of the interaction of CaF<sub>2</sub> nanoparticles with the prototypical calcium sensor calmodulin (CaM). We observed the transient formation of an intermediate encounter complex involving the structural region linking the two domains. Specific interaction of CaM with CaF<sub>2</sub> NPs is driven by the N-terminal EF-hands, which seem to recognize Ca<sup>2+</sup> on the surface of the nanoparticle. We conclude that CaF<sub>2</sub> NP-CaM interaction is fully compatible with potential applications in nanomedicine. Overall, the methods presented in this work can be extended to other systems and may be useful to quantitatively characterize structural and dynamic features of protein-NP interactions with important implications for nanomedicine and nano-biotechnology.

Nanoparticles (NPs) receive increasing attention in biomedical applications and are intensively discussed as promising drug delivery systems in disease treatment<sup>1–3</sup>. Due to their high degree of specificity and minimal side effects they are of particular interest as they can potentially be used with protein therapeutics in complex diseases. However, the mechanisms of protein-nanoparticle interactions are not fully understood.

Recently, it has been shown that CaF<sub>2</sub> NPs can specifically bind calcium sensor proteins including recoverin<sup>4</sup>, guanylate cyclase-activating protein 1 (GCAP1)<sup>5</sup> and calmodulin (CaM)<sup>6</sup>. In these latter cases, binding to NPs occurs at physiological concentrations in a fully reversible manner and most importantly, it does not alter secondary or tertiary structure of the protein<sup>6</sup>. The fact that the surface-bound protein remains structurally and functionally intact suggests that CaF<sub>2</sub> NPs might be considered as specific carriers for calcium sensors including CaM and GCAP1, and that exploiting the high surface-to-volume ratio typical of the nanoscale could constitute a general strategy for protein replacement-therapy in the case of disease-associated mutant proteins<sup>5</sup>.

CaM is a prototypical calcium sensor protein, which is highly conserved and ubiquitous in eukaryotic cells. It comprises four EF-hands (EF1–4), each containing a functional calcium binding motif and arranged in two domains, termed C-terminal and N-terminal lobe. As Ca<sup>2+</sup> ions act as important second messenger, CaM is involved in many physiological processes including cell motility, proliferation, apoptosis, cytoskeleton remodeling, metabolic homeostasis, ion transport and protein folding<sup>7,8</sup>. Focusing on CaM-dependent biochemical

<sup>1</sup>Department of Neurosciences, Biomedicine and Movement Sciences, Section of Biological Chemistry, Strada le Grazie 8, Verona, Italy. <sup>2</sup>Institute of Hygiene, Microbiology and Environmental Medicine, Medical University of Graz, Neue Stiftingtalstraße 6, 8010, Graz, Austria. <sup>3</sup>Nanomaterials Research Group, Department of Biotechnology, University of Verona and INSTM, UdR Verona, Strada Le Grazie 15, Verona, Italy. <sup>4</sup>Institute of Molecular Biosciences, University of Graz, Humboldtstraße 50/3, 8010, Graz, Austria. <sup>5</sup>Institute of Chemistry, University of Graz, Heinrichstr. 28, 8010, Graz, Austria. <sup>6</sup>Department of Human Medicine and Department of Neuroscience, University of Oldenburg, Carl-von-Ossietzky-Str. 9-11, 26131, Oldenburg, Germany. Correspondence and requests for materials should be addressed to D.D. (email: [daniele.dellorco@univr.it](mailto:daniele.dellorco@univr.it)) or N.H.M. (email: [helge.meyer@uni-oldenburg.de](mailto:helge.meyer@uni-oldenburg.de))

systems could be particularly useful for targeting cell cycle dysregulation and aberrant proliferation in tumor cells<sup>9</sup>. Very recently, point mutations in the gene encoding CaM were found in patients suffering from arrhythmogenic pathologies<sup>10</sup>, moreover, a significant over-expression of CaM in Alzheimer's disease has been found<sup>11</sup>, thus implying a possible involvement of CaM in protein therapeutics for a broad variety of diseases spanning from genetic pathologies to neurodegenerative cases.

In this work, we aim at unveiling the mechanisms of protein-NP interactions at the molecular level by focusing on a biologically relevant system, namely CaF<sub>2</sub> NP interacting with human CaM. We have used a comprehensive approach combining high-resolution spectroscopic techniques with lower-resolution, versatile methods. Specifically, we employed nuclear magnetic resonance spectroscopy (NMR) and resonance energy transfer (RET) by exploiting both paramagnetic and luminescence properties of lanthanide-doped CaF<sub>2</sub> NPs and obtained further insights in the binding process by circular dichroism spectroscopy and surface plasmon resonance (SPR). Our results suggest that kinetics of protein-nanoparticle interaction in this case is fully compatible with realistic nanomedicine applications. The methodology presented here can be extended to other protein-NP interaction systems of biomedical and biotechnological relevance.

## Methods

**Protein preparation.** Calmodulin was expressed in *E. coli* BL21(DE3) Rosetta pLysS over night at 25 °C after induction with 0.5 mM IPTG (at an OD<sub>600</sub> of 0.8) using a modified pet24a vector (Genscript). The sequence contains an N-terminal 6His-tag followed by a cleavage site for tobacco etch virus (TEV) protease. Bacteria were grown in LB medium or M9 medium supplemented with [<sup>15</sup>N]H<sub>4</sub>Cl and <sup>13</sup>C-Glucose for the production of unlabeled and uniformly <sup>15</sup>N, <sup>13</sup>C-labeled samples, respectively.

Bacterial cells were harvested by centrifugation for 15 min. at 6000 g and resuspended in 20 mM TRIS-HCl pH 8, 100 mM NaCl, 10 mM imidazole, 4 mM 2-Mercaptoethanol. After addition of protease inhibitor cocktail (Sigma Aldrich), DNase I and Lysozyme bacterial cells were lysed by sonication. Subsequent to centrifugation for 45 min at 48,000 g lysis supernatant was applied to a Ni-NTA-Agarose column (2 ml, 5Prime PerfectPro Ni-NTA Agarose, Thermofisher Scientific). The column was then washed three times each with 10 column volumes of a buffer containing 20 mM TRIS-HCl pH8, 100 mM NaCl, 4 mM 2-Mercaptoethanol and additionally either 10 mM imidazole, 500 mM NaCl or 20 mM imidazole. Protein was eluted with 400 mM imidazole in the same buffer. After removal of the His-Tag by cleavage TEV protease the protein sample was charged with 5 mM CaCl<sub>2</sub> and applied to a Phenyl-Sepharose (PS) column (GE Healthcare). The column was washed with 20 mM TRIS-HCl pH 7.5, 0.5 mM CaCl<sub>2</sub>, 1 mM DTT and eluted with 20 mM TRIS-HCl, 1 mM EGTA, 1 mM DTT. After extensive dialysis against Ca<sup>2+</sup>-free 50 mM (NH<sub>4</sub>)<sub>2</sub>CO<sub>3</sub> the protein was lyophilized and stored at -20 °C.

For NMR measurements uniformly labeled protein samples were washed twice with NMR buffer (20 mM BisTris-HCl pH 6.5, 50 mM NaCl, 500 μM CaCl<sub>2</sub>, 0.02% NaN<sub>3</sub>) by ultrafiltration (Amicon Ultra-15 Millipore) and concentrated to 1 mM.

**Protein-fluorescent dye conjugation and luminescence titrations.** The maleimide-functionalized fluorescent dye Alexa Fluor 532 (Thermofisher) was specifically coupled to human CaM by a thiol/disulfide exchange reaction. The wild type protein lacks Cys residues, therefore threonine in position 26 was mutated into cysteine using standard mutagenesis techniques. The conjugated dye exhibited  $\lambda_{exc}^{max} = 532$  nm and  $\lambda_{emi}^{max} = 554$  nm. After dissolving 1 mg of dye in DMSO, the conjugation was performed in 50 mM TRIS-HCl pH 7.2, 150 mM KCl buffer, in the presence of 10-fold excess of dye with respect to the protein. The dye was added to the protein solution dropwise in the dark, in order to prevent quenching. A buffer exchange step using a PD10 desalting column (GE Healthcare) allowed the isolation of the unconjugated dye. Finally, the conjugation efficiency was calculated using Equation 1:

$$Efficiency (\%) = \frac{A_{532 \text{ dye}} * MW_{CaM}}{\epsilon_{Alexa} * [CaM]} * 100 \quad (1)$$

in which  $\epsilon_{Alexa}$  is the dye extinction molar coefficient (78,000 M<sup>-1</sup>cm<sup>-1</sup>), MW<sub>CaM</sub> is 16,800 g mol<sup>-1</sup> and [CaM] is expressed in mg mL<sup>-1</sup>. The efficiency of conjugation was 68%.

In order to study the interaction between the conjugated CaM T26C and the CaF<sub>2</sub> NPs, titration experiments were performed. Twelve additions (8.05 μL each) of a fluorescently-labeled CaM stock solution (31 μM) were done in a dispersion of 0.5 mg mL<sup>-1</sup> NPs, moving from a protein-free condition to a final concentration of 5.5 μM CaM. Solution volumes ranged between 500 μL and ~600 μL (dilution effect was considered in the final protein concentration calculation). For each addition, a fluorescence emission spectrum (410–750 nm) was collected following excitation at 980 nm.

**NP preparation.** Er<sup>3+</sup>, Yb<sup>3+</sup> codoped CaF<sub>2</sub> NPs (nominal molar ratios Ca<sup>2+</sup>:Yb<sup>3+</sup>:Er<sup>3+</sup> = 0.78:0.20:0.02), Y<sup>3+</sup>, Gd<sup>3+</sup> co-doped CaF<sub>2</sub> NPs (nominal molar ratios Ca<sup>2+</sup>:Y<sup>3+</sup>:Gd<sup>3+</sup> = 0.78:0.21:0.01) and Y<sup>3+</sup> doped CaF<sub>2</sub> NPs (nominal molar ratios Ca<sup>2+</sup>:Y<sup>3+</sup> = 0.78:0.22) were prepared using a hydrothermal technique and stoichiometric amounts of metal chlorides<sup>12</sup>. Sodium citrate was used as a capping agent and ammonium fluoride was added as the fluorine precursor. The obtained solution was heat-treated in a Teflon lined autoclave at 190 °C for 6 hours. After the reaction, NPs were precipitated and collected by centrifugation. The NPs are easily dispersible in water or saline solution. Structural and optical characterizations are reported in previous papers<sup>4-6,13</sup>.

**Limited proteolysis.** The pattern of proteolytic digestion was first tested on CaM, in the absence or in the presence of Ca<sup>2+</sup>. In the experiments without NPs, 6 μg CaM in 5 mM TRIS-HCl pH 7.5, 150 mM KCl buffer was incubated with 0.3 μM TPCK-trypsin (trypsin:protein ratio 1:60) for a time range varying from 30 min to

120 min, in the presence of 2 mM  $\text{Ca}^{2+}$  or EGTA. Since 30 min were found to be enough to reach a complete proteolysis in the presence of EGTA and a limited proteolysis pattern in the presence of  $\text{Ca}^{2+}$ , this condition was used in further experiments with NPs. Mixtures of 21  $\mu\text{M}$  CaM in the absence or in the presence of 3.8  $\text{mg mL}^{-1}$  NPs (NPs:CaM = 1:139, stoichiometric ratio was estimated as described elsewhere<sup>4</sup>) were used in these experiments. The protein was dissolved in 5 mM TRIS-HCl pH 7.5, 150 mM KCl buffer and incubated with 240  $\mu\text{M}$  EGTA or  $\text{Ca}^{2+}$ . Protein and protein-NPs mixtures were incubated with 0.35  $\mu\text{M}$  TPCK-trypsin (trypsin:protein ratio 1:60) for 30 min at 25 °C; the reaction was stopped by adding reducing sample buffer and boiling for 5 min. For each experimental condition a parallel sample without trypsin was tested. Proteolytic patterns were visualized by 15% and 12% SDS-PAGE via Coomassie blue staining.

**Circular dichroism spectroscopy.** Circular dichroism spectra were collected with a Jasco J-710 spectropolarimeter equipped with a Peltier type thermostated cell holder. Near UV spectra were recorded at 25 °C between 250 nm and 320 nm in a 1 cm quartz cuvette, with scan rate set to 50  $\text{nm min}^{-1}$ , bandwidth of 1 nm and 4 s as integration time. Reported spectra are the mean of 5 accumulations. Spectra of buffer alone were also collected and considered as blank. Protein concentration was 40  $\mu\text{M}$ , and the spectra were collected in the presence and in the absence of 5.7  $\text{mg mL}^{-1}$  NPs (ratio NPs:CaM = 1:139), with 3-fold excess of  $\text{Ca}^{2+}$ /EGTA with respect to the calcium binding sites.

Far UV spectra were collected between 200–250 nm in a 0.1 cm quartz cuvette in the presence and in the absence of 1.75  $\text{mg mL}^{-1}$  of NPs (protein concentration was 12  $\mu\text{M}$ ). Scan rate, bandwidth, accumulations and saturating conditions were the same as for near UV spectra. CaM previously incubated with NPs was tested without additions of  $\text{Ca}^{2+}$ /EGTA unless differently specified.

Thermal denaturation profiles were monitored between 20 °C and 96 °C in the same conditions as for the far-UV experiments. The scan speed and response time were set at 1 °C/min and 4 s respectively, and the circular dichroism variations was followed at 222 nm.

**Nuclear magnetic resonance spectroscopy.** All NMR spectra were recorded on 0.1 mM uniformly  $^{15}\text{N}$ -labeled or  $^{15}\text{N}$ ,  $^{13}\text{C}$ -labeled CaM on a Bruker Avance III 700 MHz spectrometer equipped with a cryogenically cooled TCI probe-head. Spectra were processed with NMRPipe<sup>14</sup> and analyzed with Sparky (Goddard and Kneller 2004) and CCPNmr<sup>15</sup>. Backbone chemical shift assignments were obtained from CBCA(CO)NH, CBCANH and HNCA<sup>16</sup>.

For chemical shift perturbation analysis and PRE measurements  $\text{CaF}_2$  nanoparticle or diamagnetic  $\text{CaF}_2\text{:Y}^{3+}$  and paramagnetic  $\text{CaF}_2\text{:Y}^{3+}$ ,  $\text{Gd}^{3+}$  were added to the NMR sample up to a final concentration of 1.4  $\text{mg mL}^{-1}$ .

**Surface plasmon resonance spectroscopy.** Surface Plasmon Resonance (SPR) experiments were performed using a SensiQ Pioneer instrument. CaM was immobilized via amine coupling on a SensiQ COOH5 sensor chip coated by a carboxylated polysaccharide hydrogel spacer. Carboxyl groups were activated with sequential injections of 60  $\mu\text{L}$  of 10 mM  $\text{H}_3\text{PO}_4$ , 60  $\mu\text{L}$  HBS (10 mM HEPES pH 7.4, 150 mM KCl, 20 mM  $\text{MgCl}_2$ , 2 mM  $\text{CaCl}_2$ ), 60  $\mu\text{L}$  10 mM NaOH and  $2 \times 60 \mu\text{L}$  HBS. The sensor chip surface was activated with a 7-min injection of a mixture of 10 mM N-hydroxysuccinimide (NHS) and N-ethyl-N'-(dimethylaminopropyl)-carbodiimide (EDC) at a flow of 5  $\mu\text{L min}^{-1}$ . The lyophilized protein was dissolved in bidistilled water at a concentration of 1  $\text{mg mL}^{-1}$ . Subsequent injections of CaM, diluted in Na-acetate buffer and  $\text{H}_3\text{PO}_4$  (pH varying between 2.7–3.1), led the immobilization of 2400 RU (corresponding to  $\sim 2.4$  ng, 1 RU = 1  $\text{pg mm}^{-2}$ , flow cell volume <40 nL) in flow cell 1 (FC1), 200 RU in FC3 ( $\sim 0.2$  ng) while FC2 was considered as a reference (no protein injections were performed and the surface was activated/deactivated). Finally, the activated carboxy-groups were blocked via injection of 70  $\mu\text{L}$  of ethanolamine hydrochloride-NaOH pH 8.5. During the immobilization steps, HBS was used as running buffer.

The interactions between immobilized CaM and NPs were investigated by: (a) titrating five different NPs concentrations ranging from 0.1  $\text{mg mL}^{-1}$  to 0.5  $\text{mg mL}^{-1}$  and (b) injecting the same amount of NPs both in the presence and in the absence of saturating CaM concentration. Interaction experiments were performed with a flow rate of 10  $\mu\text{L min}^{-1}$ , with 600 s association time, 1800 s dissociation time and a final 180 s injection of 10 mM K-citrate in order to completely remove residual NP-CaM complex before proceeding with the next injection.

Titration data were fitted to a single exponential decay model, as in Equation 2:

$$RU = RU_0 * e^{-k^{off} * t} \quad (2)$$

**Instrumentation for luminescence measurements.** The upconversion spectra were acquired using a 980 diode laser as excitation source. The emission was analyzed using a monochromator (HR460, Jobin Yvon) equipped with a 1200 g/mm grating and a CCD detector (Spectrum One, Jobin Yvon) with a spectral resolution of 0.15 nm.

## Results and Discussion

**Conformational changes and thermal stability of  $\text{CaF}_2$  NP-bound CaM.** We compared conformational changes of CaM upon interaction with  $\text{Ca}^{2+}$  and/or NPs by circular dichroism (CD) spectroscopy, a technique particularly suitable to study proteins in solution under conditions that mimic the physiological ones. While far-UV spectra can reveal secondary structure rearrangements of polypeptides in solution, near-UV spectra provide a fingerprint of their tertiary structure, being sensitive to the micro environment of the aromatic residues. Far-UV CD spectroscopy was used to analyze the secondary structure content of apo CaM (calcium-free, in the presence of EGTA), holo CaM (calcium-bound, in the presence of  $\text{Ca}^{2+}$ ) and CaM bound to  $\text{CaF}_2$  NPs. As expected, apo CaM shows characteristics of an alpha helical protein with minima at 208 and 222 nm (Fig. 1a).

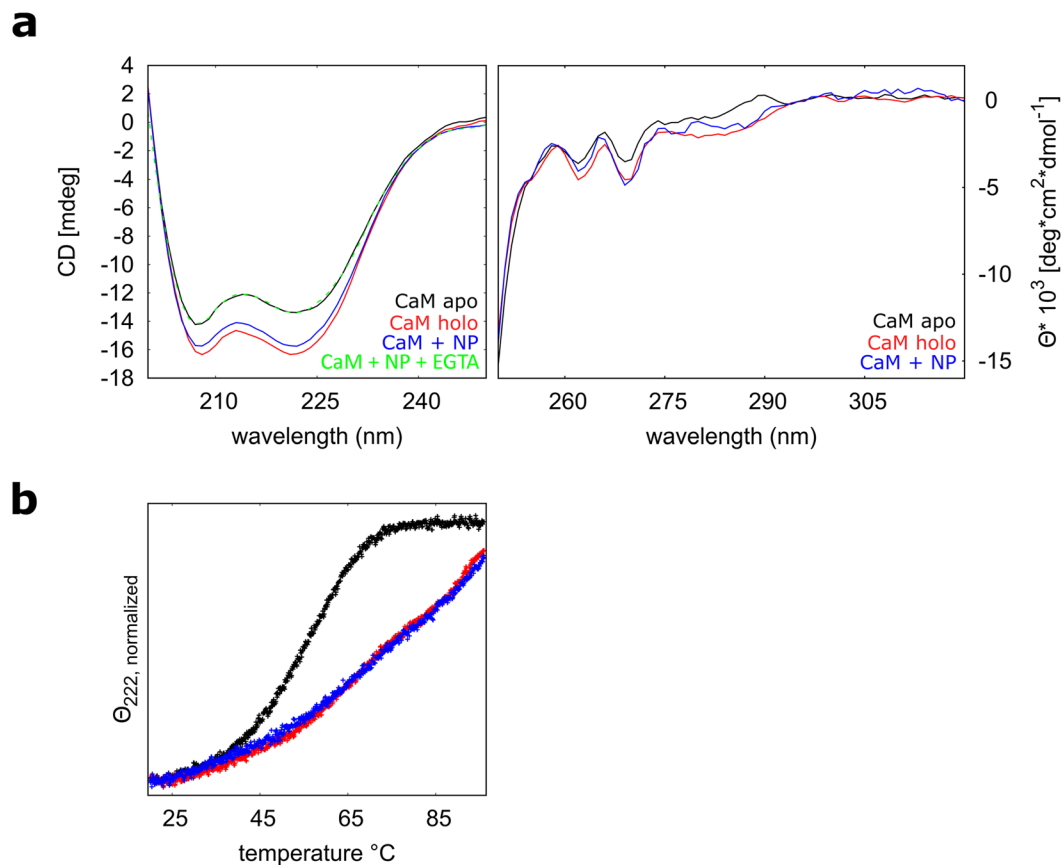


**Figure 1.** (a) Far- and near-UV spectra (of  $\sim 12 \mu\text{M}$  CaM or  $30 \mu\text{M}$ , respectively) in the presence of equal amounts ( $400 \mu\text{M}$ ) of saturating EGTA (black) or  $\text{Ca}^{2+}$  (red), and CaM previously incubated with  $5.7 \text{ mgmL}^{-1}$  NPs (blue). (b) Thermal denaturation profiles of  $\sim 12 \mu\text{M}$  CaM previously incubated with  $1.7 \text{ mgmL}^{-1}$  NPs (blue) and in the presence of saturating ( $120 \mu\text{M}$ ) EGTA (black) and  $\text{Ca}^{2+}$  (red).  $\theta_{222}$  has been normalized to account for different starting values ( $\theta_{222, \text{normalized}} = \theta_{222} / \theta_{222} \text{ at } 20^\circ\text{C}$ ).

	$\Theta_{208}$	$\Theta_{222}$	$\Theta_{222} / \Theta_{208}$	$\Delta\Theta_{222} / \Theta_{222}^a$
CaM $\text{Ca}^{2+}$	-16.34	-16.29	1.00	21.7%
CaM EGTA	-14.15	-13.38	0.95	
CaM + NPs	-15.74	-15.75	1.00	17.6%
CaM WT + NPs EGTA	-14.09	-13.39	0.95	

**Table 1.** Far-UV CD data: spectral shapes of apo CaM incubated with  $\text{CaF}_2$  NP are very similar to those of  $\text{Ca}^{2+}$ -loaded unbound protein. <sup>a</sup>Relative change in ellipticity ( $\theta$ ) at  $\lambda = 222 \text{ nm}$  as obtained by the difference in  $\theta$  in the presence of  $\text{Ca}^{2+}$  or in the apo conditions (EGTA), divided by  $\theta$  in the apo conditions.

Decrease of these minima upon addition of  $\text{Ca}^{2+}$  (21.7% relative change of  $\theta_{222}$ ) reflects a major conformational change. (Table 1). A switch in the  $\theta_{222} / \theta_{208}$  ratio from 0.95 in the apo form to 1.00 in the holo form has been attributed to an increased alpha helical content, reorganization of the alpha helices and an overall compaction of the protein upon addition of  $\text{Ca}^{2+}$ . These findings are corroborated by NMR structure analysis and SPR<sup>17,18</sup>.

Interestingly, addition of  $\text{CaF}_2$  NPs in a decalcified CaM solution evokes an alteration of the far-UV CD spectrum, which is very similar to the effect of free  $\text{Ca}^{2+}$  (17.6% relative change of  $\theta_{222}$ ) and likewise shifts the  $\theta_{222} / \theta_{208}$  ratio to 1.00, suggesting similar rearrangements in the NP-bound form of CaM. If EGTA is added in excess to the CaM-NP solution, the spectral shape shifts back to the apo CaM (Table 1, Fig. 1a), being almost undistinguishable, suggesting a dissociation of the protein-NP complex. The conformational changes of CaM in the presence of either  $\text{CaF}_2$  NPs or free  $\text{Ca}^{2+}$  also result in a very similar increase in thermal stability, as probed by almost identical thermal denaturation profiles indicating incomplete unfolding at  $96^\circ\text{C}$ , at odds with the complete unfolding observed for the apo form (Fig. 1b).

Changes of the near-UV (250–320 nm) spectra of CaM upon addition of  $\text{Ca}^{2+}$  or  $\text{CaF}_2$  NPs are indicative of reorganization of the asymmetric environment of aromatic residues which are buried in the core of the protein

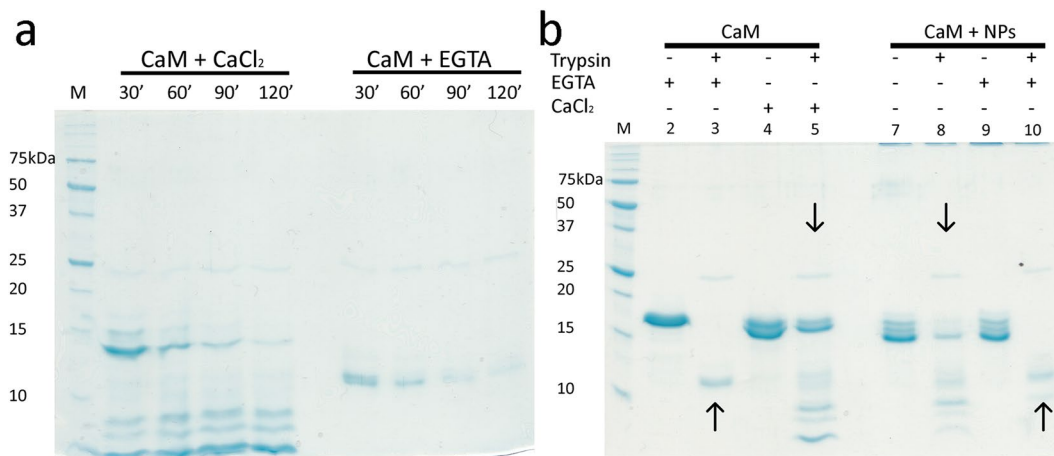


**Figure 2.** Limited proteolysis pattern of CaM in the presence and in the absence of NPs. **(a)** Proteolysis reactions were performed at 25 °C by 30–120 min incubation with saturating (2 mM) EGTA or Ca<sup>2+</sup>, using a CaM:TPCK-trypsin ratio equal to 1:60. Lane M refers to the protein marker. **(b)** Proteolysis experiments in the presence of NPs were performed by 30 min incubation with saturating (240 μM) EGTA or Ca<sup>2+</sup>, using a CaM:TPCK-trypsin ratio equal to 1:60. Lanes 3 and 5 refer to the digested apo (lane 3) and Ca<sup>2+</sup>-bound (lane 5) CaM. Lanes 8 and 10 refer to the digested CaM previously incubated with NPs (lane 8) and after the addition of EGTA (lane 10). Undigested CaM was loaded in the same conditions in lanes 2, 4, 7 and 9. The similar effect exerted by either free Ca<sup>2+</sup> or NPs and excess EGTA on the proteolytic patterns is highlighted by downwards and upwards arrows, respectively. The figure results from two separate gels, which have been reported in full-length in Supplementary Figure S1.

(Table 1). The near-UV spectra of NP bound CaM are very similar to those of holo CaM, but significantly different from the apo CaM spectrum (Fig. 1a).

To further investigate potential similarities between the Ca<sup>2+</sup>-bound and NP-bound forms of CaM we performed limited proteolysis experiments. Results are reported in Fig. 2.

The presence of free Ca<sup>2+</sup> clearly protects CaM from complete degradation (Fig. 2a) even after 120 min incubation with trypsin. The apo CaM instead undergoes complete degradation after 30 min. We therefore decided to focus on 30 min incubation for assessing the effects of CaF<sub>2</sub> NPs on the proteolytic pattern. In line with the spectroscopic results obtained by CD, the presence of CaF<sub>2</sub> NPs induces a very similar proteolysis pattern compared to the isolated protein in the presence of Ca<sup>2+</sup> (Fig. 2b, downwards arrows), while excess of EGTA does not prevent complete digestion even in the presence of NPs (Fig. 2b, upwards arrows).

Overall, we thus conclude that the NP-bound conformation of CaM resembles the Ca<sup>2+</sup> bound state of the protein (Fig. 1c). Strikingly, mutational studies performed with a CaM orthologue from *A. Thaliana* suggested that binding to CaF<sub>2</sub> NPs requires the presence of intact EF-hand motifs<sup>6</sup>.

**CaM-NP interaction occurs via a two-step process.** In order to characterize the interaction of CaM with NPs on a molecular level, we used nuclear magnetic resonance spectroscopy (Fig. 3). In particular, we recorded a series of <sup>1</sup>H, <sup>15</sup>N heteronuclear single quantum correlation (HSQC) spectra of holo CaM with increasing concentrations of CaF<sub>2</sub> NPs. This type of spectrum resolves every amide group of the protein as a single 2D peak.

Moreover, it is sensitive to changes in the chemical environment of individual amino acids, thus providing a fingerprint of the conformational state of the protein. In a titration experiment residues, which are directly or indirectly involved in the binding interface, typically experience a chemical shift perturbation (CSP) - a change in the resonance frequency of the respective nuclei. CSP has been previously utilized to characterize the binding interface of protein-NP interactions<sup>19–25</sup>. Note that the resonances of the bound state are broadened beyond detection, due to the high molecular weight of the complex. However, molecular details on the interaction can be derived under certain kinetic conditions, i.e. if the exchange between free and NP-bound CaM is fast with regard to the chemical shift timescale (Fig. 4a,b). In this case, a single peak with population averaged chemical shift is visible<sup>19</sup>. If the interaction is in the so called intermediate exchange regime CSPs can be observed as well. However, in this case the observed chemical shift does not represent a simple population weighted average of the bound and the free state. Additionally, exchange broadening of the respective peaks occurs.

In order to achieve intermediate to fast exchange condition 500 μM Ca<sup>2+</sup> was added to the NMR sample, which allows a rapid exchange between Ca<sup>2+</sup>-bound and NP-bound CaM, as no conformational rearrangement is required. Under these conditions CaM seems to bind preferably to NP, even in the presence of high [Ca<sup>2+</sup>] as significant CSPs are observed upon addition of NPs (Fig. 3a,b).

This can be attributed to the high local concentration of Ca<sup>2+</sup> on the surface of the NPs. Intriguingly, the strongest CSPs are observed for residues of the two N-terminal EF-hand motifs (EF1 and EF2) closely located near the respective calcium binding sites (Fig. 5a). EF3 and 4 in the C-terminal lobe of CaM experience only little

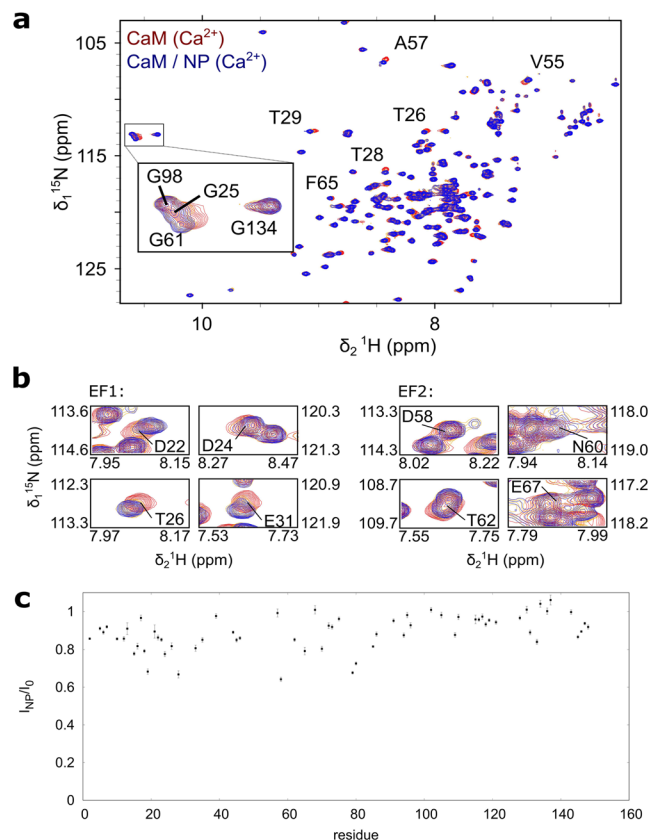


**Figure 3.** (a) Overlay of  $^1\text{H}$ ,  $^{15}\text{N}$  HSQC spectra of 1 mM holo CaM (red,  $500\ \mu\text{M}\ \text{Ca}^{2+}$ ) and NP-bound CaM (blue,  $500\ \mu\text{M}\ \text{Ca}^{2+}$ ,  $1.4\ \text{mg/mL}\ \text{CaF}_2\ \text{NP}$ ). Residues within the four EF-hands are highlighted. Down-field shifts of the amide protons of G25, G61, G98 and G134 are indicative of  $\text{Ca}^{2+}$  complexation. Mainly residues close to the N-terminal and not the C-terminal EF-hands experience CSP upon addition of  $\text{CaF}_2$  nanoparticles. (b) Close-up of residues which coordinate  $\text{Ca}^{2+}$  in the N-terminal EF-hand motifs (EF1 and EF2). (c) Signal attenuation upon addition of NPs. The ratio of intensity in the presence ( $I_{\text{NP}}$ ) and absence ( $I_0$ ) of nanoparticles is plotted against the sequence of Calmodulin.

CSP. In addition, amino acids 80–87 - the central segment of the helix, which is connecting the N- and C-terminal lobe of CaM - is also affected upon binding to NPs.

Assuming that the NMR signal is a population-weighted average of holo CaM and NP-bound CaM an attenuation of the NMR signals upon addition of NPs is expected. Indeed, we observe an overall reduction of signal intensity. The signal reduction is more pronounced in those regions that also experience CSP, namely the N-terminal lobe and the linker region. The C-terminal domain, however, shows slightly less pronounced signal reduction. We thus conclude that the C-terminal domain is not in direct contact with the NP and thus showing dynamical behavior which is significantly different from the NP in terms of molecular tumbling. The average intensity ratio  $I_{\text{NP}}/I_0$  in the N-terminal domain is  $0.84 \pm 0.08$  with the intensity in presence and absence of NPs,  $I_{\text{NP}}$  and  $I_0$ , respectively, thus 16% of CaM is bound to NP under these conditions. As the average CSP on CaM NP interaction is rather small, we conclude that the conformations of holo CaM and NP-bound CaM are very similar.

Paramagnetic relaxation enhancement (PRE) is based on a dramatic effect of unpaired electrons on NMR spectra and has been widely used to characterize dark states, e.g. transiently populated states or high molecular weight complexes, by NMR spectroscopy<sup>26,27</sup>. Recently, PRE has been used to characterize the interface of ubiquitin transiently absorbed to lanthanide-doped, paramagnetic  $\text{SrF}_2:\text{Y}^{3+}$ ,  $\text{Gd}^{3+}$  NPs<sup>24</sup>. We adapted this approach to study the interaction of CaM with  $\text{CaF}_2$  NPs. For our experiment we used paramagnetic  $\text{CaF}_2:\text{Y}^{3+}$ ,  $\text{Gd}^{3+}$  NPs and  $\text{CaF}_2:\text{Y}^{3+}$  NPs as the diamagnetic reference. Figure 5b shows the PRE, described as the signal intensity of the paramagnetic state over the intensity in the diamagnetic state ( $I^{\text{para}}/I^{\text{dia}}$ ), plotted against the sequence of CaM. Residues which experience the highest PRE fall in a region between amino acids 77 to 87, representing the centre of the interconnecting helix, congruent with the region identified by CSP. However, residues involved in calcium binding of all four EF hands show only very little PRE. This observation is consistent with the occurrence of a short-lived encounter complex, which is most likely driven by an unspecific electrostatic interaction between a negatively charged region on CaM (the sequence of the linker stretch is very acidic  $^{77}\text{MKD}\text{T}\text{D}\text{S}\text{E}\text{E}\text{E}^{87}$ ) and  $\text{Ca}^{2+}$  on the surface of the nanoparticle.

PREs are population-averaged with  $1/r^6$ , where  $r$  is the distance between the paramagnetic center and the nucleus under investigation. Therefore, even short-lived intermediates, which bind close to the paramagnetic center can yield significant PREs, although CSPs can be small or even unobservable for such transient

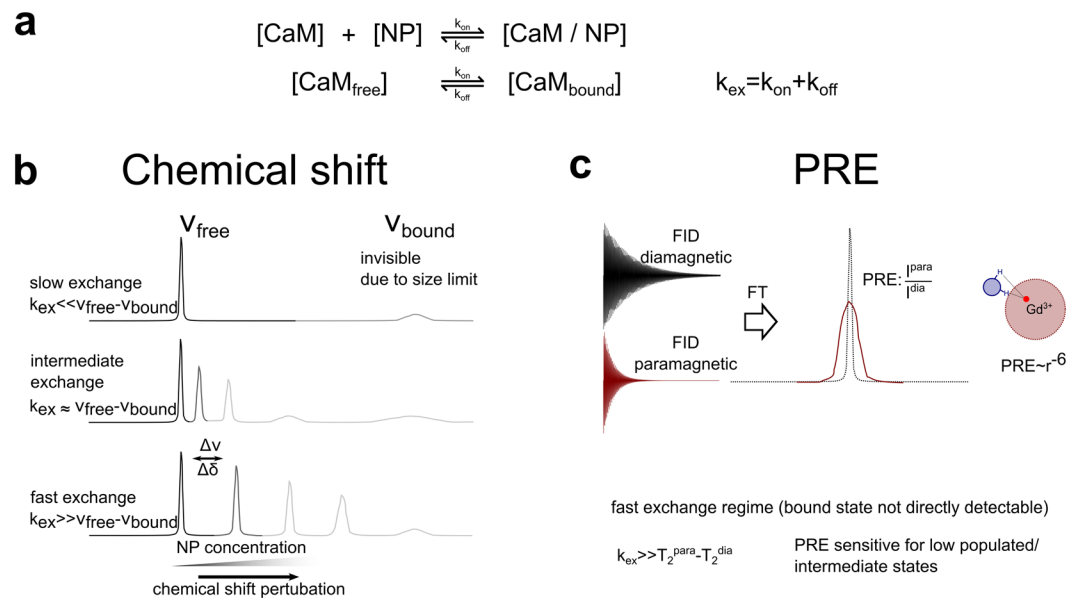


**Figure 4.** Schematic representation of the association and dissociation equilibria between CaM and CaF<sub>2</sub> NP as monitored by chemical shift perturbation (CSP) and paramagnetic relaxation enhancement (PRE). (a) Chemical equilibrium of CaM/CaF<sub>2</sub> NP interaction. Exchange between free and NP-bound CaM is determined by the exchange rate constant ( $k_{\text{ex}}$ ) which depends on the association and dissociation rate constants ( $k_{\text{on}}$  and  $k_{\text{off}}$  respectively). (b) CSP upon CaM/NP interaction. Under slow exchange condition NP-bound CaM cannot be observed by NMR. However, given that chemical exchange is fast on the chemical shift timescale, one signal with a population-weighted chemical shift is observable. In intermediate exchange, peaks experience exchange broadening in addition to CSP. (c) PRE upon addition of paramagnetic NPs. Interaction with paramagnetic CaF<sub>2</sub>:Y<sup>3+</sup>, Gd<sup>3+</sup> NPs causes signal broadening. PRE, measured as  $I^{\text{para}}/I^{\text{dia}}$ , is distance dependent<sup>33</sup>.

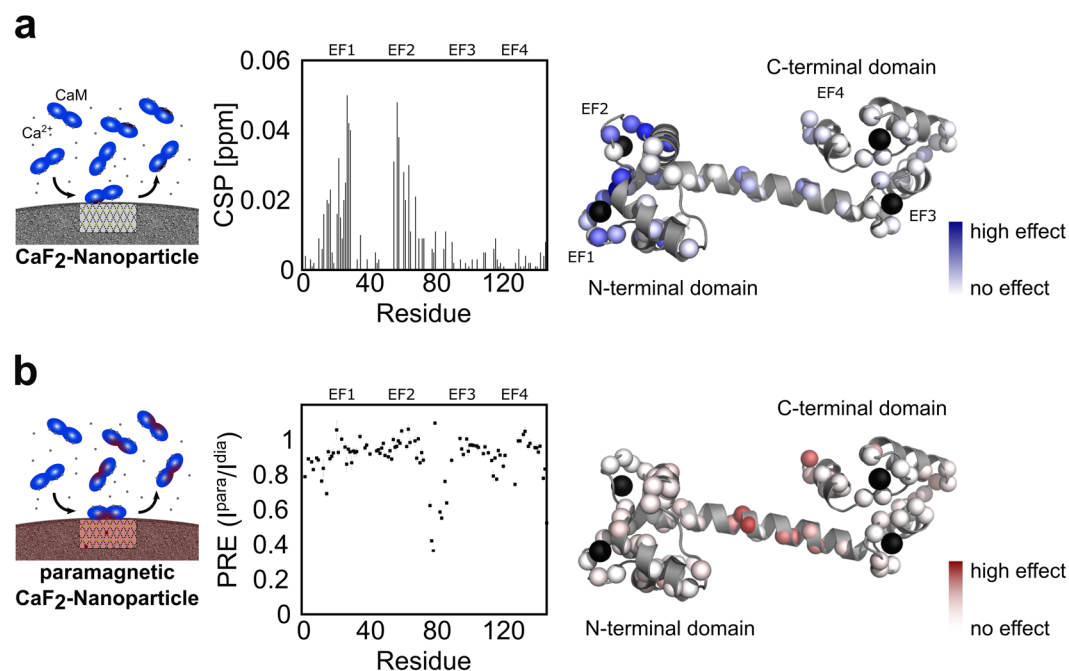


**Figure 5.** (a) Chemical shift perturbation (CSP) and (b) paramagnetic relaxation enhancement (PRE) upon CaM/NP interaction is plotted against the sequence of CaM and visualized on the protein structure. Position of the four EF-hands is indicated as EF1-4.

interactions<sup>28</sup>. On the other hand, PREs can only be observed when the complex is in fast exchange with an exchange rate  $k_{\text{ex}} > 10^2 \text{ s}^{-1}$ <sup>26</sup>. This is likely the reason for the small PREs observed in EF hands 1 and 2. Thus, the binding event can best be described by a two-step process. A transient encounter complex in fast exchange



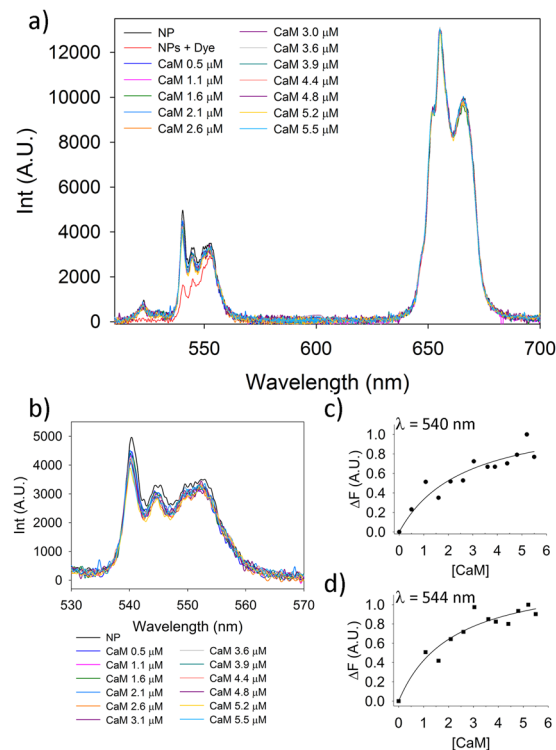


**Figure 6.** RET analysis of CaM-NP interaction (a) Upconversion spectra of CaF<sub>2</sub> NPs in CaM titration experiments. The resonance energy transfer (RET) phenomenon is evident by a strong decrease of the Er<sup>3+</sup> emission in the 520–560 nm optical range. Band assignment: (i) <sup>2</sup>H<sub>1/2</sub>→<sup>4</sup>I<sub>15/2</sub>; (ii) <sup>4</sup>S<sub>3/2</sub>→<sup>4</sup>I<sub>15/2</sub>; (iii) <sup>4</sup>F<sub>9/2</sub>→<sup>4</sup>I<sub>15/2</sub>. (b–d) Example of titration experiments of Alexa Fluor 532-conjugated CaM with a 0.5 mg/mL NPs dispersion. (b) Zoom of the spectral area showing the RET phenomenon. Notice the change in NPs emission at 540 (c) and 544nm (d).

is formed between the central helical region of CaM with the NP as indicated by PREs (Fig. 5b). This fleeting interaction is in equilibrium with a tighter complex between EF1 and EF2 with calcium sites on the nanoparticle as evidenced by CSPs (Fig. 5a).

**Affinity and kinetics of CaM-NP interactions are physiologically relevant.** In order to directly study the interaction of apo CaM and NP we utilized Resonance Energy Transfer (RET). An important feature of the CaF<sub>2</sub> host is that it can be suitably doped with luminescent lanthanide ions. In particular, Er<sup>3+</sup>, Yb<sup>3+</sup> doped CaF<sub>2</sub> NPs can generate strong upconversion (UC) emission upon excitation in the near infrared (NIR) region by using a cheap 980 nm diode laser<sup>29,30</sup>. UC emission generated by the Er<sup>3+</sup>/Yb<sup>3+</sup>-doped CaF<sub>2</sub> NPs upon NIR excitation (donor) was used to excite the suitably labelled protein (acceptor). A single point mutation in between the two N-terminal EF-hands, namely T26C, was introduced in CaM and used to site-specifically label the protein with a fluorophore (Alexa Fluor 532) that is excited at 530 nm and emits fluorescence at a maximum wavelength of 554 nm.

Indeed, a clear RET signal can be detected upon the interaction of CaM with NPs. Furthermore, titration experiments show a concentration-dependent RET phenomenon, as demonstrated by the decrease in intensity of emission bands at 540 and 544 nm, with conserved spectral intensity in the 650/670 nm range, compatible with an apparent K<sub>D</sub> of 2.5 μM for CaM-NP binding. (Fig. 6) This is in line with previous data obtained by ITC with orthologue CaM (K<sub>D</sub> = 2 μM) from *A. Thaliana*<sup>6</sup>.

The kinetics of CaM-NP interactions was monitored by SPR. Similarly to what was recently observed with GCAP1<sup>5</sup>, CaF<sub>2</sub> NPs interact with immobilized CaM if the surface of the particle is uncoupled to other CaM molecules. In the case of a “protein corona” formed by CaM molecules previously incubated with NPs, no association was indeed observed (Fig. 7). The dashed grey line in Fig. 7a reports, as an example, the case of 1.6 μM CaM incubated at room temperature with 0.1 mg mL<sup>-1</sup> NPs; similar results were obtained with other amounts of NP/protein. Several injections of NPs in a 0.1–0.5 mg mL<sup>-1</sup> concentration range showed that, similar to the GCAP1 case<sup>5</sup>, the association process does not follow a Langmuir adsorption model, as no specific dependency on the NP concentration could be detected for the SPR signal. Moreover, approximately 400 s are needed for the system to relax after NP injection (Fig. 7a), a phenomenon that was previously interpreted as a combination of protein conformational change<sup>31,32</sup> and NP diffusion in the polysaccharide matrix on the sensor chip<sup>5</sup> that reflects in a ~200 s continuous increase in the SPR signal after the injection of NPs was interrupted. When real dissociation is concerned, however, the dissociation phase could be nicely fitted to a single exponential function, leading to a k<sup>off</sup> = (3.5 ± 0.4) × 10<sup>-3</sup> s<sup>-1</sup>, compatible with a fairly faster dissociation, which appeared to be completed in 2000 s,

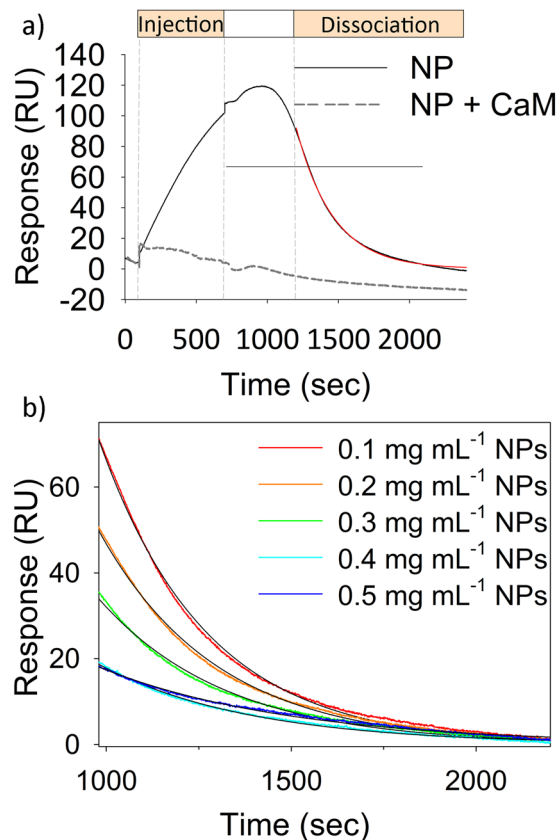


**Figure 7.** SPR analysis of CaM-NP interaction. **(a)** Example of sensorgram obtained by flowing NPs (0.1 mg/mL) on a flow cell, where 2400 RU of CaM were previously immobilized via amine coupling. Injection was performed for 600 s (flow rate 10  $\mu$ L/min) and dissociation was followed for 1800 s. The red curve refers to data fitting using a single exponential function. The dashed grey line refers to injection of the same amount of NPs previously incubated with 1.6  $\mu$ M CaM. **(b)** Example of dissociation curves obtained by SPR overlapped to the fitting curves according to a single exponential in the 0.1–0.5 mg/mL NP range.

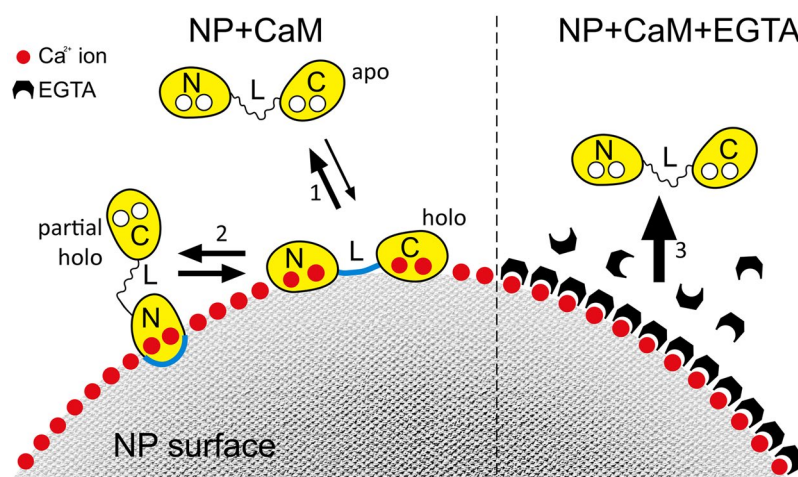


**Figure 8.** Schematic representation of NP-CaM interactions. Left side: when apo CaM is incubated with NPs, two different equilibria establish. PRE experiments suggest that the first contact between CaM and NP is mediated by the central linker (L) region. At this point, CaM can either return to the apo state (1) through a rapid dissociation by the NP surface, or be converted into a more stable NP-bound conformation (holo), via an interaction mostly involving the N-terminal domain (2), as suggested by CSP experiments. Right side: when an excess of EGTA (black blocks) is added, the chelator binds  $\text{Ca}^{2+}$  ions on the NP surface, thus restoring the apo-CaM conformation (3), as suggested by near- and farUV spectra (Fig. 1a). Blue thick lines represent the areas mostly involved in CaM/NPs interaction.

thus being fully compatible with potential nanomedicine applications. The fact that the complete dissociation for GCAP1 was observed after ~6500 s under similar conditions probably reflects the significantly higher affinity of GCAP1 for CaF<sub>2</sub> NPs (12 nM)<sup>5</sup>.

## Conclusions

In this study, we present a general methodology to comprehensively describe the binding of proteins to NPs by using a combination of biophysical techniques. As a specific example, we found that the binding of the prototypical calcium sensor CaM to CaF<sub>2</sub> NPs can be described by a two-step process, involving the formation of an intermediate encounter complex involving the linker region. Specific interaction of CaM to CaF<sub>2</sub> NPs is driven by the N-terminal EF-hands, which seem to recognize Ca<sup>2+</sup> on the surface of the nanoparticle. If high amounts of chelating molecules such as EGTA are added to the system, the dissociation of CaM from the NP surface is favored and brings the protein back to its apo-form. Interestingly, some of us previously demonstrated that CaM dissociated from the CaF<sub>2</sub> NP surface is functional and can fully activate a protein target<sup>6</sup>. We summarize the emerging model of interaction between CaM and CaF<sub>2</sub> NPs in Fig. 8.

A major advantage of our comprehensive analysis is that, beside a static picture of the protein-NP system at the equilibrium that can be obtained by several physicochemical approaches, it offers a more dynamic description that provides information as to the kinetics of the association/dissociation processes. While further studies are needed to thoroughly decipher the complex kinetics of association, we clearly showed that once the association to CaF<sub>2</sub> NPs has occurred, for instance by previous incubation, the dissociation of CaM from the NP surface is complete in 2000 s, thus pointing to physiological relevance of the process.

The unique feature of having a large surface-to-volume ratio confers NPs the possibility to safely carry a functional protein on the surface of the device. This could be exploited in future studies for delivery purposes in the increasing cases in which CaM has been shown to be associated to specific disease states.

**Availability of materials and data.** All materials, data and protocols associated with this manuscript are promptly available to readers without undue qualifications in material transfer agreements.

## References

- Colvin, V. L. The potential environmental impact of engineered nanomaterials. *Nat Biotechnol* **21**, 1166–1170 (2003).
- Davis, M. E., Chen, Z. & Shin, D. M. Nanoparticle therapeutics: an emerging treatment modality for cancer. *Nat Rev Drug Discov* **7**, 771–782 (2008).
- Cheng, C. J., Tietjen, G. T., Saucier-Sawyer, J. K. & Saltzman, W. M. A holistic approach to targeting disease with polymeric nanoparticles. *Nat Rev Drug Discov* **14**, 239–247 (2015).
- Marino, V., Astegno, A., Pedroni, M., Piccinelli, F. & Dell'Orco, D. Nanodevice-induced conformational and functional changes in a prototypical calcium sensor protein. *Nanoscale* **6**, 412–423, <https://doi.org/10.1039/c3nr04978g> (2014).
- Marino, V., Borsatto, A., Vocke, F., Koch, K. W. & Dell'Orco, D. CaF<sub>2</sub> nanoparticles as surface carriers of GCAP1, a calcium sensor protein involved in retinal dystrophies. *Nanoscale*, <https://doi.org/10.1039/c7nr03288a> (2017).
- Astegno, A. *et al.* Structural plasticity of calmodulin on the surface of CaF<sub>2</sub> nanoparticles preserves its biological function. *Nanoscale* **6**, 15037–15047, <https://doi.org/10.1039/c4nr04368e> (2014).
- Carafoli, E. Calcium signaling: a tale for all seasons. *Proc Natl Acad Sci USA* **99**, 1115–1122, <https://doi.org/10.1073/pnas.032427999> (2002).
- Chin, D. & Means, A. R. Calmodulin: a prototypical calcium sensor. *Trends Cell Biol* **10**, 322–328 (2000).
- Berchtold, M. W. & Villalobo, A. The many faces of calmodulin in cell proliferation, programmed cell death, autophagy, and cancer. *Biochim Biophys Acta* **1843**, 398–435, <https://doi.org/10.1016/j.bbamcr.2013.10.021> (2014).
- Crotti, L. *et al.* Calmodulin mutations associated with recurrent cardiac arrest in infants. *Circulation* **127**, 1009–1017, <https://doi.org/10.1161/CIRCULATIONAHA.112.001216> (2013).
- Esteras, N. *et al.* Calmodulin levels in blood cells as a potential biomarker of Alzheimer's disease. *Alzheimers Res Ther* **5**, 55, <https://doi.org/10.1186/alzrt219> (2013).
- Pedroni, M. *et al.* Water (H<sub>2</sub>O and D<sub>2</sub>O) Dispersible NIR-to-NIR Upconverting Yb<sup>3+</sup>/Tm<sup>3+</sup> Doped MF<sub>2</sub> (M = Ca, Sr) Colloids: Influence of the Host Crystal. *Cryst Growth Des* **13**, 4906–4913, <https://doi.org/10.1021/cg401077v> (2013).
- Dong, N. N. *et al.* NIR-to-NIR Two-Photon Excited CaF<sub>2</sub>: Tm<sup>3+</sup>, Yb<sup>3+</sup> Nanoparticles: Multifunctional Nanoprobes for Highly Penetrating Fluorescence Bio-Imaging. *ACS Nano* **5**, 8665–8671, <https://doi.org/10.1021/nn202490m> (2011).
- Delaglio, F. *et al.* Nmrpipe - a Multidimensional Spectral Processing System Based on Unix Pipes. *J Biomol Nmr* **6**, 277–293 (1995).
- Vranken, W. F. *et al.* The CCPN data model for NMR spectroscopy: Development of a software pipeline. *Proteins* **59**, 687–696 (2005).
- Sattler, M., Schleucher, J. & Griesinger, C. Heteronuclear multidimensional NMR experiments for the structure determination of proteins in solution employing pulsed field gradients. *Prog Nucl Mag Res Sp* **34**, 93–158 (1999).
- Zhang, M., Tanaka, T. & Ikura, M. Calcium-induced conformational transition revealed by the solution structure of apo calmodulin. *Nat Struct Biol* **2**, 758–767 (1995).
- Sulmann, S., Dell'Orco, D., Marino, V., Behnen, P. & Koch, K. W. Conformational changes in calcium-sensor proteins under molecular crowding conditions. *Chemistry* **20**, 6756–6762, <https://doi.org/10.1002/chem.201402146> (2014).
- Assfalg, M. *et al.* The study of transient protein-nanoparticle interactions by solution NMR spectroscopy. *Biochim Biophys Acta* **1864**, 102–114, <https://doi.org/10.1016/j.bbapap.2015.04.024> (2016).
- Zanzoni, S. *et al.* Polyhydroxylated [60]fullerene binds specifically to functional recognition sites on a monomeric and a dimeric ubiquitin. *Nanoscale* **7**, 7197–7205, <https://doi.org/10.1039/c5nr00539f> (2015).
- Shrivastava, S. *et al.* Identifying specific protein residues that guide surface interactions and orientation on silica nanoparticles. *Langmuir* **29**, 10841–10849, <https://doi.org/10.1021/la401985d> (2013).
- Calzolari, L., Franchini, F., Gilliland, D. & Rossi, F. Protein-nanoparticle interaction: identification of the ubiquitin-gold nanoparticle interaction site. *Nano Lett* **10**, 3101–3105, <https://doi.org/10.1021/nl101746v> (2010).
- Mangini, V. *et al.* Amyloid transition of ubiquitin on silver nanoparticles produced by pulsed laser ablation in liquid as a function of stabilizer and single-point mutations. *Chemistry* **20**, 10745–10751, <https://doi.org/10.1002/chem.201402934> (2014).
- Zanzoni, S., Pedroni, M., D'Onofrio, M., Speghini, A. & Assfalg, M. Paramagnetic Nanoparticles Leave Their Mark on Nuclear Spins of Transiently Adsorbed Proteins. *J Am Chem Soc* **138**, 72–75, <https://doi.org/10.1021/jacs.5b11582> (2016).
- Lundqvist, M., Sethson, I. & Jonsson, B. H. High-resolution 2D 1H-15N NMR characterization of persistent structural alterations of proteins induced by interactions with silica nanoparticles. *Langmuir* **21**, 5974–5979, <https://doi.org/10.1021/la050569j> (2005).
- Anthis, N. J. & Clore, G. M. Visualizing transient dark states by NMR spectroscopy. *Q Rev Biophys* **48**, 35–116, <https://doi.org/10.1017/S0033583514000122> (2015).

27. Otting, G. Protein NMR using paramagnetic ions. *Annu Rev Biophys* **39**, 387–405, <https://doi.org/10.1146/annurev.biophys.093008.131321> (2010).
28. Liu, Z., Gong, Z., Dong, X. & Tang, C. Transient protein-protein interactions visualized by solution NMR. *Biochim Biophys Acta* **1864**, 115–122, <https://doi.org/10.1016/j.bbapap.2015.04.009> (2016).
29. Cantarelli, I. X. *et al.* Multifunctional nanoprobe based on upconverting lanthanide doped CaF<sub>2</sub>: towards biocompatible materials for biomedical imaging. *Biomater Sci-Uk* **2**, 1158–1171, <https://doi.org/10.1039/c4bm00119b> (2014).
30. Pedroni, M. *et al.* Lanthanide doped upconverting colloidal CaF<sub>2</sub> nanoparticles prepared by a single-step hydrothermal method: toward efficient materials with near infrared-to-near infrared upconversion emission. *Nanoscale* **3**, 1456–1460, <https://doi.org/10.1039/c0nr00860e> (2011).
31. Sulmann, S., Dell'Orco, D., Marino, V., Behnen, P. & Koch, K. W. Conformational changes in calcium-sensor proteins under molecular crowding conditions. *Chemistry* **20**(22), 6756–62 <https://doi.org/10.1002/chem.201402146> (2014).
32. Dell'Orco, D., Müller, M. & Koch, K. W. Quantitative detection of conformational transitions in a calcium sensor protein by surface plasmon resonance. *Chemical Communications* **46**(39), 7316 <https://doi.org/10.1039/c0cc02086a> (2010).
33. Battiste, J. L. & Wagner, G. Utilization of site-directed spin labeling and high-resolution heteronuclear nuclear magnetic resonance for global fold determination of large proteins with limited nuclear overhauser effect data. *Biochemistry* **39**, 5355–5365 (2000).

## Acknowledgements

This work was partly supported by a Telethon Italy grant (GGP16010) to D.D.O. P.C. and A.S. acknowledge the University of Verona, Verona, Italy, for financial support in the framework of “Ricerca di Base 2015” project. The Centro Piattaforme Tecnologiche of the University of Verona is acknowledged for the use of the SPR instrument. DK Molecular Enzymology (to KMP) from the Austrian Science Fund is gratefully acknowledged.

## Author Contributions

G.D.C. performed limited proteolysis, CD and, together with D.D.O., SPR measurements. G.E.W., K.Z. and N.H.M. performed NMR analysis. P.C. and A.S. synthesized nanoparticles. P.C., A.S., D.D.O. and G.D.C. performed RET measurements and analysis. K.M.P., G.W. and N.H.M. prepared protein samples. D.D.O. and N.H.M. conceived the project and wrote the manuscript with contributions from all authors.

## Additional Information

**Supplementary information** accompanies this paper at <https://doi.org/10.1038/s41598-018-21571-y>.

**Competing Interests:** The authors declare no competing interests.

**Publisher's note:** Springer Nature remains neutral with regard to jurisdictional claims in published maps and institutional affiliations.



**Open Access** This article is licensed under a Creative Commons Attribution 4.0 International License, which permits use, sharing, adaptation, distribution and reproduction in any medium or format, as long as you give appropriate credit to the original author(s) and the source, provide a link to the Creative Commons license, and indicate if changes were made. The images or other third party material in this article are included in the article's Creative Commons license, unless indicated otherwise in a credit line to the material. If material is not included in the article's Creative Commons license and your intended use is not permitted by statutory regulation or exceeds the permitted use, you will need to obtain permission directly from the copyright holder. To view a copy of this license, visit <http://creativecommons.org/licenses/by/4.0/>.

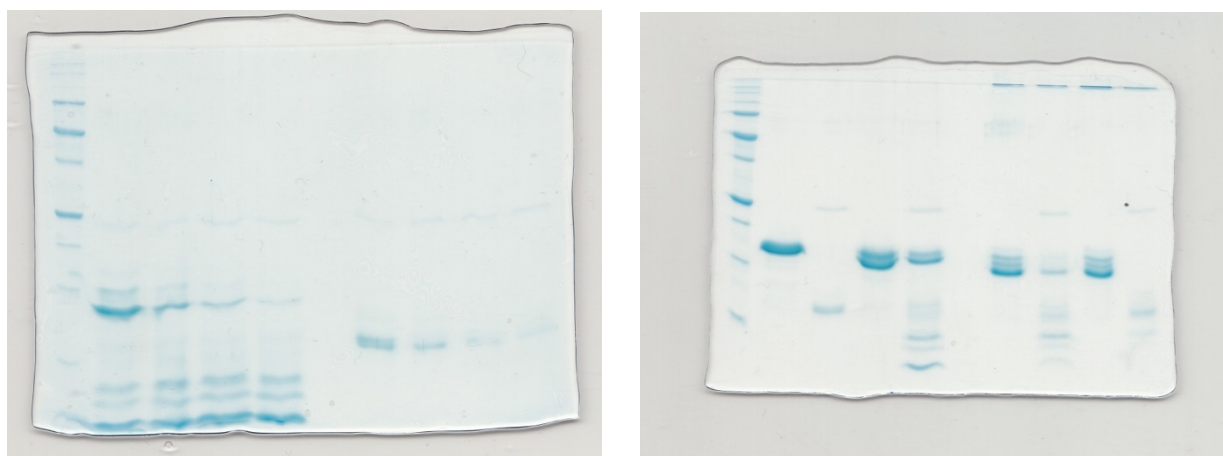
© The Author(s) 2018

## Supplementary information

### **Luminescent and paramagnetic properties of nanoparticles shed light on their interactions with proteins**

by Giuditta Dal Cortivo, Gabriel E. Wagner, Paolo Cortelletti, Krishna Mohan Padmanabha Das, Klaus Zangger, Adolfo Speghini, and Daniele Dell'Orco, N. Helge Meyer

#### **Supplementary Figure S1**



Full-length gels (uncropped) used to prepare panels **a** (left) and **b** (right) in Figure 2, respectively.